



中国科学院大学
University of Chinese Academy of Sciences



国立大学法人
群馬大学
GUNMA UNIVERSITY

Time-resolved Dynamics of Horizontal Particle-laden Jets

**A dissertation submitted to
Institute of Process Engineering, Chinese Academy of Sciences
and Gunma University
in partial fulfillment of the requirement
for the degree of
Doctor of Philosophy
in Mechanical Engineering**

By

Qingzhan Li (T202B602)

Supervisor : Professor Wei Wang

Professor Tomohiko Furuhashi

Assist Supervisor : Associate Professor Yanpei Chen

Associate Professor Fei Li


Institute of Process Engineering, Chinese Academy of Sciences

Gunma University, Japan

May 2023

Statement of Originality

I solemnly declare that the dissertation submitted is the result of my independent research work under the guidance of my supervisors. To the best of my knowledge, this paper does not contain any other published or written research by individuals or groups, except for those already cited in the text. Other individuals and collectives who have contributed to the research work covered by the paper are clearly indicated or acknowledged in the text.

Signature: Li Qingshan 

Date: 5/2023

Abstract

The dynamics of particle-laden jet is a challenging issue, and it is important to both jet-related industry applications and understanding the transmission of virus through violent expiratory events. The high-speed gas turbulence, being strongly interacted with and modulated by the collective motion of particles over a wide range of time and length scales, composes the major difficulties of the issue. The polydispersity of particles adds more complexities into the interaction between the gas turbulence and particle motion.

Numerous efforts have been endeavored to tackle these difficulties through using experimental or simulation methods. However, most experimental studies rely on steady 2D measurements, which is insufficient for revealing the time-resolved, 3D expansion behavior of the jet flow. Whereas the simulation of circular gas jet flows, let alone the particle-laden jet flows, is also hindered by the poor understanding of the key factors such as the turbulence modulation, jet diffusivity and entrainment, and gas-solid interphase forces, especially the drag force. For example, due to the absence of a suitable dilute-phase drag model, the single-particle drag model is often used in simulations, which often makes the simulation results inconsistent with reality. Therefore, it is necessary to develop a time-resolved, 3D multiphase flow measurement method to investigate the key factors and thereby reveal the dynamics of particle-laden jet flows.

To this end, recognizing the polydispersity of normally encountered jet flow systems, this thesis combines both experimental and simulation methods to analyze the dynamics of a horizontal jet flow system with three typical particles (classified by the Stokes number: tracer particles, small particles, and large particles), with particular

emphasis on the jet velocity field, jet dispersion process (particle concentration / clusters), drag model, particle volume fraction model, etc. The main contents and results are as follows:

1. To better understand the dynamics of the particle-laden jet at the particle level, we construct a hybrid 3D-PTV & PIV platform, thereon develop a real tracking-precede-reconstruction, time-resolved, 3D particle flow field reconstruction method. Based on that platform, we are able to study both the gas and particle flow fields with high resolution, the interphase drag force, the expansion and turbulence behavior of the jet flow.

2. For the high-Stokes-number particle-laden jet with large particles (glass beads), the hybrid measurement of 3D-PTV and PIV shows that the presence of particles significantly changes the gas turbulence and stretches the gas flow field downstream. The PDF of the axial particle velocity shows a non-Gaussian distribution and deviates significantly from that of the spanwise velocities, indicating strong non-equilibrium and anisotropic states. A new drag model is obtained based on the reconstructed particle trajectories and gas flow field. And the simulation with this new drag is found in better agreement with the experimental data than using the standard single-particle drag model. A simple particle volume fraction model is also developed based on the self-similarity theory of the jet, showing good agreement with the experimental measurements.

3. The dynamics of low- and middle- Stokes-number particle-laden jets (tracer particles and SiO₂ microspheres) are investigated with PIV measurements. It is found that the jet velocity decay in both the gas and particles can be described by the classical jet velocity decay model. The small particle velocity decay is better predicted with an error of up to 16%. Both the gas and particle velocity exhibit self-similarity. The mesoscale structure and particle concentration of small particles are studied based on

the large-field measurement, Voronoi method and a new cluster characterization method. The particle clustering process in the jet is dynamically stable. As the Stokes number tends to be unity, the preferential concentration effect is more significant. The distribution of small clusters satisfies the power-law distribution of the penetration theory. And the new particle volume fraction model is also suitable for middle-Stokes-number particle-laden jet with small particles.

4. Both the high- and middle- Stokes-number particle-laden jets are simulated using the CFD-DPM method. 11 different drag models are constructed based on the new drag correlation, Standard drag and Rudinger drag. The effects of different drag models on jet velocity and the sensitivity to the Re is revealed, and the effects of entrainment, inlet velocity distribution, and outlet boundary conditions on the jet are discussed. The results indicate that the new drag model for horizontal particle-laden jets (HPJ) more accurately predict the velocity of large particles/ high-Stokes-number particle-laden jets while the single-particle drag model, Wen-Yu/Gidaspow drag model, and Rudinger drag model all underestimate the particle velocity. As for middle-Stokes-number particle-laden jet with small particles, the new drag model partially agrees with the current limited experimental data. In addition, there are strong entrainment and a velocity distribution which neither parabolic nor log-linear in circular turbulent jets.

In summary, with the time-resolved 3D-PTV measurement at the particle level, the dynamics of three typical particles are studied in terms of the mean velocity, fluctuating velocity, particle concentration, and mesoscale structures. The interaction between gas turbulence and particle motion is analyzed. A new HPJ drag model is established and verified, bridging the gap on the drag modeling in the field of particle-laden jets.

Keywords: Multiphase Turbulence; Particle-laden Jet; Drag; PIV&PTV; CFD–DPM

Contents

| | |
|---|----|
| Chapter 1 Introduction | 1 |
| 1.1 Background and Significance | 1 |
| 1.2 Spatiotemporal Evolution of Particle-laden Jet Flows..... | 3 |
| 1.2.1 Mesoscale Structure | 3 |
| 1.2.2 Particle Concentration..... | 6 |
| 1.2.3 Velocity | 10 |
| 1.2.4 Deposition Distance of Particles | 11 |
| 1.2.5 Interaction of Turbulence and Particles | 13 |
| 1.3 Experimental Measurement Techniques for Multiphase Flow | 14 |
| 1.4 Reconstruction Methods of 3D Particle Flow Field | 20 |
| 1.5 Drag Models and Simulations..... | 21 |
| 1.5.1 Single Particle Drag Models | 22 |
| 1.5.2 Uniform Particle Swarm Drag Models | 23 |
| 1.5.3 Heterogeneous Particle Swarm Drag Models | 25 |
| 1.5.4 Dilute Particle Swarm Drag Models | 28 |
| 1.5.5 Simulations of Particle-laden Jets..... | 29 |
| 1.6 Research Contents..... | 30 |
| Chapter 2 Experimental Methods | 33 |
| 2.1 Overview..... | 33 |

| | |
|---|-----------|
| 2.2 Experimental Setup..... | 34 |
| 2.3 Materials | 36 |
| 2.3.1 Gas Tracer Particles | 36 |
| 2.3.2 Small Particles | 36 |
| 2.3.3 Large Particles..... | 37 |
| 2.4 Particle Image Velocimetry..... | 39 |
| 2.4.1 Camera Calibration | 39 |
| 2.4.2 Velocity Calculation Principle | 39 |
| 2.5 Time-resolved 3D Particle Tracking Velocimetry..... | 41 |
| 2.5.1 Camera Calibration | 43 |
| 2.5.2 Image Pre-processing..... | 44 |
| 2.5.3 Particle Detection..... | 45 |
| 2.5.4 Lagrangian Particle Tracking..... | 46 |
| 2.5.5 Multi-view 3D Reconstruction | 51 |
| 2.5.6 Comparison with Other 3D-PTV Methods | 56 |
| 2.6 Conclusions..... | 58 |
| Chapter 3 Dynamics of High-Stokes-number Particle-laden Jets | 61 |
| 3.1 Overview..... | 61 |
| 3.2 Experimental Parameters | 61 |
| 3.3 Gas Flow Characteristics: Effects of Particles..... | 62 |
| 3.4 Particles Flow Characteristics..... | 68 |

| | |
|---|-----------|
| 3.4.1 Global Particle Profiles | 68 |
| 3.4.2 Particle-level Velocity Tracking..... | 70 |
| 3.4.3 Mean and Fluctuating Particle Velocity | 71 |
| 3.4.4 Particle Volume Fraction..... | 74 |
| 3.5 Modeling for Particle Dispersion and Drag | 76 |
| 3.5.1 Particle Volume Fraction..... | 76 |
| 3.5.2 Drag Correlation | 79 |
| 3.5.3 More Discussions..... | 85 |
| 3.6 Conclusions..... | 86 |
| Chapter 4 Dynamics of Low- and Middle-Stokes-number Particle-laden Jets..... | 89 |
| 4.1 Overview..... | 89 |
| 4.2 Experimental Parameters | 90 |
| 4.3 Low-Stokes-number Particle-laden jets (Gas Flow) Characteristics | 93 |
| 4.3.1 Instantaneous Gas Velocity | 93 |
| 4.3.2 Mean and Fluctuating Gas Velocity | 94 |
| 4.3.3 Gas Velocity Decay..... | 99 |
| 4.3.4 Eulerian Self-similarity Properties..... | 102 |
| 4.4 Middle-Stokes-number Particle-laden jets (Particle Flow) Characteristics..... | 103 |
| 4.4.1 Instantaneous Particle Velocity | 103 |
| 4.4.2 Mean and Fluctuating Particle Velocity | 105 |

| | |
|---|------------|
| 4.4.3 Particle Velocity Decay | 111 |
| 4.4.4 Eulerian Self-similarity Properties..... | 113 |
| 4.5 Mesoscale Structure and Particle Concentration of Middle-Stokes-number Particle-laden jets..... | 114 |
| 4.5.1 Clusters and Preferential Concentration | 114 |
| 4.5.2 Particle Volume Fraction..... | 124 |
| 4.6 Conclusions..... | 129 |
| Chapter 5 Simulations of Particle-laden Jets | 131 |
| 5.1 Overview..... | 131 |
| 5.2 Mathematical Models..... | 131 |
| 5.2.1 Continuous Phase Models..... | 131 |
| 5.2.2 Discrete Phase Models | 135 |
| 5.3 Drag Models for Simulations..... | 140 |
| 5.4 Simulation Settings | 145 |
| 5.4.1 Material Properties..... | 145 |
| 5.4.2 Geometric Models..... | 146 |
| 5.4.3 Meshing..... | 147 |
| 5.4.4 Fluent Operations..... | 148 |
| 5.4.5 Mesh-independence Verification..... | 151 |
| 5.4.6 Case Outline..... | 151 |
| 5.5 Simulation Results of High-Stokes-number Particle-laden Jets | 152 |

| | |
|--|-----|
| 5.5.1 Effects of Drag Models | 152 |
| 5.5.2 Effects of Entrainment on Jet Velocity | 154 |
| 5.5.3 Effects of Inlet Velocity Distribution on Jet Velocity | 155 |
| 5.5.4 Effects of Outlet Type on Jet Velocity | 157 |
| 5.6 Applicability of Drag Models to Middle-Stokes-number Particle-laden Jets.. | 158 |
| 5.6.1 Effects of Drag Models | 158 |
| 5.6.2 Discussions of Different Initial Velocities | 161 |
| 5.7 Conclusions..... | 162 |
| Chapter 6 Summary and Outlook | 165 |
| 6.1 Main Conclusions | 165 |
| 6.2 Outlook | 166 |
| Appendix A Drag Models for Single Particle | 167 |
| Appendix B Drag Models for Uniform Particle Systems..... | 169 |
| Appendix C Parameters of EMMS Drag Model for Heterogeneous Systems | 173 |
| Appendix D Filtered Drag Models for Heterogeneous Systems | 175 |
| Appendix E Drag Model Selection in Pneumatic Conveying and Jet Flow Scenarios | 177 |
| Appendix F Drag Model Selection in Violent Expiratory Events | 179 |
| Appendix G Case Settling..... | 181 |
| References..... | 183 |

Acknowledgments.....205

Author's Resume and Academic Papers and Research Results Published
During Degree Study207

Figures catalog

| | |
|---|----|
| Figure 1.1 Scenarios for multiphase jets ^{1, 2, 6, 12, 13} | 1 |
| Figure 1.2 Schematic diagram of a typical single-phase gas jet ²¹ | 2 |
| Figure 1.3 (a) Unforced single-phase flow and (b) unforced particle-laden flow ²⁴ | 4 |
| Figure 1.4 (a) Forced single-phase flow and (b) forced particle-laden flow (c) cartoon of particles interacting with vortex ring ²⁴ | 4 |
| Figure 1.5 Schematic diagram of oscillations and their location relative to a vortex structure. ⁵³ | 7 |
| Figure 1.6 (a) Particle concentration contour and (b) particle number probability density distribution ⁶² | 9 |
| Figure 1.7 (a) Original particle image. (b) Voronoi diagram of this image in which white dots denote the original particles. ⁶⁵ | 9 |
| Figure 1.8 Comparison of normalized Voronoi area PDF and random Poisson distribution ⁶¹ | 10 |
| Figure 1.9 Sketch of a typical setup for PIV/PTV measurement in a wind tunnel ¹¹⁴ .. | 16 |
| Figure 1.10 The frame straddling technique sketch for PIV | 17 |
| Figure 1.11 Curves of various single-particle drag models | 23 |
| Figure 1.12 Errors curves of single-particle drag models relative to standard drag model | 23 |
| Figure 1.13 Comparison of Rudinger drag curve with the standard drag curve | 28 |
| Figure 1.14 Schematic diagram of the research framework | 32 |

| | |
|---|----|
| Figure 2.1 Schematic diagram of experimental device..... | 35 |
| Figure 2.2 Tracer particle seeder (a) and Solid particle seeder (b). | 37 |
| Figure 2.3 The measured particle size distribution of glass beads..... | 37 |
| Figure 2.4 Schematic diagram of the hopper feeding | 38 |
| Figure 2.5 CAMSIZER X2 | 38 |
| Figure 2.6 The measured particle size distribution of glass beads..... | 38 |
| Figure 2.7 Effects of different lenses on captured images | 39 |
| Figure 2.8 Velocity calculation principle of PIV | 41 |
| Figure 2.9 Snapshots of the jet using DOS tracer particles and corresponding gas velocity vector..... | 41 |
| Figure 2.10 Schematic of the processing routines of 4D-PTV..... | 42 |
| Figure 2.11 Schematic diagram of the placement of the calibration board and the camera | 43 |
| Figure 2.12 Calibration results (a,b) and errors (c)..... | 43 |
| Figure 2.13 Particles detection steps: (a) raw image, (b) image segmentation, (c) binary image, (d) particle detection results. | 45 |
| Figure 2.14 Lagrangian particle tracking flowchart | 48 |
| Figure 2.15 Schematic diagram of Kalman Filter..... | 49 |
| Figure 2.16 Kalman Filter flowchart | 49 |
| Figure 2.17 Particle trajectories of 100 frames at (a) front view, (b) top view. | 51 |
| Figure 2.18 Results of reconstruction of the particle flow field | 55 |

Figure 2.19 Comparison of different time-resolved 3D-PTV (T: tracking; R: reconstruction). 57

Figure 3.1 Instantaneous gas velocity profiles..... 63

Figure 3.2 Contour maps of time-averaged gas velocity and fluctuating velocity of XY plane: single-phase jet (a-d) and two-phase jet (e-h). 65

Figure 3.3 Time-averaged gas velocity and fluctuating velocity on axial (a~f) and spanwise (g~l) planes..... 67

Figure 3.4 Fluctuation frequency of particle flux at the ejector exit. 68

Figure 3.5 Profiles of the number of the particles along (a) x -axis, (b) y -axis, and (c) z -axis. 69

Figure 3.6 Lagrangian tracking u_p , corresponding u'_p , particle TKE, K_i : (a) $u_{p,x}$ rising, (b) $u_{p,x}$ invariant, (c) $u_{p,x}$ declining; and (d) variation of average particle TKE, K , along the jet centerline. 70

Figure 3.7 Time-averaged PDFs of particle velocity of the whole shooting region and on the YZ plane along the axis of the jet : (a) PDFs of $u_{p,x}$, (b) PDFs of $u_{p,y}$, and (c) PDFs of $u_{p,z}$ 71

Figure 3.8 Contours of time-averaged and fluctuating particle velocities of central XY and XZ planes..... 72

Figure 3.9 The axial evolution of the time-averaged $u_{p,x}$, $u'_{p,x}$ and spanwise evolution of the time-averaged $|u_{p,y}|$, $u'_{p,y}$ of XY plane (a~d), XZ plane (e~h)..... 74

Figure 3.10 Time-averaged particle volume fraction PDF in the whole shooting region determined by the 3D Voronoi method. 75

Figure 3.11 Contour of the experimental values of time-averaged particle volume

| | |
|--|----|
| fraction on XY plane (a) and XZ plane (b)..... | 75 |
| Figure 3.12 Schematic of the trajectory of a particle and cloud with radius r at position s from a jet. | 77 |
| Figure 3.13 Axial evolution of particle volume fraction along the jet centerline calculated with (a) different C_θ , (b) different η , (c) different combinations of C_θ and η with $\eta C_\theta^3 = 2.7 \times 10^5$ | 78 |
| Figure 3.14 (a) Axial evolution of time-averaged $u_{p,x}$; (b) $u_{g,x}$ of single- and two-phase jets, and $u_{p,x}$, $u_{slip,x}$ of two-phase jet along the jet centerline; (c) comparison of the drag coefficients obtained in this work with those in the literatures; (d) comparison of model prediction and experimentally averaged data of $u_{p,x}$ for 100 particles along the jet centerline. | 83 |
| Figure 4.1 Schematic diagram of low-Stokes-number experimental measurement | 92 |
| Figure 4.2 Schematic diagram of middle-Stokes-number experimental measurement | 92 |
| Figure 4.3 Macroscale experiment of Exp.1: Transient gas velocity field of the gas jet. The dotted line indicates the location of the velocity maximum..... | 93 |
| Figure 4.4 Mesoscale experiments of Exp.1: Transient gas velocity field of the gas jet | 94 |
| Figure 4.5 Mesoscale experiments of Exp.1: Transient gas velocity vector field of the gas jet | 94 |
| Figure 4.6 Mean gas velocity field of Macroscale experiments: (a) Exp.1, (b) Exp.2, (c) Exp.3, (d) Exp.4, (e) Exp.5, (f) Exp.6..... | 95 |
| Figure 4.7 Mean gas velocity field of Mesoscale experiments of Exp.1: (a-g) means gradually away from the nozzle exit..... | 95 |

Figure 4.8 Mesoscale experiments of Exp.1: Gas velocity (a) and vector (b) field near the nozzle 95

Figure 4.9 Mean gas velocity evolution along the jet centerline 96

Figure 4.10 Mean gas fluctuating velocity field of Macroscale experiments: (a) Exp.1, (b) Exp.2, (c) Exp.3, (d) Exp.4, (e) Exp.5, (f) Exp.6 97

Figure 4.11 Mean gas fluctuating velocity field of Mesoscale experiments of Exp.1: (a-g) means gradually away from the nozzle exit 98

Figure 4.12 Mean gas velocity field (a) and fluctuating velocity field (b) near the nozzle of Exp.1 98

Figure 4.13 Gas fluctuating velocity evolution along the jet centerline 99

Figure 4.14 Variation of K_d with $u_{g,0}$ 101

Figure 4.15 Variation of K_d with Re 101

Figure 4.16 Variation of x_p with $u_{g,0}$ 101

Figure 4.17 Variation of β with $u_{g,0}$ 101

Figure 4.18 Comparison of model prediction and experimental values of gas velocity decay along the jet centerline 102

Figure 4.19 Profile transverse gas velocity at different axial positions of Exp.1 103

Figure 4.20 Profile transverse gas velocity of different experiments 103

Figure 4.21 Macroscale experiment of Exp.1: Transient particle velocity field of particle-laden jet 104

Figure 4.22 Mesoscale experiments of Exp.1: Transient particle velocity field of particle-laden jet 104

Figure 4.23 Mesoscale experiments of Exp.1: Transient particle velocity vector field of particle-laden jet..... 104

Figure 4.24 Mean particle velocity field of Macroscale experiments: (a) Exp.1, (b) Exp.2, (c) Exp.3, (d) Exp.4, (e) Exp.5, (f) Exp.6..... 105

Figure 4.25 Mean particle velocity field of Mesoscale experiments of Exp.1: (a-g) means gradually away from the nozzle exit..... 105

Figure 4.26 Mesoscale experiments of Exp.1: Particle velocity field (a) and vector field (b) near the nozzle..... 106

Figure 4.27 Particle velocity evolution along the jet centerline 107

Figure 4.28 Normalized particle velocity along the jet centerline compared to literature 107

Figure 4.29 Comparison of gas and particle velocities along the jet centerline 108

Figure 4.30 Mean particle fluctuating velocity field of Macroscale experiments: (a) Exp.1, (b) Exp.2, (c) Exp.3, (d) Exp.4, (e) Exp.5, (f) Exp.6..... 108

Figure 4.31 Mean particle fluctuating velocity field of Mesoscale experiments of Exp.1: (a-g) means gradually away from the nozzle exit..... 109

Figure 4.32 Comparison of fluctuating velocities of the gas and particles along the jet centerline..... 110

Figure 4.33 Normalized particle velocity along the jet centerline compared to literature 110

Figure 4.34 Variation of K_d with u_0 112

Figure 4.35 Variation of K_d with Re 112

| | |
|---|-----|
| Figure 4.36 Variation of x_p with u_0 | 112 |
| Figure 4.37 Variation of β with u_0 | 112 |
| Figure 4.38 Comparison of model prediction and experimental data of particle velocity decay along the jet centerline..... | 113 |
| Figure 4.39 Profile transverse particle velocity at different axial positions of Exp.1 | 113 |
| Figure 4.40 Profile transverse particle velocity of different experiments..... | 113 |
| Figure 4.41 Particles detection steps: (a) raw image, (b) image segmentation, (c) particle detection results. | 115 |
| Figure 4.42 Schematic diagram of the identification process of clusters. | 117 |
| Figure 4.43 Variation curve of σ_{rel} with St | 118 |
| Figure 4.44 Geometric characterization of particle clusters. | 119 |
| Figure 4.45 PDF of cluster area | 120 |
| Figure 4.46 Time evolution of cluster ratio | 120 |
| Figure 4.47 Cluster size distributions for different time periods | 121 |
| Figure 4.48 The relationship among the characteristic size parameters of clusters... | 122 |
| Figure 4.49 Influencing factors of cluster perimeter | 122 |
| Figure 4.50 Shapes of different clusters..... | 123 |
| Figure 4.51 Influencing factors of circularity of clusters | 124 |
| Figure 4.52 Mean particle volume fraction contour within 1 s..... | 125 |
| Figure 4.53 Evolution curves of particle volume fraction of Exp.1 | 126 |
| Figure 4.54 Evolution curves of particle volume fraction in different experiments.. | 127 |

Figure 4.55 Particle volume fraction model validation 128

Figure 5.1 Schematic of particle and eddy interaction ²⁵⁸ 139

Figure 5.2 Drag curves for simulations..... 140

Figure 5.3 Extension curves of HPJ drag model in different Reynolds number ranges
..... 143

Figure 5.4 Viscosity-temperature curves under different pressures..... 145

Figure 5.5 Fluid domain geometry..... 147

Figure 5.6 Meshing results: (a) overall view; (b) section view; (c) zoom-in view... 148

Figure 5.7 Some examples from the simulation results: Gas velocity fields (a, c) and
particle velocity fields (b, d) of high- and middle- Stokes number particle-laden
jet, respectively. 150

Figure 5.8 Mesh-independence verification results 151

Figure 5.9 Effects of different drag models on centerline velocity of high-Stokes-
number particle-laden jet 153

Figure 5.10 Centerline velocity of high-Stokes-number particle-laden jet predicted with
the extrapolated drag models of HPJ with different Reynolds number ranges.. 154

Figure 5.11 Entrainment at the nozzle exit 155

Figure 5.12 VDs under different C_e 155

Figure 5.13 Simulation results of high-Stokes-number particle-laden jet centerline
velocity under different C_e 155

Figure 5.14 Different VD curves under the same flow rate..... 156

Figure 5.15 Simulation results of high-Stokes-number particle-laden jet centerline

| | |
|--|-----|
| velocity under different VDs..... | 157 |
| Figure 5.16 Centerline velocity of high-Stokes-number particle-laden jet predicted with different outlet boundary type..... | 157 |
| Figure 5.17 Comparison of the jet centerline velocity predicted by different drag models with Exp.1 data of middle-Stokes-number particle-laden jet | 160 |
| Figure 5.18 Comparison of the jet centerline velocity predicted by the HPJ-SR4 drag model with different experiments of middle-Stokes-number particle-laden jet | 162 |

Tables catalog

| | |
|--|-----|
| Table 1.1 Summary of multiphase flow experimental measurement technology | 19 |
| Table 2.1 Valve settings | 36 |
| Table 3.1 Experimental parameters..... | 62 |
| Table 4.1 Experimental parameters..... | 91 |
| Table 4.2 Image parameters | 91 |
| Table 4.3 The values of K_d and x_p in the literature..... | 101 |
| Table 5.1 Values of empirical parameters | 133 |
| Table 5.2 Drag models for simulations | 141 |
| Table 5.3 The extrapolated drag models of HPJ for different Re range..... | 143 |
| Table 5.4 Physical properties of particles | 146 |
| Table 5.5 Mesh parameters | 151 |

Nomenclature

| | |
|------------|--|
| A | The area of the Voronoi cell, (m ²) |
| A_c | The area of the equivalent ellipse of the particle cluster obtained from the Voronoi area calculation, (m ²) |
| A_{exit} | The area of nozzle exit, (m ²) |
| A_p | The windward area of a particle, (m ²) |
| B_t | External control variable matrix, (-) |
| C | The set of common frames of two particles, (frame) |
| C_e | Entrainment coefficient, (-) |
| C_D | Drag coefficient, (-) |
| C_{D0} | Single particle drag coefficient, (-) |
| C_L | Lift force coefficient, (-) |
| C_θ | The dispersion coefficient, (-) |
| C_μ | Eddy-viscosity coefficient, (-) |
| D | The ejector outlet diameter, (m) |
| D_σ | The deviation of the particle number density distribution from the random Poisson distribution, (-) |
| d_p | Particle diameter, (μm) |
| d_{cl} | Particle cluster equivalent diameter, (μm) |
| E | System posteriori estimation error, (-) |
| F_B | Basset force, (N) |
| F_D | The drag force, (N) |
| F_{D0} | The single-particle drag force, (N) |

| | |
|-----------|--|
| F_G | Gravitational force, (N) |
| F_L | Lift force force, (N) |
| F_M | Magnus force, (N) |
| F_o | Other force, (N) |
| F_P | Pressure gradient force, (N) |
| F_S | Saffman force, (N) |
| F_t | Prediction process coefficient, (-) |
| F_{vm} | Virtual mass force, (N) |
| f | Dense phase volume share, (-) |
| G_b | Turbulent kinetic energy due to buoyancy, (J) |
| H | Transmission coefficient, (-) |
| i | The number of a particle, (-) |
| K | Turbulent kinetic energy, (J) |
| K_K | Kalman gain matri, (-) |
| K_d | Decay coefficient, (-) |
| k | Turbulent kinetic energy, (J) |
| k_e | The product of the ellipsoidal axis length ratios, (-) |
| L | The frame length of the particle trajectory, (frame) |
| L_e | The length scale of the turbulent vortex, (m) |
| L_{maj} | The major axis of the ellipse, (m) |
| L_{min} | The minor axis of the ellipse, (m) |
| L_d | The equivalent circle diameter of the cluster, (m) |
| L_v | The length scale of the formed coherent vortex, (m) |
| M | The start frame number of set C, (-) |
| M_p | Solid mass loading rate, (-) |

| | |
|-----------|--|
| m | Particle mass, (kg) |
| N | The end frame number of set C, (-) |
| N_{st} | Energy consumption of unit mass of particles transported in the gas phase, (J) |
| n | The number of particles in a specified space, (pcs) |
| n_c | The number of particles in the cluster, (pcs) |
| P_c | The perimeter of the cluster, (m) |
| P_g | The gas pressure of ejector inlet, (KPa) |
| P_{t-1} | The covariance matrix of the particle state quantity at time $t-1$, (-) |
| P_t | The covariance matrix of the particle state quantity at time t , (-) |
| Q_g | Gas volume flow rate, (L/min) |
| Q_p | Particle mass flow rate, (g/s) |
| Q_t | Covariance matrix of state prediction noise, (-) |
| Re | Reynolds number, (-) |
| Re_p | Particle Reynolds number, (-) |
| R_t | The covariance matrix of the system observation noise, (-) |
| St | Stokes number, (-) |
| S_f | The set of frame numbers where the particles exist in the front view, (frame) |
| S_t | The set of frame numbers where the particles exist in the top view, (frame) |
| r | The dispersion radius, (m) |
| r_p | The particle radius, (m) |
| s | The displacement, (m) |
| T | Temperature, (K) |

| | |
|-----------------|--|
| t | Time, (s) |
| X | The set of x-coordinates of the particle trajectory, (mm) |
| \hat{X}_{t-1} | The particle state quantity at time $t-1$, (-) |
| \hat{X}_t^- | The particle state quantity at time t , (-) |
| U | The set of x-direction velocities of the particles, (m/s) |
| U_g | No-load gas velocity, (m/s) |
| u | Velocity, (m/s) |
| u_g | Gas velocity, (m/s) |
| $u_{g,0}$ | Initial gas velocity, (m/s) |
| u'_g | Fluctuating gas velocity, (m/s) |
| u_{gde} | Dense phase apparent gas velocity, (m/s) |
| u_{gdi} | Dilute phase apparent gas velocity, (m/s) |
| u_p | Particle velocity, (m/s) |
| $u_{p,0}$ | Initial particle velocity, (m/s) |
| u'_p | Fluctuating particle velocity, (m/s) |
| u_{pde} | Dense phase apparent particle velocity, (m/s) |
| u_{pdi} | Dilute phase apparent particle velocity, (m/s) |
| u_t | The profile transverse velocity, (m/s) |
| V_p | Particle volume, (m ³) |
| V_{3D} | The volume of the Voronoi polyhedron, (m ³) |
| W_{st} | Energy consumption of the unit volume of the gas phase suspension conveying particles, (J) |
| x_p | The distance from the nozzle exit to the virtual origin of the jet, (m) |
| Z_t | the observed value of the system state quantity, (-) |

Greek letters

| | |
|--------------------|--|
| α_g | Gas volume fraction, (-) |
| α_p | Particle volume fraction, (-) |
| α_{de} | Dense phase porosity, (-) |
| α_{di} | Dilute phase porosity, (-) |
| β | Half-width spread angle of the jet, ($^{\circ}$) |
| ρ | Density, (kg/m^3) |
| η | The shape coefficient, (-) |
| θ | Dispersion angle, ($^{\circ}$) |
| ε | The turbulent kinetic energy dissipation rate, (-) |
| μ | Viscosity, ($\text{Pa}\cdot\text{s}$) |
| μ_t | The eddy viscosity, ($\text{Pa}\cdot\text{s}$) |
| μ_{eff} | The effective shear viscosity, ($\text{Pa}\cdot\text{s}$) |
| λ | The mean number of particles in each box, (pcs) |
| σ | The standard deviations for the measured particle number density distribution, (-) |
| σ_{rel} | The degree of particles clustering, (-) |
| σ_{RPP} | The standard deviation of the RPP distribution, (-) |
| $\sigma_{Poisson}$ | The standard deviations for Poisson distribution, (-) |
| σ_v | The standard deviations for Voronoi distribution, (-) |
| τ | Relaxation time, (s) |
| τ_e | The existence time of the turbulent vortex, (s) |
| τ_g | Gas relaxation time, (s) |
| τ_p | Particle relaxation time, (s) |
| ω_k | The angular velocity, (rad/s) |

Subscripts

| | |
|-----------|----------------------------|
| cl | Cluster |
| de | Dense phase |
| di | Dilute phase |
| f | Front view |
| g | Gas phase |
| maj | Major |
| min | Minor |
| p | Particle phase |
| rms | The root mean square error |
| <i>st</i> | Stokes |
| t | Top view |
| <i>t</i> | Time |

Abbreviation

| | |
|----------|--|
| 2D | Two dimensional |
| 3D | Three dimensional |
| 4D | Four dimensional |
| CFD | Computational fluid dynamics |
| CHN | China |
| COVID-19 | Corona virus disease 2019 |
| DM | Drag model |
| DPM | Discrete phase model |
| DRe | Drag-Re |
| EC | Entrainment coefficient |
| EMMS | Energy-minimization multi-scale drag model |

| | |
|--------|---|
| Exp. | Experiment |
| FFT | Fast Fourier transform |
| HPJ | Horizontal particle-laden jet |
| HPJ-SR | HPJ-Standard drag and Rudinger drag |
| JP | Japan |
| LDV | Laser Doppler velocimetry |
| MDM | Middle-Stokes-number drag model |
| OT | Outlet type |
| PDV | Phase Doppler velocimetry |
| PDF | Probability density function |
| PIV | Particle image velocimetry |
| PN | Planar nephelometry |
| PSV | Particle streak velocimetry |
| PTV | Particle tracking velocimetry |
| RT | Tay-traversal |
| RPP | Random Poisson process distribution |
| SARS | Severe acute respiratory syndrome coronavirus |
| SFM | Structure from motion |
| SLR | Solid load ratio |
| STB | Shake-the-box |
| TFM | Two-fluid model |
| UDF | User-defined function |
| USA | American |
| VD | Velocity distribution |

Chapter 1 Introduction

1.1 Background and Significance

Multiphase jets, especially particle-laden jets, are complex fluid flows that are widely encountered in various industrial and environmental applications and human life, such as chemical processes^{1,2}, gas-solid mixing²⁻⁴, combustion^{3,5,6}, spray⁷⁻⁹, sandstorm air pollution¹⁰, violent expiratory events (e.g. sneezing, coughing)¹¹⁻¹³ and the spread of COVID-19¹⁴⁻¹⁶, as shown in Figure 1.1. The multiphase flow problem is inherently one of the most challenging issue in fluid mechanics. In a particle-laden jet, the particles can have a significant impact on the momentum, heat, and mass transfer rates, and the gas turbulence is coupled with the stochastic motion of particles to make the problem even more complicated¹⁷.

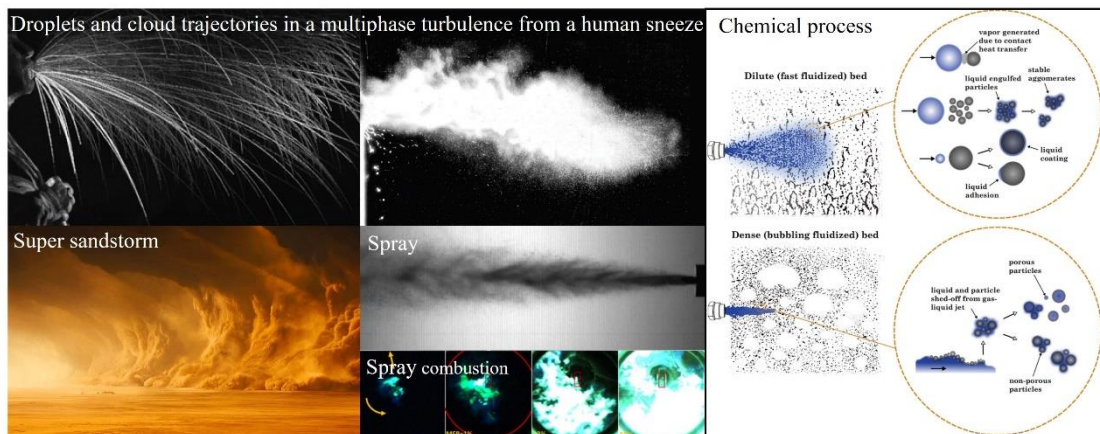


Figure 1.1 Scenarios for multiphase jets^{1, 2, 6, 12, 13}

The motion of a particle-laden jet is a “point-emission”¹⁸, unidirectional, “cone-shaped”, multiphase field, featuring self-similar dispersion^{12, 19, 20} with a specific angle as in a single-phase gas jet shown in Figure 1.2, exhibiting a region of strong turbulent

mixing and dispersion surrounding the potential cone and centerline^{12, 20, 21}. The dynamics of polydisperse particle systems, and the interaction mechanism between turbulence and particle motion remain unclear¹⁷. Accurate tracking and prediction of the motion of the particle-laden jet, in terms of, e.g., the trajectories, concentration, and dispersion of particles, are of great significance. However, they are heavily dependent on the knowledge of the particle-level dynamics and the particle-fluid interactions, say, the drag force. For example, the transmission of the COVID-19 virus and thereby the best social distance in the pandemic^{22, 23}, is adhered to our understanding of the dynamics of a jet of different-sized particles caused by violent respiratory events. However, the uncertainty of the drag force modeling in such a particle-laden jet makes it still a challenging task for accurate prediction^{11, 12}. Therefore, it is necessary to study the evolution of particle-laden jets and the dispersion laws of particles in depth.

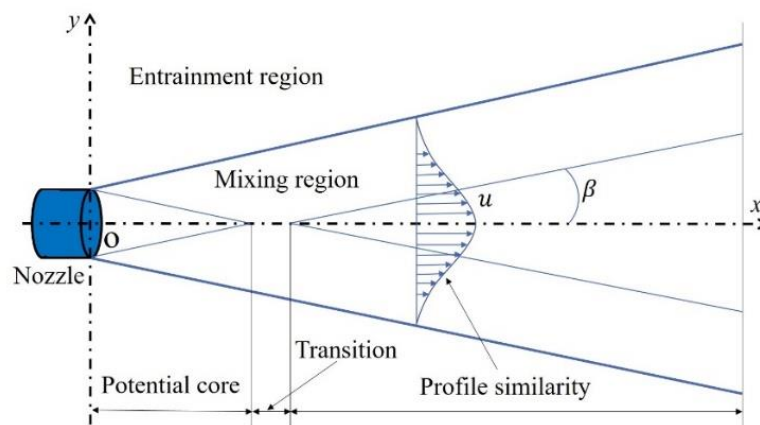


Figure 1.2 Schematic diagram of a typical single-phase gas jet²¹

The behavior of a two-phase flow is influenced by various factors such as the Stokes number and vortex structures²⁴, which are further affected by e.g., the nozzle type, air outlet mode, gas velocity distribution, load rate, and particle size²⁵⁻³¹. Furthermore, in a particle-laden jet flow, physical quantities have strong scale

dependence, such that the gas-solid flow state changes significantly with respect to the time and space over a wide range of scales. Definitions and statistical results of a physical quantity are hence closely related to the existence of mesoscale structures³². As a result, the characterization and quantification of mesoscale structures are very important for understanding particle-laden jets.

1.2 Spatiotemporal Evolution of Particle-laden Jet Flows

In a particle-laden jet, as the distance increases away from the nozzle, both the gas and particle flow fields develop and influence each other. In particular, the dispersion of particles is one of the most important behavior³³. Many researchers have studied the dispersion behavior of particle-laden jets from the interrelated aspects of coherent vortex structures²⁴, preferential concentration³⁴, velocity distribution^{24, 35, 36}, and penetration or deposition distance^{12, 37-39}, indicating that the dispersion is self-similar. For example, Bourouiba et al.¹² used $r = C_{\theta}s$ to quantify this self-similarity, which means the dispersion radius of a particle-laden jet, r , is proportional to the dispersion angle and the distance away from the nozzle^{12, 40}, s . And the nozzle diameter is normally used as the scale parameter of jet geometric similarity²⁰. To detail the self-similar behavior, in what follows we will review the mesoscale flow structure, particle concentration, velocity, particle deposition distance, and interaction of turbulence and particles in particle-laden jet flows.

1.2.1 Mesoscale Structure

The mesoscale structure in jet flows, either in forms of clusters or vortexes, has

been studied in both experiments and simulations^{24, 41-44}. Longmire and Eaton²⁴ took the smoke to visualize the gas-phase flow field and studied the jet flow pattern evolution of unforced single-phase flows and unforced particle-laden flows. The results indicated that the gas-phase vortex experienced three states: emergence, merger, and fragmentation. The gas-phase flow pattern is significantly affected by the carrier particles, as shown in Figure 1.3. In addition, they also studied the jet flow pattern transformation of the single-phase flow and particle-laden flow under acoustic forcing and found that the macroscale structure of the gas phase and particles changed at the same frequency, and the particle motion was obviously affected by the gas-phase vortex, as shown in Figure 1.4. The research results of Wark⁴⁵ et al. indicated that the acoustically forced particle-laden jet will form a periodic flow pattern of "core" and "wing", leading to an uneven distribution of particles.

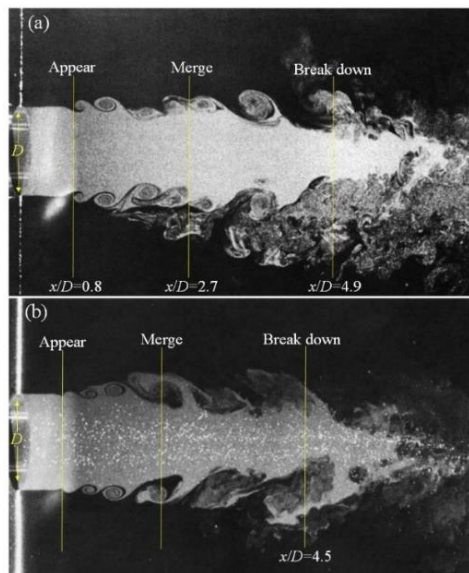


Figure 1.3 (a) Unforced single-phase flow and (b) unforced particle-laden flow²⁴

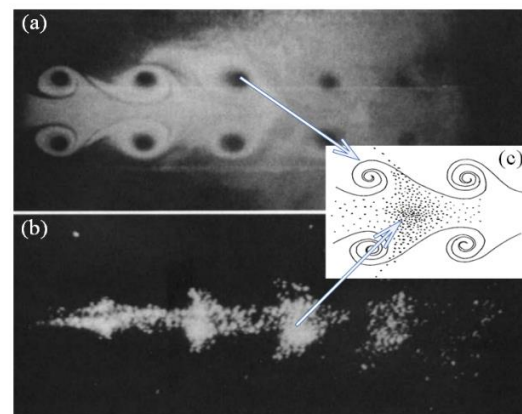


Figure 1.4 (a) Forced single-phase flow and (b) forced particle-laden flow (c) cartoon of particles interacting with vortex ring²⁴

The impact of the vortex on particles dispersion (clustering) is related to the Stokes number (St)⁴⁶. The St is a dimensionless number defined as the ratio of the particle

relaxation time to the fluid time scale²⁴, written as

$$St = \frac{\tau_p}{\tau_g} \quad (1-1)$$

where τ_p is the particle relaxation time, expressed by the aerodynamic response time, that is

$$\tau_p = \frac{\rho_p d_p^2}{18\mu_g} \quad (1-2)$$

The fluid time scale τ_g is usually calculated from the length scale L_v of the formed coherent vortex and the fluid propagation velocity u , defined as

$$\tau_g = \frac{L_v}{u} \quad (1-3)$$

The influence of the vortex on particle dispersion decreases with the increase of Stokes number^{24, 47}. When $\tau_p \gg \tau_g$, the particles do not respond to fluctuations in the airflow. When $\tau_p \ll \tau_g$, the particles will fully respond to the airflow and follow any fluctuations in the airflow. When τ_p and τ_g are of the same magnitude, the particles partially respond to fluctuations in the airflow. Although the particles cannot completely follow the airflow, their path will be changed by the airflow fluctuations²⁴.

Research has shown that clustering is caused by the inability of finite inertial particles to satisfy the different time scales of turbulent flow fields³. The results of Maxey⁴⁸ and Eaton³⁴ indicated that when the particle characteristic time is similar to the turbulence characteristic time, the particles always stay away from the vortex core and the preferential concentration effect of particles is more obvious in the high strain rate and low vorticity region. While eddy pairing can homogenize the particle field, the degree of homogenization is strongly dependent on the particle relaxation time, eddy turnover time, and how long the particle interacts with each scale prior to the pairing

event. Therefore, even though small-sized particles are well mixed in a large vortex, the dispersion of large-sized particles is still inhomogeneous⁴⁹. Wang and Maxey⁵⁰ studied isotropic turbulence using the DNS method and found that preferential concentration has the strongest effect when the particle time scale and fluid time scale based on the Kolmogorov tend to be unify. Yang et al.⁵¹ indicated that the vortex structure in the planar wake can disperse the middle St particles into highly ordered patterns. Research by Brandon et al.⁵² indicated that particles with St less than 0.1 behave similarly to fluid, particles with St between 0.1 and 0.5 are more easily dispersed than fluid, and particles with St greater than 1 are largely unaffected by the wake.

However, the motion of particles in the near field is still poorly understood. Additionally, physical quantities in jet flows have strong scale dependence and change significantly in time and space, making it difficult to define and characterize mesoscale structures. More research is required to understand particle-laden jet flows.

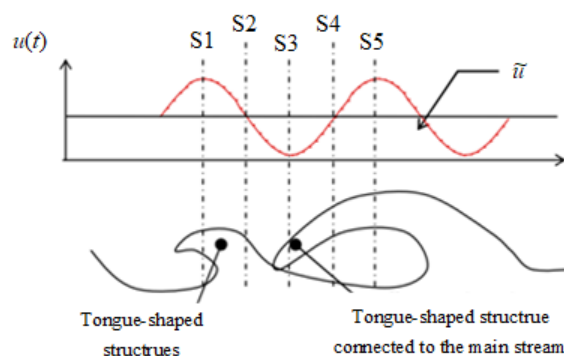
1.2.2 Particle Concentration

The study of particle concentration in multiphase jets is a significant topic to which many industrial applications are relevant. For example, particle dispersion and concentration can directly affect the performance and efficiency of combustion systems⁵³. The degree to which the vortex changes the transient particle concentration is related to Stokes number (St). For small particles (middle-Stokes-number), the particle concentration is often closely related to the flow pattern evolution.

The research on particle concentration in particle-laden jets mainly focuses on the preferential concentration caused by turbulence and large-scale structures^{34, 54}. Some

studies⁵⁵⁻⁵⁷ indicated that the preferential concentration effect is more significant as the Stokes number tends to be uniform. However, the particle response does not change much for a given St as the particle Re changes⁵⁶. Cerecedo⁵³ obtained the large-scale structure in the jet by using the phase average experimental method, as shown in Figure 1.5. They analyzed the local particle concentration of five vortices of two successive vortices. Longmire²⁴ and Lázaro^{58, 59} et al. demonstrated that the concentration of particles depends not only on the size of the particles but also on the flow mesoscale structure. In a pioneering experimental study of a particle-laden jet with ash particles (average diameter 24 μm), Hayashi and Branch⁶⁰ indicated that the jet forcing does not change the particle distribution of over the nozzle cross-section. And similar jet flows were observed by Anderson and Longmire⁴⁷.

Figure 1.5 Schematic diagram of oscillations and their location relative to a vortex structure.⁵³



In terms of concentration research methods, the local concentration of particles has a strong scale dependence. At different scales of spatial average, there is a significant difference in particle concentration. It is difficult to accurately characterize the local details of the particle concentration using general global or Euler methods^{61, 62}. For example, Fessler et al.⁶² divided each picture into a regular box grid, calculated the number density of particles in each grid and obtained the probability distribution curve of the number density of particles and the contour map of the particle

concentration of the entire picture, and compared with random Poisson process (RPP) distribution, defined as⁶² the equation below, as shown in Figure 1.6.

$$F(n) = \frac{e^{-\lambda} \lambda^n}{n!} \quad (1-4)$$

where λ is the average particle number in each box, and $F(n)$ represents the probability that an integer number of particles, n , will be found in a given box. To quantify the deviation of the particle number density distribution from the random Poisson distribution in this way, they defined the parameter D_σ

$$D_\sigma = \frac{\sigma - \sigma_{\text{Poisson}}}{\lambda} \quad (1-5)$$

where σ and σ_{Poisson} are the standard deviations for the experimental particle number density distribution and the RPP distribution, respectively. The clustering of particles causes to a very high particle concentration in the grid, thus also a large positive value of D_σ . If the distribution of particles is uniform, each grid has the same particle number, then D_σ is negative. D_σ approaches zero when the distribution of particles in the grid is random. Thus, the data obtained in this manner are highly dependent on the size of grid division.

To characterize the local concentration of each particle, some researchers^{32, 63} adopted the Voronoi⁶⁴ method that is independent of the choice of spatial scale. Voronoi is composed of a set of continuous polygons, each polygon surrounds a point (particle), and the distance from each side of the polygon to the adjacent point is equal⁶⁵, shown as Figure 1.7. Thereby the local concentration of each particle can be obtained.

Monchaux⁶¹, Petersen⁵⁷, and Manish⁶³ et al. applied the Voronoi method to identify particle clusters. By obtaining the normalized Voronoi area occupied by

particles, they compared the normalized Voronoi area probability density distribution with the random Poisson process distribution, as shown in Figure 1.8. The two intersection points on the curves of these two distributions are then used as the dividing points to divide the dense and dilute phases.

Although most researchers take into account the effect of spatial location, few considers the effect of time scale. The Lagrangian study of particle dynamics and local concentration field dynamics using the Voronoi method bears time scale information and may provide new insights⁶¹. In particular, the 3D information of the concentration of particles along particle trajectories in a jet flow is very important^{66, 67}, though there is few report on it.

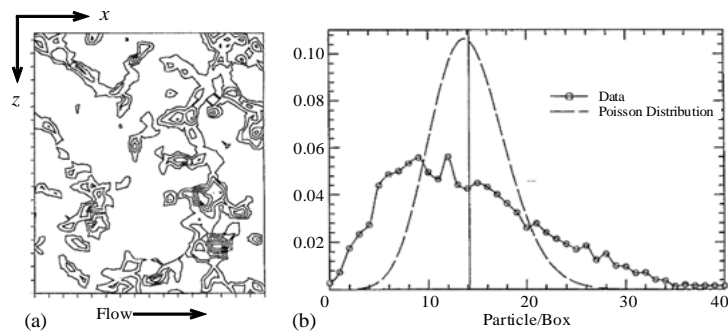


Figure 1.6 (a) Particle concentration contour and (b) particle number probability density distribution⁶²

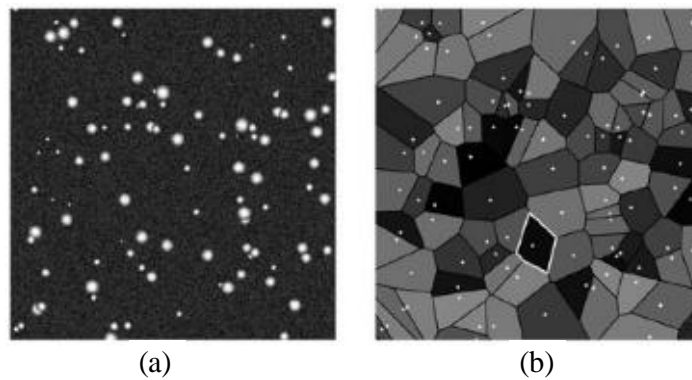


Figure 1.7 (a) Original particle image. (b) Voronoi diagram of this image in which white dots denote the original particles.⁶⁵

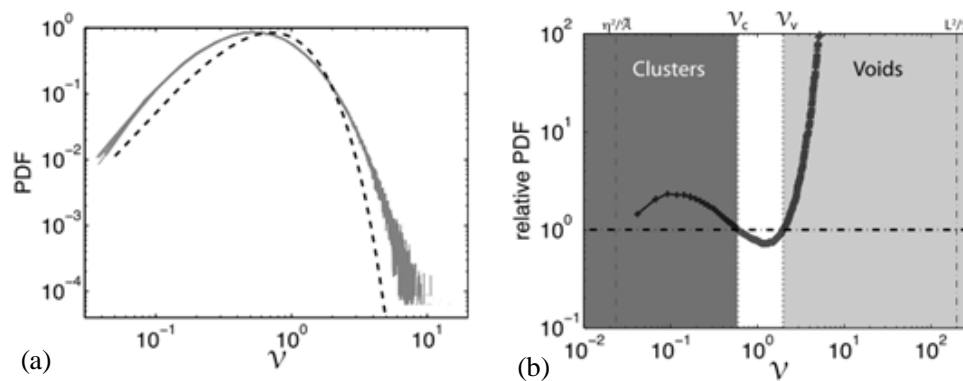


Figure 1.8 Comparison of normalized Voronoi area PDF and random Poisson distribution⁶¹.

1.2.3 Velocity

The axial velocity component of particles is the most representative factor for a particle-laden jet²⁰. It normally first increases and then decreases along the axial direction^{24, 36, 53}. Prevost et al.³⁶ measured jet dynamics of an axisymmetric polydisperse particle tube jet using PDA, revealing the mean particle axial velocity field and the downstream evolution of particle radial and axial turbulence components. The results indicated that with an increase of particle relaxation time, the anisotropy of the particle axial and radial wave velocity increases. The particle velocity gradient is an important mechanism that affects the turbulent velocity of the flow-to-particles.³⁶ Cerecedo et al.⁶⁸ used PDPA to measure non-dilute two-phase coflowing natural (unforced) jet, and studied the evolution of mean particle axial velocity and fluctuating velocity downstream of the jet at different acoustic forcing frequencies. Subsequently, coherent structures were frozen based on phase-average velocity experiments. The findings suggested that fluctuating velocity is related to the coherent structure, which is enhanced by forcing. In addition, to follow the vortex, Cerecedo et al.⁵³ obtained the phase average on five different cross-flow sections (see Figure 1.5), and studied the

phase-average axial velocities of the gas and particle at different vortex structures. The results indicated that the large spatial gradient of axial velocity in the vortex is an important factor affecting particle dispersion. In addition, the loading rate, particle diameter, and initial gas velocity also significantly affect the gas-solid two-phase diffusion^{25, 69}. Tsuji et al.³¹ found that the two-phase velocity distribution in a pipeline changes with the loading rate and particle diameter. As the loading rate and particle diameter increased, the gas phase velocity distribution gradually decreased in the middle and increased at the top and bottom. This was also observed in simulation studies by Song³⁰ et al.

Although there have been many experimental studies on the particle-laden jet velocity field before, most of them are limited in two-dimensional, with three-dimensional velocity fields and Lagrangian tracking rarely reported. Moreover, studies on the slip velocity between the gas and particles³⁰, and the related drag force, are still far from maturity⁵³.

1.2.4 Deposition Distance of Particles

The study of deposition distance is mainly involved in the study of particle/droplet-laden jets driven by violent respiratory events. Here droplets can be treated as deformable particles. Especially in recent years, the COVID-19¹⁶ outbreak around the world has prompted an increasing number of studies on the deposition distance of particle-laden jets due to violent respiratory events to reveal the spread of the virus⁷⁰⁻⁷². Typically, the size distribution of droplets expelled by violent expiratory events ranges from 1 to 2000 μm ⁷³⁻⁷⁶. For many influenza diseases, including SARS and COVID-19,

viral transmission by particle-laden jets driven by violent respiratory events can be divided into long-distance small particle transmission and short-distance large particle transmission^{77, 78}. It has been suggested that aerosol transmission of the virus may be an important mode of long-distance transmission^{16, 38, 79}. However, most new infections are caused by short-distance direct contact with large particles emanating from infected individuals^{77, 80}. For many diseases, including SARS and COVID-19, the underlying mechanisms of direct and indirect transmission of pathogens remain poorly understood.

It is generally accepted that large droplets follow ballistic trajectories and are largely unaffected by turbulent clouds, while smaller particles (droplets) may be suspended in clouds, where they circulate until they settle¹². Therefore, the gas phase dynamics and small particles are thought to be more complex and studied in detail, but no special attention has been given to the dynamics of large particles. Recent experiments⁸¹ have shown that thermodynamic factors including evaporation and buoyancy are small until the airflow velocity drops to ambient velocity. Moreover, preferential concentration can increase local humidity, preventing evaporation and significantly extending the droplet lifetime⁸². Therefore, evaporation can be negligible in the near-mouth region, and studies of large-particle (droplet) dispersion in the near-mouth region are also helpful for understanding the transmission of short-distance large-particle viruses.

Furthermore, many researches^{39, 40, 83, 84} have tried to predict the droplet dispersion with simulations. The single-particle drag model was normally applied, and the droplet deposition distance predicted was often smaller than in actual situations where the maximum deposition distance is up to 6-8 meters^{11, 13, 40, 70}. In addition to the factors of

evaporation and humidity, underestimation of the drag force can also lead to this result. Indeed the uncertainty of the drag force can lead to a prediction error of up to a factor of 130¹². However, there are few reports about the drag model of the dilute-phase particles. It is necessary to explore the drag model of dilute-phase particle-laden jets through experiments to improve simulation accuracy.

1.2.5 Interaction of Turbulence and Particles

Turbulent flow and multiphase flow are the most challenging problems in fluid mechanics. The random coupling motion of the gas turbulence and particles makes the problem more complicated. Adding particles to a jet makes its dynamics more complex due to the dispersion of particles and more related factors, e.g., the particle size distribution and concentration^{24, 62}, the complex interplay between the particle and fluid^{36, 85}, and so on. Even at very low particle concentrations, the state of vortices can be changed due to the presence of particles^{24, 53, 58}. The interaction mechanism between gas turbulence and particle motion and the details of particle-scale flow still need to be further explored¹⁷.

In a particle-laden jet, the interaction between turbulence and particles is mainly manifested in the following aspects: (1) Kinetic energy exchange between particles and fluid^{86, 87}; (2) Enhancement of turbulent dissipation by particles^{17, 35}; (3) Wake effect^{17, 41, 88}. Among them, the first point is mainly realized by the interphase force, such as the drag force, which we will introduce in detail in Section 1.5. The latter two points are also known as turbulence modulation.

Turbulence modulation refers to the change in gas turbulence due to the existence

of solid particles, that is, the attenuation or increase in gas-phase turbulence by adding particles to the airflow. On the one hand, a large number of gas-particle two-phase flow experiments have confirmed that the turbulent kinetic energy of the fluid can be dissipated after adding particles⁸⁹⁻⁹⁵, as the fluid kinetic energy is consumed to carry particles, and the inertia of particles damps the fluctuation of the fluid^{94, 96-98}. On the other hand, particle-enhanced turbulence has also been observed, especially for flows with large particles⁸⁹. The wake vortex effect is usually used to explain the turbulence enhancement caused by large particles^{92, 93, 97, 99}. Though there are many factors affecting turbulent modulation, such as particle size, concentration, and Reynolds number, special attention has been paid to particle size. Some preliminary consensus has been reached currently in turbulence modulation models^{96, 100-105}, in the sense that the weakening of turbulence is attributed to the consumption of fluid kinetic energy to carry particles in the fluid, and the enhancement of turbulence is attributed to the wake vortex effect^{96, 102, 103, 106}. It should be noted that the quantitative relationship of turbulence modulation is hard to be clear.

1.3 Experimental Measurement Techniques for Multiphase Flow

For a particle-laden jet, precise modeling of the drag relies on the direct measurement of the highly resolved particle velocity field and gas velocity field³⁰, which, in principle, should be based on the time-resolved positions and velocities of all the particles as well as the interstitial flow field with a resolution down to the Kolmogorov length scale^{107, 108}. Such a high-resolution time-space field is challenging for both physical modeling and experimental measurement^{17, 35}. With regard to the

experimental measurement of particle-laden jet flows, many noninvasive (non-contact) techniques have been developed, to capture the time-resolved particle movement as well as the gas velocity field, to mention but a few, the laser-Doppler velocimetry⁵⁷ (LDV), phase Doppler velocimetry (PDV), planar nephelometry (PN)¹⁰⁷, and high-speed camera techniques such as particle image velocimetry(PIV)¹⁰⁹, particle tracking velocimetry (PTV)^{19, 110} and particle streak velocimetry(PSV)¹¹¹. In particular, PIV and PTV found many applications in experimental fluid mechanics as full-field visualization methods^{17, 112}. In addition, contact measurements such as pitot tube speed measurement and hot wire anemometer speed measurement have also been used. However, contact measurements disturb the flow itself, resulting in compromised measurement results. Below we briefly introduce some of the most commonly used non-contact measurement methods.

LDV is a single-point measurement technique that measures particle velocity by using the Doppler effect to relate the velocity of a moving particle to the frequency shift of the light scattered by the particle. It has the advantages of non-invasiveness, high spatial resolution, fast response and output results that are only sensitive to particle velocity. Based on this method, adding tracer particles to the flow field can also measure the fluid velocity. To obtain the velocity of the two-phase flow field, at least two sets of measurement systems are usually required¹¹³, making the structure complex, signal processing difficult, and interphase interference prone to occur¹¹⁴, which usually requires complex debugging to eliminate the interference.

PIV and PTV are full-field transient measurement technologies, breaking the limitations of spatial single-point measurement technology. They can be used to record

information on the entire measurement plane, so as to obtain the time-resolved positions, velocity field, and fluctuation velocity field and vorticity field, etc. PIV focuses on collections of tracer particles, and PTV focuses on individual particles, so the two require different data processing algorithms. However, for the experimental setup, the two are largely similar¹¹⁴. Figure 1.9 illustrates the schematic of a PIV device.

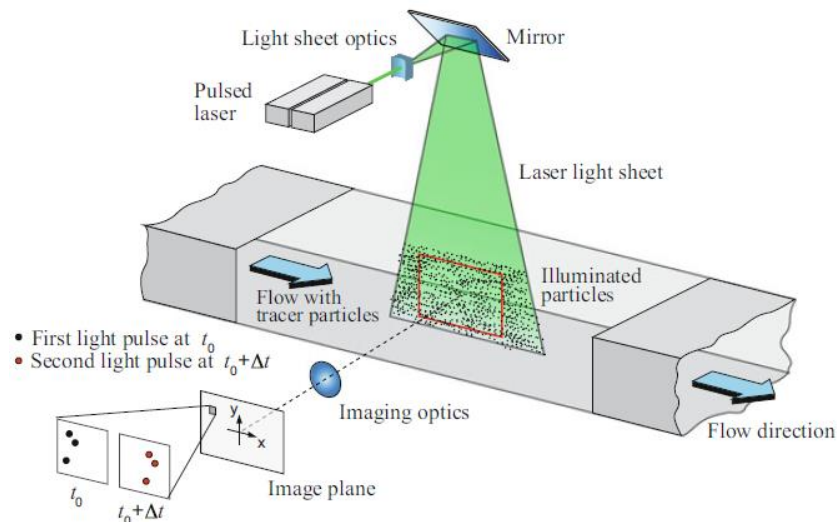


Figure 1.9 Sketch of a typical setup for PIV/PTV measurement in a wind tunnel¹¹⁴

In short, the composition of PIV/PTV experimental device includes hardware and software. The hardware part includes (1) seeding, usually small particles for PIV and larger particles for PTV; (2) light source, usually a laser for PIV, and can be a uniform LED light source for PTV; and (3) high-speed cameras for taking images of particle motion. The software part includes: (1) pre-processing: also called camera calibration. To eliminate camera shooting errors and determine the spatial resolution of the image, it is necessary to use an algorithm to calibrate the camera before experiment. (2) post-processing, mainly image processing algorithms and target parameters calculation algorithms, such as velocity algorithms.

The measurement principle of PIV is to use laser light to illuminate the flow field,

and sow tracer particles in it for visualization. Based on the cross-frame technology, the pulsed YAG laser and the high-speed camera can simultaneously record two continuous particle images with a short time interval. The schematic diagram of cross-frame technology is shown in Figure 1.10. The upper dashed line donates two camera exposures and the lower solid line donates two laser pulses. This laser pulse spans the interframe time between two camera exposures, known as a frame span. The pulsed laser and high-speed camera are synchronized by a timing controller. Since the pulse laser has two independent laser heads, laser oscillation can be performed in a very short span regardless of the length of non-exposure time between two frames of the high-speed camera.

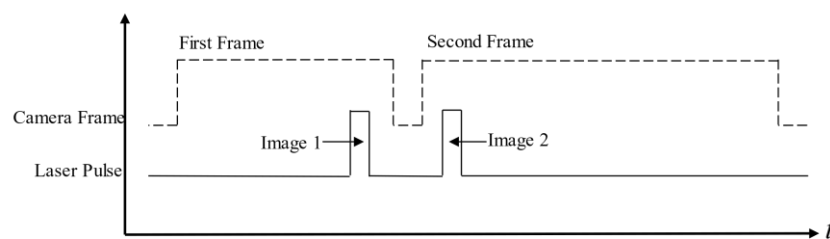


Figure 1.10 The frame straddling technique sketch for PIV

Upon acquiring appropriate images via cross-frame shooting, Particle Image Velocimetry (PIV) analysis can be conducted. Initially, the image is subdivided into numerous small search areas based on pixel distribution. These areas are referred to as interrogation windows. For each interrogation window, a correlation surface is obtained through implementation of a cross-correlation algorithm. Subsequently, peak detection and motion calculation are executed to determine the velocity of each window. The velocity analysis diagram is illustrated in Figure 2.8. Over the past years, the PIV algorithm has matured considerably. Pioneering researchers, including those from Dantec and LaVision^{109, 115, 116}, have extensively explored various PIV methodologies

such as 2D macroscopic and microscopic PIV, 2D time-resolved PIV, 3D tomographic PIV, and stereoscopic PIV. These advancements have significantly improved accuracy, resolution, dynamic range, and high-dimensional measurement capabilities.

PTV differs from PIV in that it does not need cross-frame technology or even pulsed lasers. In addition, since PTV focuses on single particle analysis, image post-processing algorithms are also different from PIV. The most difficult point of the PTV algorithm lies in the identification, matching, and tracking of the same particle, which requires a higher resolution (or, number of pixels) of single particles. Compared with PIV, the search target of the PTV algorithm is no longer interrogation windows but each single particle, aiming to obtain the trajectory of each particle. Therefore, as the particle concentration increases, the computation loading increase accordingly. At present, there is no mature commercial PTV software, and related PTV algorithms include, e.g., TracTrac¹¹⁷, Part2Track¹¹⁸, DEPTV¹¹⁹, TP-T¹²⁰, 4BE-ETI¹²¹, 2D particle tracker¹²², Shake-The-Box¹²³, and Ray-Traversal¹²⁴. To provide a reference and guidance for the design of experimental schemes and parameter settings in measurement, a summary of multiphase flow experimental measurement techniques is shown in Table 1.1.

According to the results of literature survey, most of the research is based on 2D measurement^{57, 125-127}, such that only the information of particles in the laser-sheet^{62, 126, 127} or on the projection of a particular view^{70, 128-130} can be provided. The recent development of the stereo X-ray PTV^{131, 132} provides a powerful approach to track the 3D particle velocity field of fluidized beds but is still limited to a single tagged cylindrical particle with ergodicity assumption. In light of the 3D feature of jet flows, one can expect that time-resolved, 3D-PTV measurement technology will be of greater

importance in future.

Table 1.1 Summary of multiphase flow experimental measurement technology

| Researchers | Method | Particles | d_p mm | Frequency | Resolution |
|-----------------------------------|--------|-------------|--------------|-----------|--------------------|
| | | | | Hz | Pixel ² |
| Carlson et al. ¹³³ | LDV | Glass beads | 0.044/0.214 | / | / |
| Lee et al. ^{134, 135} | LDV | Glass beads | 0.1~0.8 | 500 | / |
| Tsuji et al. ³¹ | LDV | PS | 0.2/3.4 | 40000 | / |
| Longmire et al. ²⁴ | LDV | Smoke | 0.001 | 5600 | / |
| | | Glass beads | 0.05~0.06 | | |
| Kulick et al. ⁸⁵ | LDA | Glass beads | 0.05/0.09 | 20~6000 | / |
| | | Copper | 0.07 | | |
| Hassan et al. ¹³⁶ | PIV | Oil | 0.07 | 10 | 1024×1024 |
| Sakakibara et al. ³⁵ | PIV | Glass beads | 0.001 | 2000 | 500×750 |
| | | | 0.055/0.086 | | |
| Sommerfeld et al. ¹³⁷ | PTV | Glass beads | 0.1/0.5 | 250 | 736×581 |
| Wicker et al. ^{138, 139} | PIV | Glass beads | 0.055/0.09 | / | 450×675 |
| | | | 0.15 | | |
| Kiger et al. ¹⁴⁰ | PIV | Glass beads | 0.045~0.36 | 333 | 1008×1018 |
| Khalitov et al. ¹⁴¹ | PIV | Air | 0.33 | / | 1008×992 |
| | | Glass beads | 0.63 | | |
| Groszmann et al. ¹⁴² | PTV | Glass beads | 0.1/0.4/0.65 | 60 | 768×494 |
| Virdung et al. ¹⁴³ | PIV | Glass beads | 1.5 | 667 | 1008×1008 |
| Birzer et al. ¹⁴⁴⁻¹⁴⁶ | PIV | Glass beads | 0.02 | / | 1018×1008 |
| | | | 0.008~0.012 | | |
| Diez et al. ¹⁴⁷ | PIV | Water | 0.008~0.012 | 1000 | 1024×1024 |
| | | Al2O3 | 0.1 | | |
| Capone et al. ¹⁴⁸ | PIV | Glass beads | 0.01 | 500 | 1021×1024 |
| | | Polyamide | 0.32 | | |
| Schanz et al. ¹⁴⁹ | PIV | Water | 0.056 | 500 | 672×1024 |
| Cerqueira et al. ¹⁵⁰ | PTV | Bubble | 1.51~4.05 | 400~1200 | 1568×640 |
| | PIV | Water | 0.001~0.02 | | |
| Manish et al. ⁶³ | PIV | Droplets | Polydisperse | 1000 | 1040×1392 |
| Carter et al. ¹²⁶ | PIV | Droplets | Polydisperse | 250 | 3000 |
| | | | | | ×3500 |

1.4 Reconstruction Methods of 3D Particle Flow Field

The particle-laden jet is a 3D, cone-shaped flow field. Long-duration, continuous particle tracking with 2D-PTV can only be constrained to the positions of particles in a thin projection plane and is not fit for describing the jet expansion behavior. Therefore, some research work in recent years has focused on time-resolved 3D-PTV (also referred to as four-dimensional particle tracking velocimetry (4D-PTV)¹⁴⁹). According to the sequence of tracking and reconstruction, the 4D-PTV algorithm can be divided into two categories. One is a typical reconstruction-precede-tracking algorithm such as SFM (structure from motion)¹⁵¹ and RT (ray-traversal)¹²⁴, the other is the tracking-precede-reconstruction algorithm¹⁴⁹, namely STB (shake-the-box) and seemingly opposite to the typical 4D particle flow reconstruction process. However, the triangulation method^{152, 153} in STB for the initial trajectory construction of the particles in the first four-time steps is still a method to first reconstruct the 3D positions of the particles. That is, the STB method is essentially a reconstruction-tracking-reconstruction method.

It is also worth noting that in all these algorithms, the reconstructed 3D positions of the particles are recalculated relative to the cameras and not based on the 3D space of the image itself. Thus, the calibration of complex multi-camera optics is essential to the quality of tracking^{154, 155}. Especially both the SFM and STB algorithms have to generate a mapping function between image coordinates (x, y) and physical coordinates (x, y, z) through calibration¹⁵⁶, and then it will be combined with the triangulation method to realize particle detection. Moreover, the number of samples in the calibration image significantly affects the accuracy of the mapping function and particle detection, as well as the reconstruction. For spherical particles, only a few geometric features are

available, making the matching difficult. And it usually requires at least three cameras to complete the reconstruction. The RT algorithm also requires at least three cameras to calibrate the complex optical system, because the pose parameters between cameras and the position parameters between cameras and particles are necessary for the “Center to Rays” operation. Developing a simple reconstruction method for 3D particle flow fields will contribute to the experimental research of this paper.

1.5 Drag Models and Simulations

An accurate drag model is very important for the simulation accuracy of a particle-laden jet. With regard to the physical modeling, the drag force in a particle-laden jet is normally closed with the Stokes drag¹⁵⁷ or the standard drag law for a single, isolated particle^{25, 40, 83}. However, such a simplification may lead to significant errors when comparing the simulation results with experiments^{12, 158-160}. For example, when the single-particle drag model was applied, the droplets deposition distance of coughing was often smaller than the actual situation, as the actual maximum deposition distance is up to 6-8 meters^{11, 13, 40, 161, 162}. For the ballistic motion of large particles, the prediction error of the particle deposition distance could reach 130 times due to the uncertainty of the drag¹⁶³. Moreover, most of the drag force for a swarm of particles is investigated in fluidized suspension systems, where the drag force is constrained by balancing the buoyed weight of particles^{108, 164-166}. The key drag factors under this constraint are found to include the particle concentration, turbulent kinetic energy, slip velocity, two-phase covariance terms, and so on. The discrepancy between these drag correlations is as high as up to three orders of magnitude^{164, 167}. Further, for a horizontal

particle-laden jet flow, where the drag force is not constrained by gravity, we can expect a different functional dependence of the drag force^{30, 108}, though the relevant study is scarcely reported.

The current research on the drag model can be divided into those for single particles and those for particle swarms. Below we review the existing drag models.

1.5.1 Single Particle Drag Models

The essence of drag force is the area division projected in the direction of fluid flow by the integral of the normal stress on the surface of the particle and the tangential frictional stress caused by the viscosity of the fluid.

The single particle drag force, F_{D0} , in a fluid is generally defined as proportional to the dynamic pressure of the fluid and the windward area of the particle, written as¹⁶⁸

$$F_{D0} = \frac{1}{2} \rho_g (u_g - u_p) |u_g - u_p| A_p C_{D0} \quad (1-6)$$

where C_{D0} is the drag coefficient of a single particle, u_g the fluid velocity, u_p the particle velocity, ρ_g the fluid density, and A_p the windward area, that is, the projected area of the particles perpendicular to the incoming flow velocity. For spherical particles,

$$A_p = \frac{1}{4} \pi d_p^2 \quad (1-7)$$

The drag coefficient depends on the particle size, fluid physical property parameters, and the particle Reynolds number, defined by

$$Re_p = \rho_g |u_g - u_p| d_p / \mu_g \quad (1-8)$$

where d_p donates the particle diameter and μ_g the fluid dynamic viscosity.

Figure 1.11 summarizes the curves of single-particle drag models in the literature.

Figure 1.12 shows the errors curve of these single-particle drag models relative to the standard drag model. The equations of these single-particle drag models are shown in Appendix A. It can be seen from the figure that Schiller & Naumann¹⁶⁹ drag model and Xu¹⁷⁰ drag model are close to the standard drag model values and have a small error.

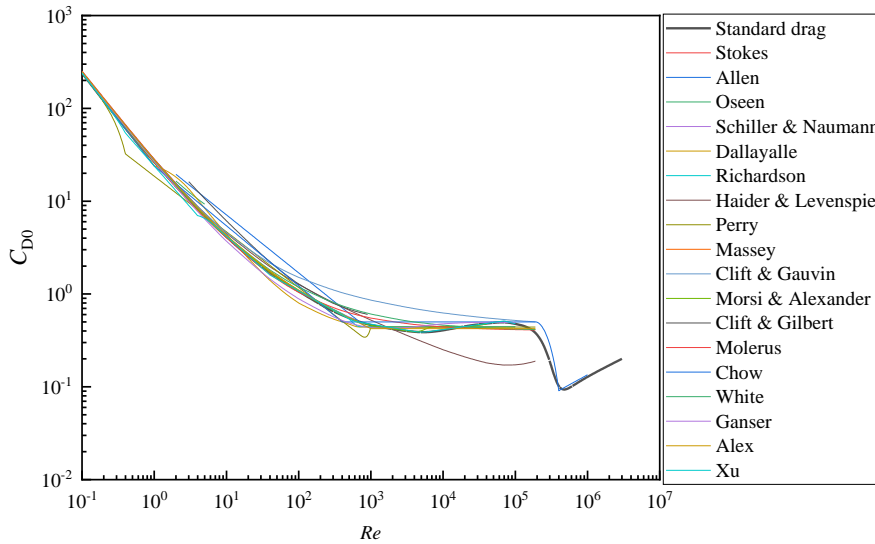


Figure 1.11 Curves of various single-particle drag models

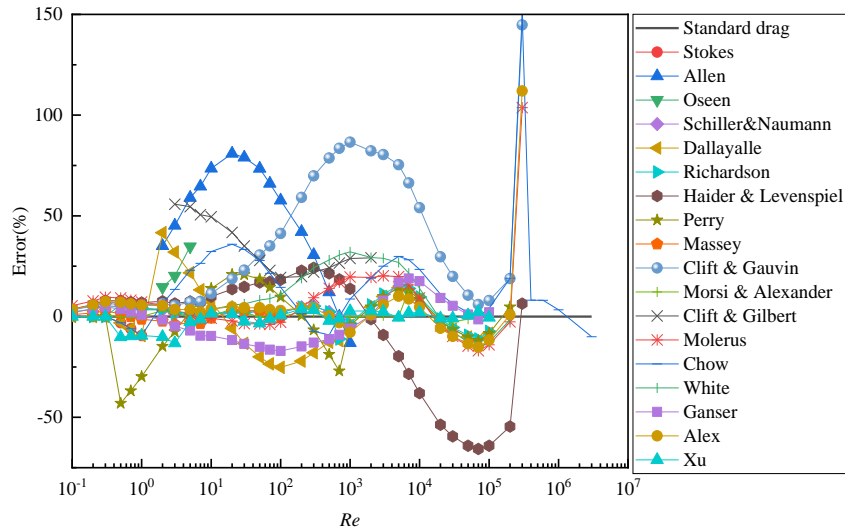


Figure 1.12 Errors curves of single-particle drag models relative to standard drag model

1.5.2 Uniform Particle Swarm Drag Models

For a uniform particle swarm, the drag force for each particle is

$$F_D = \frac{1}{2} \rho_g u_s |u_s| A_p C_D \quad (1-9)$$

where u_s is the slip velocity, defined as

$$u_s = u_g - u_p \quad (1-10)$$

The drag model of a uniform particle swarm is usually obtained by two methods:

(1) particle concentration correction method; (2) pressure drop method. The so-called concentration correction method is to multiply a particle concentration (or, voidage) correction function with the single-particle drag model, typical of which is the Wen–Yu model¹⁷¹:

$$C_{DWen-Yu} = f(\alpha_g, Re_p) C_{D0} \quad (1-11)$$

where $f(\alpha_g, Re_p)$ is the correction function and Re_p is the Reynolds number of the particle swarm.

$$Re_p = \frac{\alpha_g \rho_g d_p |u_s|}{\mu_g} \quad (1-12)$$

The pressure drop method is calculated by measuring the pressure drop per unit height of a particle swarm, typically the Ergun equation¹⁷²:

$$\frac{\Delta P}{\Delta L} = 150 \frac{\alpha_p^2 \mu_g U_g}{\alpha_g^3 d_p^2} + 1.75 \frac{\alpha_p \rho_g |U_g| U_g}{\alpha_g^3 d_p} \quad (1-13)$$

where U_g is the superficial gas velocity in a fixed bed or the superficial slip velocity in a system with non-zero velocity of particles, $U_g = \alpha_g u_s$. The two-phase pressure drop per unit height is related to the drag force per unit volume¹⁷³

$$\frac{\Delta P}{\Delta L} \alpha_g = \beta u_s \quad (1-14)$$

so

$$\beta = 150 \frac{\alpha_p^2 \mu_g}{\alpha_g d_p^2} + 1.75 \frac{\alpha_p \rho_g |u_s|}{d_p} \quad (1-15)$$

where β is the drag function, which means the drag coefficient per unit volume, also

known as the interphase exchange coefficient, which is usually used in the momentum equation of the TFM model, and its relationship to the drag force is as follows¹⁷⁴:

$$\beta u_s = \alpha_g n_p F_D \quad (1-16)$$

where n_p is the particle number density, defined as

$$n_p = \frac{6\alpha_p}{\pi d_p^3} \quad (1-17)$$

Combining the above we get

$$\beta = \frac{3}{4} \frac{\alpha_g \alpha_p}{d_p} \rho_g |u_s| C_D \quad (1-18)$$

where α_p donates the particle volume fraction, α_g is the volume fraction of the gas phase or voidage, and C_D is the drag coefficient of the particle swarm, defined as

$$\alpha_g + \alpha_p = 1 \quad (1-19)$$

$$C_D = C_{D0} f(\alpha_g, Re_p) \quad (1-20)$$

The drag coefficient and drag correction function of the uniform particle swarm are shown in Appendix B.

1.5.3 Heterogeneous Particle Swarm Drag Models

In practice, the distribution of particles in gas-solid two-phase systems is often non-uniform, especially in large industrial plants, and the use of uniform particle swarm drag force for non-uniform flow can lead to large errors. In the literature¹⁷⁵⁻¹⁷⁸, the energy-minimization multi-scale (EMMS) drag model and the filtered drag model are widely used. The EMMS model was proposed by Jinghai Li and Mooson Kwauk¹⁷⁹⁻¹⁸¹ (see Appendix C). They argued that in a gas-particle concurrent-up two-phase flow, the fluid tends to choose the path with the least resistance to flow, whereas particles tend to choose their positions with the smallest potential energy. Due to the mutual constraints

between the particles and the fluid, they compromise in competition with each other in the process of achieving their respective extremum tendencies, thus forming a steady state.

Through multi-scale analysis, Li and Kwauk believed that there are three scales of action in the actual non-uniform gas-solid system: (1) microscale interaction between fluid and single particles; (2) mesoscale interactions between dense clusters and dilute broth (with disperse particles); (3) macroscale interaction of the gas-particle system and the surrounding environment. The actual non-uniform gas-particle system was divided into three approximately uniform subsystems: "dense phase", "dilute phase" and "inter-phase", and eight parameters were used to characterize the flow state of the non-uniform gas-solid system, i.e., dense-phase porosity α_{de} , dilute-phase porosity α_{di} , dense-phase volume fraction f , dense-phase superficial gas velocity u_{gde} , dilute-phase superficial gas velocity u_{gdi} , dense-phase superficial particle velocity u_{pde} , dilute-phase superficial particle velocity u_{pdi} , and equivalent diameter of clusters d_{cl} .

$$flow\ state \sim (\alpha_{de}, \alpha_{di}, f, u_{gde}, u_{gdi}, u_{pde}, u_{pdi}, d_{cl}) \quad (1-21)$$

Over the flow structure determined by these eight parameters, only six hydrodynamic conservation equations can be formulated, as follows^{182, 183}:

(1) Force balance of dense-phase particles

$$n_{de}F_{Ddef} + n_{int}F_{bulk} - (1 - \alpha_{de})(\rho_p - \rho_g)fg = 0 \quad (1-22)$$

(2) Force balance of dilute-phase particles

$$n_{di}F_{Ddi}(1 - f) - (1 - \alpha_{di})(\rho_p - \rho_g)(1 - f)g = 0 \quad (1-23)$$

(3) Pressure drop balance

$$\Delta P_{de} - \Delta P_{di} - \Delta P_{int}/(1 - f) = 0 \quad (1-24)$$

(4) Conservation of fluid mass

$$u_g = u_{gdef} + u_{gdi}(1 - f) \quad (1-25)$$

(5) Conservation of particle mass

$$u_p = u_{pdef} + u_{pdi}(1 - f) \quad (1-26)$$

(6) Cluster equivalent diameter

$$d_{cl} = \frac{d_p \left[\frac{u_p}{1 - \alpha_{max}} - \left(u_{mf} + \frac{\alpha_{mf} u_p}{1 - \alpha_{max}} \right) \right] g}{N_{st} \frac{\rho_p}{\rho_p - \rho_g} - \left(u_{mf} + \frac{\alpha_{mf} u_p}{1 - \alpha_{max}} \right) g} \quad (1-27)$$

where α_{max} approximation is 0.9997. The parameters/variables outnumber the hydrodynamics equations, indicating an infinite set of solutions if solving the model solely from these hydrodynamic equations. That contradicts the reality that a steady-state can be normally determined for such a two-phase flow system. Jinghai Li and Mooson Kwauk¹⁷⁹⁻¹⁸¹ proposed a stability condition to close this problem by assuming that the energy consumption rate for suspending and transporting particles per unit mass of particles, N_{st} , tends to minimum, as follows:

$$\begin{aligned} N_{st} &= (N_{st})_{de} + (N_{st})_{di} + (N_{st})_{int} \\ &= \frac{\rho_p - \rho_g}{\rho_p} \left[u_g - u_{gdi}(1 - f) f^2 \frac{\alpha_{di} - \alpha_{de}}{1 - \alpha_g} \right] g \rightarrow \min \end{aligned} \quad (1-28)$$

Its counterpart, the energy consumption rate for suspending and transporting particles per unit volume of space, W_{st} , is written as follows:

$$W_{st} = N_{st}(1 - \alpha_g)\rho_p \quad (1-29)$$

The Filtered drag models widely cited in the literature mainly include the Sarkar¹⁷⁸ model, Radl¹⁸⁴ model, Gao–Sarkar¹⁷⁷ model (see Appendix D). The Sarkar¹⁷⁸ model is a sub-grid “two-marker” model (α_g and u_{slip}) of fluidized gas–particle flows. The

Radl¹⁸⁴ model is a “one-marker” model derived from the high-resolution simulation of CFD-DEM in a periodic domain, with its non-uniform index fitted as a function of the filter size and particle concentration. The Gao–Sarkar¹⁷⁷ model is a modification to the Sarkar model especially at the dense regime and is thus suitable for simulating fluidization of Geldart A particles over a wide range of regimes covering both dense and dilute flows.

1.5.4 Dilute Particle Swarm Drag Models

For jets, pneumatic transport, various respiratory events, and droplet dispersion, the volume fraction (or loading ratio) of particles tends to be small, usually less than 1% by volume. For these physical scenarios, single-particle drag models or dilute phase drag models are widely used, but the simulation results may show large errors. The drag model selection in pneumatic conveying and jet flow scenarios can be found in Appendix E. The drag model selection in violent expiratory events and droplet dispersion can be found in Appendix F.

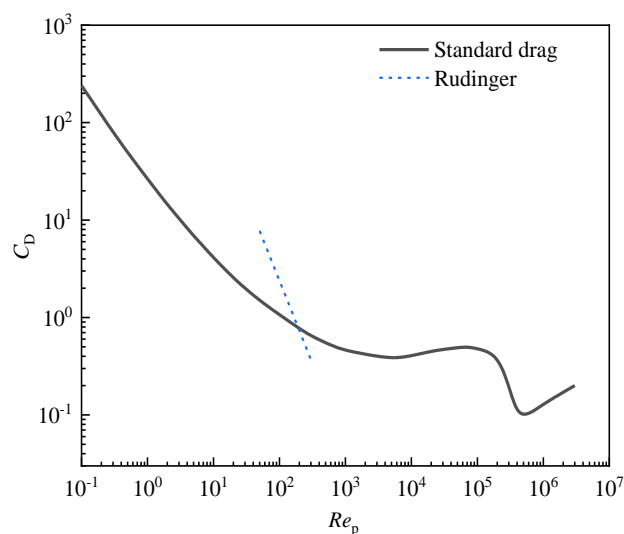


Figure 1.13 Comparison of Rudinger drag curve with the standard drag curve

The drag model studies of dilute particle swarm systems (say, $\alpha_p \leq 0.01$) have

rarely been reported. Rudinger¹⁸⁵ studied the motion of particles in the shock tube using fringe photography and light scattering methods, and obtained the drag coefficient, as shown in Eq. (1-30). As can be seen from Figure 1.13, it differs greatly from the single-particle standard drag curve.

$$C_D = \frac{6000}{Re_p^{1.7}}, 50 < Re_p \leq 300, \alpha_p \leq 0.001 \quad (1-30)$$

1.5.5 Simulations of Particle-laden Jets

Accurate simulation of particle-laden jets is based on the premise that the gas turbulence simulation results are accurate. However, circular gas jet simulations are notoriously inaccurate for several reasons.

- (1) The velocity distribution in the nozzle of a circular jet^{30, 31} is hard to be quantitatively described. Its distribution form is related to the load rate and particle diameter, but is few reported, resulting in a poor situation of setting the inlet boundary conditions.
- (2) The prediction of circular jet diffusivity in the turbulence model is unexpectedly poor, and the main reason is considered to be the modeling difficulty of turbulent dissipation rate¹⁸⁶.
- (3) The circular jet is a strong free shear jet with a strong convolitional entrainment effect^{12, 20, 21}, but there are few reports on quantitative studies on convolitional entrainment, so it is difficult to accurately apply the boundary conditions of convolitional entrainment.
- (4) The problem of outlet boundary conditions, different outlet boundary conditions also have an impact on the jet velocity field.

The simulation of a single gas-phase circular jet is already complex and difficult, let alone a particle-laden jet, and the increase in the loading of particles will make the simulation even more difficult. The most important and dominant force between the gas and particles is the drag force, however, due to the lack of a suitable drag model for the dilute particle group, the single particle drag model was usually applied without consideration of the effect of neighboring particles, leading to large errors when comparing with experimental measurements^{12, 158-160}.

1.6 Research Contents

Targeting the complex behavior of polydisperse, particle-laden jet flows, this thesis tries to combine both experimental and simulation methods to investigate the gas-particle dynamics in horizontal jet flows with consideration of three types of particles (categorized with the Stokes number: tracer particles, small particles, and large particles). The gas-particle dynamics here involve the jet velocity field, jet diffusion process (particle concentration/clustering), drag model, particle volume fraction model, and so on.

For high-Stokes-number particle-laden jets with large particle diameters, it is possible to reveal the multiscale dynamic behavior of the jet by starting from the particle-scale observation, and integrating it into a spatiotemporal field analysis. To this end, we establish a particle-laden jet experimental platform and develop a real tracking-precise-reconstruction, time-resolved 3D-PTV method, and combine it with PIV method for gas-phase flow, thus revealing the two-phase dynamics simultaneously of high-Stokes-number particle-laden jets.

For middle- and low-Stokes-number particle-laden jets, the particle diameter is so small that it is difficult to perform particle-scale dynamic studies. Therefore, this thesis primarily utilizes the PIV method to investigate the flow field behavior of middle- and low-Stokes-number particle-laden jets.

The major contents of this thesis are outlined below, with a schematic diagram of the research framework shown in Figure 1.14.

(1) Establishment of Experimental Platform and Research Methods

This section first completes the construction of the particle-laden jet experimental platform. This is a complex and difficult work, with high requirement for the structural design, practical operation, and experimental coordination. Based on that, a real tracking-precede-reconstruction, time-resolved 3D PTV method is developed, which includes algorithms of digital image processing, particle tracking matching, and 3D reconstruction of particle flow field. This section, elaborated in Chapter 2, lays the foundation for subsequent research work.

(2) Dynamics of High-Stokes-number Particle-laden Jet

In this section, the analysis at particle scale on both the particle dynamics and particle concentration are performed for a high-Stokes-number particle-laden jet, with details on the velocity field, fluctuating velocity field, and particle concentration field of gas-solid two-phase. Moreover, a new drag model and particle concentration evolution model are proposed. This part of the work is elaborated in Chapter 3.

(3) Dynamics of Low- and Middle- Stokes-number Particle-laden Jet

In this section, the velocity, fluctuating velocity, and particle concentration fields of the low- and middle- Stokes-number particle-laden jet flow are studied. The analysis

of velocity decay and self-similarity are carried out, so as to investigate the applicability of the classical jet velocity decay model to the jet flow here. In addition, based on large-field macroscale measurements and the Voronoi method, the cluster structure, characteristic parameter scale, and concentration evolution of small particles are studied. The applicability of the new particle volume fraction model to a middle-Stokes-number particle-laden jet is verified. This part of the work is elaborated in Chapter 4.

(4) Simulations of Particle-laden Jets

To verify the applicability and accuracy of the new drag model, this section, as elaborated in Chapter 5, conducts simulations of both high-Stokes-number and middle-Stokes-number, particle-laden jet flows with CFD-DPM approach. The influence of drag relations is emphasized with analysis of the jet velocity and the sensitivity of drag correlation to Reynolds number. In addition, the entrainment, inlet velocity distribution, and the effects of outlet boundary types on the jet are also discussed.

The conclusions and outlooks are drawn finally.

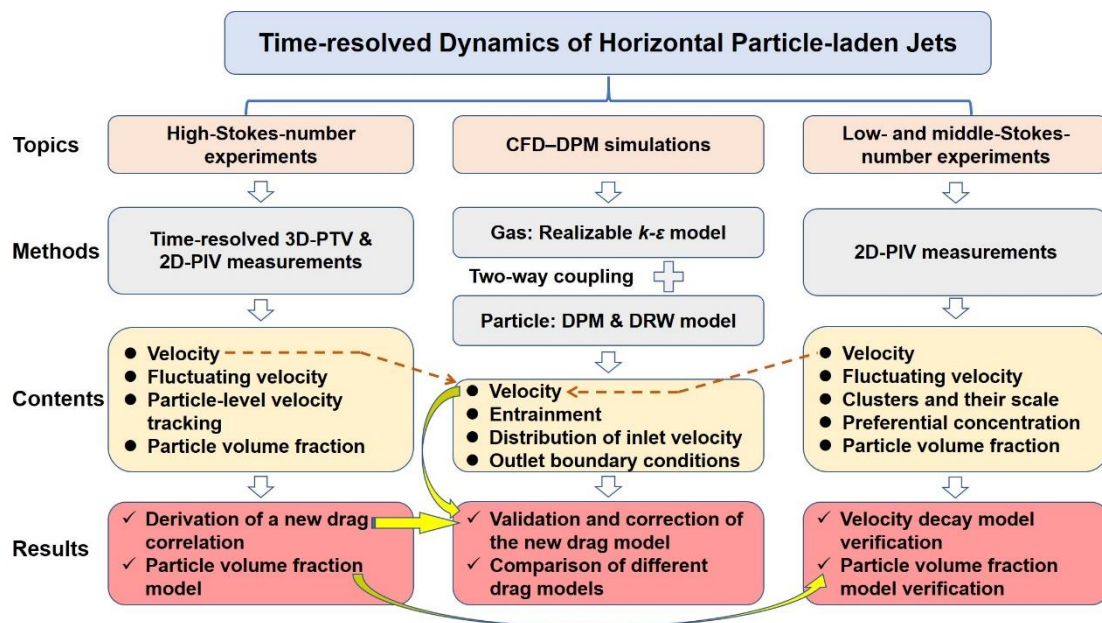


Figure 1.14 Schematic diagram of the research framework

Chapter 2 Experimental Methods

2.1 Overview

This chapter introduces the experimental method employed in this paper, which encompasses the experimental platform, data acquisition methods, and definitions of variables. The focus of the investigation is particle-laden jets from an experimental perspective, for which a particle-laden jet experimental platform has been established. The experimental platform comprises a jet system, a Particle Image Velocimetry (PIV) measurement system, and a time-resolved 3D Particle Tracking Velocimetry (3D-PTV) measurement system.

The primary objective of this chapter is to conduct measurement on gas-phase jets and low-Stokes-number particle-laden jets using PIV, with the ultimate aim of obtaining motion information of small particles through PIV. Additionally, this chapter presents a time-resolved 3D-PTV method based on the author's recently developed time-resolved particle tracking and 3D reconstruction technique. This innovative approach constitutes a tracking-preceded reconstruction, time-resolved, 3D particle flow field reconstruction method, which is implemented using a dual-camera recording. The paper employs this method to examine the dynamics of particle-laden jets at the particle level. Lastly, this chapter defines the primary physical quantities under investigation in this thesis, ensuring clarity and precision in presenting experimental results.

2.2 Experimental Setup

As shown in Figure 2.1, our experimental system consists of three parts: the jet device, PIV and PTV. Part one is the jet device. The compressed air, filtered into the ejector (FOX-1/2, USA) with an exit diameter of 12 mm, is used as the gas source for the jet. The particles enter the ejector through a hopper and get mixed with the air in the ejector, and then ejected into the measurement chamber, which is a hollow cuboid space of 2 m × 1 m × 1.5 m (length × depth × height), composed of tempered glass and metal frame. The ejector is mounted 0.3 m below the top of the chamber. The hopper is adopted to stabilize a uniform feeding of particles¹⁸⁷. High-frequency (1000 Hz) sensors are used to measure the gas flow rate and pressure at the ejector inlet. The sensor signal is transmitted to the computer through a multi-functional I/O device (NI, USA). The acquisition accuracy of the flow sensor (TKL50-DN15, CHN) and pressure sensor (PCM300, CHN) are ±0.2% and ±0.1%, respectively.

Part two, the PIV setup, includes two high-speed cameras #2 and #3 (HX-5E, NAC, JP) for larger shooting area, double pulsed laser (TOLAR-527, Beamtech Optronics Co., Ltd., CHN), beam expander (BZ-61, Seika Digital Image Co., Ltd., JP), synchronizer (LC-880, Labsmith, USA), and computer. The tracer particle seeder (CTS-1000, Seika Digital Image Co., Ltd., JP) and solid particle seeder (Solid-3 Seika Digital Image Co., Ltd., JP) connected with the ejector is switched on when PIV is used to measure the gas or SiO₂ velocity. The laser has a 527 nm wavelength and a thickness of 1 mm. The synchronizer ensures simultaneous switching of the high-speed camera and the laser with a synchro-precision of 0.1 ns.

Part three, the time-resolved 3D-PTV device, consists of two high-speed cameras (HX-5E, NAC, JP), a LED source (Jinshang, CHN), a synchronizer (LC-880, Labsmith, USA), and the computer. The two high-speed cameras are mounted perpendicular to each other, with camera #1 shooting the top view and camera #2 the front view. After the camera setting is completed, a simple calibration is performed on each of the two cameras to obtain the exact spatial resolution and eliminate the distortion of the image (distortion elimination is necessary for wide-angle and magnifying lenses). The experimental devices are grounded to minimize the static charging of particles. The following data analysis takes the center of the ejector exit as the coordinate origin, the axial direction of the jet is set as the x -axis, the height direction is the y -axis, and the depth direction is the z -axis.

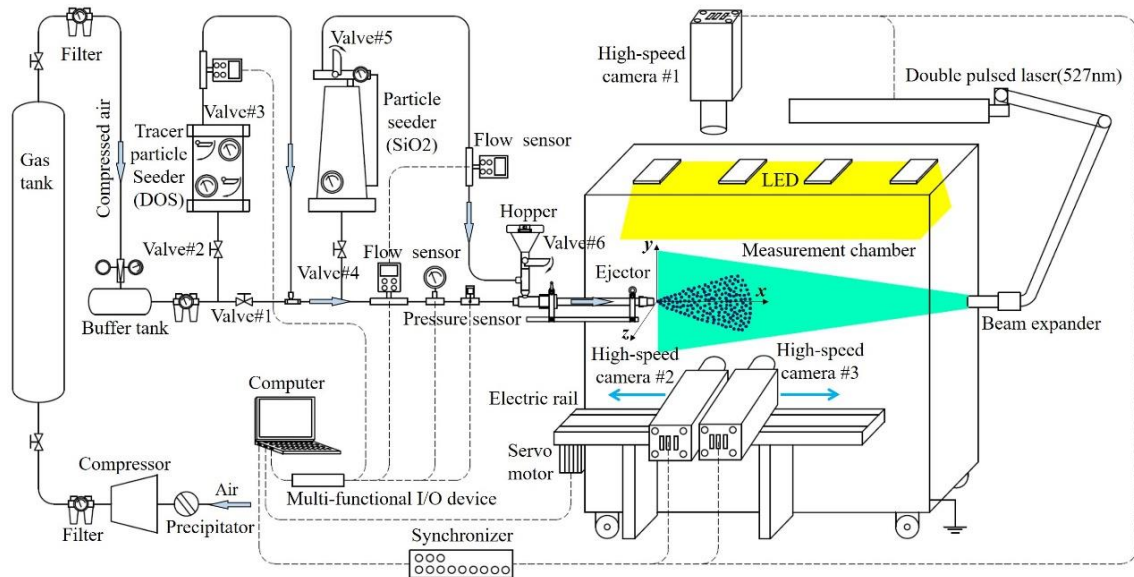


Figure 2.1 Schematic diagram of experimental device.

In this paper, three kinds of particle-laden jet experiments will be carried out, and the valve settings of each experiment are different. In order for readers to understand the valve settings more clearly, we list them in Table 2.1.

Table 2.1 Valve settings

| Valve number | #1 | #2 | #3 | #4 | #5 | #6 |
|---|----|-----|-----|-----|-----|-----|
| Gas tracer particles/low-Stokes-number particle-laden jet experiments | On | On | On | Off | Off | Off |
| Small particles/middle-Stokes-number particle-laden jet experiments | On | Off | Off | On | On | Off |
| Large particles/high-Stokes-number particle-laden jet experiments | On | On | On | Off | Off | On |

2.3 Materials

The experiments in this paper require three kinds of particles, namely gas tracer particles (DOS oil) for low-Stokes-number particle-laden jets, SiO₂ microspheres (small particles) for middle-Stokes-number particle-laden jets, and glass beads (large particles) for high-Stokes-number particle-laden jets. This section presents the details of the three types of particles and how they are fed.

2.3.1 Gas Tracer Particles

The material of gas tracer particles is DOS oil with a density of 918kg/m³. The tracer particles are generated by a gas-driven tracer particle seeder (CTS-1000), shown as Figure 2.2 (a). The mean particle diameter is about 2~3μm, and its relaxation time is 0.0113~0.0255 ms. The Stokes number of the tracer particles in the experimental range is between 0.0106 and 0.0616, which is much smaller than 1 and can track the gas phase movement well.

2.3.2 Small Particles

The material of small particles is SiO₂ microspheres with a density of 2000 kg/m³.

The small particles are produced by a gas-driven solid particle seeder (Solid-3), shown as Figure 2.2 (b). The mean particle diameter is $40.86 \mu\text{m}$, the $d_{p,\text{rms}}$ is $10.29 \mu\text{m}$, and its relaxation time is 0.0103 s . The small particles have a Stokes number between 9.61 and 24.89 in the experimental range. The measured particle size distribution of SiO_2 microspheres is shown in Figure 2.3.

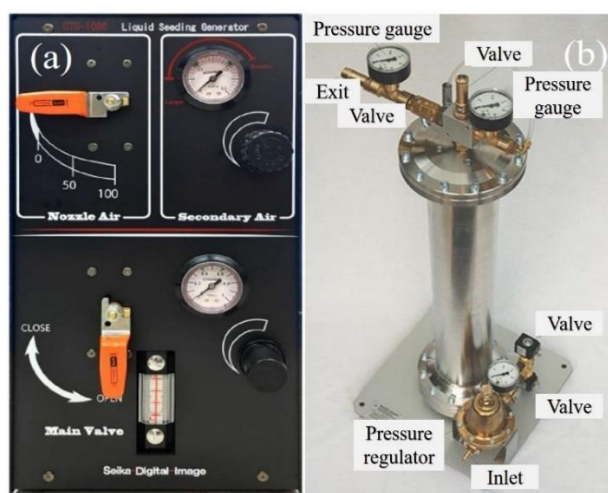


Figure 2.2 Tracer particle seeder (a) and Solid particle seeder (b).

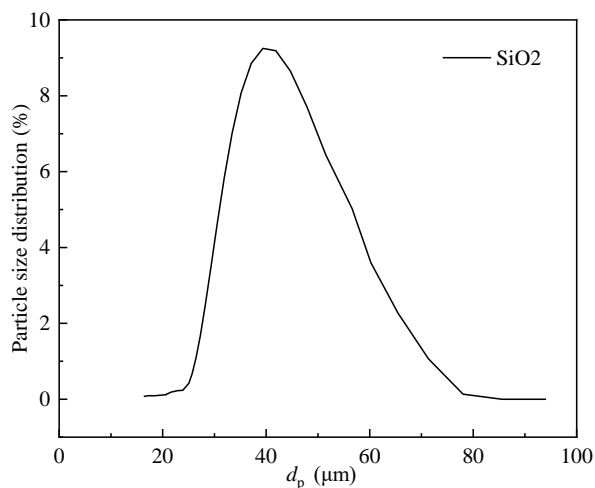


Figure 2.3 The measured particle size distribution of SiO_2 microspheres.

2.3.3 Large Particles

The material of large particles is glass beads with a density of 2490 kg/m^3 . The

large particles are fed through a hopper, shown in Figure 2.4. The particle gravity and the adjustable funnel diameter are used to realize the uniform and adjustable particle feeding rate and the continuous and loose feeding of the particles. The diameter of the hopper is 5mm. The PSD (particle size distribution) and sphericity were measured using a particle size analyzer (CAMSIZER X2, GER, shown as Figure 2.5). The measured average particle diameter is 1051.6 μm , $d_{p,\text{rms}}$ is 39.31 μm , sphericity is 0.975, and its relaxation time is 8.473 s. The Stokes number of the large particles in the experimental range is greater than 1000. The measured particle size distribution of glass beads is shown as Figure 2.6.

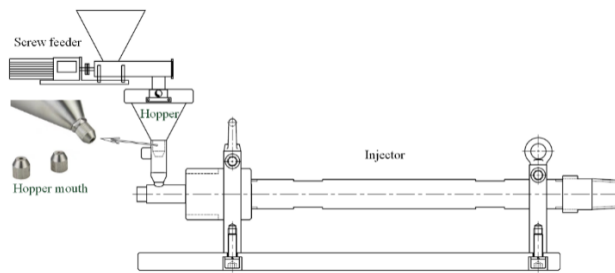


Figure 2.4 Schematic diagram of the hopper feeding



Figure 2.5 CAMSIZER X2

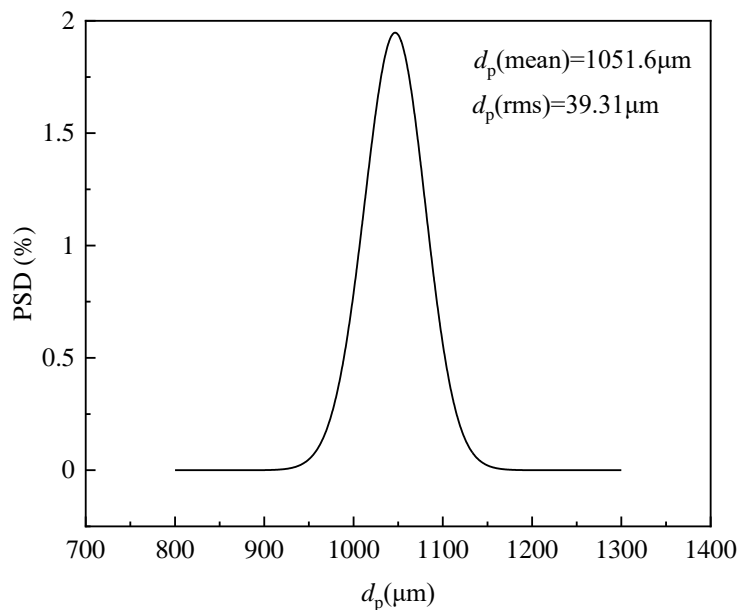


Figure 2.6 The measured particle size distribution of glass beads.

2.4 Particle Image Velocimetry

2.4.1 Camera Calibration

Camera calibration is to obtain the spatial resolution and image distortion parameters of the image. It can be carried out by shooting a calibration plate with known spatial dimensions. The position of the calibration plate coincides with the illumination position of the laser sheet light source, and its angle should be parallel to the camera lens. The spatial resolution can be obtained by converting the known size on the calibration plate and the pixel of the corresponding captured image. Furthermore, the post-image processing needs to remove the distortion of the image according to the camera calibration results and restore the real image. Distortion is low for standard lenses and high for wide-angle and telephoto lenses (see Figure 2.7) and must be undistorted.

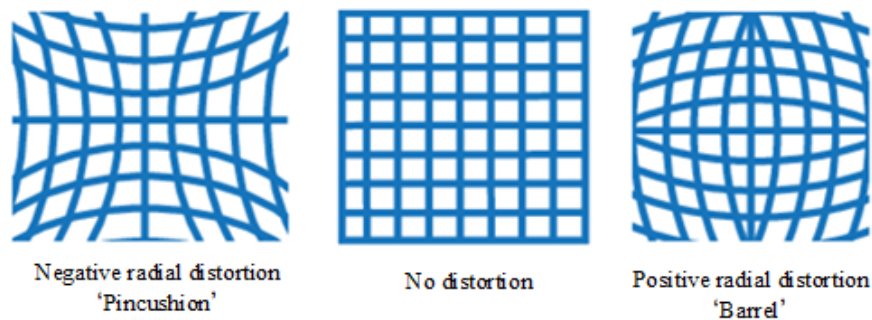


Figure 2.7 Effects of different lenses on captured images

2.4.2 Velocity Calculation Principle

A timing controller synchronizes the double-pulsed laser and the high-speed camera. A very short time separation is used to record a pair of images. Once the images are successfully recorded, the velocity can be determined. A typical PIV velocity evaluation process can be found in Westerweel's¹¹² introduction, and we also introduced

it in Chapter 1. Here we briefly describe it. The *Koncerto II* software developed by Seika Digital Image and German Aerospace Center is applied to determine the velocity of gas tracer particles. A pair of images is divided into a large number of 32×32 pixels interrogation windows, the size of which is selected according to the velocity. The multiple-pass cross-correlation algorithm¹⁸⁸ is applied to the interrogation windows of the pair of images, and then the displacement of each interrogation window is obtained by peak detection and displacement estimation. The gas/small particle velocity can be obtained by calculating the displacement, Δs , and time interval, Δt . The velocity u_i can be written as

$$u_i = \frac{\Delta s}{\Delta t} \quad (2-1)$$

where i is the index of an interrogation window. It should be noted that the velocity calculation methods of PIV and PTV are the same, the difference is that the gas/small particle velocity relates with the displacement of an interrogation window in PIV, whereas the large particle velocity relates with that of a particle in PTV. For PTV, Δt is the interframe time; for PIV, Δt is the cross-frame time of the laser. Furthermore, the multiple-pass correlation algorithm moves the interrogation window of the second image based on standard cross-correlation¹⁸⁹. Repeated use of this operation can achieve higher resolution accuracy with a cost of computation time. A median filter is applied to eliminate the particle phase influence. A simple schematic diagram of the velocity calculation principle for PIV is shown in Figure 2.8.

Figure 2.9 shows the snapshots of the jet using DOS oil as tracer particles and the corresponding velocity vector diagram determined by PIV, with (a): the snapshot of the single-phase gas jet, (b): the corresponding gas velocity vector, (c): the snapshot of

high-Stokes-number particle-laden jet, and (d): the corresponding gas velocity vector.

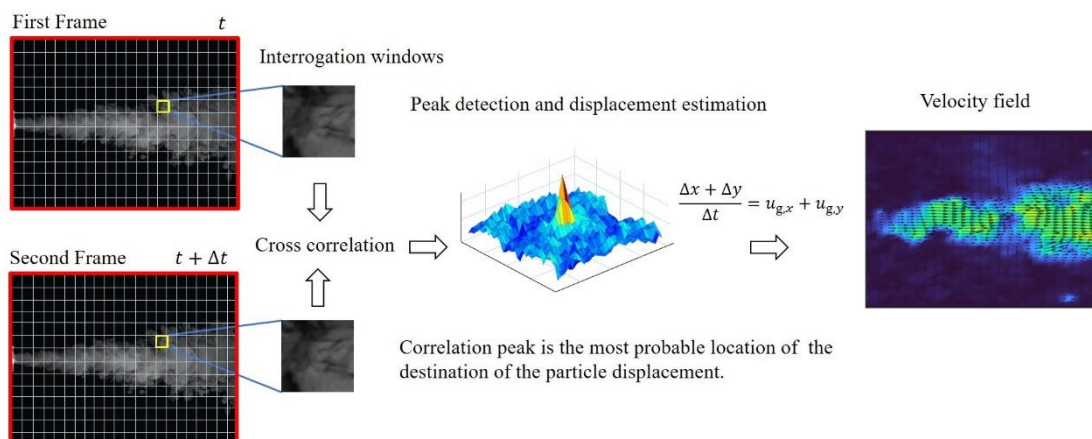


Figure 2.8 Velocity calculation principle of PIV

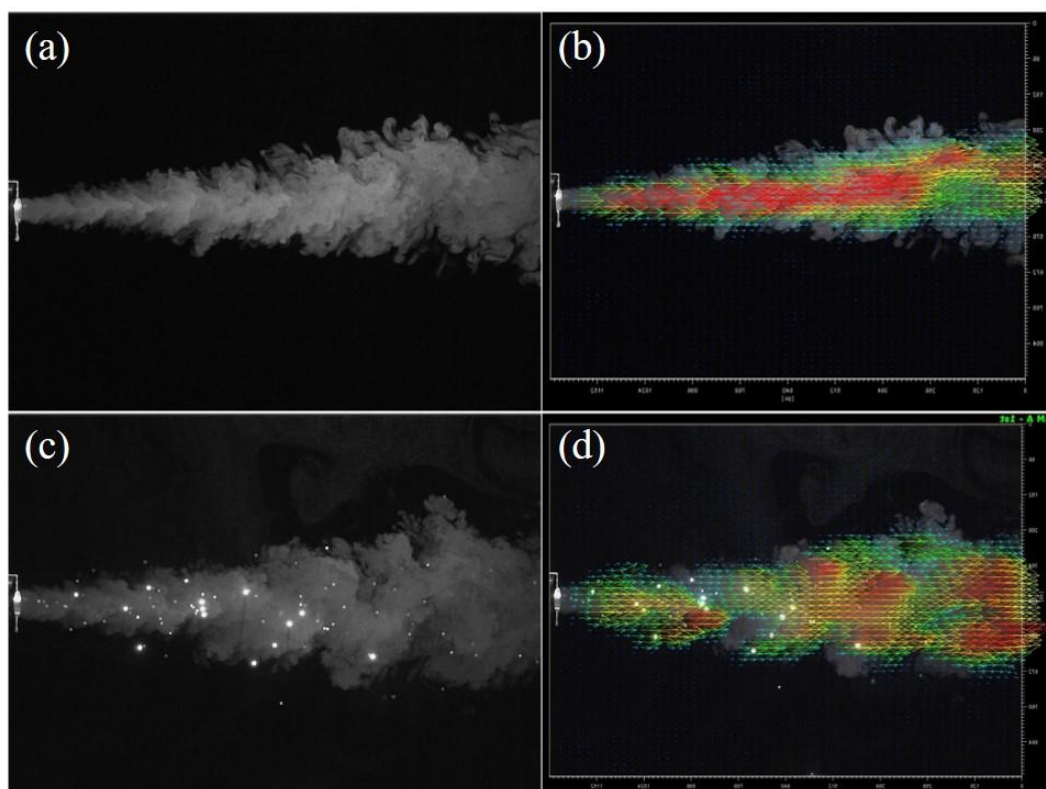


Figure 2.9 Snapshots of the jet using DOS tracer particles and corresponding gas velocity vector
 (a) single-phase gas jet; (b) single-phase gas velocity vector; (c) high-Stokes-number particle-laden jet; (d) two-phase gas velocity vector.

2.5 Time-resolved 3D Particle Tracking Velocimetry

Here we develop a 4D-PTV method based on dual-camera shooting, which is a

purely tracking-precède-reconstruction approach implemented in MATLAB. This method does not need to generate a mapping function between image coordinates (x, y) and physical coordinates (x, y, z) by calibration or complex calibration of multi-camera optical systems. A typical 2D-PTV calibration method is sufficient. The schematic diagram of the central processing procedure of 4D-PTV includes three aspects (shown in Figure 2.10): particle detection, Lagrangian particle tracking, and reconstruction.

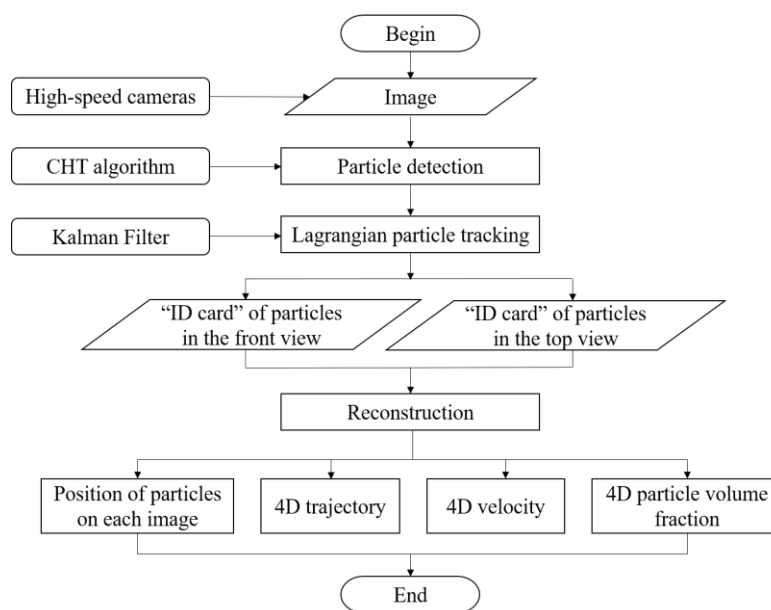


Figure 2.10 Schematic of the processing routines of 4D-PTV.

Once the raw images are obtained with the high-speed camera, we first complete the detection of particles and obtain the 2D positions of particles in each frame, and then the Lagrangian tracking algorithm is applied to obtain 2D trajectories of particles. According to the characteristics of the trajectory of each particle, we build their own unique “ID”. The above operations are performed on the data of the front view and the top view, respectively. According to the differences between IDs, the particles in the two views are matched, thereby completing the particle flow field reconstruction with time-resolved 3D positions, and trajectories. The implementation steps of this method

will be introduced in detail below.

2.5.1 Camera Calibration

Different from the PIV, the PTV needs to calibrate two cameras separately. The angle between the calibration plate and the camera should be less than 45° , as shown in Figure 2.11. The calibration results and errors are shown in Figure 2.12. The rest of the calibration operations are the same as PIV.

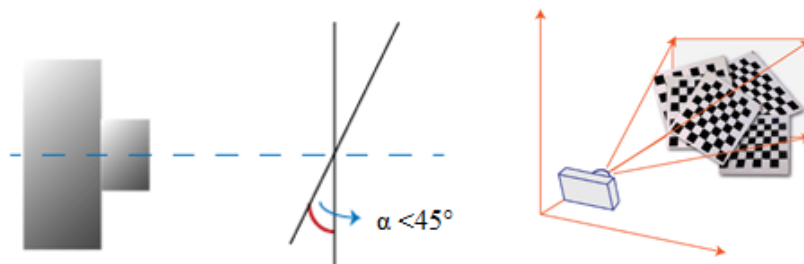


Figure 2.11 Schematic diagram of the placement of the calibration board and the camera
(Taken from MATLAB Help)

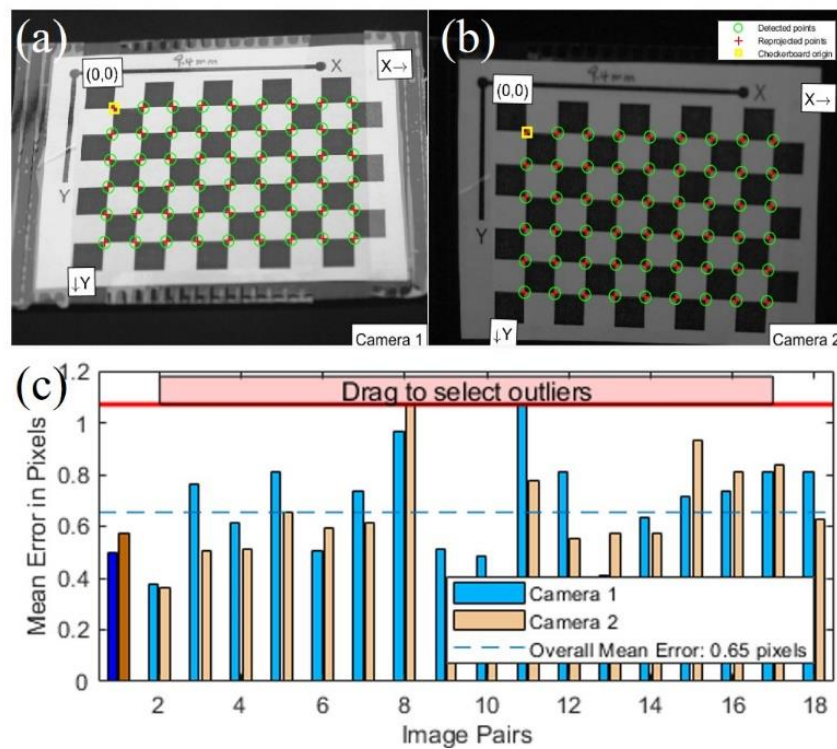


Figure 2.12 Calibration results (a,b) and errors (c)

2.5.2 Image Pre-processing

MATLAB software is used to preprocess the images taken by the front view and the top view respectively, and the processing consists of the following three steps.

(1) Load the images

MATLAB software is used to read the raw image, crop the raw image according to the target image area, and convert the image into a grayscale image.

(2) Threshold the images

Due to the influence of illumination, the background brightness of the image may be unevenly distributed, and it is difficult to segment the target image area by directly performing global threshold segmentation. To solve this problem, the adaptive thresholding method¹⁹⁰ is used to process the image. The so-called adaptive threshold method automatically determines the threshold value of each region of the image through a series of algorithms. Compared with the global threshold method, for different regions of the image with uneven brightness distribution, the adaptive threshold method has a higher accuracy. The adaptive threshold algorithm adopted in this paper was proposed by Bradley¹⁹⁰. This is a method of calculating a local threshold based on the local mean intensity of each pixel's neighborhood. Its advantage is that it takes into account the adjacent pixels on all sides of each pixel, rather than calculating the average of pixels in a segmented area of the image.

(3) Images Denoising

Perform morphological operations on the image and perform area opening to remove noisy pixels.

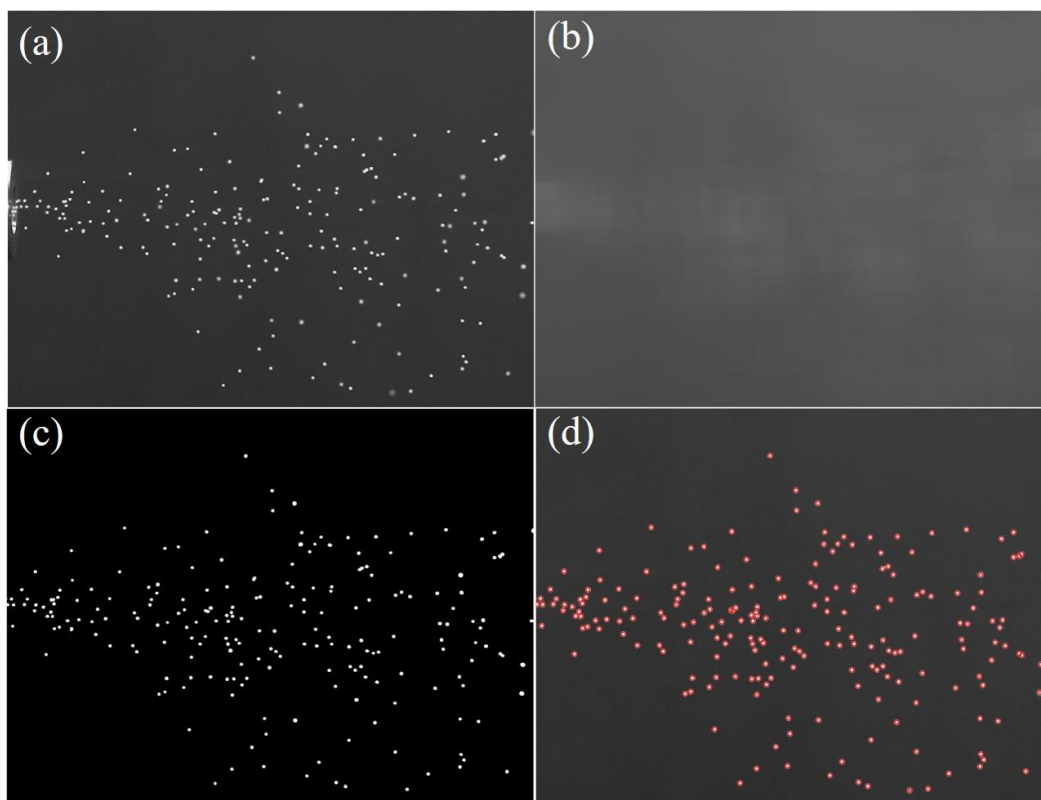


Figure 2.13 Particles detection steps: (a) raw image, (b) image segmentation, (c) binary image, (d) particle detection results.

2.5.3 Particle Detection

As shown in Figure 2.13, particle detection can be divided into four steps: (a) obtaining the raw images, (b) calculating the image background, thereby realizing the image segmentation, (c) obtaining the binary image, and (d) detecting and marking particles. Due to the influence of illumination, the background brightness of the image may be unevenly distributed. Thus, the adaptive threshold method¹⁹⁰ is used to realize image segmentation. The coordinates of particles in the target flow field are extracted using the particle detection method, i.e., x and y coordinates are determined from the front view image, then the x and z coordinates from the top view image.

The particle position detection directly affects the accuracy of subsequent particle

match and velocity calculation. The commonly used particle detection method^{118, 124} is based on the measurement of the attributes of the image area of particles, i.e., calculation of the area, center, and roundness of particles by counting the number of pixels occupied by particles. However, some particles may overlap, so they cannot be effectively distinguished in either the front or top view. To solve this problem, the circle Hough transform (CHT) method^{191, 192} is applied to find circles in the image for detecting and identifying particles. That is more robust than the traditional method when there are noise, occlusion, and variant illumination conditions.

2.5.4 Lagrangian Particle Tracking

The minimum Euclidean distance method is usually used in the PTV algorithm to realize particle tracking^{193, 194}. This simple nearest neighbor algorithm is often unable to provide accurate tracking results, while the iterative method^{153, 194} needs a high computational cost¹⁹⁵. It has been found that in a very short duration, the dispersion of particles follows a ballistic regime (purely kinematic)¹⁸. Based on this finding, various motion predictors were proposed to realize particle tracking^{117, 118, 124, 149, 196}. For example, the Wiener filter was applied to predict the movement of particles in the STB algorithm¹⁴⁹. Similarly, we establish a motion predictor to realize particle tracking from two groups of 2D images (both front and top views), and the four-frame velocity estimate method^{121, 196} is used to establish the initialization trajectory of the motion predictor. Considering that the experiment is not stationary and the influences of noise on each frame/particle are different, the Kalman filter¹⁹⁷ is more suitable for our situation than the Wiener filter. The Kalman filter is an optimal regression data

processing method, proposed by the mathematician Kalman, and is often used in the fields of guidance and navigation control systems, computer vision systems and signal processing. The main role of the Kalman filter is to estimate the optimal system state from noise-affected measurements. The core ideas of it are mathematical model prediction (Prediction) and measurement feedback update (Measurement). Since Prediction and Measurement include the effects of system noise and external noise, the optimal estimation can also be seen as a filtering process. For particle jet motion, the diffusion of particles follows the trend of a (purely kinematic) ballistic regime¹⁸ over short time intervals, so the Kalman filter is able to track particles well. Hungarian Algorithm was proposed by Hungarian mathematician Edmonds¹⁹⁸. Hungarian algorithm is a partial graph-matching algorithm based on Hall's theorem to prove ideas fully. The core of the algorithm is to achieve the maximum matching of bipartite graphs by constantly looking for augmenting paths. In this paper, Hungarian algorithm is used to solve the matching problem in the particle tracking process.

The specific implementation steps of Lagrangian particle tracking are as follows:

- (1) Set acceleration error, position error, and noise error. Each error can be adjusted by calculating the theoretical value and the results of the initialization trajectory to find the most suitable error reference value for the experiment.
- (2) Based on the Kalman filter, the fitted particle initialization trajectory is obtained by using the first K -frame data. The initialization trajectory information includes the ID number of the trajectory, the total number of trajectory frames, the number of visible trajectory frames, and the number of continuous invisible trajectory frames.
- (3) Based on the initialization trajectory, the Kalman filter predicts the particle position (prediction) at the next moment.
- (4) Detect the particle position (measurement) in the next frame.

- (5) The cost matrix is created to calculate the residual between the prediction and measurement. The Kalman gain matrix¹⁹⁹ that minimizes the posterior estimation error of the system is solved, and the results are stored in the cost matrix. The Mahalanobis distance²⁰⁰ is selected as the motion estimation residual.
- (6) Based on the Kuhn & Munkres Hungarian algorithm²⁰¹⁻²⁰³ and the weighted sum of the Mahalanobis distance between the measured values and the known trajectories, the known trajectories are matched with all newly identified particles according to the cost matrix, and the matching results are returned. The matching results include successfully matched trajectories and particles, unmatched trajectories and particles.
- (7) The obtained Kalman gain matrix is used to calculate the optimal particle position that minimizes the posterior estimation error of the system, and the successful trajectory is updated to correct the Kalman filter.
- (8) Update the unmatched trajectories. If the number of consecutive invisible frames is greater than the threshold, the particle is considered missing and the trajectory is no longer updated.
- (9) Create a new trajectory for an unmatched particle when the number of visible frames of the particle is greater than the threshold.
- (10) Iterate steps (3) ~ (9) until the last frame. A simple flowchart shown in Figure 2.14 can help readers understand the Lagrangian particle tracking.

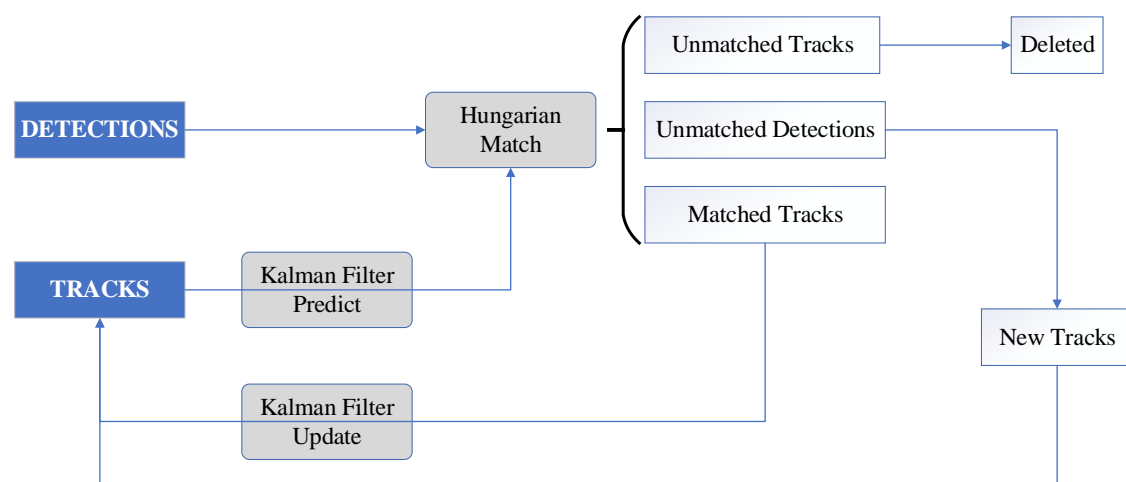


Figure 2.14 Lagrangian particle tracking flowchart

In addition, because the Kalman Filter is more complicated, the following briefly introduces the implementation process of the Kalman Filter in this article. To put it simply, when the kinematic process and observation process of particles conform to the Gaussian distribution, the essence of the Kalman Filter is to use two Gaussian distributions to determine an optimal weighting ratio and obtain a new Gaussian distribution. The schematic diagram of the key steps of the Kalman Filter is shown in Figure 2.15.

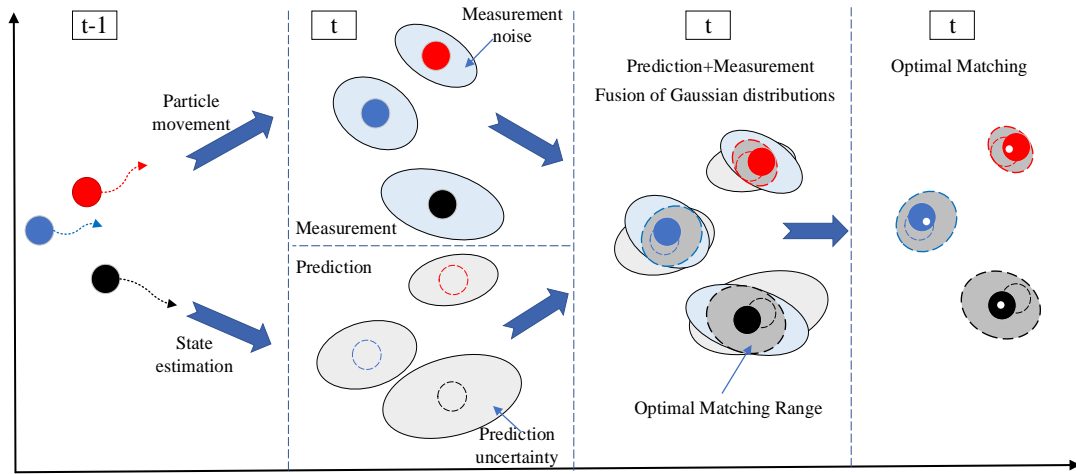


Figure 2.15 Schematic diagram of Kalman Filter

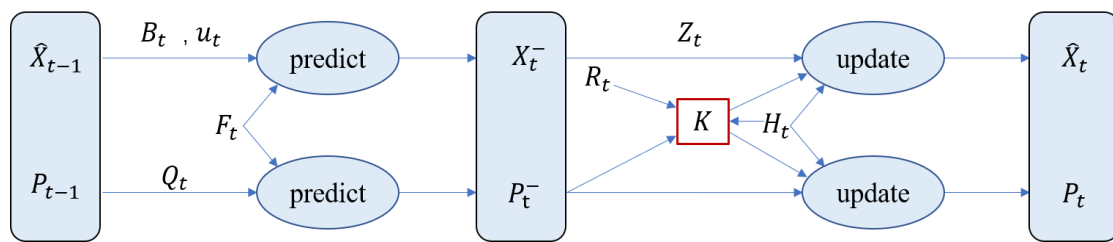


Figure 2.16 Kalman Filter flowchart

The algorithm flow chart of the Kalman Filter is shown in Figure 2.16. According to the flowchart, here is a brief description of the algorithm implementation of the Kalman Filter. First, the particle state quantity at time $t - 1$ is expressed as \hat{X}_{t-1} , the covariance matrix of the particle state quantity at time $t - 1$ is expressed as P_{t-1} . On

this basis, do a step-by-step recursion to obtain the priori system variable \hat{X}_t^- and the covariance matrix P_t^- of the prior estimation error:

$$\hat{X}_t^- = F_t \hat{X}_{t-1} + B_t u_t \quad (2-2)$$

$$P_t^- = F_t P_{t-1} F_t^T + Q_t \quad (2-3)$$

where, F_t is the prediction process coefficient; B_t is the external control variable matrix; u_t is the external control vector; Q_t is the covariance matrix of state prediction error (external noise). Calculate the predicted value of the state quantity and the residual e of the observed value:

$$e = H \hat{X}_t^- - Z_t \quad (2-4)$$

where, H is the transmission coefficient, indicating the relationship between the prediction of the state quantity and the prior system variable; Z_t is the observed value of the system state quantity.

Assuming that the kinematic process and the observation process of the particle conform to the Gaussian distribution, then the corrected posterior system variable \hat{X}_t can be obtained through linear fusion:

$$\hat{X}_t = \hat{X}_t^- + e K_K \quad (2-5)$$

where, the Kalman gain matrix K_K , $K_K \in [0, H]$, represents the proportion of the prediction and the observed value of the state quantity relative to the optimal value.

Now let's find the optimal K value for the result. Assuming that the actual value of the system state quantity is X_t , then the system posterior estimation error is:

$$E = X_t - \hat{X}_t \quad (2-6)$$

And furthermore, the covariance matrix P_t of the system posterior estimation error is:

$$P_t = P_t^- - K_K H P_t^- \quad (2-7)$$

If the prediction result is accurate, the trace of P_t (the sum of each element on the main diagonal of the matrix) should be minimized, that is:

$$\frac{dtr(P_t)}{dt} = 0 \quad (2-8)$$

At this time, the Kalman gain matrix K_K that satisfies the conditions is:

$$K_K = P_t^- H^T (H P_t^- H^T + R_t)^{-1} \quad (2-9)$$

where, R_t is the covariance matrix of the system observation noise.

This algorithm effectively suppresses the “ghost” particles that do not form a continuous trajectory, thus avoiding creating trajectories for continuous multi-frame unmatched particles. Figure 2.17 shows the particle trajectories of the front and top view by tracking 100 frames.

2.5.5 Multi-view 3D Reconstruction

With 2D trajectories of particles obtained from the front and top views, as shown in Figure 2.17 (a) and (b), respectively, we need to find out the trajectories from both views in common, then match them to complete the time-resolved 3D reconstruction of the particle flow field.

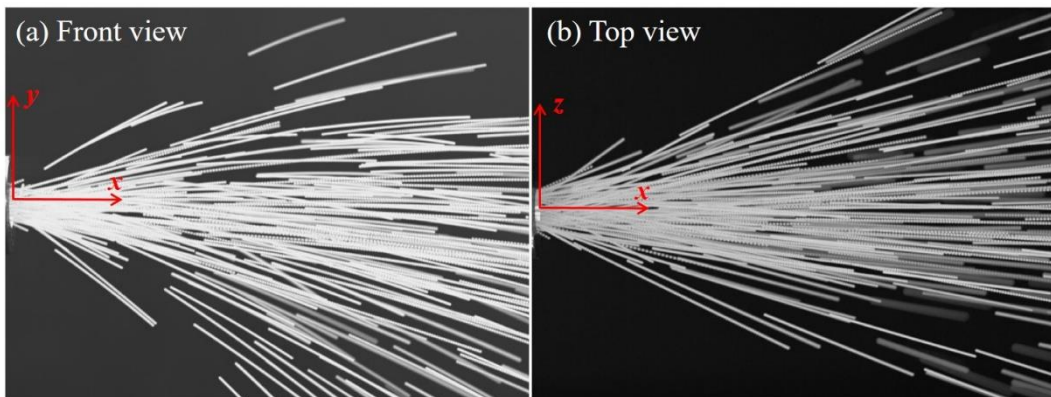


Figure 2.17 Particle trajectories of 100 frames at (a) front view, (b) top view.

The following characteristics of particles/trajectories are used for matching and reconstruction:

- Each particle has its own trajectory;
- The x -coordinate is shared by both the front and top views;
- The variations of x - coordinates of the same particle in the same time series are consistent in both views;
- The variations of x - velocity of the same particle in the same time series are consistent in both views;
- In most cases, the spatial length and time span (number of frames) of the same particle trajectories are the same.

Based on the above characteristics, we can construct a unique “ID card” for each particle. For example, a particle, named \mathbf{a} , is located in the front view, indexed as Num_f , the set of frame numbers where the particles exist is $S_f = [F_f^s, F_f^e]$, the set of x -coordinates of the particle trajectory is $X_f = [x_f^s, x_f^e]$, F represents the frame number, x the x -axis coordinate of the particle, the subscript f the front view, and the superscript s and e represent the start and end points, respectively. The frame length of the particle trajectory is $L_f = F_f^e - F_f^s + 1$, the set of x -direction velocities of the particles is $U_f = [u_f^s, u_f^e]$. Similarly, the view where particle \mathbf{b} is located is the top view, indexed as Num_t , and $B = [F_t^s, F_t^e]$, $X_t = [x_t^s, x_t^e]$, $L_t = F_t^e - F_t^s + 1$, $U_t = [u_t^s, u_t^e]$, the subscript t represents the top view. So the “ID cards” of particle \mathbf{a} and particle \mathbf{b} can be defined as

$$\mathbf{a} = \{front, Num_f, S_f, X_f, L_f, U_f\} \quad (2-10)$$

$$\mathbf{b} = \{top, Num_t, S_t, X_t, L_t, U_t\} \quad (2-11)$$

Particle matching is realized by comparing the differences between particle “ID

cards”. For instance, the initial frame error of particle trajectory is $F_{error} = |F_f^s - F_t^s|$. The set of common frames of particle **a** and particle **b** is $C = S_f \cap S_t = [M, N]$, M and N represent the start and end frame numbers of set C , respectively. If C is a non-empty set, the average value of the x -axis coordinate differences between the two particles on the same time series is

$$X_{error1} = \frac{1}{N - M + 1} \sum_M^N (X_f - X_t) \quad (2-12)$$

The average value of the velocity differences in the x -direction between the two particles on the same time series is

$$U_{error1} = \frac{1}{N - M + 1} \sum_M^N (U_f - U_t) \quad (2-13)$$

The difference between the average value of the x -axis coordinates of the two particles is

$$X_{error2} = \frac{1}{L_f} \sum_{F_f^s}^{F_f^e} (X_f) - \frac{1}{L_t} \sum_{F_t^s}^{F_t^e} (X_t) \quad (2-14)$$

The difference between the average value of the velocities in the x -direction of the two particles is

$$U_{error2} = \frac{1}{L_f} \sum_{F_f^s}^{F_f^e} (U_f) - \frac{1}{L_t} \sum_{F_t^s}^{F_t^e} (U_t) \quad (2-15)$$

Mismatch usually appears when using any single bias criterion to match particles. However, combining the above multiple bias criteria can enhance the accuracy and robustness of particle matching. We call this method “multi-view coaxial trajectory matching method (MCTM)”. This method is found to effectively avoid the misjudgment and omission of particles. In our experiments, the particle matching accuracy reaches $95 \pm 2\%$ by comparing the projection of the reconstructed position with the original position.

Based on the reconstruction results with time-resolved 3D positions and trajectories, we can calculate the velocities and volume fractions of the particles. The particle velocity, u_i , is obtained by calculating the short time displacement of the two frames of images, Δs , and interframe time, Δt . The velocity u_i can be written as

$$u_i = \frac{\Delta s}{\Delta t} \quad (2-16)$$

where i is the index of a particle. As for the particles in Lagrangian tracking, the average velocity \bar{u}_i over a time interval ΔT at the time t , its relevant root-mean-square (RMS) fluctuating velocity u'_i and particle turbulent kinetic energy (TKE) K_i , can be determined by³²

$$\bar{u}_i(t) = \frac{1}{\Delta T} \int_{t-0.5\Delta T}^{t+0.5\Delta T} u_i dt \quad (2-17)$$

$$u'_i(t) = \sqrt{\frac{1}{\Delta T} \int_{t-0.5\Delta T}^{t+0.5\Delta T} [u_i - \bar{u}_i(t)]^2 dt} \quad (2-18)$$

$$K_i(t) = \frac{1}{2\Delta T} \int_{t-0.5\Delta T}^{t+0.5\Delta T} (\overline{u'^2_{i,x}} + \overline{u'^2_{i,y}} + \overline{u'^2_{i,z}}) dt \quad (2-19)$$

where the subscripts x , y , and z denote the three coordinates, respectively. The average velocity \bar{u} over a specified space, its relevant fluctuating velocity u' and average particle turbulent kinetic energy, K , can be defined as³²

$$\bar{u} = \frac{1}{n} \sum_{i=1}^n u_i \quad (2-20)$$

$$\bar{u}' = \sqrt{\frac{1}{n} \sum_{i=1}^n [u_i - \bar{u}]^2} \quad (2-21)$$

$$K = \frac{1}{n} \sum_{i=1}^n K_i \quad (2-22)$$

where n is the number of particles in the specified space.

To characterize the local concentration of each particle, the Voronoi diagram method^{39, 61, 63} is applied. In light of the dynamic feature of the particle-laden jet, we focus on the evolution of 3D concentration in 3D space²⁰⁴. The particle volume fraction α_p based on the 3D Voronoi method and the particle volume fraction $\alpha_{p,2D}$ based on the 2D Voronoi method can be written as, respectively

$$\alpha_p = \frac{V_p}{V_{3D}} \quad (2-23)$$

$$\alpha_{p,2D} = \frac{A_p}{A_{2D}} \quad (2-24)$$

where V_{3D} denotes the volume of the Voronoi polyhedron, V_p the particle volume, A_{2D} the area of the 2D Voronoi cell, A_p the area of the section of the particle.

Figure 2.18 shows a typical reconstruction result, with (a): the instantaneous 3D particle flow field, (b): the trajectories of particles, (c): the front view, and (d): the top view.

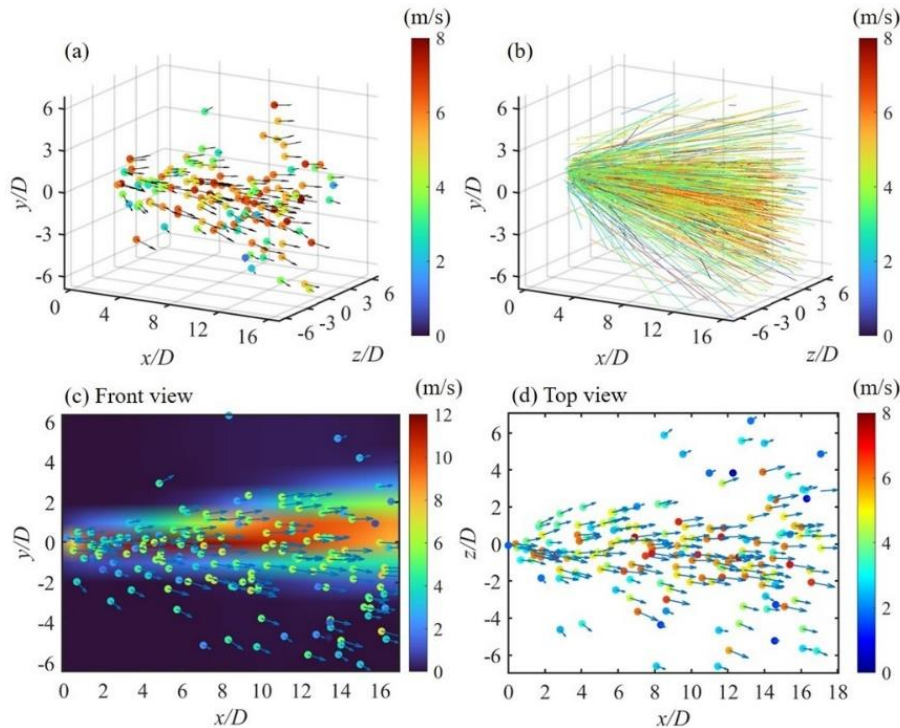


Figure 2.18 Results of reconstruction of the particle flow field

(a) instantaneous 3D particle flow field; (b) trajectories for 1s; (c) front view, with the gas velocity field measured using PIV as the background, and (d) top view.

2.5.6 Comparison with Other 3D-PTV Methods

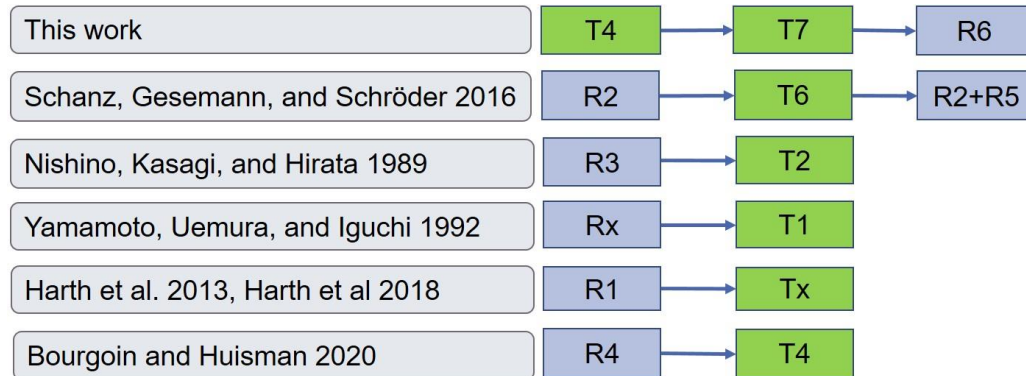
The time-resolved 3D-PTV method developed in this work is compared with the typical 3D-PTV method in the literature as shown in Figure 2.19. In this work, we adopted the four time-step estimate method¹⁹⁶ and Kalman filter^{197, 205, 206} proposed by those predecessors, and we did not create new points on them. Instead, our method innovation is mainly based on the two points: tracking-precede-reconstruction and multi-view coaxial trajectory matching method (MCTM), as detailed in the following.

First, the time-resolved 3D-PTV method developed in this work basically reverses the typical process of evaluation, i.e., the tracking precedes the 3D position reconstruction, instead of the normally applied scheme of 3D position reconstruction followed by the tracking^{18, 124, 207-209}. In other words, this method does not reconstruct the instantaneous 3D positions of particles, but first obtains the trajectories of the particles in different views, then reconstructs the particle flow field at all time steps through trajectory matching under different views.

Second, the multi-view coaxial trajectory matching method (MCTM) newly proposed in this work has higher accuracy for 3D trajectory reconstruction. In MCTM, the common characteristics of the coaxial trajectories in different views, such as the velocity and acceleration embedded in the trajectories, are used to complete the trajectory matching between different views, thereby complete the reconstruction, as detailed in Section 2.5.5 of the thesis. This method is no longer simply matching with the geometric or distribution characteristics of the particles at a certain instant, but matching with all the dynamics (namely, velocity and acceleration) of particles along their trajectories over the whole period of observation. Therefore, this reconstruction

accuracy of the particle flow field is higher.

To make it easier to understand the novelty of this work, Figure 2.19 shows the comparison of different time-resolved 3D-PTV methods applied in the literature with their detailed schemes of tracking and reconstruction. It is clearly that in previous 3D-PTV methods the 3D coordinates of each particle are already determined from simultaneously captured images. That is to say, the two sets of coordinates of particle images, with respect to the time t and $t + \Delta t$, respectively, are known²⁰⁸. Then, the critical issue of these methods is how to match a pair of particles in the first frame at time t and in the second frame at $t + \Delta t$, respectively, to complete the tracking. The details of different tracking and reconstruction methods in the Figure 2.19 are also attached below.



T: Tracking, $x: x=1\sim n$.

T1: Binary cross-correlation method; T2: Two time-step estimate method; T3: Triple pattern matching algorithm;
T4: Four time-step estimate method; T5: Nearest neighbor heuristic; T6: Wiener filter; T7: Kalman filter.

R: Reconstruction, $x: x=1\sim n$.

R1: SFM method; R2: IPR method; R3: RT-1 method; R4: RT-2 method; R5: STB method; R6: MCTM (This work).

Figure 2.19 Comparison of different time-resolved 3D-PTV (T: tracking; R: reconstruction).

The methods to accomplish tracking include: (T1) Binary cross-correlation method²¹⁰ for assessing the similarity between particle pairs; (T2) Two time-step estimate method²⁰⁷ for tracking by evaluating displacement and velocity in a search volume in the next time step and one-to-one correspondence is established if only one

tracer particle is found; (T3) Triple pattern matching algorithm²¹¹ that integrates both geometrical similarity and predictability of particle motions information in three consecutive particle image frames; (T4) Four time-step estimate methods^{121, 193, 194, 196, 212} for tracking by evaluating the smoothness of velocity or acceleration; (T5) Nearest neighbor heuristic¹⁹⁶ suitable for low velocity and large particle size; (T6) Wiener filter¹⁴⁹ for the prediction of steady-state information in a stationary random process; (T7) Kalman filter¹⁹⁷ for predicting unsteady signals.

The methods to accomplish 3D reconstruction (3D coordinates) include: (R1) SFM method¹⁵² for multi-shape feature objects by triangulation, it should be noted that for spherical single-featured particles, its accuracy will be poor; (R2) IPR¹⁵³ for iterative reconstruction of volumetric particle distributions by triangulation; (R3) RT-1 method²⁰⁷ and (R4) RT-2¹²⁴ based on based on the traversal of rays, originating from detected particles, through a three-dimensional grid of voxels; (R5) STB method¹⁴⁹ of reconstruction is accomplished by creating an estimated particle distribution with priori velocity information and "shaking" all particles to correct for residual errors. They all complete 3D reconstruction of a certain moment in time t by simultaneously capturing images from different angles. So, at least three cameras (at least two cameras for SFM) are required to capture as much particle information as possible. And they all need to carry out spatial coordinate transformation, which requires a complex camera calibration process.

2.6 Conclusions

In this chapter, the experimental platform is introduced in detail, and the

construction of the experimental platform is completed. At the same time, the material information used in the experiment and the PIV and PTV methods are introduced in detail, and the definitions of physical quantities in each method are clarified. In addition, we realize the time-resolved 3D reconstruction of the particle flow field of the particle-laden jet, based on the high-resolution time-resolved 3D-PTV & PIV experimental system and a new time-resolved 3D particle flow field reconstruction method. This method features particle tracking before performing trajectory matching, and lays the foundation for the study of particle-laden jet dynamics at the particle level.

Chapter 3 Dynamics of High-Stokes-number Particle-laden Jets

3.1 Overview

In order to comprehend the intricate particle-level dynamics in particle-laden jets, we have developed a hybrid measurement method as detailed in Chapter 2. This method combines time-resolved, 3D-PTV and PIV techniques. The time-resolved, 3D particle flow field reconstruction method, referred to as real tracking-preceded reconstruction, is achieved through dual-camera recording.

Given the complexity of particle-laden jets, our investigation begins by examining the fluid dynamics in the near-field region of a dilute particle-laden jet containing large particles. Utilizing the acquired data from particles and gas fields, we employ the Eulerian averaging and Lagrangian tracking approaches to analyze the gas-solid two-phase velocities and their fluctuations. Subsequently, a novel drag model is developed and validated for particle-laden jets based on the measured two-phase flow fields. Lastly, we predict the evolution of particle volume fraction using a straightforward volume fraction model.

3.2 Experimental Parameters

The image resolution of the high-speed camera is set to 1280×960 pixels, and the corresponding shooting region is about 220×165 mm². The frequency of the synchronizer and the high-speed camera is set to 5000 fps, the cross-frame time of the laser is 60 μ s and the exposure time is 10 μ s. The particles used in the experiment are uniformly spherical, white, glass beads with a density of 2490 kg/m³. The particle

diameter is 1051.6 μm , and the sphericity is 0.975. The measured particle size distribution is shown in Section 2.2.3. In this work, the particle mass flow rate is fixed at 2.162 g/s, the volumetric gas flow rate at the ejector gas inlet is fixed at 50.08 L/min, and the flow rate caused by negative gauge pressure at the ejector particle inlet is about 88 L/min. Thus, the solid mass loading rate, defined as the ratio of the solid mass flow rate to that of the gas, is 0.78. The DOS oil with a density of 918 kg/m^3 is used as the gas tracer with an average particle size of 2.2 μm . In operation, the main valve pressure of the tracer particle seeder is 0.2MPa, and the internal circulation pressure is 0.05MPa. An overview of experimental parameters is summarized in Table 3.1.

Table 3.1 Experimental parameters

| Parameters | Value | Parameters | Value |
|--|-------------|--|-----------------------|
| Particles | Glass beads | Gas | Air |
| Particle density ρ_p , kg/m^3 | 2490 | Gas density ρ_g , kg/m^3 | 1.205 |
| Particle diameter d_p , μm | 1051.6 | Gas viscosity μ_g , $\text{Pa} \cdot \text{s}$ | 1.8×10^{-5} |
| RMS of d_p , μm | 39.31 | Gas volume flow Q_g , L/min | 50.08 |
| Particle mass flow Q_p , g/s | 2.162 | RMS of Q_g , L/min | 0.34 |
| RMS of Q_p , g/s | 0.011 | The ejector inlet gas pressure P_g , KPa | 25.186 |
| Solid mass loading rate M_p | 0.78 | RMS of P_g , KPa | 0.077 |
| Particle relaxation time $\tau_{p,St}$, s | 8.473 | Tracer particle relaxation time $\tau_{g,St}$, s | 1.37×10^{-5} |

3.3 Gas Flow Characteristics: Effects of Particles

Figure 3.1 shows the effects of particles on the gas jet flow by comparing the instantaneous gas vector fields (a): without particles and (b): with particles laden, respectively. u_g is the gas velocity, and $u_{g,x}$ the gas velocity component in the x -direction. The image coordinates in the following analysis are scaled by the jet diameter, as practiced in the literature²⁰. It is clear that the instantaneous gas streamline is not

straight²¹³ in the pure gas case, as shown in Figure 3.1 (a), showing oscillating turbulence around the central jet, where the gas velocity magnitude is generally higher than the other areas. In Figure 3.1 (b), due to the adding of particles, the spanwise dispersion of the gas is larger. The black dotted line marks the profile of the maximum value of $u_{g,x}$. As we can see from Figure 3.1 (c) and (d), regardless of single- or two-phase jet, the maximum value of instantaneous $u_{g,x}$ is not along the jet centerline, but fluctuates around it.

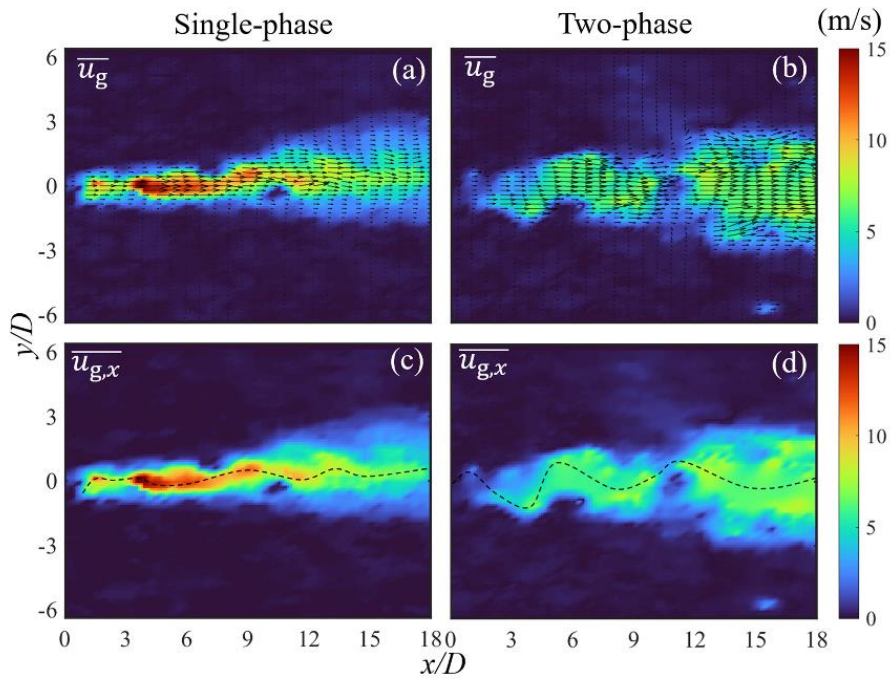


Figure 3.1 Instantaneous gas velocity profiles

(a) $\overline{u_g}$ of single-phase jet; (b) $\overline{u_g}$ of two-phase jet; (c) $\overline{u_{g,x}}$ of (a); (d) $\overline{u_{g,x}}$ of (b). The black dotted line represents the maximum value of $\overline{u_{g,x}}$. (Hereinafter, the sliding step size of the interrogation window is $0.1D$)

Figure 3.2 shows the contours of time-averaged gas velocity and fluctuating velocity of the single-phase jet (a~d) and two-phase jet (e~h). $u_{g,x}$ of the single-phase gas jet peaks along the jet core, especially near the exit of the ejector, and the gas dispersion angle is small, as shown in Figure 3.2 (a). With the jet evolving away from

the ejector, the gas stream goes slightly upward as shown by $|u_{g,y}|$ in Figure 3.2 (c). A probable reason is that the jet causes a large number of vortices with density lower than that of the surrounding fluid²¹⁴, thus leading to an upward buoyancy. Another possible reason is that the ejector is closer to the top of the measurement chamber than to the bottom, making the jet easier to diffuse downward, thus, the downward gas stream speed is smaller than that of the upward. According to Bernoulli's theorem, the pressure on the upper edge of the stream is lower than that on the lower edge, so the jet bends upward subject to the lift. The fluctuation $u'_{g,x}$ is large in the core of the jet, and decays away from the jet origin, as shown in Figure 3.2 (b). That is because the gas velocity is high in the early stage of the jet, resulting in strong turbulence with large $u'_{g,x}$. As the jet evolves, the gas velocity decreases with the turbulent energy dissipated, resulting in the decrease of $u'_{g,x}$. Similar to the gas velocity, the fluctuation $u'_{g,y}$ is also larger in the jet core than on the sides, and larger on the upper side than on the lower side, as shown in Figure 3.2 (d).

Compared with the single-phase jet, the gas velocity of the two-phase jet is smaller. The dispersion angle of the two-phase jet is slightly larger than that of the single-phase jet, and the distribution of $u_{g,x}$ becomes more symmetrical, as shown in Figure 3.2 (e). However, $|u_{g,y}|$ is smaller in the jet core than on both sides and slightly larger on the upper side than on the lower side, as shown in Figure 3.2 (g). Based on Figure 3.2 (f) and Figure 3.2 (h), it can be found that particles obviously change the distribution of gas fluctuating velocity. Compared with the single-phase jet, the gas fluctuation in the jet core is greatly reduced, indicating that the particles weaken the gas turbulence significantly. The probable reason is that, in the near-field region along the central axis,

the gas kinetic energy is more consumed to carry particles (see Figures. 3.8 and 3.9), leading to a more significant attenuation of turbulence^{85, 215}. By comparison, the increased gas fluctuation on both sides of the jet, as shown in Figure 3.2 (f), may be induced by the dispersed particles and their wake eddy effects⁹⁹.

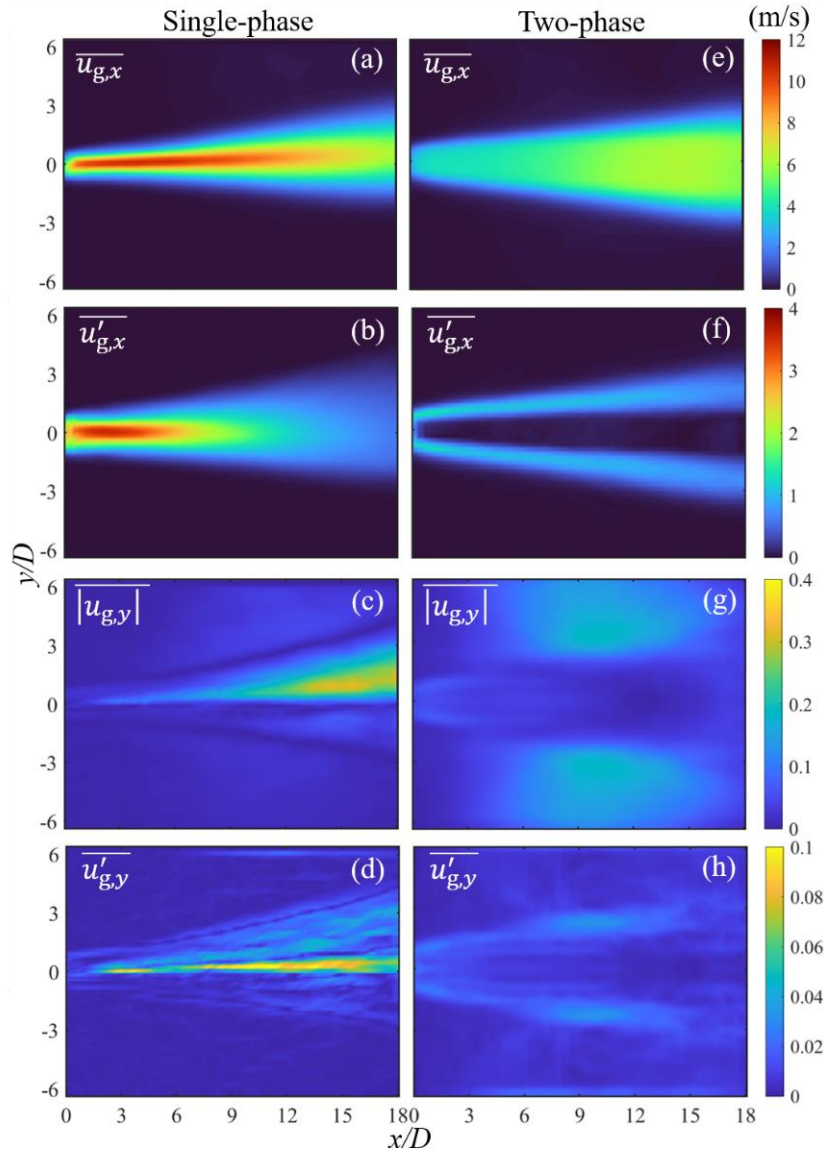


Figure 3.2 Contour maps of time-averaged gas velocity and fluctuating velocity of XY plane: single-phase jet (a-d) and two-phase jet (e-h).

In the single-phase jet, the $|u_{g,y}|$ gradually increases, which can be attributed to the energy transfer between the turbulent scales in the x - and y -directions^{85, 215}. In the

two-phase jet, the $|u_{g,y}|$ at the edge is greater than at the center. We speculate that the particles are driving the airflow during the outward (y -direction) dispersion (see Figure 3.8), resulting in an increase in the $|u_{g,y}|$ at the edge. The particle velocity in the y direction at the center is very close to 0 (see Figure 3.2), which does not affect on $|u_{g,y}|$, but the energy in the x direction of the airflow at the center transfers to the particles.

Figure 3.3 shows the time-averaged gas velocity and fluctuating velocity in axial (a~f) and spanwise (g~l) directions. At $y/D=3$, the gas velocity increases with the axial distance, and the gas velocity of the single-phase jet gradually exceeds that of the two-phase jet, due to a larger dispersion angle downstream of the two-phase jet, as described in Figure 3.2. Along the centerline ($y/D=0$), both the axial gas velocity and its fluctuation first rise and then decline, as was reported in the literature^{85, 215-217}. The rising part can be attributed to the “potential cone” at the ejector exit, the end of which is located at around $x/D = 4\sim 17$, similar to the value in the literature^{20, 215}, and there are weak compression and expansion waves in the “potential cone”^{20, 215}. The maximum gas velocity of the two-phase jet appears later than that of the single-phase jet. That is because the presence of particles changes the gas distribution and extends the whole gas flow field, together with its maximum point, to the downstream⁹⁹. At the same time, the gas fluctuating velocity of the two-phase jet along the jet centerline is significantly reduced due to the existence of a large number of particles^{85, 215}. Since the gas tends to go upward in the single-phase jet and the presence of particles makes the gas velocity distribution more symmetrical, the gas velocity of the two-phase jet is greater than that of the single-phase jet below the jet centerline ($y/D=-3$), as shown in Figure 3.3 (e). A similar trend applies to their fluctuating counterparts as the wake effect of large particles

enhances the gas turbulence⁹⁹.

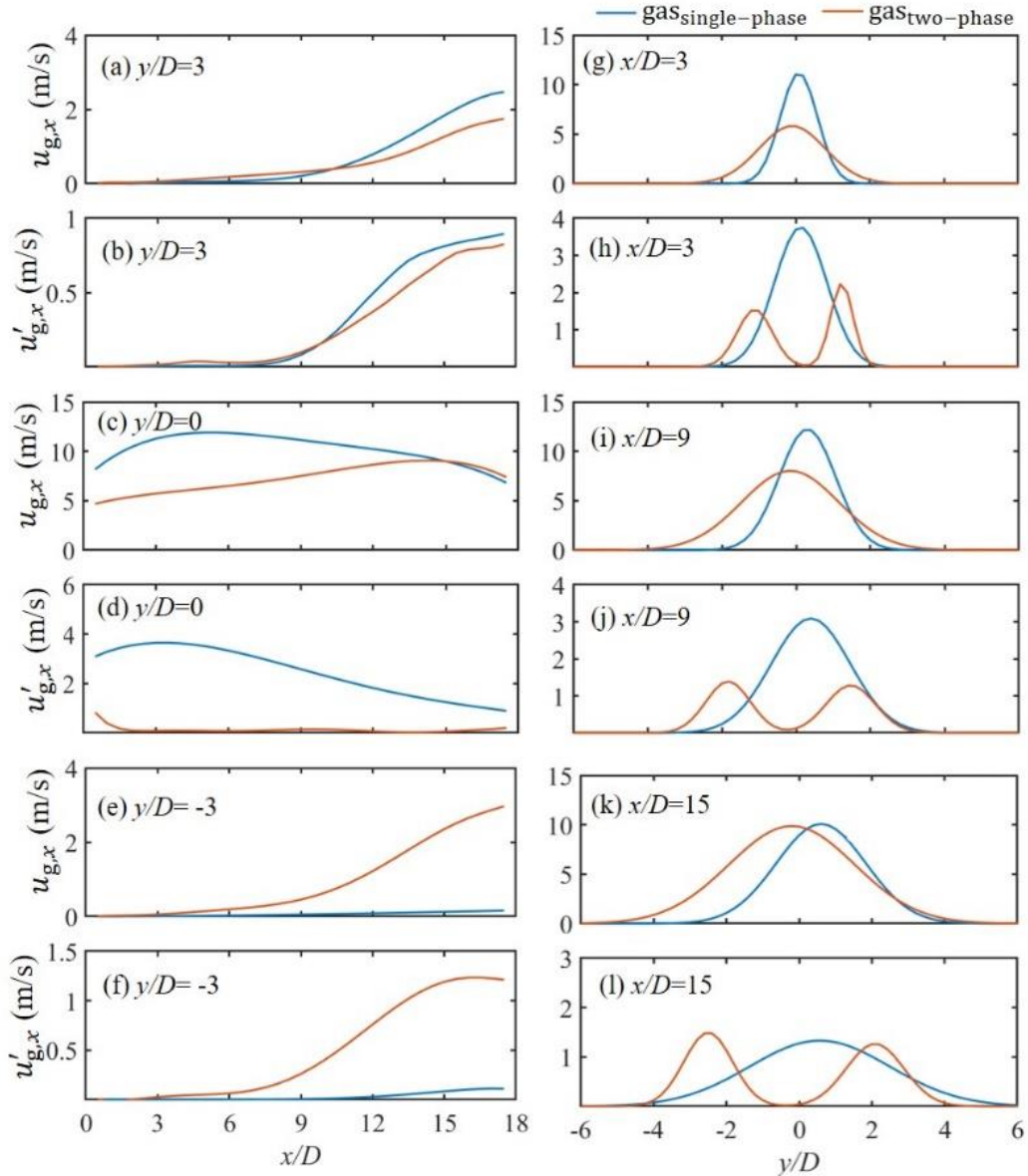


Figure 3.3 Time-averaged gas velocity and fluctuating velocity on axial (a~f) and spanwise (g~l) planes.

Figure 3.3 (g~l) shows the evolution of mean and fluctuating gas velocities along the y -direction at different x/D . Both the mean velocity distributions of the single-phase and two-phase jets show a single-peak distribution, as shown in Figure 3.3 (g), (i), (k). The peak velocity is also reduced in the two-phase jet accompanied by a much wider distribution, indicating that the particles change the gas velocity distribution

significantly. We can conclude from Figure 3.3 (h), (j), (l) that the gas fluctuating velocity distribution of the single-phase jet shows a single-peak distribution which is also shown in Krothapalli's²¹⁵ research, while the gas fluctuating velocity distribution of the two-phase jet shows a double-peak distribution. The reason is that particle weakens the gas-phase turbulence in the center of the jet, while the large particle wake effect enhances the gas-phase turbulence at the jet edge.

3.4 Particles Flow Characteristics

3.4.1 Global Particle Profiles

First, we determine the duration for statistical analysis. Figure 3.4 shows a fast Fourier transform (FFT) of the particle number flux at the ejector exit (in the range of $x/D=0\sim 1$). The main frequency is found within the range of 100 ~ 150 Hz. Therefore, the time span for averaging of particle field is selected to be 0.1s and 1s, about 10 and 100 times the fluctuation period, to smooth out the influence of particle number fluctuation.

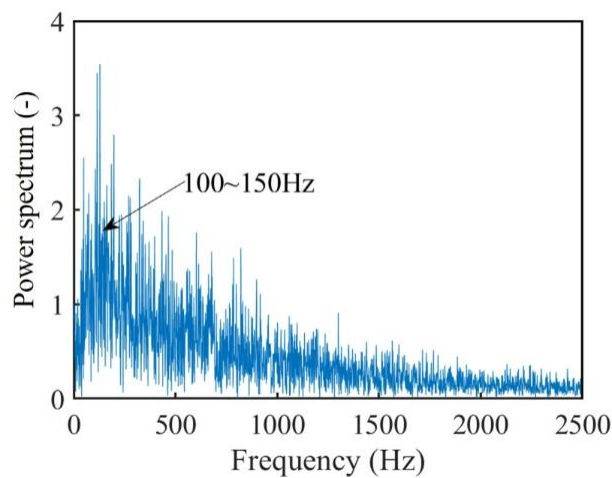


Figure 3.4 Fluctuation frequency of particle flux at the ejector exit.

To investigate the axial variation of particle concentration, the shooting area (measurement domain) is divided into 17 sections spaced with D along the x -axis, over which the numbers of particles are counted, as shown in Figure 3.5 (a). Similarly, we also show in Figure 3.5 (b) and Figure 3.5 (c), respectively, the distributions along the y - and z -axis directions with the same spatial resolution of D . The time averaging lasts for 0.1s (500 frames) and 1s (5000 frames), respectively. We can see that the time-average distributions are quite stable, especially along the y - and z - directions. Along the x -axis, the number of particles rises first and then declines a little bit, staying around between 12.3 and 12.6. The rising part near the exit of the ejector may be attributed to the fact that the particle concentration there is relatively high, and so is the particle overlap, resulting in an underestimation of the number of particles. As the particles move away from the ejector, the particles disperse gradually, reducing the degree of overlap and thus improving the recognition accuracy with higher numbers of particles. When the particles disperse to a certain extent, some particles may move outside and get lost from the shooting area, thus the particle concentration decreases. The particle number profiles of z -axis is basically symmetrical as expected, whereas the negative part of the y -axis direction ($y/D < 0$) is larger than the positive part due to gravity.

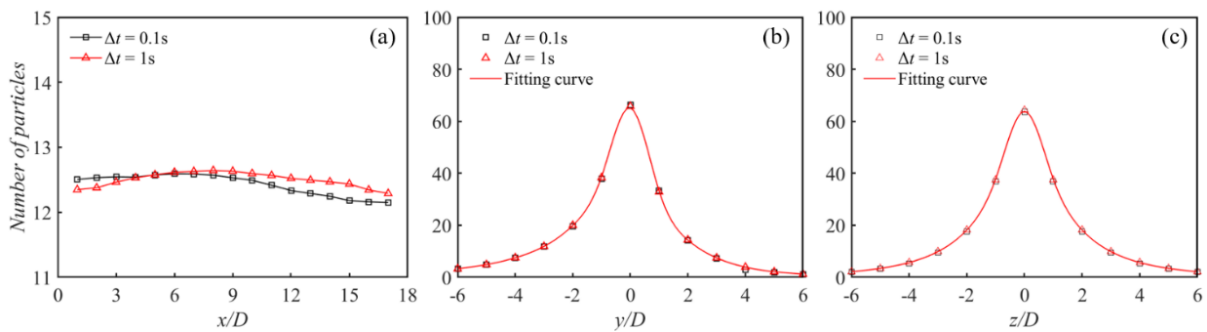


Figure 3.5 Profiles of the number of the particles along (a) x -axis, (b) y -axis, and (c) z -axis.

3.4.2 Particle-level Velocity Tracking

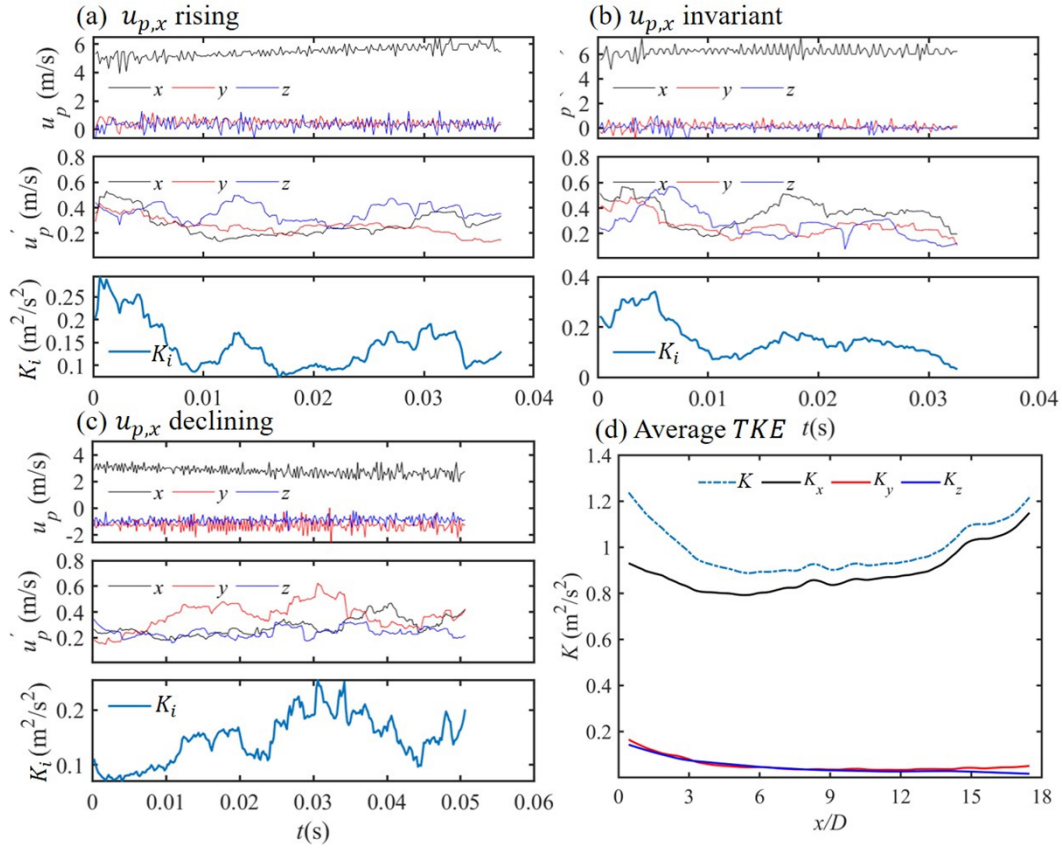


Figure 3.6 Lagrangian tracking u_p , corresponding u'_p , particle TKE, K_i : (a) $u_{p,x}$ rising, (b) $u_{p,x}$ invariant, (c) $u_{p,x}$ declining; and (d) variation of average particle TKE, K , along the jet centerline.

Figure 3.6 (a-c) show several typical time series of particle velocity of Lagrangian, single particles, their fluctuating velocities, and the particle TKE, respectively. Figure 3.6 (d) shows the variation of the average particle TKE along the jet centerline. The sliding span for time-averaging is 5×10^{-3} s. Three typical $u_{p,x}$ trends are chosen with respect to the rising (Figure 3.6 (a)), statistically invariant (Figure 3.6 (b)) and declining (Figure 3.6 (c)). The single particle velocity shows strong anisotropy with x component obviously larger than the other two components. The average particle TKE along the jet centerline shows a similar anisotropy (Figure 3.6 (d)), with the dominant x component, K_x , declining first then rising, whereas the other two components, K_y and

K_z , declining along the axis. By comparison, the particle TKE in Figure 3.6 (a-c) shows no such clear trend.

3.4.3 Mean and Fluctuating Particle Velocity

Figure 3.7 shows the time-averaged probability density functions (PDFs) of particle velocity components, i.e., $u_{p,x}$, $u_{p,y}$ and $u_{p,z}$, on the whole shooting region and three YZ planes with x/D equal to 3, 9, and 15, respectively. The Gaussian fitting curves for these components are also given in the literature¹⁴².

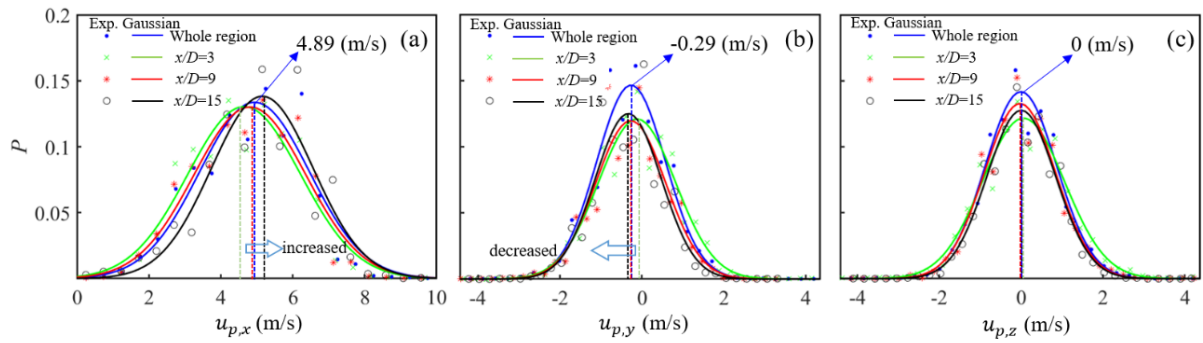


Figure 3.7 Time-averaged PDFs of particle velocity of the whole shooting region and on the YZ plane along the axis of the jet : (a) PDFs of $u_{p,x}$, (b) PDFs of $u_{p,y}$, and (c) PDFs of $u_{p,z}$.

Points of different shapes represent the experimental data, the solid lines represent the Gaussian fitting results of the points, and the dotted lines represent the center of the Gaussian fitting curves.

The PDF of $u_{p,z}$ is quite close to the Gaussian as the external force in the z direction is negligible¹⁴², whereas those of the other two components show obvious deviation from the Gaussian distribution, implying strong non-equilibrium and anisotropic states along these directions. The peak value of $u_{p,x}$ in the whole shooting region is around 4.89 m/s, and that of each x/D plane gradually increases with x/D as shown in Figure 3.7 (a), reflecting the acceleration of particles in the jet. The peak $u_{p,y}$ in the whole shooting region is negative, -0.29 m/s, caused by gravity. The magnitude

of the peak $u_{p,y}$ in each x/D plane also increases with x/D as shown in Figure 3.7 (b), reflecting the gravitational acceleration. The peak $u_{p,z}$ in the whole shooting region is around zero. Different from $u_{p,x}$ and $u_{p,y}$, the peak $u_{p,z}$ in each x/D plane does not change with x/D as shown in Figure 3.7 (c).

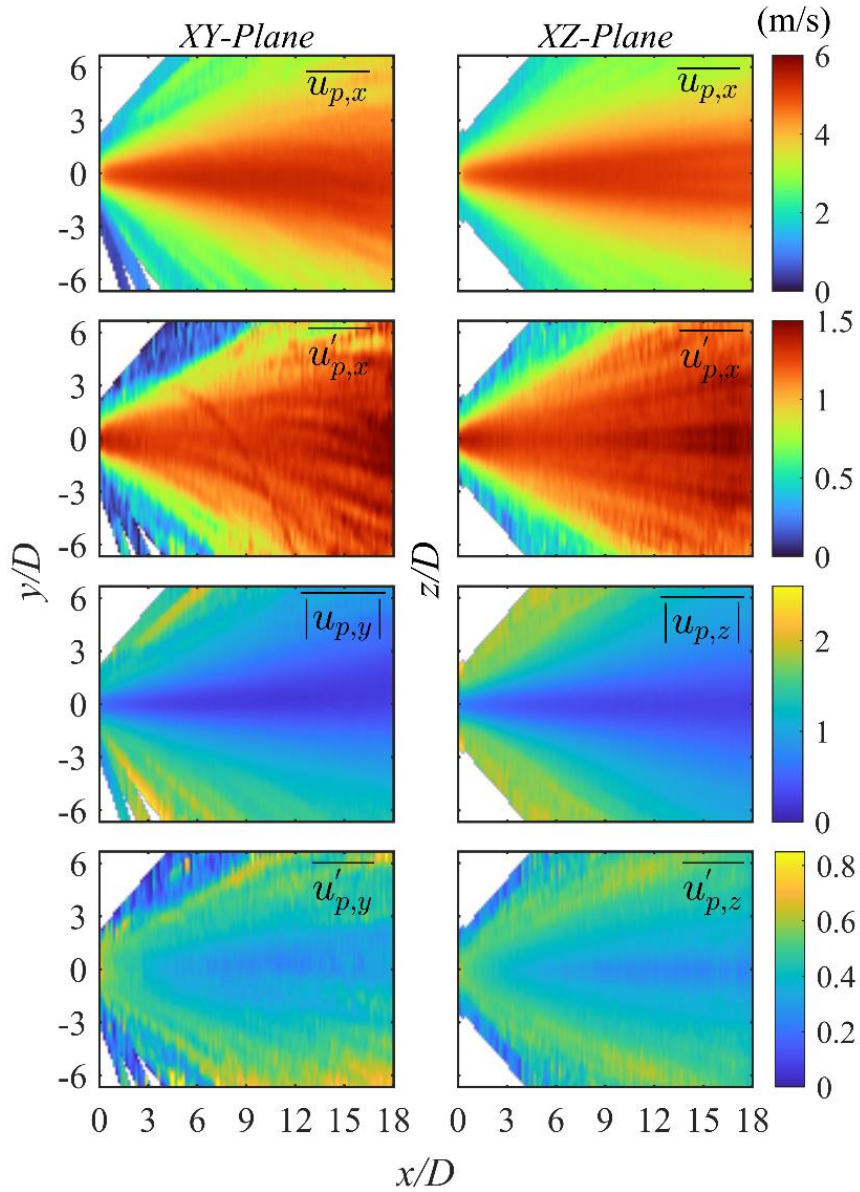


Figure 3.8 Contours of time-averaged and fluctuating particle velocities of central XY and XZ planes.

The contours of time-averaged and fluctuating particle velocities over the central XY and XZ planes are shown in Figure 3.8. $u_{p,x}$ peaks around the center and decays

along the lateral directions, while gravity causes asymmetry distribution in the XY plane. A similar distribution can also be found for $u'_{p,x}$. By comparison, the other two velocity components along y - and z - directions, as well as their fluctuations, $u'_{p,y}$ and $u'_{p,z}$ are small in the center and large on both side wings of the jet, reflecting the transmission of the particle kinetic energy and fluctuating energy from the x -direction to the y - and z -directions, whereas the XZ plane is more symmetrical.

To give a more quantitative analysis, Figure 3.9 shows the axial evolution of the time-averaged $u_{p,x}$, $u'_{p,x}$, and spanwise evolution of the time-averaged $|u_{p,y}|$, $u'_{p,y}$ of XY plane (a~d), XZ plane (e~f). In all different planes, $u_{p,x}$ increases first with x/D in the near-ejector region, but this trend fades away when far from the ejector, as revealed in previous PDA/LDA results^{36, 158}. $u_{p,x}$ is large on the central axis ($y/D = 0$ and $z/D = 0$), and decays along the lateral directions (say, $y/D = \pm 3$ and $z/D = \pm 3$). In the downstream, $u_{p,x}$ at $y/D = -3$ is larger than that at $y/D = 0$ probably due to the gravity. $u'_{p,x}$ decreases initially and then increases with x/D , but the change is small, which is also consistent with previous PDA/LDA results³⁶. As above, this phenomenon is due to both the flow-particle interaction in the ejector and the presence of rebounds of particles along the wall of the ejector. In this way, both particles originating from regions of low velocity (near the ejector wall) and particles originating from regions of larger velocity (along the axis of the stream) are mixed in the stream at the exit of the ejector, such that the mixed contributions tend to decrease the mean particle velocity and enhance the fluctuating velocity near the ejector exit^{36, 218}. The profiles of $u'_{p,x}$ at the other locations are consistent with those of $u_{p,x}$. As for $|u_{p,y}|$ and $u'_{p,y}$, both the mean velocity and fluctuating velocities tend to be low in the middle and high on both sides,

which are consistent with the previous analysis.

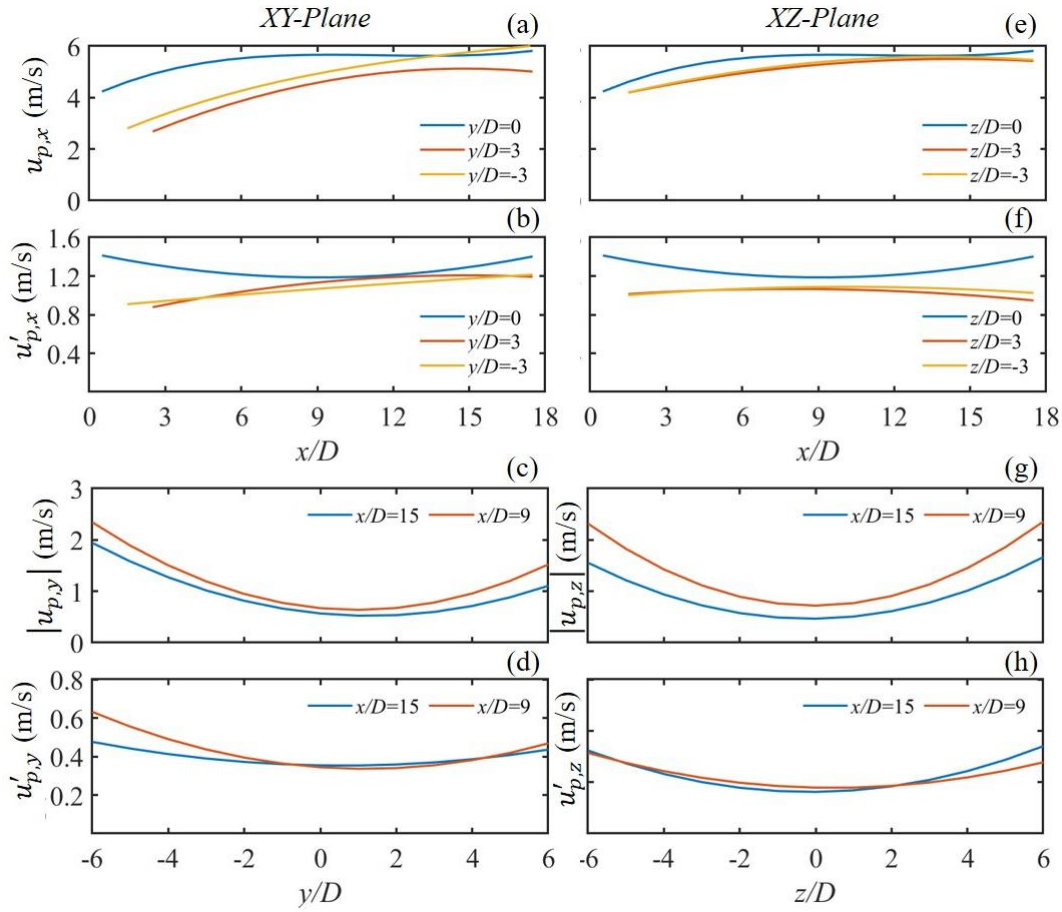


Figure 3.9 The axial evolution of the time-averaged $u_{p,x}$, $u'_{p,x}$ and spanwise evolution of the time-averaged $|u_{p,y}|$, $u'_{p,y}$ of XY plane (a~d), XZ plane (e~h).

3.4.4 Particle Volume Fraction

To characterize the local concentration characteristics, the 3D Voronoi diagram method²⁰⁴ is applied to calculate particle volume fraction. Each Voronoi polyhedron surrounds a point (particle), and the distances between the surface of the polyhedron and the adjacent point are equal. The volume fraction of all the particles in the shooting region is between 10^{-4} and 10^{-2} , with most of the particles between 10^{-4} and 10^{-3} . The PDF of the time-averaged particle volume fraction in the whole shooting region is shown in Figure 3.10.

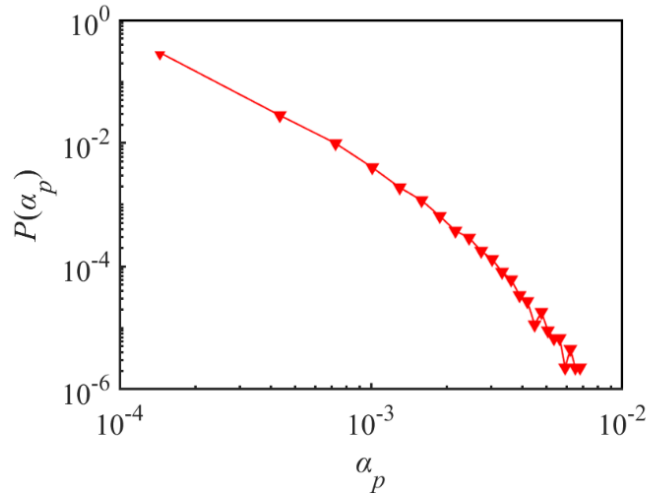


Figure 3.10 Time-averaged particle volume fraction PDF in the whole shooting region determined by the 3D Voronoi method.

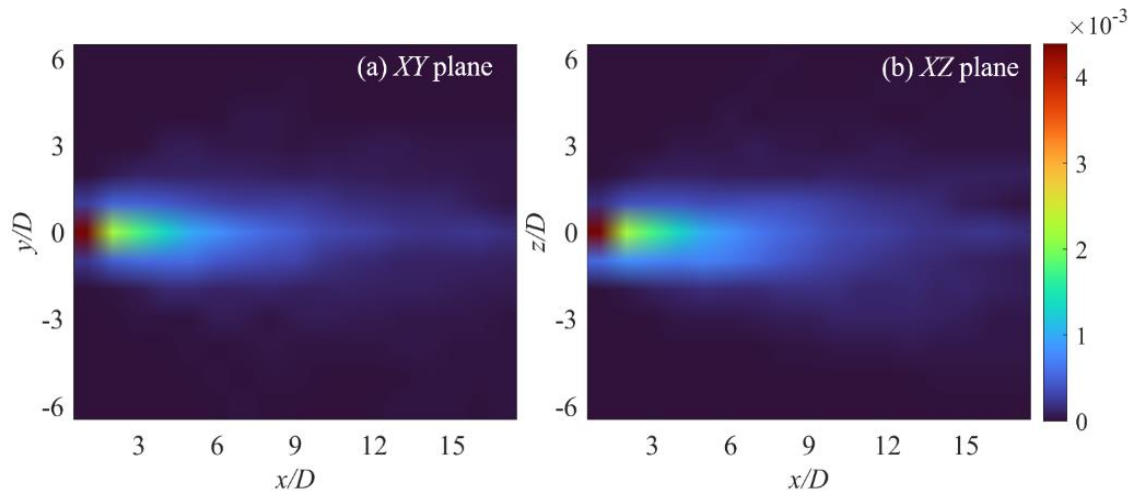


Figure 3.11 Contour of the experimental values of time-averaged particle volume fraction on *XY* plane (a) and *XZ* plane (b).

Figure 3.11 shows time-averaged 3D particle volume fractions on the *XY*- and *XZ*-planes. As expected, the particles are concentrated in the middle and near the ejector exit and decay away from the ejector exit both axially and laterally. Such a dispersion is consistent with the above discussion with gas and particle velocity distributions. It is widely recognized that in a particle-laden jet, the particles leave the nozzle with a certain initial velocity, and under the action of inertia and fluid, they move in a "cone-shaped" self-similar dispersion motion with a certain angle¹⁸. During this process, the

particle spacing and void ratio gradually increase. In the classic work of Bourouiba et al¹². on expiratory events, they recognized two phases of cloud evolution, with the first phase dominated by jet-like dynamics, followed by the second phase dominated by “puff-like” dynamics. Their theoretical model based on a scenario of the violent expiratory event as a discrete emission of droplet/particle-laden multiphase turbulent clouds was found well describing the dispersion of the particles observed in their analogous experiment. This model also provides the basis for our modeling efforts on the dispersion and the drag force in the particle-laden jet in the following section.

3.5 Modeling for Particle Dispersion and Drag

3.5.1 Particle Volume Fraction

As the axial component of the jet is the most representative²⁰, here we attempt to develop a particle volume fraction model to quantify the dispersion of particles along the jet centerline. Assuming that each particle with a diameter of d_p is surrounded by a cloud (hereinafter considered as a Voronoi polyhedron), which gradually expands as it follows the particle trajectory (s, θ) , where s denotes the motion distance and θ denotes the dispersion angle. As assumed in the classic work^{12, 40}, this expansion is self-similar and proportional to the distance s , as shown in Figure 3.12, where r denotes the dispersion radius, C_θ denotes the dispersion coefficient depending on θ , α_p the particle volume fraction, V_p the volume of a single particle, and V_{3D} the volume of the cloud. $u_{p,x}, u_{p,y}, u_{p,z}$ denote the velocity components of the particle and its surrounding cloud.

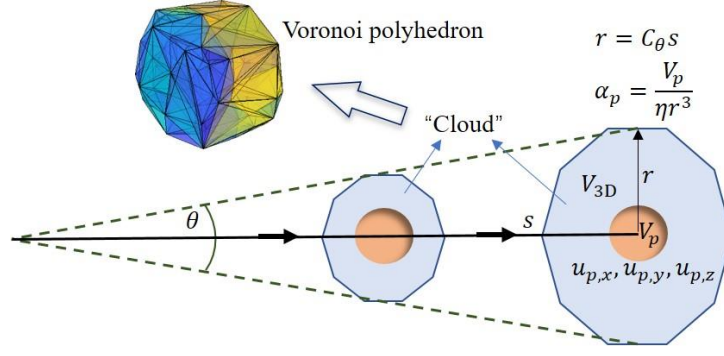


Figure 3.12 Schematic of the trajectory of a particle and cloud with radius r at position s from a jet.

The distance s can be defined as

$$s = \sqrt{(x_t - x_0)^2 + (y_t - y_0)^2 + (z_t - z_0)^2} \quad (3-1)$$

where (x_t, y_t, z_t) denotes the position of the particle at time t and (x_0, y_0, z_0) the initial position. The volumes of the cloud (Voronoi polyhedron, V_{3D}) and the particle (V_p) can be written as

$$V_{3D} = \eta r^3 \quad (3-2)$$

$$V_p = \frac{1}{6} \pi d_p^3 \quad (3-3)$$

where η is the shape coefficient related to the shape of the Voronoi polyhedron. $\eta = 4\pi/3$, if the Voronoi polyhedron is a sphere, and $\eta = 4\pi k_e/3$, if it is ellipsoidal, where k_e is the ellipsoidal axis length ratio¹². The shape of the Voronoi polyhedron is time-dependent, i.e., η is a function of time. Moreover, the volume of the cloud is strongly related with the displacement of the cloud²¹⁹ and the expansion of the cloud is self-similar, satisfying^{12, 40}

$$r = C_\theta s \quad (3-4)$$

Combining Eqs. (3-2), (3-3) and (3-4), the particle volume fraction based on the Voronoi method can be written as

$$\alpha_p = \frac{V_p}{\eta C_\theta^3 s^3} \quad (3-5)$$

where ηC_θ^3 can be regarded as the volume coefficient of the Voronoi polyhedron. The average volume fraction of particles along the centerline of the jet can thus be expressed as

$$\bar{\alpha}_p = \frac{V_p}{\bar{\eta} \bar{C}_\theta^3 x^3} \quad (3-6)$$

where x , $\bar{\eta}$, \bar{C}_θ denote the axial displacement, the average shape coefficient and the average dispersion coefficient of the particle moving along the centerline, respectively.

According to the Bourouiba model^{12, 220}, \bar{C}_θ and $\bar{\eta}$ are determined by

$$0.015 \leq \bar{C}_\theta \leq 0.037; \bar{\eta} = 3 \quad (3-7)$$

Figure 3.13 is compared with the experimental data with different fitting values of the dispersion coefficient \bar{C}_θ and shape coefficient $\bar{\eta}$.

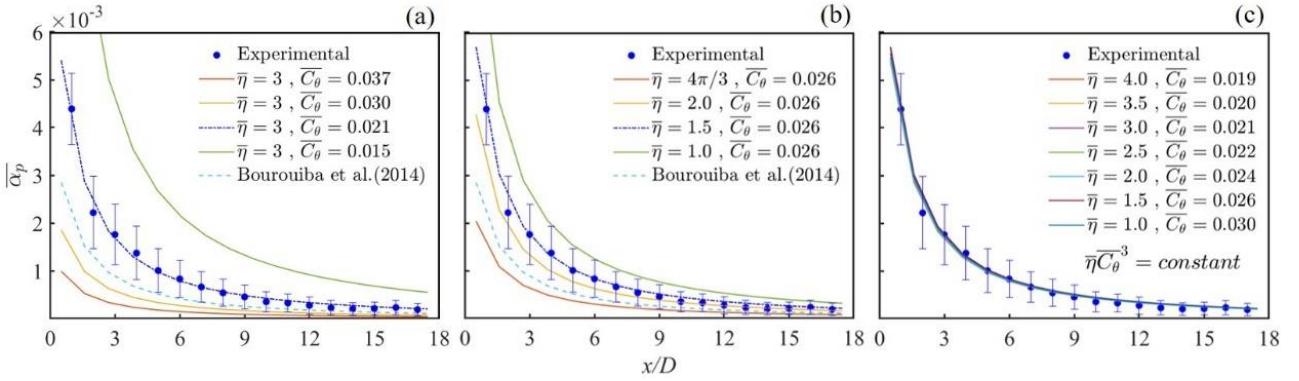


Figure 3.13 Axial evolution of particle volume fraction along the jet centerline calculated with (a) different C_θ , (b) different η , (c) different combinations of C_θ and η with $\eta C_\theta^3 = 2.7 \times 10^5$.

Figure 3.13 (a)-(b) show that the average particle volume fraction increases with the decrease of \bar{C}_θ or $\bar{\eta}$, and gives the best fitting when $\bar{\eta}=3$, $\bar{C}_\theta=0.021$. These parameters are in the same scope as suggested in the Bourouiba model. And a constant $\bar{\eta} \bar{C}_\theta^3 = 2.7 \times 10^{-5}$ fits very well with the experiment as shown in Figure 3.13 (c), and

the results in the literature¹² are also close to this value. So, we may recommend this constant value for different shapes of Voronoi polyhedrons.

3.5.2 Drag Correlation

As discussed in the introduction, for a horizontal particle-laden jet flow, the drag force is the key factor to the dispersion of particles. To deduce the drag model in this case, we extract the experimental data on the axial particle and gas velocities along the jet centerline. Figure 3.14 (a) gives the axial evolution of the time-averaged $u_{p,x}$, showing a gradual increase along the centerline, then flattening downstream, as reported in the literature^{24, 36, 53, 158}. The time-averaged gas and slip velocities are shown in Figure 3.14 (b) for both single and two-phase cases. Clearly, $u_{g,x}$ of both cases increases initially and then declines, due to the weak compression and expansion waves in the “potential cone” as described in Figure 3.3. By comparison, $u_{g,x}$ declines earlier for the single-phase jet, at about $x/D = 5$, than for the two-phase jet, at about $x/D = 15$, as the presence of particles stretches the gas flow field to the downstream direction⁹⁹. The single-phase speed of $u_{g,x}$ is larger than that of the two-phase one in the early evolution, until the opposite result appears in the later stage, at about $x/D = 15$, as the particles flatten the velocity distribution. The particle velocity change is small due to the large inertia of large particles, so the axial evolution of slip velocity is close to that of the gas velocity.

With the gas and slip velocity obtained above, we can further obtain the drag coefficient in the jet along the centerline and compare it with different drag models, as shown in Figure 3.14 (c). Similarly, we also present the particle velocities predicted by

using these drag models, as shown in Figure 3.14 (d). The detailed procedure is as follows:

Considering that the particle-laden jet flow is rather dilute, $\alpha_p \ll 1\%$, the particle density is large compared with gas density, $\rho_p \gg \rho_g$, we can assume that the trajectory of each particle can be integrated explicitly over time without collisions. Thus, the motion of a single particle can be obtained by applying Newton's second law, as follows:

$$m \frac{d\vec{u}_p}{dt} = m \frac{\rho_p - \rho_g}{\rho_p} \vec{g} + \vec{F}_D + \vec{F}_o \quad (3-8)$$

where $m = \frac{1}{6} \pi d_p^3 \rho_p$ donates the particle mass, \vec{u}_p the particle velocity, ρ_g the gas density, ρ_p the particle density, \vec{g} gravitational acceleration, \vec{F}_D the drag force, \vec{F}_o is the other force which can be ignored here. This equation can be simplified in the x direction as

$$\frac{du_{p,x}}{dt} = \frac{3\rho_g C_D}{4\rho_p d_p} |u_{g,x} - u_{p,x}| (u_{g,x} - u_{p,x}) \quad (3-9)$$

where C_D is the drag coefficient. Eq. (3-9) can be rewritten as²²¹

$$\frac{du_{p,x}}{dt} = \frac{1}{\tau} (u_{g,x} - u_{p,x}) \quad (3-10)$$

where τ is the particle relaxation time and $\tau_{p,St}$ is the particle relaxation time corresponding to the Stokes drag force, defined as

$$\tau = \frac{\tau_{p,St}}{f_{Re_p}} \quad (3-11)$$

$$\tau_{p,St} = \frac{\rho_p d_p^2}{18\mu_g} \quad (3-12)$$

$$f_{Re_p} = \frac{Re_p}{24} C_D \quad (3-13)$$

where μ_g is the viscosity of the gas phase, the particle Reynolds number $Re_p =$

$\rho_g d_p |u_{g,x} - u_{p,x}| / \mu_g$, and $50 < Re_p \leq 300$ in this experiment. The solution of particle velocity, i.e., Eq. (3-10), depends on the drag model or the relaxation time. Figure 3.15 (c) compares different drag models in the literature. Xu and Li¹⁷⁰ drag coefficient represents a piecewise simplification to the standard drag coefficient. For the convenience of solving, we use the Xu and Li drag coefficient to calculate the particle velocity. And the solution of Eq. (3-10) in the form of Xu and Li drag coefficient is given as follows.

$$\frac{du_{p,x}}{dt} = \begin{cases} \frac{(u_{g,x} - u_{p,x})}{\tau_{p,st}}, & Re_p \leq 0.3 \\ \frac{(u_{g,x} - u_{p,x})}{\tau_{p,st}} \frac{9Re_p^{0.11}}{8}, & 0.3 < Re_p \leq 4 \\ \frac{(u_{g,x} - u_{p,x})}{\tau_{p,st}} \frac{17Re_p^{0.31}}{20}, & 4 < Re_p \leq 40 \\ \frac{(u_{g,x} - u_{p,x})}{\tau_{p,st}} \frac{13Re_p^{0.57}}{40}, & 40 < Re_p \leq 600 \\ \frac{(u_{g,x} - u_{p,x})}{\tau_{p,st}} \frac{29Re_p^{0.87}}{600}, & 600 < Re_p \leq 5000 \\ \frac{(u_{g,x} - u_{p,x})}{\tau_{p,st}} \frac{Re_p^{1.11}}{160}, & 5000 < Re_p \leq 70000 \\ \frac{(u_{g,x} - u_{p,x})}{\tau_{p,st}} \frac{71Re_p^{0.81}}{400}, & 70000 < Re_p \leq 10^5 \end{cases} \quad (3-14)$$

In particular, by correlating the measured particle velocity at each position and the time-averaged gas velocity measured by PIV, we also obtain a new drag fitting relation by using the finite difference method as follows:

$$C_D = \frac{5.25 \times 10^6}{Re_p^{2.55}}, \quad 50 < Re_p \leq 300 \quad (3-15)$$

Details of the calculation of experimental C_D are given as follows. We solve the experimental drag coefficient at each position on the jet centerline through MATLAB.

The particles whose trajectories are always near the jet centerline (the release time

of particles is different) are selected, and the constraint conditions of particle trajectory are set to

$$-\frac{D}{2} < y < \frac{D}{2}, -\frac{D}{2} < z < \frac{D}{2} \quad (3-16)$$

100 particles and their trajectories are selected to reduce random errors as well as computational load. In this step, the drag coefficient based on the experimental data can be calculated at the same time. As described in the literature for steady state measurement or modeling^{222, 223}, this method, based on the time-averaged axial gas velocity and then averaged over 100 cases of the time series of particle velocity, yields the average drag coefficient. According to Eq.(3-9), C_D is defined as

$$C_D = \frac{du_{p,x}}{dt} \frac{4\rho_p d_p}{3\rho_g |u_{g,x} - u_{p,x}| (u_{g,x} - u_{p,x})} \quad (3-17)$$

Since $u_{p,x}$ along the particle trajectory has been obtained through experiments, the particle acceleration along the particle trajectory can be written as

$$\frac{du_{p,x}}{dt} = \frac{\Delta u_{p,x}}{\Delta t} \quad (3-18)$$

where $\Delta u_{p,x}$ represents the particle velocity difference at a time step, Δt , which is the inter-frame time interval (1/5000 s) of the images. Combined with Eq. (3-17), the drag coefficient under different particle Reynolds numbers can be obtained. And a drag coefficient correlation can be obtained by curve fitting as shown in Figure 3.14 (c).

The new drag obtained by experimental fitting is obviously larger than the other drag relations in the range $Re_p < 500$. Compared with the Rudinger¹⁸⁵ drag correlation, which was obtained by measuring the particle motion in a shock tube with fringe photography and the light scattering method at very low particle concentrations ($\alpha_p < 0.1\%$), our drag correlation shows a similar trend, but the value is approximately

an order of magnitude higher. The reason for the large difference between the new drag model and the other drag models may be attributed to the heterogeneous particle distribution and turbulence. It was reported in the literature^{87, 224, 225} that when the Reynolds number is in the range $10 < Re_p < 500$, the drag coefficient is always higher than the values in the standard curve due to turbulence effects. In this particle-laden jet flow case, the situation is more complex, as the particles distribution in the jet stream may also affect the turbulence, though the voidage is not explicitly included as a factor here as the flow is quite dilute.

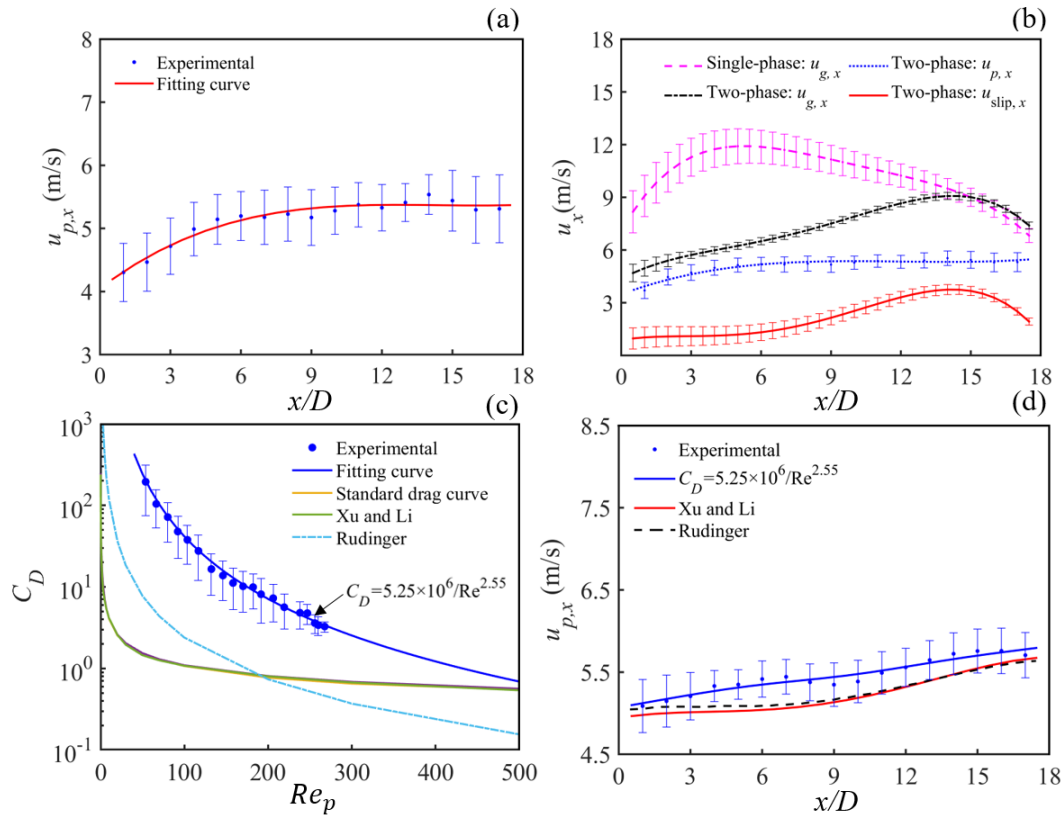


Figure 3.14 (a) Axial evolution of time-averaged $u_{p,x}$; (b) $u_{g,x}$ of single- and two-phase jets, and $u_{p,x}$, $u_{slip,x}$ of two-phase jet along the jet centerline; (c) comparison of the drag coefficients obtained in this work with those in the literatures; (d) comparison of model prediction and experimentally averaged data of $u_{p,x}$ for 100 particles along the jet centerline.

It should be pointed out that the experimental uncertainty associated with the

obtained drag relation is significant, partly due to the measurements in unsteady turbulent flows. As the time-averaged gas field instead of a transient one is used here, the drag correlation here should rather be viewed as a time-averaged relation without accounting for the dynamic response of a particle to the turbulent eddies^{222, 223}. A more elaborate drag relation with consideration of dynamics response could be measured with a higher spatial and temporal resolution of the gas flow field, which definitely needs more efforts beyond the scope of this work.

Figure 3.14 (d) shows the axial evolution curves predicted by using these drag models, against the experimentally averaged data of $u_{p,x}$ for 100 particles along the jet centerline. When the Rudinger drag coefficient and standard drag coefficient or its piecewise simplification, Xu and Li¹⁷⁰ drag model, are applied, we can find an obvious discrepancy between the experimental data and the prediction, especially in the early stage of the jet, owing to its underestimation of the drag force. The best agreement is found when using our new drag model as expected. The particle velocity calculation method based on different drag coefficients is detailed as follows:

We give the scheme via the finite difference method to solve the particle velocity through MATLAB.

- (1) The starting point of the particle trajectory is set as the initial position and $u_{p,x}$ at the starting point of the particle trajectory is set as the initial velocity.
- (2) Different drag models can be applied to calculate the force on the particle at the current position. Since the gas velocities at all positions have been obtained from PIV measurement, once the particle positions are known, the gas velocities are also known.

- (3) The Leap-frog method²²⁶ is applied to calculate the new position and velocity of the particle with Δt as a time step and the lifetime of particle trajectory as the calculation time.
- (4) Update the position and velocity of particles, and then return to step 3.
- (5) Through the above steps, the theoretical values of $u_{p,x}$ along the particle trajectory can be obtained. Steps 1–4 are performed on the 100 selected particles to obtain their theoretical values of $u_{p,x}$ along their respective trajectories.
- (6) Calculate the average values of the $u_{p,x}$ of these 100 particles at each spatial position along the x -axis. The predicted results are compared with the experimental measurement as shown in Figure 3.14 (d).

3.5.3 More Discussions

In this section, we discuss the limitations of our models. As shown in Eq. (3-5), the particle volume fraction is determined based on the assumption of self-similar dispersion¹², as it relates only to the particle volume and the self-similar dispersion of the gas-phase cloud, or, the volume of the Voronoi polyhedron. The self-similar dispersion theory applies only to the near-field region of the jet^{18, 227, 228}, in the sense that the central trajectory of a gas-phase cloud is generally of regular linear shape in the near-field region^{12, 18, 228}. For irregular trajectories in e.g., the far-field region, the self-similar dispersion theory may not be applicable.

In addition, the particle trajectory is strongly dependent on the Stokes number, St . For a large particle with $St \gg 1$, as is the case in this work, it follows a ballistic trajectory largely unaffected by the turbulent cloud^{12, 24}. Thus, the dispersion of large particles

can be assumed uniform, and the dispersion of gas clouds surrounding the particles along the ballistic trajectories is self-similar. In other words, the gas cloud self-similar dispersion is suitable for large particles. For smaller particles with $St \approx 1$, or even $St \ll 1$, however, they may be strongly affected by the turbulent motion and experience violent dispersion, thereon the dispersion of gas cloud is hard to be self-similar along the central axis. Considering the wide distribution of particle size in normally encountered particle-laden jets, e.g., violent expiratory events such as coughing and sneezing, more experimental efforts are needed in the future to understand the dependency of the particle-laden jet on particle properties.

Furthermore, the drag correlation derived in this work is also based on large particles following ballistic trajectories. Its deviation from the standard drag law can be attributed to the turbulent gas flow field, which is far from that surrounding an isolated particle as encountered in the standard drag law. Considering the striking difference of the turbulent effects on particles under different Stokes numbers, it is necessary in the future to extend our experiments to smaller particles. It is worth noting that, the smaller the particle size, the more difficult it is to obtain the particle-level trajectory in experiments. As a result, it could be a good start to first obtain the average velocity of small particles in a jet flow, then perform simulations to verify the applicability of the drag correlations in literature or newly derived.

3.6 Conclusions

In the present work, we perform high-Stokes-number particle-laden jet experiments based on the high-resolution time-resolved 3D-PTV & PIV experimental

system and a new time-resolved 3D particle flow field reconstruction method. And further analyzed in terms of the particle distribution and particle velocity distributions. The gas velocity fields of the jet with and without the addition of particles are measured using PIV. A new drag model is developed based on the experimental data of both the gas and particle flows. And the evolution of particle volume fraction along the jet centerline is also explained with a simple model. The major conclusions can be summarized as follows:

- (1) Particles significantly change the gas turbulence and stretch the gas flow field to the downstream direction of the jet. In the central region of the jet, a large number of particles weakens the gas turbulence. In the boundary region of the jet, the wake effect due to large particles enhances the gas turbulence.
- (2) $u_{p,x}$ is larger in the core region of the jet and smaller in the jet edge region. $u_{p,y}$ and $u_{p,z}$ are smaller in the core region and larger in the edge region. The fluctuating velocity shows a similar distribution. On the YZ plane, the PDF of $u_{p,z}$ is quite close to the Gaussian distribution as the external force in the z direction is negligible, whereas those of the other two components show obvious deviation from the Gaussian distribution, implying strong non-equilibrium and anisotropic states along these directions. The peak $u_{p,x}$ increases with x/D , the peak $u_{p,y}$ decreases with the increase of x/D , whereas the peak $u_{p,z}$ does not change with x/D . $u_{p,x}$ along the centerline of the jet increases first with x/D and then gradually flattens, so is the trend of the slip velocity.
- (3) A new drag model for the dilute particle-laden jet flow with particle Reynolds numbers between 50 and 300 is derived based on the reconstructed particle

trajectories and gas flow field. The new drag correlation, $C_D = 5.25 \times 10^6 / Re_p^{2.55}$, is found in better agreement with the experimental data than the standard single-particle drag model.

- (4) The 3D particle volume fraction along particle trajectory is obtained, a simple model relating the particle volume fraction and time/displacement is developed based on the self-similar theory of the jet. The predicted particle volume fraction and its evolution agree well with the experimental measurement.

Finally, it is worth noting that the current work is constrained to the particle-laden jet flow with large particles of large Stokes number, where the particle-level tracking measurement is feasible, and the self-similar dispersion assumption holds. More efforts are necessary to understand the dynamics of a particle-laden jet flow with smaller particles. In particular, the drag correlation derived in this work needs to be verified for small particles in further work.

Chapter 4 Dynamics of Low- and Middle-Stokes-number Particle-laden Jets

4.1 Overview

This chapter aims to understand the dynamics of low- and middle- Stokes-number particle-laden jets and provide experimental data for drag model verification and particle volume fraction model verification. Particle-laden jet experiments for two Stokes-number systems are conducted using Particle Image Velocimetry (PIV).

For low-Stokes-number particle-laden jets, the relaxation time and Stokes number of gas-phase tracer particles (DOS oil) are significantly less than 1, enabling them to follow the airflow closely. As a result, this chapter examines dynamics of the gas jet by analyzing the motion information of the gas-phase tracer particles. For middle-Stokes-number particle-laden jets, the relaxation time of SiO₂ microspheres is comparable to the gas time scale. In this scenario, the particles neither completely follow the airflow nor remain unresponsive to it; instead, they partially respond to fluctuations in the airflow, resulting in more complex dynamics than those observed in gas-phase jets.

In this chapter, six sets of experiments are performed for particle-laden jets with both types of low- and middle- Stokes-number particles, i.e., gas-phase tracer particles and SiO₂ microspheres. The dynamics of the two types particle-laden jet covers the fields of velocity and fluctuating velocity, the decay of jet velocity, the self-similarity of velocity and concentration, the characteristics of particle clusters, and the evolution of particle concentration among other aspects. The experimental data presented in this chapter serve as a basis for extending the validation of the newly derived drag correlation to cases of small particles.

4.2 Experimental Parameters

This section presents six sets of low- and middle- Stokes-number particle-laden jet experiments involving gas-phase tracer particles (DOS oil) and SiO₂ microspheres. Figure 2.1 depicts the schematic diagram of the test bench. The main pipeline gas enters the ejector through the left inlet, while the gas-phase tracer particles and SiO₂ microspheres are introduced into the ejector via the upper inlet.

The gas tracer particles are generated by a CTS-1000 tracer particle generator, with a driving gas flow rate of 50.27 L/min. SiO₂ microspheres are produced using a Solid-3 particle generator, with a driving gas flow rate of 50.31 L/min and a corresponding SiO₂ particle flow rate of 0.01042 g/s. Section 2.3 provides the material parameters for the gas tracer and SiO₂ particles.

The control parameters for the gas tracer particles and SiO₂ particles remain constant throughout the experiment. The gas flow rate in the main pipeline is adjusted to modify the gas velocity and loading rate. Table 4.1 displays the detailed experimental parameters, where the macroscale and mesoscale parameters are consistent for each experiment number.

In order to obtain detailed flow information over a wide range of scales, this section presents measurements of two resolutions, with respect to the overall flow field and close-up of flow details, respectively. The overall flow field measurement (hereinafter referred to as the macroscale experiment) yields an image with 2560×1080 pixels and a corresponding spatial resolution of 0.246 mm. And the close-up flow detail measurement (hereinafter referred to as the mesoscale measurement) produces an image with 2560×1920 pixels and a corresponding spatial resolution of 0.037 mm. Table 4.2 provides further details on these measurements.

Table 4.1 Experimental parameters

| Experiment number | Exp.1 | Exp.2 | Exp.3 | Exp.4 | Exp.5 | Exp.6 |
|----------------------------|---------|---------|---------|---------|---------|---------|
| $Q_{g,inlet}$ (L/min) | 0 | 20.29 | 40.31 | 60.37 | 80.19 | 95.22 |
| $Q_{g,inlet}(rms)$ (L/min) | 0 | 0.26 | 0.33 | 0.50 | 0.62 | 0.76 |
| St | 9.61 | 12.20 | 16.06 | 19.98 | 22.97 | 24.89 |
| M_p | 0.01592 | 0.00970 | 0.00660 | 0.00465 | 0.00316 | 0.00235 |

It is crucial to note that for the jet, the characteristic size of its dynamics is represented by the nozzle exit diameter (12 mm). When the size of the "interrogation window" is comparable to the nozzle diameter, significant errors may arise in the velocity calculations near the nozzle.

Table 4.2 Image parameters

| Parameters | | Macroscale measurement | Mesoscale measurement |
|--------------------------------|----------------|------------------------|-----------------------|
| Image pixel resolution, pixels | | 2560×1080 | 2560×1920 |
| Image spatial resolution, mm | | 0.246 | 0.037 |
| Image-space size, mm | | 630×266 | 95×71 |
| Interrogation window size, | 24 × 24 pixels | 5.904×5.904 | 0.888×0.888 |
| mm ² | 32 × 32 pixels | 7.872×7.872 | 1.184×1.184 |

The schematic diagrams illustrating the macroscale and mesoscale measurements of low- and middle- Stokes-number particle-laden jet experiments are presented in Figure 4.1 and Figure 4.2, respectively. The image space captured by the macroscale measurement is larger and more axisymmetric. The mesoscale measurement is achieved by traversing and capturing images along the jet axis, providing flow details specific along this axis. Consequently, the resulting image space is smaller in size. In this chapter, we discuss the implementation of the mesoscale experiment at seven sequential positions along the jet axis. The endpoint of each window serves as the starting point

for the subsequent window, with precise positioning facilitated by a guide rail controlled by a servo motor.

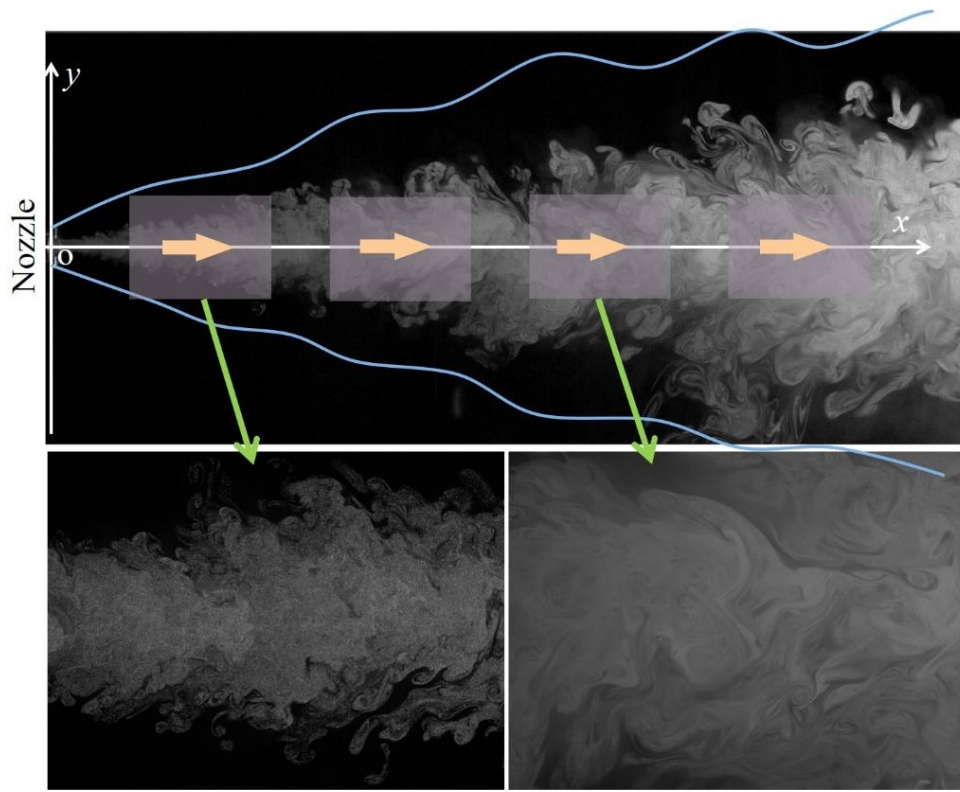


Figure 4.1 Schematic diagram of low-Stokes-number experimental measurement

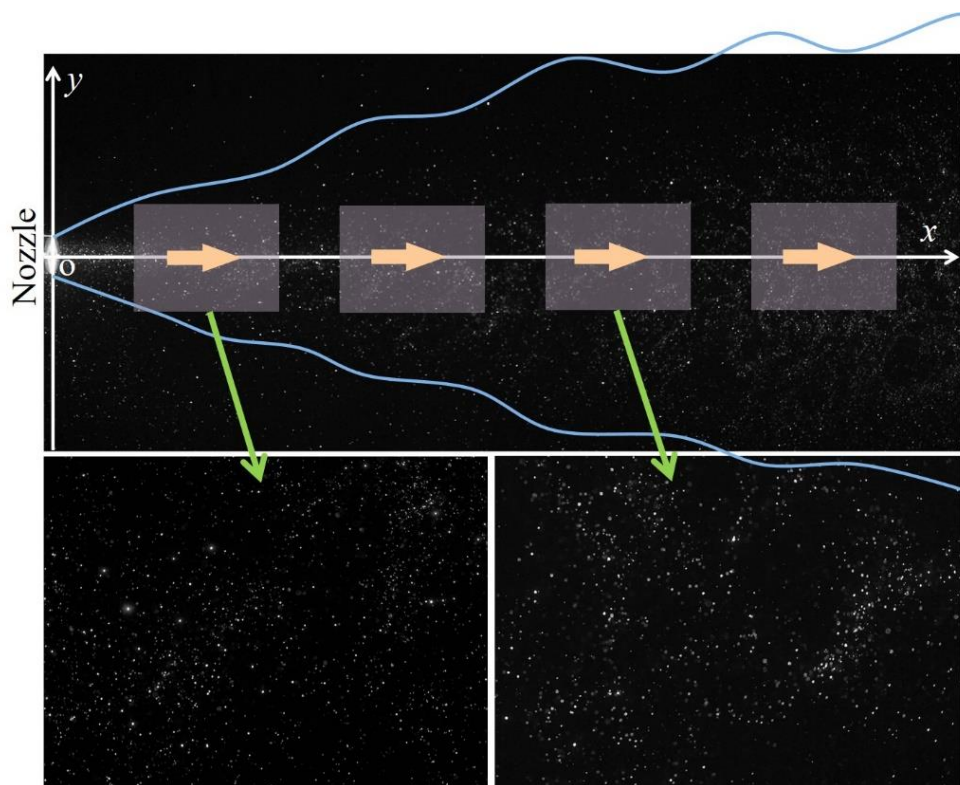


Figure 4.2 Schematic diagram of middle-Stokes-number experimental measurement

4.3 Low-Stokes-number Particle-laden jets (Gas Flow) Characteristics

Since the Stokes number of low-Stokes-number particle-laden jets is very small, this section studies the dynamics of gas jets by analyzing the motion information of gas-phase tracer particles, that is, low-Stokes-number particle-laden jets are gas-phase jets.

4.3.1 Instantaneous Gas Velocity

A transient snapshot of macroscale and mesoscale gas-phase jet experiments, obtained through tracer particle visualization, is depicted in Figure 4.1. Evidently, the gas-phase jet constitutes a powerful turbulent mixing process, encompassing numerous large and small vortex structures, with its velocity field illustrated in Figure 4.3. As can be discerned from the figure, the velocity peak during the jet process does not consistently align with the jet centerline, but rather fluctuates. The gas-phase velocity field and vector field, as measured by the mesoscale experiments, are displayed in Figures 4.4 and 4.5. The fluctuations in both the flow field and the velocity field can be more distinctly observed in these figures.

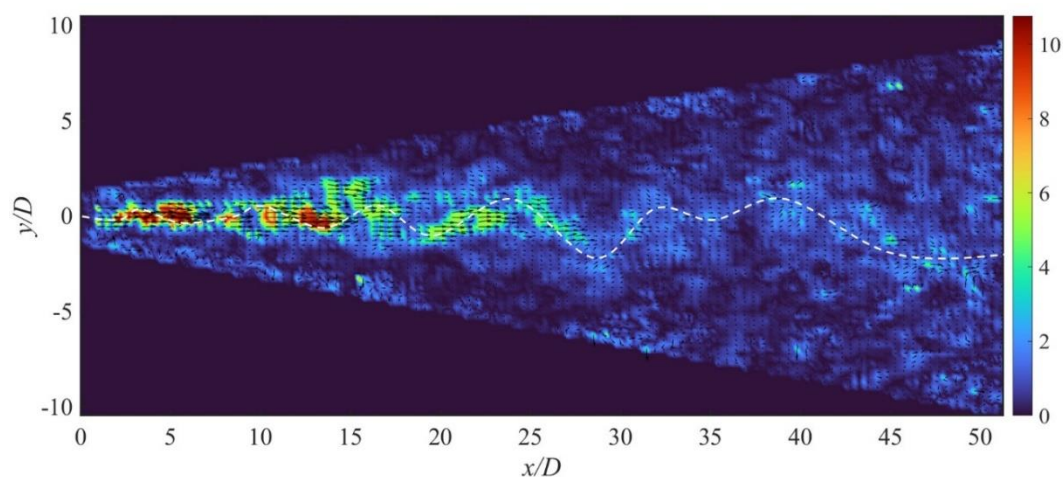


Figure 4.3 Macroscale experiment of Exp.1: Transient gas velocity field of the gas jet. The dotted line indicates the location of the velocity maximum

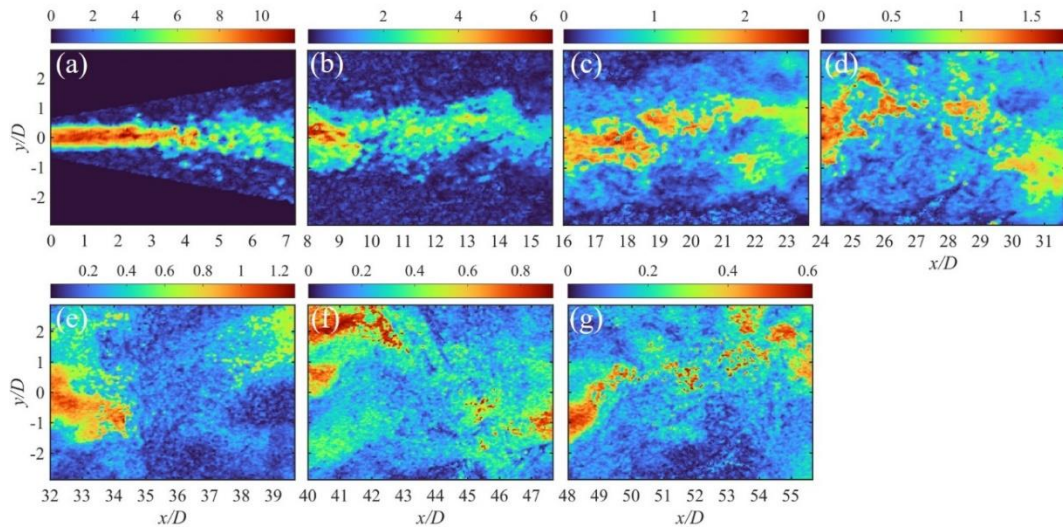


Figure 4.4 Mesoscale experiments of Exp.1: Transient gas velocity field of the gas jet

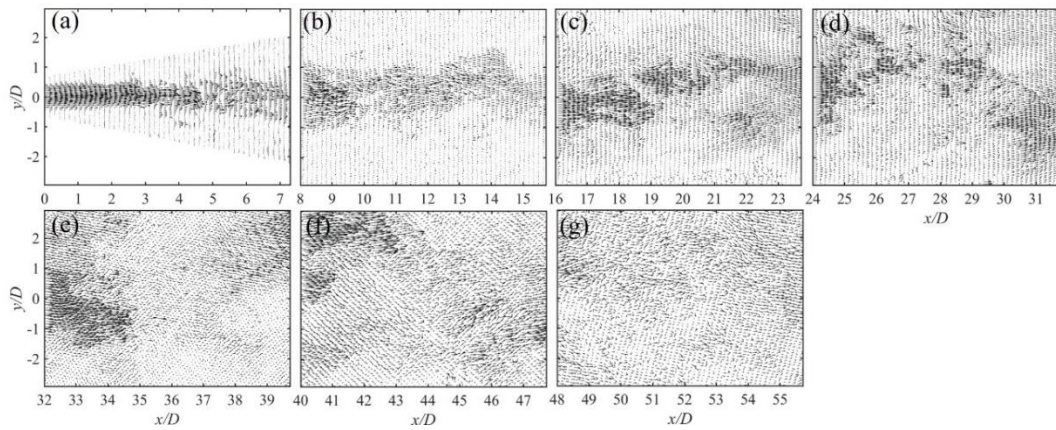


Figure 4.5 Mesoscale experiments of Exp.1: Transient gas velocity vector field of the gas jet

4.3.2 Mean and Fluctuating Gas Velocity

The mean velocity fields with average duration of 1s of the gas phase, measured by the macroscale experiment, are depicted in Figure 4.6. As the gas moves away from both the nozzle exit and the jet centerline, the velocity gradually decays, exhibiting a distribution pattern characterized by a larger center and smaller edges. The mean velocity fields of the gas, as measured by the mesoscale experiment, are presented in Figure 4.7 and Figure 4.8. The velocity distribution pattern is consistent with that of the macroscale experiment, but the mesoscale experiment offers greater detail, as shown in Figure 4.8, the velocity near the nozzle exhibits a hat-shaped distribution.

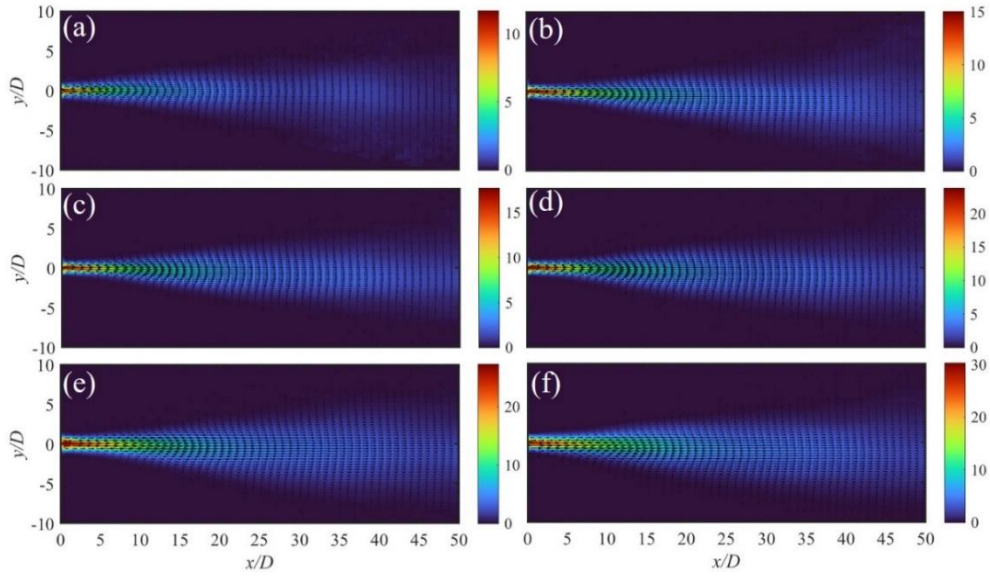


Figure 4.6 Mean gas velocity field of Macroscale experiments: (a) Exp.1, (b) Exp.2, (c) Exp.3, (d) Exp.4, (e) Exp.5, (f) Exp.6

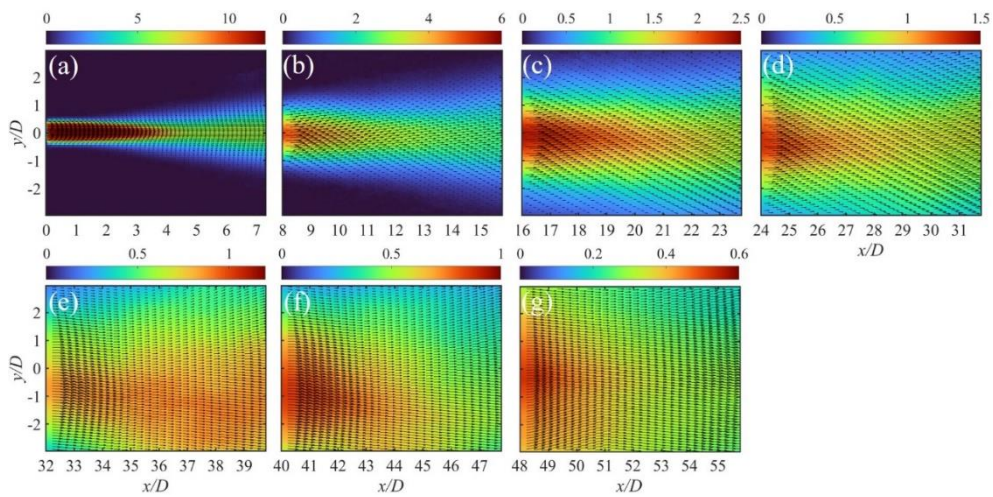


Figure 4.7 Mean gas velocity field of Mesoscale experiments of Exp.1: (a-g) means gradually away from the nozzle exit.

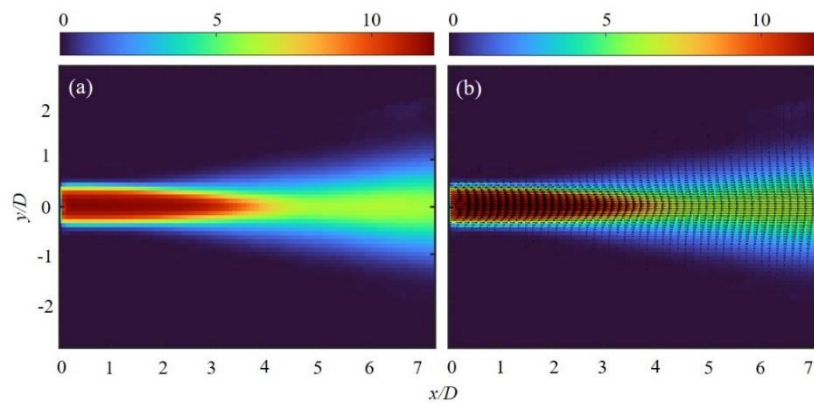


Figure 4.8 Mesoscale experiments of Exp.1: Gas velocity (a) and vector (b) field near the nozzle

The mean gas velocity evolution along the jet centerline is illustrated in Figure 4.9. The figure reveals that both the macroscale and mesoscale measurements display the same velocity decay trend—a slight increase followed by a decrease—although there is a minor difference in values. The slight increase in velocity might be attributed to the weak compression and expansion waves at the exit of the nozzle²¹⁵. The numerical discrepancy arises from the large spatial resolution of the images measured by the macroscale, resulting in a larger interrogation window size for the PIV correlation algorithm. This size is on a par with the jet feature size (12mm), as indicated in Table 4.2, leading to insufficient accuracy in velocity calculation. In contrast, the mesoscale measurements do not have this issue, and their results are more precise. Consequently, the subsequent analysis of velocity decay will be based on the mesoscale measurement results.

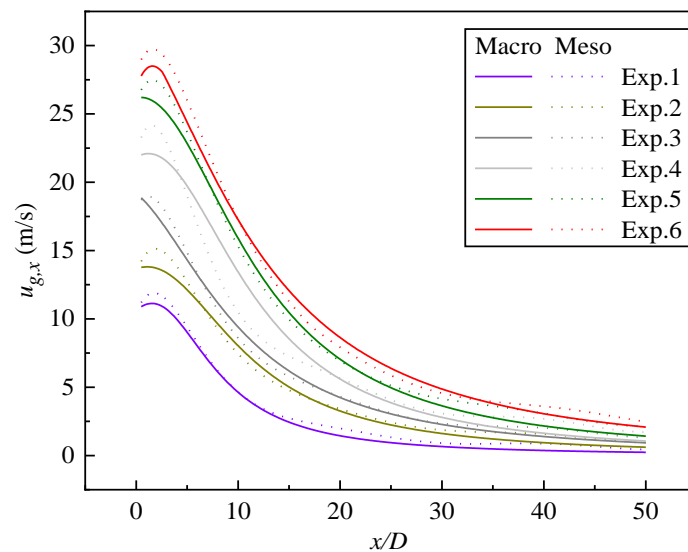


Figure 4.9 Mean gas velocity evolution along the jet centerline

The mean fluctuating velocity fields, as measured by the macroscale experiments, are depicted in Figure 4.10. It is evident that the fluctuating velocity field is similar to that of the mean velocity field. Specifically, as the distance from both the nozzle exit and the jet centerline increases, the fluctuating velocity gradually decays, displaying a

distribution trend characterized by a large center and smaller edges. The mean fluctuating velocity field, as measured by the mesoscale experiments, is illustrated in Figure 4.11. With the exception of the area near the nozzle exit, the fluctuating velocity distribution trend is fundamentally consistent with the macroscale measurements. So far as we know, there is no fluctuating velocity field measurement in proximity to a nozzle over such minuscule scales in the literature. Generally, it is assumed that the distribution of fluctuating velocity aligns with that of mean velocity. In conjunction with the experiment presented in this chapter, this assumption holds true for areas beyond the vicinity of the nozzle. However, the distribution of fluctuating velocity and mean velocity in the area adjacent to the nozzle exhibits significant difference, as demonstrated in Figure 4.12. In relation to Figure 1.1, it can be deduced that the velocity fluctuation in the "Potential Core" region is minimal, whereas the fluctuation in the "Mixing Region" and "Transition" areas is pronounced.

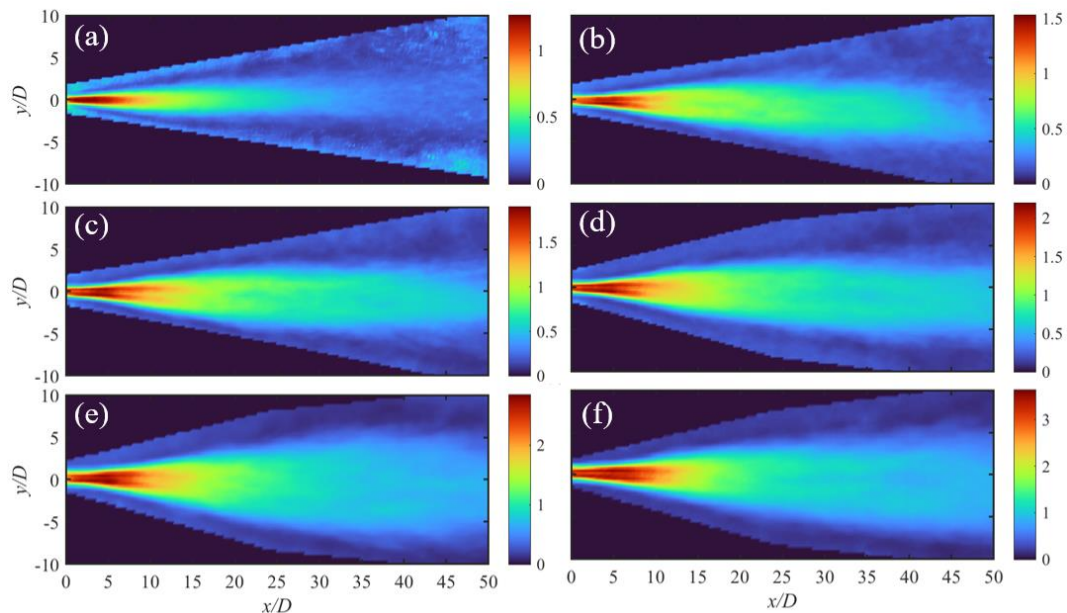


Figure 4.10 Mean gas fluctuating velocity field of Macroscale experiments: (a) Exp.1, (b) Exp.2, (c) Exp.3, (d) Exp.4, (e) Exp.5, (f) Exp.6

The evolution of fluctuating velocity along the jet centerline is depicted in Figure 4.13. For ease of comparison, the fluctuating velocity is normalized using the initial gas

velocity in Figure 4.13 (b). As observed in the figure, the axial fluctuating velocity first increases and then decreases as the gas leaves away from the nozzle. This pattern is consistent with experimental results obtained by Prevost et al.³⁶ who employed alcohol particles (droplets) as gas-phase tracer particles under the condition of a nozzle diameter of 10mm and an initial gas velocity of 20 m/s. The underlying cause for this trend is the relative stability of the flow within the "potential core" region, which exhibits minimal velocity fluctuations. In contrast, the edge and "transition" regions experience significant velocity fluctuations due to entrained mixing and high-speed to low-speed transitions.

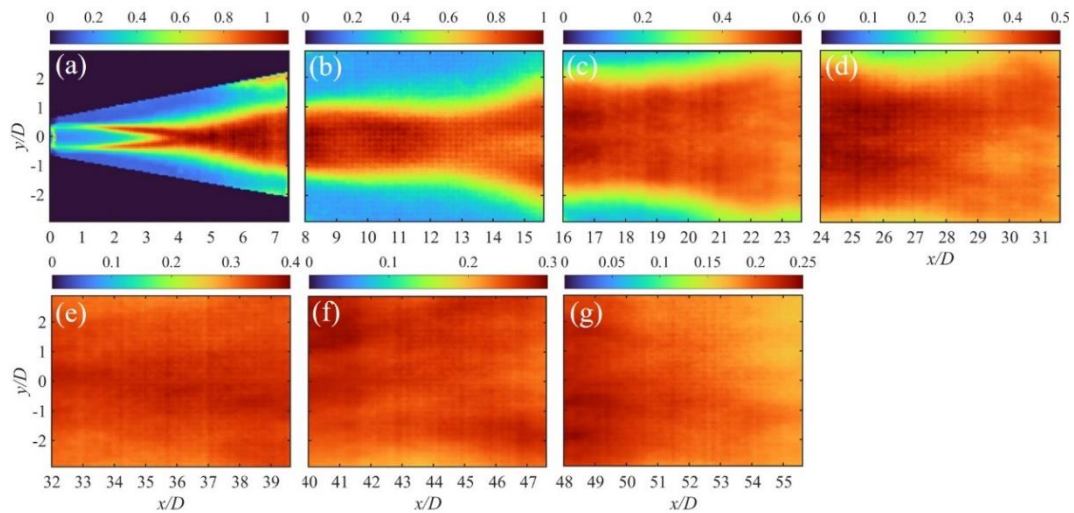


Figure 4.11 Mean gas fluctuating velocity field of Mesoscale experiments of Exp.1: (a-g) means gradually away from the nozzle exit

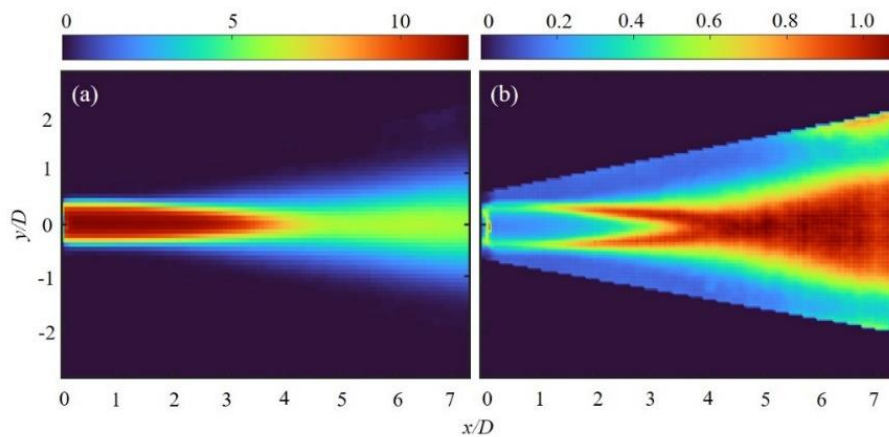


Figure 4.12 Mean gas velocity field (a) and fluctuating velocity field (b) near the nozzle of Exp.1

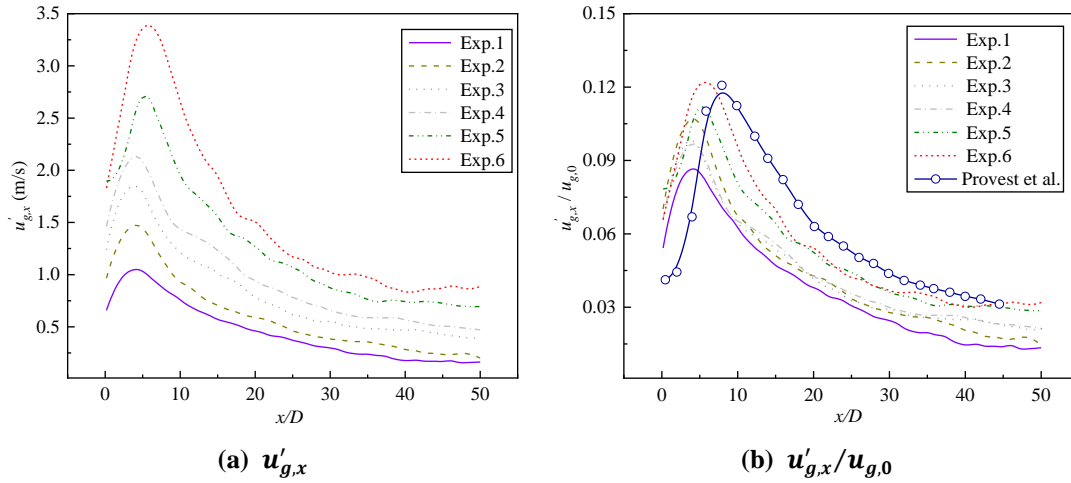


Figure 4.13 Gas fluctuating velocity evolution along the jet centerline

4.3.3 Gas Velocity Decay

The investigation of jet flows predominantly emphasizes the decay rate of velocity along the centerline as well as other higher-order statistical analyses on the axis²²⁹. The jet flow can be classified into four regions along the axis: potential core, transition region, profile similarity region, and termination region where the centerline velocity drops rapidly. The first three regions are shown in Figure 1.1.

It is generally believed that the velocity changes in the potential core region are negligible^{20, 21, 228}. But there are also some studies that have shown the potential core region may experience a slight increase in velocity due to weak expansion²¹⁵ and the existence of exit velocity distribution³¹, especially in the case of multiphase jets. The transition region marks the zone where the centerline velocity begins to decline. The profile similarity region, which is the most extensive part of the jet flow, exhibits similar lateral velocity distributions at different distances from the nozzle. Research into velocity decay is focused primarily on this region. Batchelor²²⁷ indicated that Taylor's theory²³⁰ of fluid particles can be extended to non-homogeneous, self-preserving flows, such as circular jets or wakes. Moreover, the decay coefficient of axisymmetric jet is

sensitive to the exit conditions such as the initial velocity and nozzle size²²⁸.

The centerline velocity decay in the profile similarity region of axisymmetric jets is typically modeled by^{228, 231}

$$\frac{u_x}{u_0} = \frac{K_d D}{x - x_p} \quad (4-1)$$

where u_x is the centerline mean velocity in the x -direction, u_0 the jet exit velocity, K_d the decay coefficient, D the diameter of the nozzle exit, x_p the distance from the nozzle exit to the virtual origin of the jet.

Warren et al.²³² derived the correlation between the centerline axial velocity and the profile transverse velocity, expressed as^{232, 233}

$$\frac{u_t}{u_x} = e^{-\ln 2 \eta^2} \quad (4-2)$$

$$\eta = \frac{y}{y_{1/2}} \quad (4-3)$$

where u_t is the profile transverse velocity, y the coordinate in the y - direction, $y_{1/2}$ is the coordinate in the y - direction where $u_t/u_x = 0.5$ can be defined as

$$y_{1/2} = (x - x_p) \tan \beta \quad (4-4)$$

where β is the jet half-width angle, its relation to K_d is

$$\tan \beta = \frac{(0.5 \ln 2)^{1/2}}{K_d} \quad (4-5)$$

so Eq. (4-2) can also be written as^{228, 234}

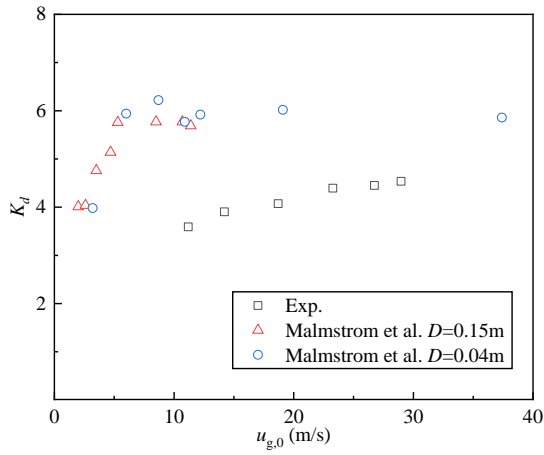
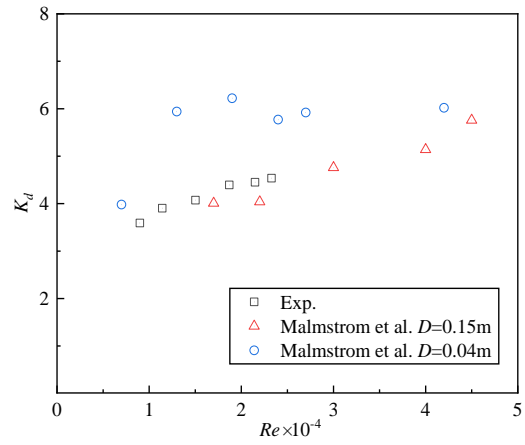
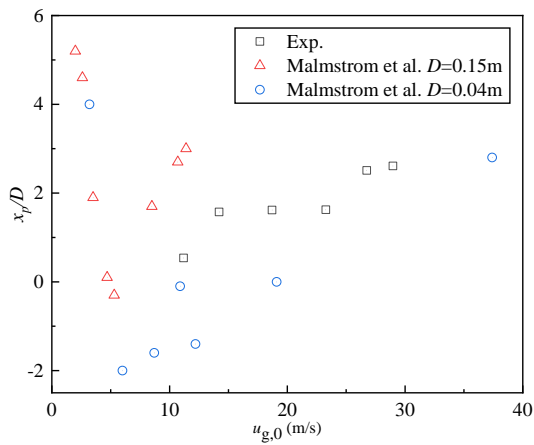
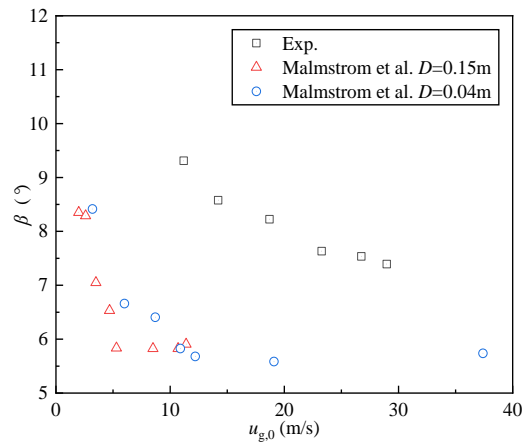
$$\frac{u_t}{u_x} = e^{-K_d^2 n^2} \quad (4-6)$$

$$n = \frac{y}{x - x_p} \quad (4-7)$$

Based on Eq. (4-1) and Eq. (4-6), K_d and x_p were obtained by least squares fitting in this paper. The author summarizes K_d and x_p under different jet outlet conditions in the literature, as shown in Table 4.3.

Table 4.3 The values of K_d and x_p in the literature

| Parameters | $u_{g,0}$ (m/s) | D (mm) | Re ($\times 10^4$) | $\tan\beta$ | K_d | x_p/D |
|---------------------------------|--------------------|-------------|---------------------------|-------------|-------|---------|
| Wyganski et al. ²³⁵ | 51 | 25.4 | 10 | 0.086 | 5.7 | 3 |
| Hussein et al. ²³¹ | 56.2 | 25.4 | 9.55 | 0.094 | 5.8 | 4 |
| | 56.2 | 25.4 | 9.55 | 0.102 | 2.9 | 2.7 |
| Malmstrom et al. ²²⁸ | 3~40 | 0.04 | 0.5~4.5 | 0.09~0.15 | 4~6.5 | -2~4 |
| | 1~15 | 0.15 | 1.5~4.5 | 0.09~0.15 | 4~6 | -1~5.5 |


Figure 4.14 Variation of K_d with $u_{g,0}$

Figure 4.15 Variation of K_d with Re

Figure 4.16 Variation of x_p with $u_{g,0}$

Figure 4.17 Variation of β with $u_{g,0}$

The preliminary numerical ranges of K_d and x_p can be obtained from Table 4.3,

assisting in evaluating the rationality of the fitted values. The relationship between K_d and nozzle exit velocity $u_{g,0}$ and Re are depicted in Figures 4.14 and 4.15 respectively, and the relationship between x_p and β and exit velocity $u_{g,0}$ are shown in Figure 4.16 and Figure 4.17 respectively. By examining Figures 4.15~4.17 and Table 4.3, the variation trends and values of each parameter display a strong agreement with the existing literature.

Upon acquiring suitable values of K_d and x_p , the prediction of jet centerline velocity can be achieved using the aforementioned model. A comparison of model predictions and experimental data for velocity decay along the jet centerline is presented in Figure 4.18. The figure demonstrates that the model accurately predicts jet velocity decay with minimal error when compared to experimental data.

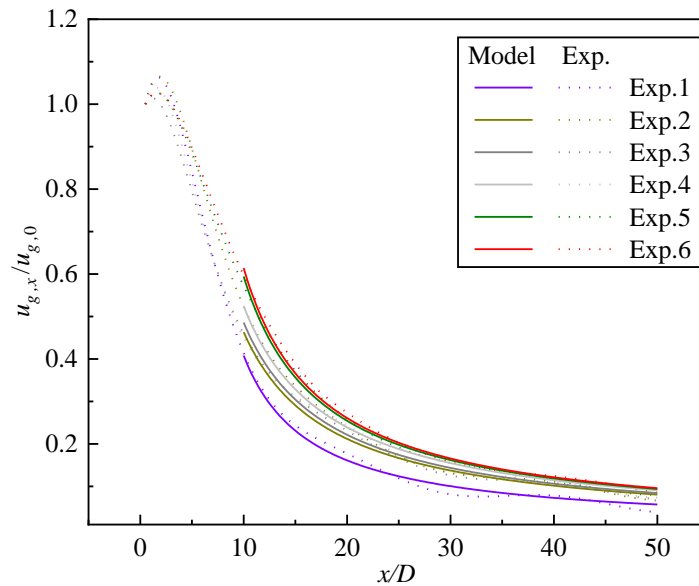


Figure 4.18 Comparison of model prediction and experimental values of gas velocity decay along the jet centerline

4.3.4 Eulerian Self-similarity Properties

Profile transverse velocities for various axial positions and experiments are presented in Figures 4.19 and 4.20, respectively. The figures indicate a strong

agreement between the model prediction and experimental values. In conjunction with Figures 4.18 and 4.19, it can be deduced that when x/D exceeds 10, the profile transverse velocity in the downstream of the jet demonstrates enhanced self-similarity, corroborating the findings ($x/D > 5\sim 17$) reported in the literature^{18, 20, 215}.

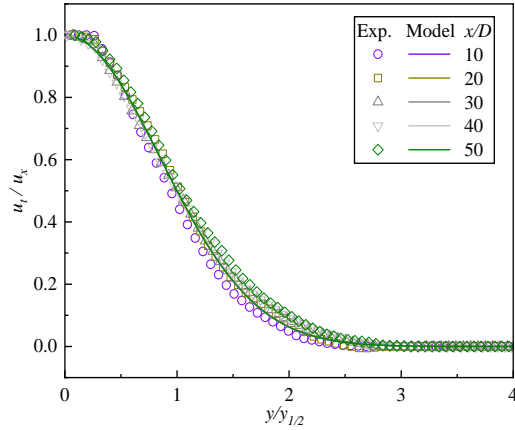


Figure 4.19 Profile transverse gas velocity at different axial positions of Exp.1

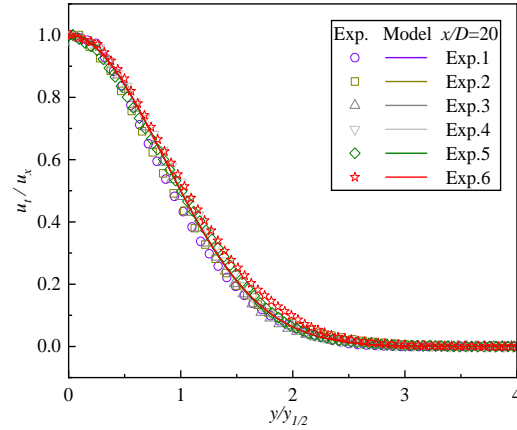


Figure 4.20 Profile transverse gas velocity of different experiments

4.4 Middle-Stokes-number Particle-laden jets (Particle Flow) Characteristics

In this section, SiO₂ microspheres neither completely follow the gas flow nor remain unresponsive to it. We study the dynamics of SiO₂ microspheres in middle-Stokes-number particle-laden jets.

4.4.1 Instantaneous Particle Velocity

A transient snapshot of macroscale and mesoscale middle-Stokes-number particle-laden jet experiments is depicted in Figure 4.2. The transient particle velocity field of the macroscale experiment is shown in Figure 4.21. Similar to the gas phase velocity field, the particle velocity peak in the jet process is not always on the jet centerline but fluctuates around it. The particle velocity fields and vector fields obtained from the mesoscale experiments are shown in Figure 4.22 and 4.23. Smaller-scale experiments offer more precise and detailed velocity fields. Moreover, they can attain more accurate

velocity fields.

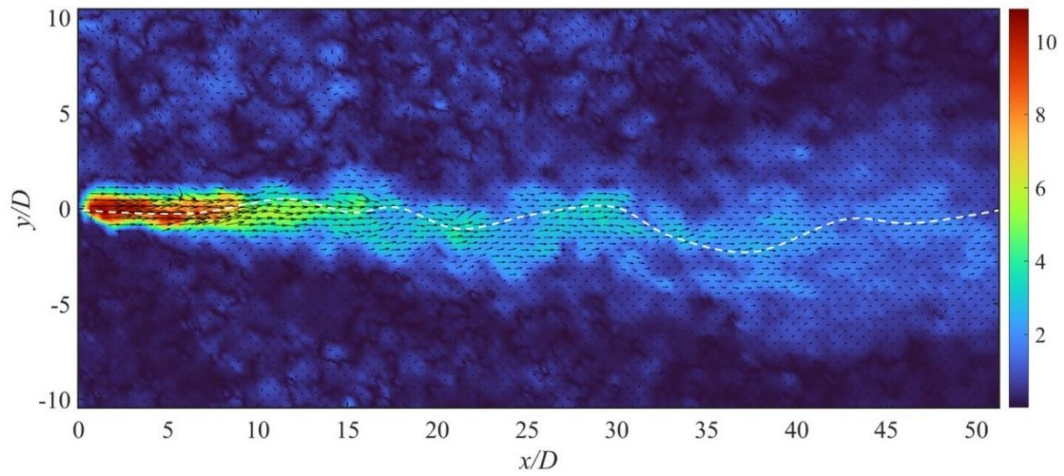


Figure 4.21 Macroscale experiment of Exp.1: Transient particle velocity field of particle-laden jet.
The dotted line indicates the location of the velocity maximum

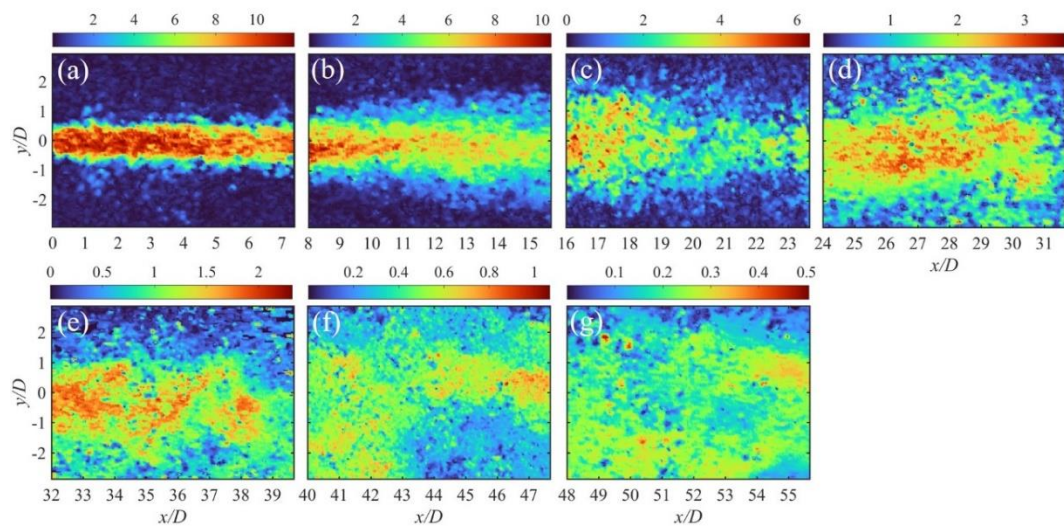


Figure 4.22 Mesoscale experiments of Exp.1: Transient particle velocity field of particle-laden jet

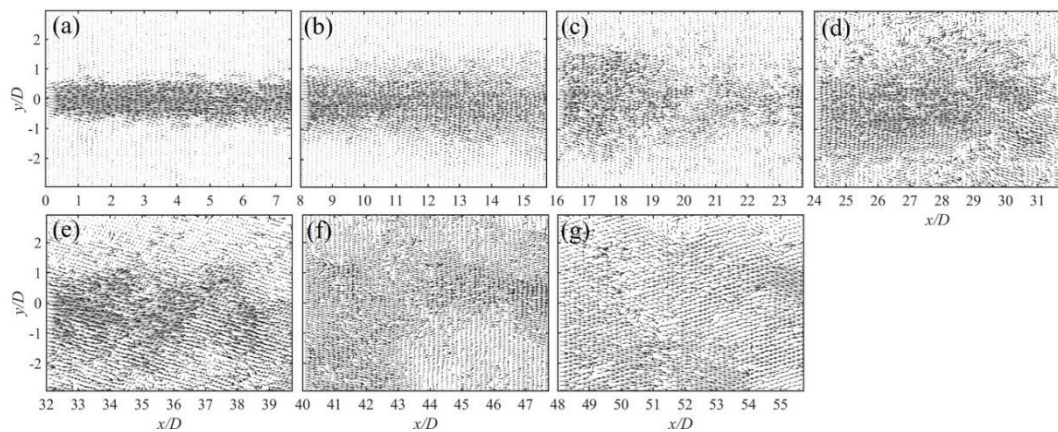


Figure 4.23 Mesoscale experiments of Exp.1: Transient particle velocity vector field of particle-laden jet

4.4.2 Mean and Fluctuating Particle Velocity

The mean velocity fields with average duration of 1s of particles, as obtained from the macroscale experiments, are depicted in Figure 4.24. As it moves away from the nozzle exit and the centerline of the jet, the velocity gradually decays, exhibiting a distribution trend characterized by a large center and small edges, analogous to the velocity field of the gas phase.

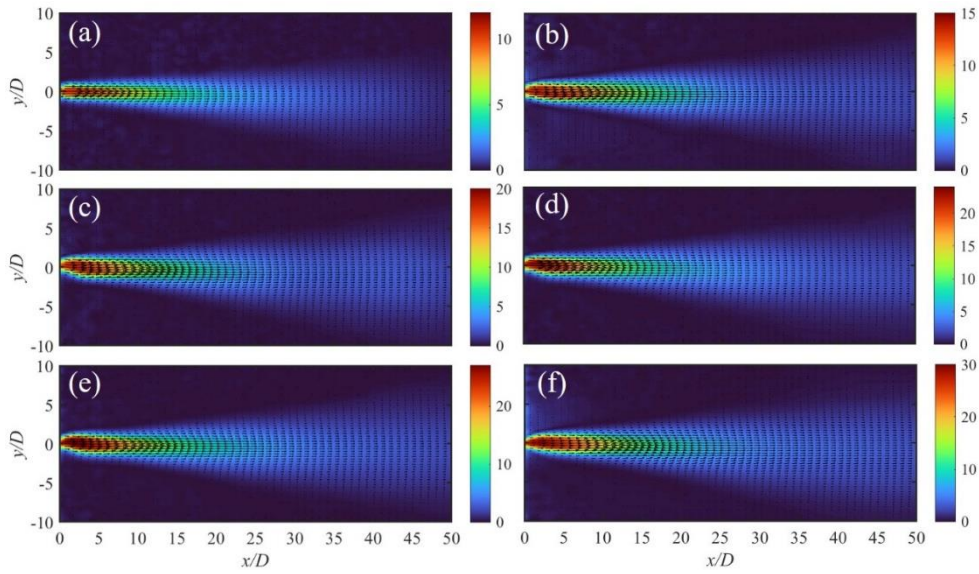


Figure 4.24 Mean particle velocity field of Macroscale experiments: (a) Exp.1, (b) Exp.2, (c) Exp.3, (d) Exp.4, (e) Exp.5, (f) Exp.6

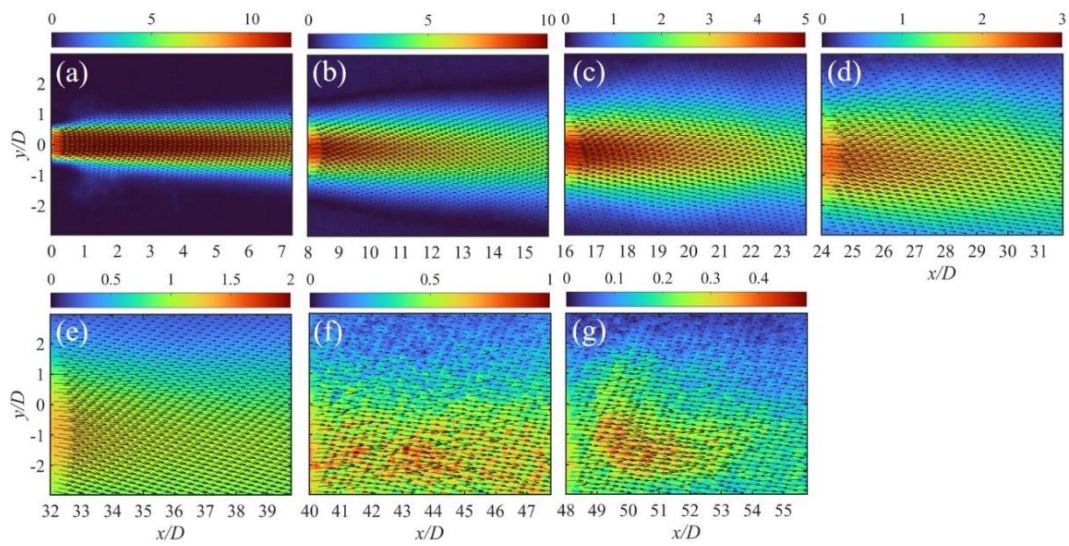


Figure 4.25 Mean particle velocity field of Mesoscale experiments of Exp.1: (a-g) means gradually away from the nozzle exit

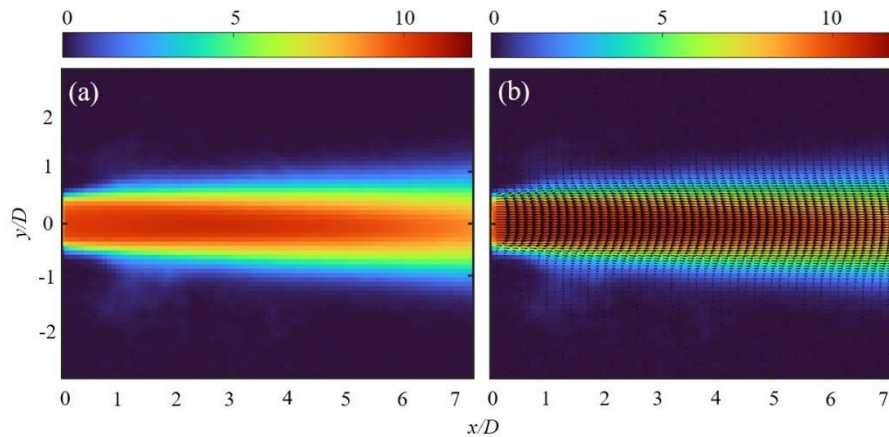


Figure 4.26 Mesoscale experiments of Exp.1: Particle velocity field (a) and vector field (b) near the nozzle

The mean velocity fields of particles obtained by the mesoscale experiments are shown in Figures 4.25 and 4.26. The velocity distribution trend aligns with that of the macroscale measurements, but the mesoscale measurements demonstrate higher accuracy. Figure 4.26 (b) distinctly reveals a trapezoidal distribution of particle velocity at the nozzle exit.

The evolution of particle velocity along the centerline of the jet is depicted in Figure 4.27. As observed in the figure, the macroscale and mesoscale experiments exhibit a consistent velocity decay trend, initially increasing slightly before decreasing. Prevost³⁶, Kennedy²³⁶, Krothapalli²¹⁵, and Calvo⁴⁴ et al. also observed this phenomenon, where the increase in velocity is attributed to the gas velocity at the nozzle outlet being higher than the particle velocity, thus causing particle acceleration. The discrepancies in values between the two scales are due to the limited accuracy of macroscale measurements. Consequently, the analysis of particle velocity decay in the subsequent sections will rely on the mesoscale experiment results.

Figure 4.28 presents the normalized particle velocity decay trend in comparison to the findings from the literature results. Among them, the particles used in the Prevost et al.³⁶ experiment are glass beads of about 45 μm , with a nozzle diameter of 10mm,

and an initial gas velocity of 20 m/s. Meanwhile, the particles used in Kennedy et al.²³⁶ utilized droplets of around 60 μm , with a nozzle diameter of 7 mm, and an initial gas velocity of 64.5 m/s. As illustrated in the figure, the particle velocity profile aligns with that in the literature. The particle velocity decay is more rapid in this study, due to larger and more inertial particles used by Prevost³⁶ and Kennedy²³⁶ et al.

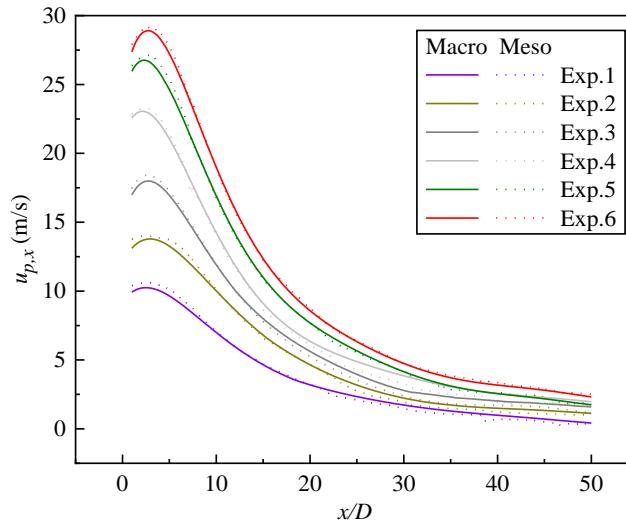


Figure 4.27 Particle velocity evolution along the jet centerline

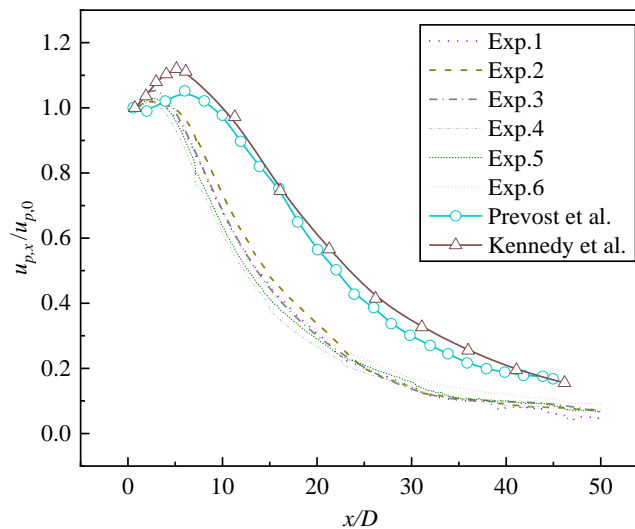


Figure 4.28 Normalized particle velocity along the jet centerline compared to literature

Figure 4.29 illustrates the evolution of gas and particle phase velocities along the jet centerline of both the gas jet and particle-laden jet under the identical experimental conditions. The velocity decay trends of the gas and solid phases appear similar,

although the gas phase decays faster. Furthermore, the gas phase velocity near the nozzle exceeds the particle velocity, while the particle velocity surpasses the gas phase velocity further from the nozzle. This observation aligns with the findings of Prevost³⁶ and Fan²³⁷ et al. as particles have greater inertia than gases, resulting in a slower velocity decay.

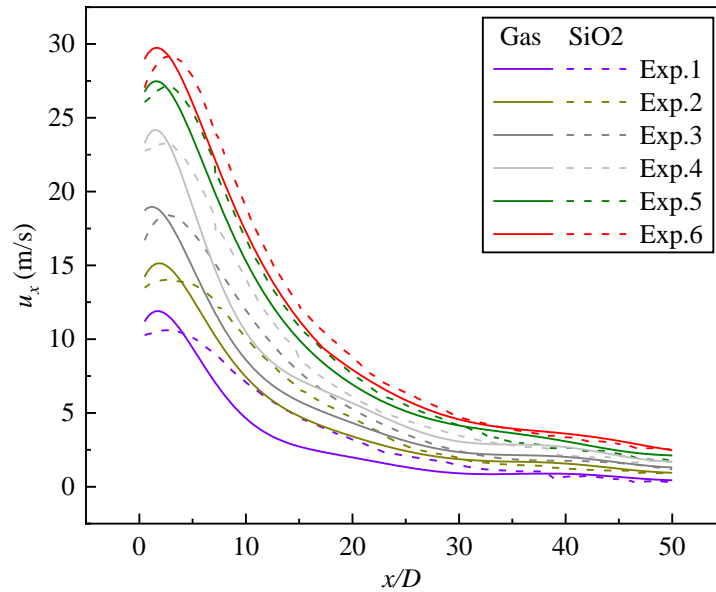


Figure 4.29 Comparison of gas and particle velocities along the jet centerline

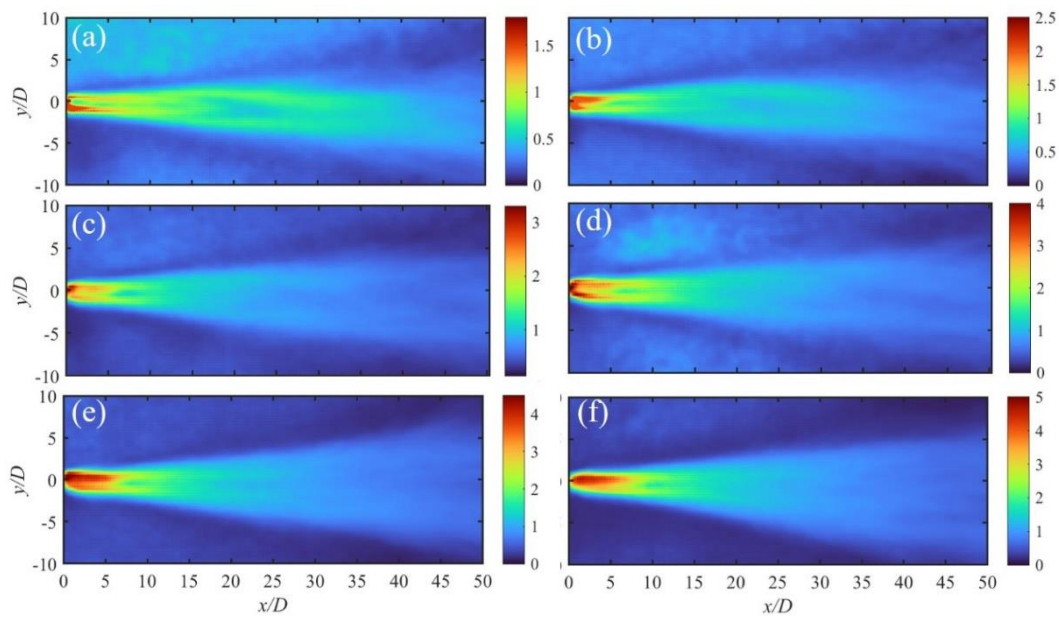


Figure 4.30 Mean particle fluctuating velocity field of Macroscale experiments: (a) Exp.1, (b) Exp.2, (c) Exp.3, (d) Exp.4, (e) Exp.5, (f) Exp.6

Figures 4.30 and 4.31 display the average fluctuating velocity fields derived from macroscale and mesoscale experiments, respectively. The distribution of fluctuating velocity fields for particles closely resembles that of the gas phase. The author has not encountered particle fluctuating velocity field measurements near nozzles at such a small scale in existing literature. It is presumed that the distribution of fluctuating velocities near the nozzle would mirror that of gas-phase jets, as depicted in Figure 4.31(a), which is not elaborated upon here.

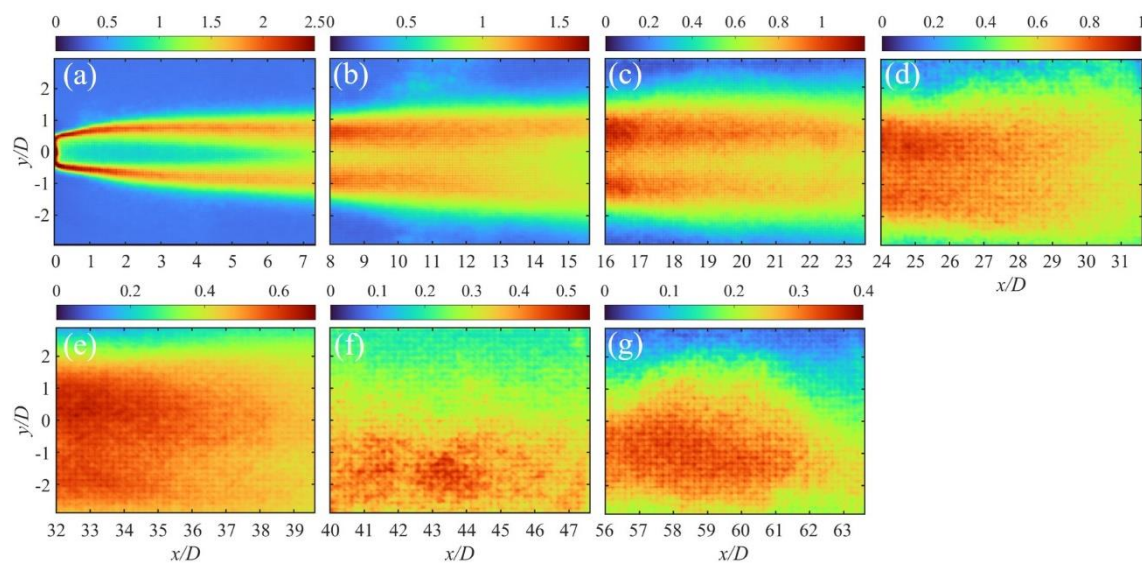


Figure 4.31 Mean particle fluctuating velocity field of Mesoscale experiments of Exp.1: (a-g) means gradually away from the nozzle exit

Figure 4.32 compares the fluctuating velocities of the gas phase and particles along the jet centerline. The gas phase fluctuating velocity initially increases before decreasing, while the particle fluctuating velocity exhibits a pattern of decreasing first, then increasing, and finally decreasing. This phenomenon was also mentioned in the study of Prevost et al.³⁶, shown in Figure 4.33, attributing it to the presence of flow-particle interactions in the ejector and particle bouncing along the ejector wall. Consequently, particles originating from regions of low velocity (near the ejector wall) and those from regions of higher velocity (along the axis of the stream) mix within the

stream at the ejector exit, causing a reduction in mean particle velocity and an increase in fluctuating velocity near the ejector exit^{36,218}. In the downstream of the jet, analogous to the velocity decay result, the fluctuating velocity of the particles exceeds that of the gas phase due to the velocity decay and large inertia of the particles.

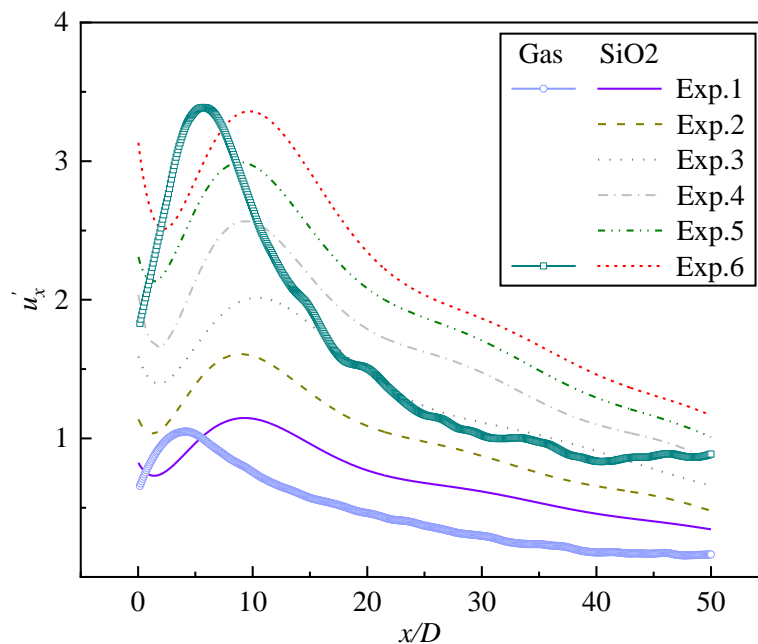


Figure 4.32 Comparison of fluctuating velocities of the gas and particles along the jet centerline

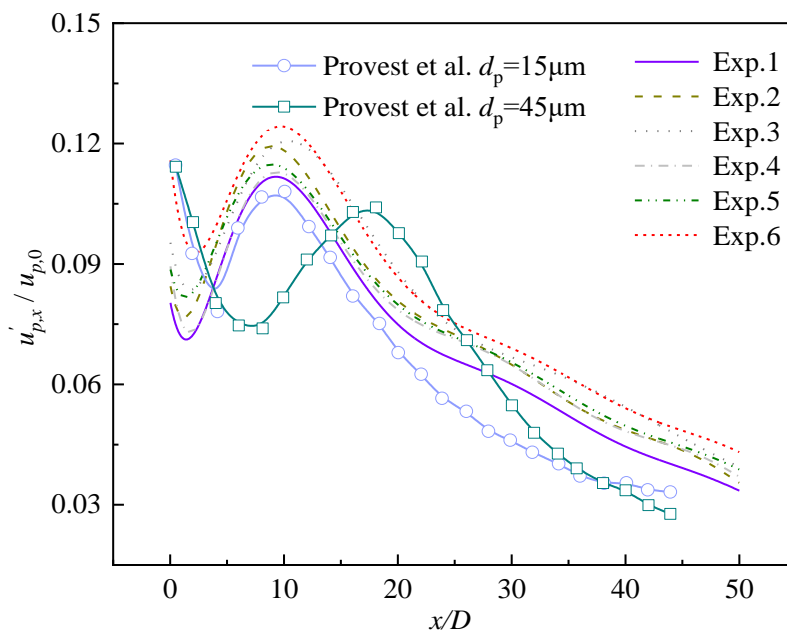


Figure 4.33 Normalized particle velocity along the jet centerline compared to literature

4.4.3 Particle Velocity Decay

The addition of particles renders the jet flow more complicated, by factors such as the particle diameter, particle density, turbulence, and various gas-solid interaction forces. Currently, there is no predictive model for particle velocity decay for particle-laden jets. For middle-Stokes-number particles, though the particles do not fully respond to the airflow, they partially follow the airflow. So, this section attempts to employ the classic velocity decay model in the gas phase jet to predict the particle velocity, and assess its applicability to middle-Stokes-number particle-laden jets.

K_d , x_p and β and their variation trends obtained based on the model are shown in Figures 3.34 ~ 3.37, together with the results reported in the literature²²⁸. From Figure 4.34 and Figure 4.35, it is evident that for both the gas and particles (SiO₂ microspheres), K_d increases with the rising velocity and Re , and K_d of particles is slightly smaller than that of the gas. This indicates that the velocity of the gas decays faster than that of the particles, as in Figure 4.29. Figure 4.36 shows that x_p of the gas and particles both increase with the velocity, but x_p of particles is larger than that of the gas, and their difference is large. This reveals that the "potential core" region of the gas is smaller than that of particles, and its virtual origin is situated closer to the nozzle, potentially due to the large inertia of particles. This observation can be qualitatively discerned by combining Figure 4.12 and Figure 4.26. From Figure 4.37, it can be seen that β decreases with velocity, and β of particles is slightly larger than that of the gas phase, which indicates that the degree of radial dispersion of particles is larger than that of the gas.

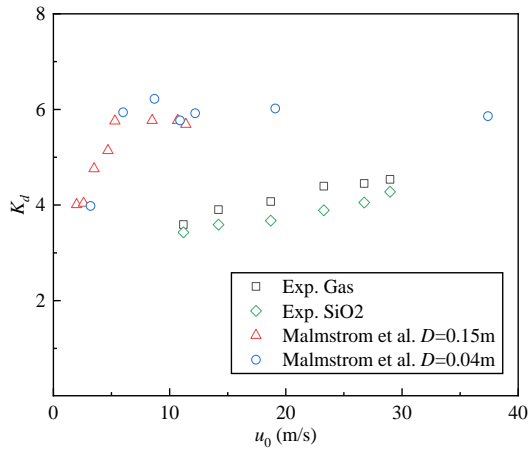
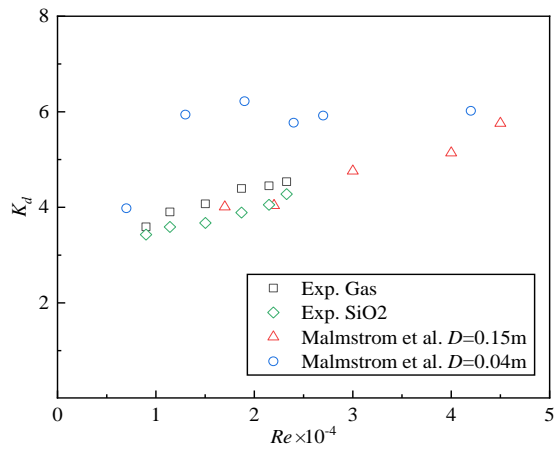
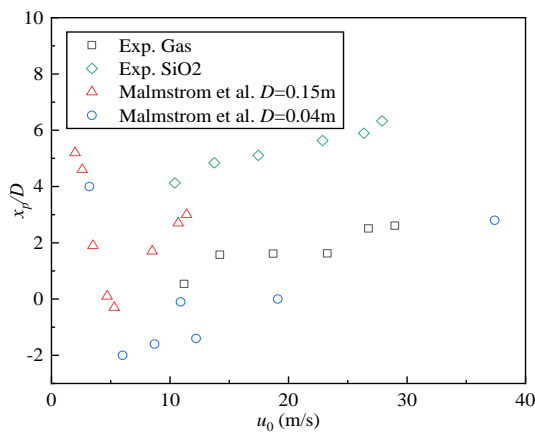
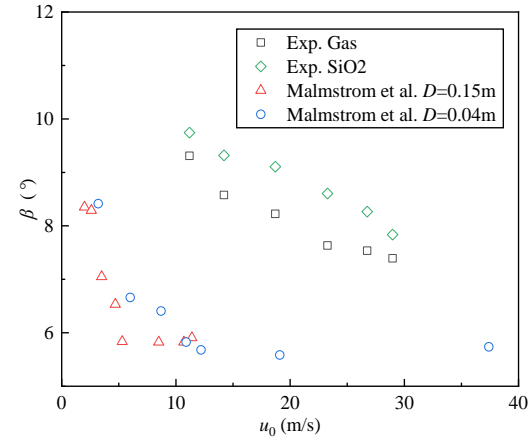
Figure 4.34 Variation of K_d with u_0 Figure 4.35 Variation of K_d with Re Figure 4.36 Variation of x_p with u_0 Figure 4.37 Variation of β with u_0

Figure 4.38 compares model prediction and experimental data of particle velocity decay along the jet centerline. Generally, the model can predict the decay trend of particle velocity. From a numerical point of view, the model prediction results in the early stage of jet flow smaller than the experimental, and the measurement error is relatively large, with a maximum of 16%. The prediction results in the later stage of the jet flow are slightly larger than the experimental data. This indicates that the velocity decay prediction model of the gas phase is applicable to middle-Stokes-number particle-laden jets with small particles to a certain extent, especially in the later stage of the jet flow.

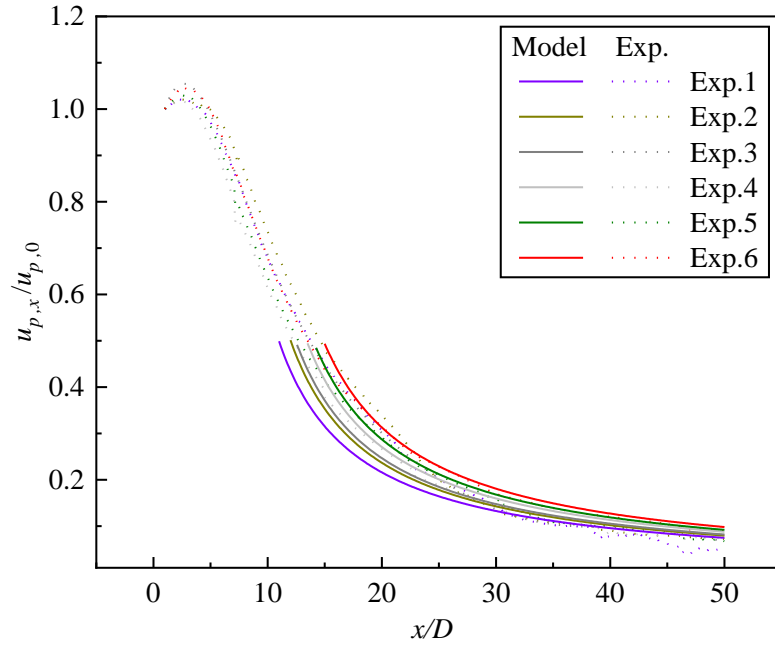


Figure 4.38 Comparison of model prediction and experimental data of particle velocity decay along the jet centerline

4.4.4 Eulerian Self-similarity Properties

The profile transverse particle velocities for different axial positions of different experiments are shown in Figures 4.39 and 4.40, respectively.

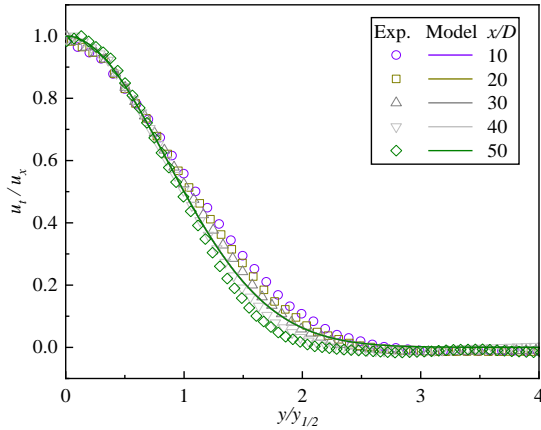


Figure 4.39 Profile transverse particle velocity at different axial positions of Exp.1

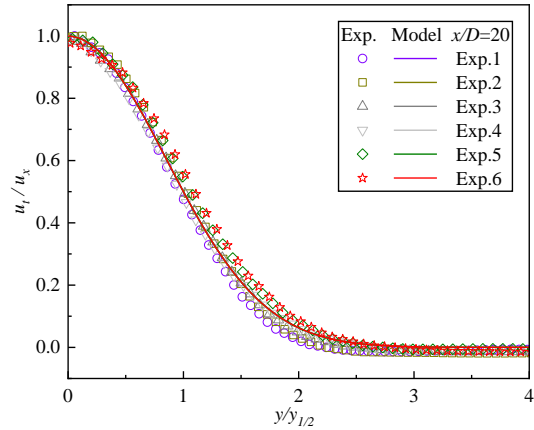


Figure 4.40 Profile transverse particle velocity of different experiments

From the figures, we can find that the model predictions agree well with the experimental data, regardless of the different jet downstream positions or different experiments, indicating that self-similarity also exists in the particles of the jet.

Combining Figure 4.19 and Figure 4.20, the degree of agreement is not as high as that of the gas phase due to the self-similarity of particle velocity decreases faster due to the strong inertial effect of heavy particles^{236, 238}.

4.5 Mesoscale Structure and Particle Concentration of Middle-Stokes-number Particle-laden jets

The instantaneous concentration of particles is often related to the structure of clusters. Gaining a comprehensive understanding of the dynamics of particle clusters in particle-laden jets can help elucidate the non-uniform dispersion process of particles, which is also very important for industrial applications. The flow inhomogeneity and air entrainment of circular jets make the dispersion of particles in the gas flow more complicated than in uniform isotropic turbulent flow which has been relatively well studied⁶³. The research presented in this section aims to understand the dynamics of particle clusters in a circular particle-laden jet.

4.5.1 Clusters and Preferential Concentration

4.5.1.1 Clusters Identification Method

To determine the local concentration of each particle irrespective of spatial scale choice, this section adopts the Voronoi analysis method to define the particle concentration (or, particle volume fraction). The Voronoi method has been introduced in Section 1.2.2 and will not be repeated here. Determining the position of particles is a prerequisite for using the Voronoi method. To achieve this, we first use MATLAB software to process the captured images. The image processing process is shown in Figure 4.41, during which particle positions are obtained through particle detection. Figure 4.41 (c) displays the detection results of the particles.

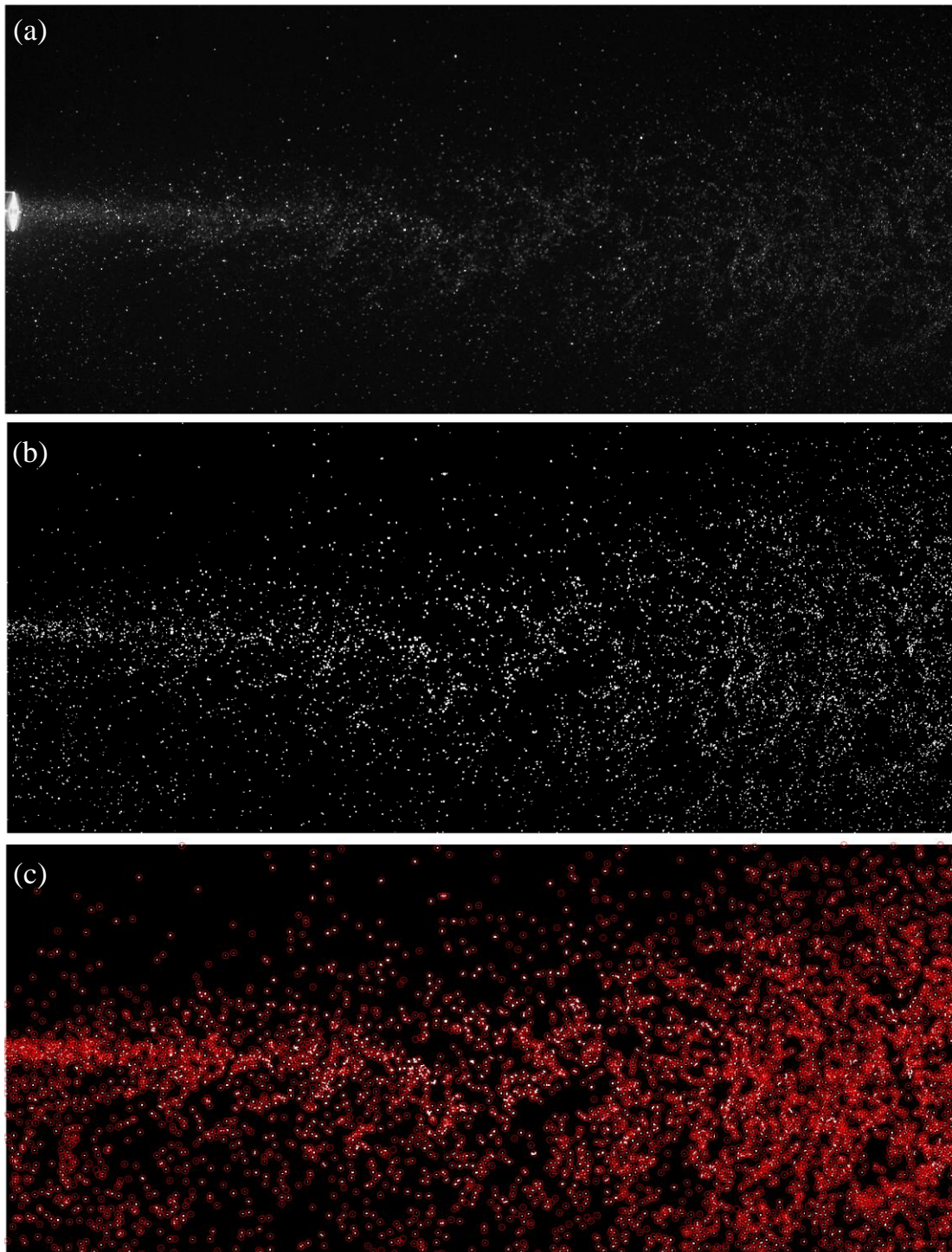


Figure 4.41 Particles detection steps: (a) raw image, (b) image segmentation, (c) particle detection results.

Once the location information is acquired, a Voronoi map can be generated, as illustrated in Figure 4.42 (a). The local concentration of each particle can be determined

from the Voronoi tessellation diagram, with particle concentration equating to the ratio of particle size to Voronoi cell size. Subsequently, particle clusters can be identified. This section employs the method of comparing the normalized Voronoi area probability density distribution (PDF) with the random Poisson process distribution (RPP) to discern particle clusters^{57, 61, 63}. The PDF of the normalized Voronoi area (normalized by the mean area of the Voronoi cell) of the experiment is compared to the PDF of a random Poisson process, identifying the intersection points of the two PDFs. Generally, the curves intersect twice, and Voronoi cells with areas smaller than the first intersection point are regarded as clusters, while Voronoi cells with an area greater than the second intersection point are regarded as voids⁶¹, as shown in Figure 4.42 (b).

RPP is a type of Gamma distribution, defined as²³⁹

$$f_{2D-RPP} = \frac{343}{15} \sqrt{\frac{7}{2\pi}} \left(\frac{A}{\bar{A}}\right)^{2.5} e^{-3.5\left(\frac{A}{\bar{A}}\right)} \quad (4-8)$$

where A represents the area of the Voronoi cell and \bar{A} is the mean area of the Voronoi cell.

The cluster identification results are displayed in Figure 4.42 (c), with red markers signifying cluster particles. The distribution of clusters is notably uneven, with a higher concentration of particle clusters near the nozzle and in the later stage of the jet. This may be attributed to the fact that the particles near the nozzle are not dispersed yet, and the particle velocity diminishes very low in the later stage of the jet, then the particles accumulate together again. Moreover, the particle concentration on the lower side is substantially greater than that on the upper side, possibly due to the influence of gravity.

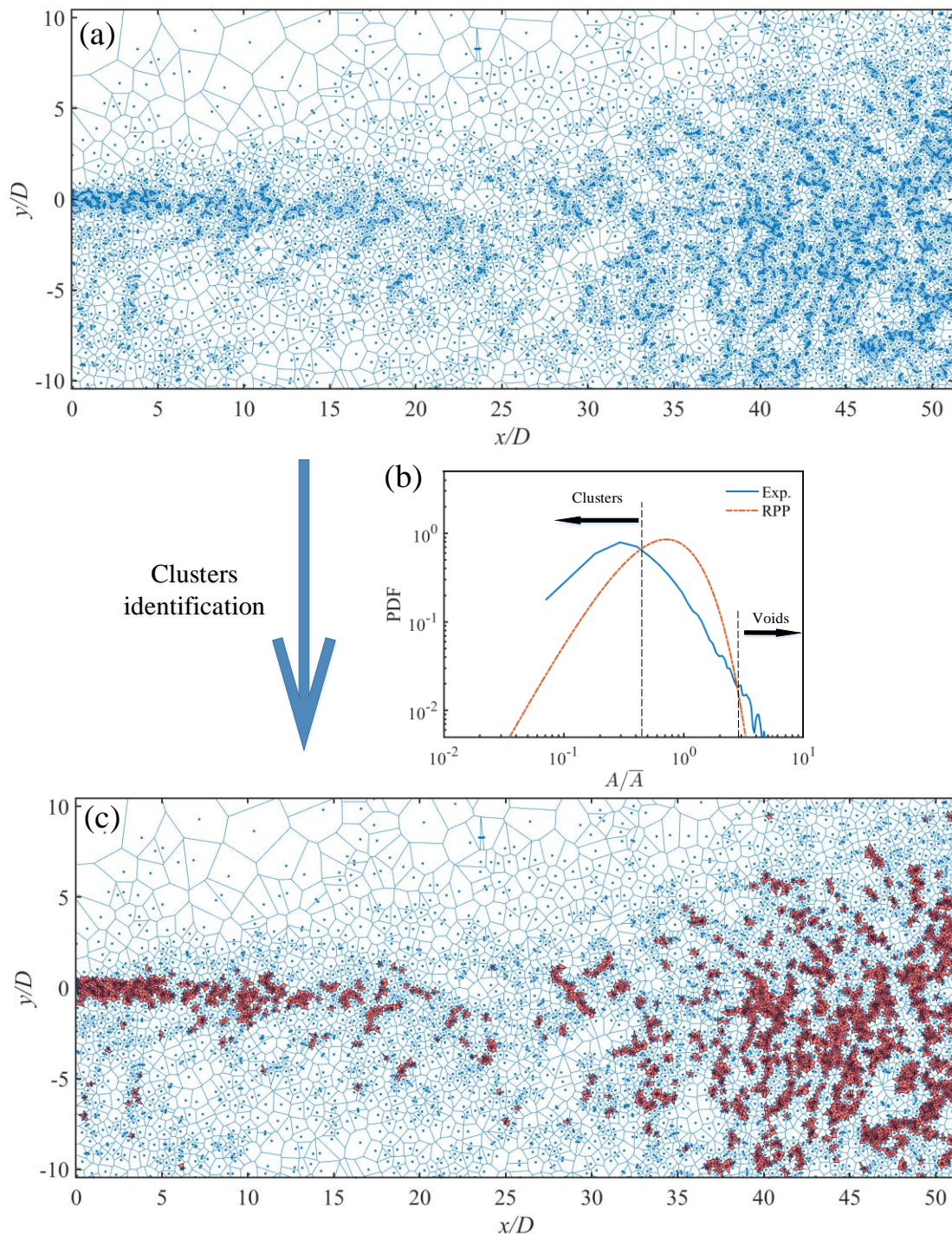


Figure 4.42 Schematic diagram of the identification process of clusters.

(a) Voronoi diagram of particles, (b) identification of clusters, (c) identification results of clusters

4.5.1.2 Extent of Clustering

Moreover, it is crucial to determine the extent of particle clustering. The clustering extent can be quantified by calculating and comparing the standard deviations of the

measured Voronoi and RPP distributions⁶³. When particles preferentially accumulate in certain regions of the flow, their distribution is non-random and the standard deviation of the corresponding Voronoi region is larger than that of the RPP distribution. Consequently, we introduce the parameter σ_{rel} to quantitatively characterize the degree of particle clustering⁶³.

$$\sigma_{\text{rel}} = \frac{\sigma_v - \sigma_{RPP}}{\sigma_{RPP}} \quad (4-9)$$

where σ_{RPP} denotes the standard deviation of the RPP distribution, $\sigma_{RPP}=0.53$, and σ_v the standard deviation of the normalized Voronoi area. σ_{rel} greater than zero means that the particles are non-randomly distributed, and a higher value means stronger particle aggregation⁶³.

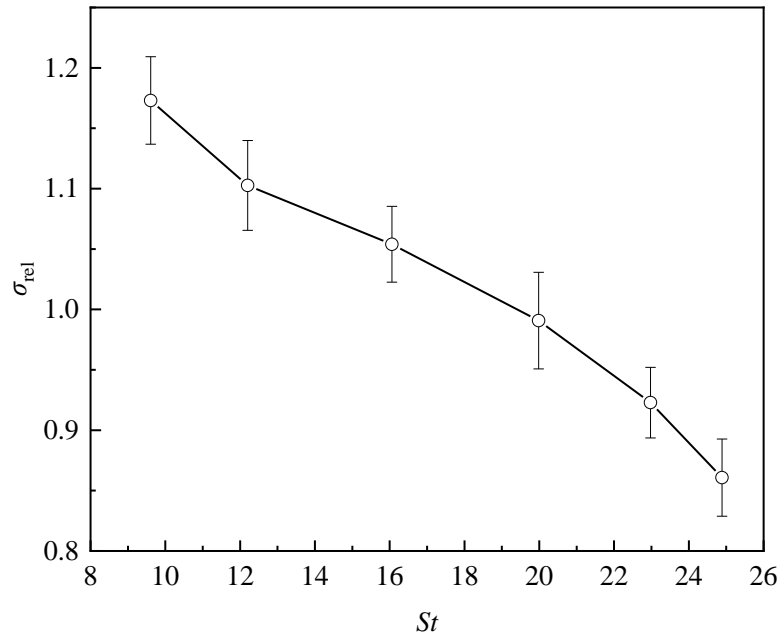


Figure 4.43 Variation curve of σ_{rel} with St

It is widely accepted that preferential concentration is primarily related to the Stokes number (St)^{55-57, 61}. Accordingly, we analyze σ_{rel} alongside the St , as shown in Figure 4.43. The figure reveals that σ_{rel} diminishes as St increases, which is consistent with the view described in the literature that as the St tends to be unify, the preferential concentration effect of particles is more significant^{55, 57}.

4.5.1.3 Cluster Characterization Method and Scale

The particle clustering in jets has been found to be a multiscale process spanning a wide range, from tens of Kolmogorov scales to the jet half-width⁶³. The shapes of particle clusters are rich and varied, ranging from dimers, trimers to multimers. This section uses a new cluster characterization method⁶³ to study the scale of particle clusters, as shown in Figure 4.44. We use different ellipses to approximate the shape of particle clusters. In the figure, A_c is the area of the equivalent ellipse of the particle cluster obtained from the Voronoi area calculation. L_{maj} and L_{min} are the major and minor axis of the ellipse, respectively. We can analyze the scale of particle clusters through these several characteristic scale parameters.

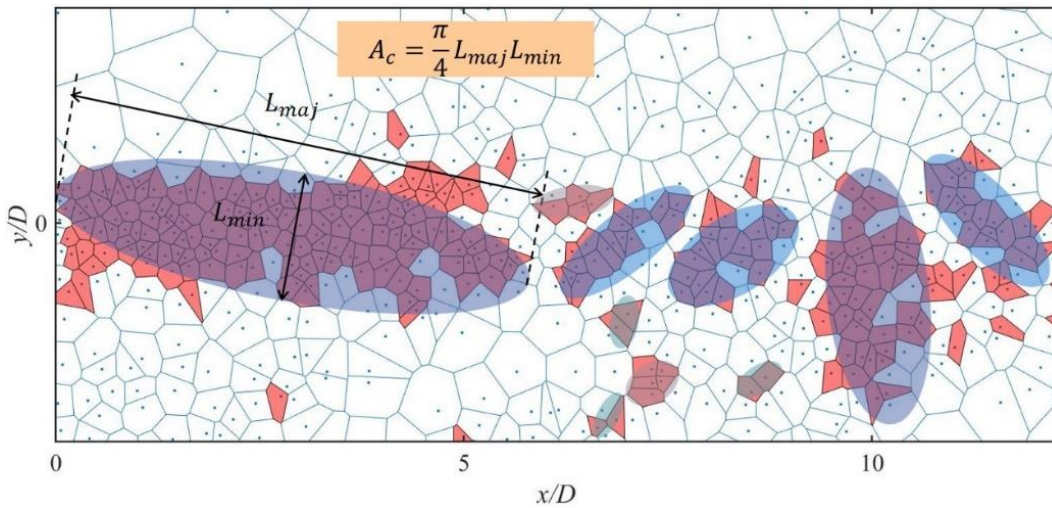


Figure 4.44 Geometric characterization of particle clusters.

A_c is the area of the equivalent ellipse of the particle cluster obtained from the Voronoi area calculation. L_{maj} and L_{min} are the major and minor axis of the ellipse, respectively.

Figure 4.45 presents the probability density function (PDF) of the particle cluster area, normalized by the nozzle area. The cluster area is 0.002~5 times the nozzle area, and the scale of the largest number of clusters is about 0.01 times the nozzle area. The distribution trend of PDF is consistent with the research results of Monchaux⁶¹ and Manish⁶³ et al. Figure 4.46 is the dynamic change of cluster ratio (defined as the ratio

of particles in the cluster to all particles) over time during the jet flow. Notably, the cluster ratio exhibits minimal variation over time, indicating a dynamic and stable clustering process of particles throughout the injection process.

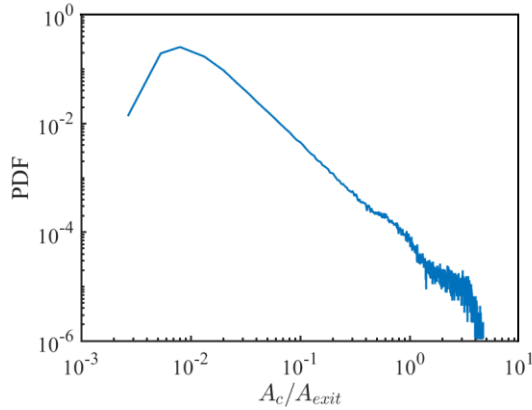


Figure 4.45 PDF of cluster area

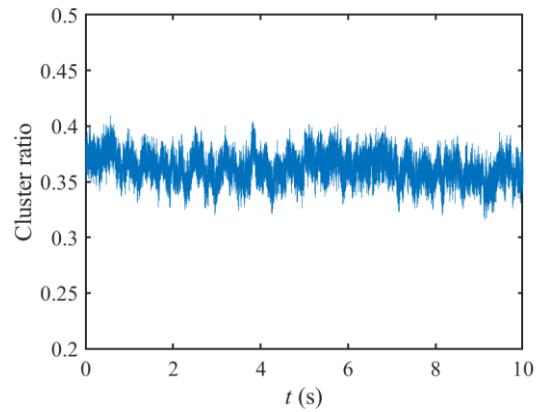


Figure 4.46 Time evolution of cluster ratio

Figure 4.47 depicts the distribution of particles within clusters in the shooting area across varying statistical time spans. The number of clusters of different-sized is normalized by the total cluster count, with n_c representing the number of particles in the cluster. The number distribution of clustered particles remains consistent throughout the statistical process, and the power-law relationship is largely unaffected by the statistical time scale. Consequently, the particle clustering process within the injection system can be considered dynamically stable. Furthermore, the distribution of small-sized clusters adheres to the power-law distribution of percolation theory²⁴⁰. However, when the number of particles in the cluster exceeds 50, the distribution of clusters is significantly higher than the power-law distribution. Some researchers^{241, 242} have posited that the formation process of clusters in a uniform cooling system closely resembles the infiltration process, and thus, infiltration theory can effectively describe the nature of clusters in particle systems. This is corroborated by the findings in this section.

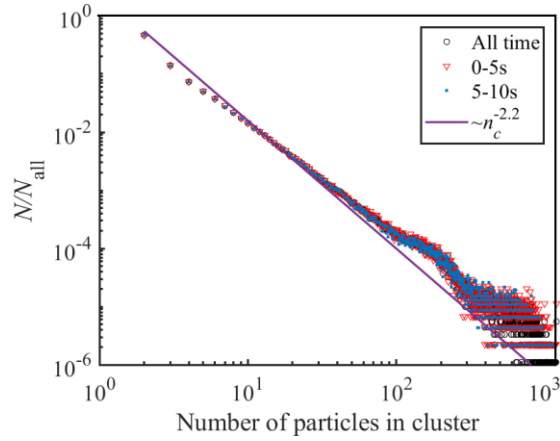


Figure 4.47 Cluster size distributions for different time periods

The relationships among the characteristic size parameters of clusters are depicted in Figure 4.48, where A_{exit} represents the area of the nozzle, L_d the equivalent circle diameter of the cluster, defined by

$$L_d = \sqrt{4A_c/\pi} \quad (4-10)$$

The PDFs of cluster characteristic size are shown in Figure 4.48 (a). The dimensions of the characteristic parameters are normalized using the nozzle diameter D . The distribution of PDFs of the three characteristic parameters is observed to be identical. The scale of the major axis is about 0.16 to 20 times the diameter of the nozzle, and the scale of the major axis of the largest number of clusters is about 0.5 times the diameter of the nozzle. The size of the minor axis is about 0.12 to 10 times the diameter of the nozzle, and the size of the minor axis of the most numerous clusters is about 0.25 times the diameter of the nozzle. The PDF distribution and scale of equivalent diameters lie between these ranges.

The ratio of L_{maj} to L_{min} of the clusters is presented in Figure 4.48 (b). It can be seen that the ratio of the major axis to the minor axis can reach up to 12, indicating that the major axis is the main characteristic dimension of the clusters. The ratio of the L_{maj} and L_{min} to L_d of the clusters are shown in Figure 4.48 (c) and Figure 4.48 (d), respectively. It is evident that the major axis to equivalent diameter ratio varies from 1

to 4.5, while the minor axis is close to the equivalent diameter, and the ratio is mainly in the range of 0.5 to 1.5. This further substantiates that the major axis is the primary characteristic dimension of the clusters.

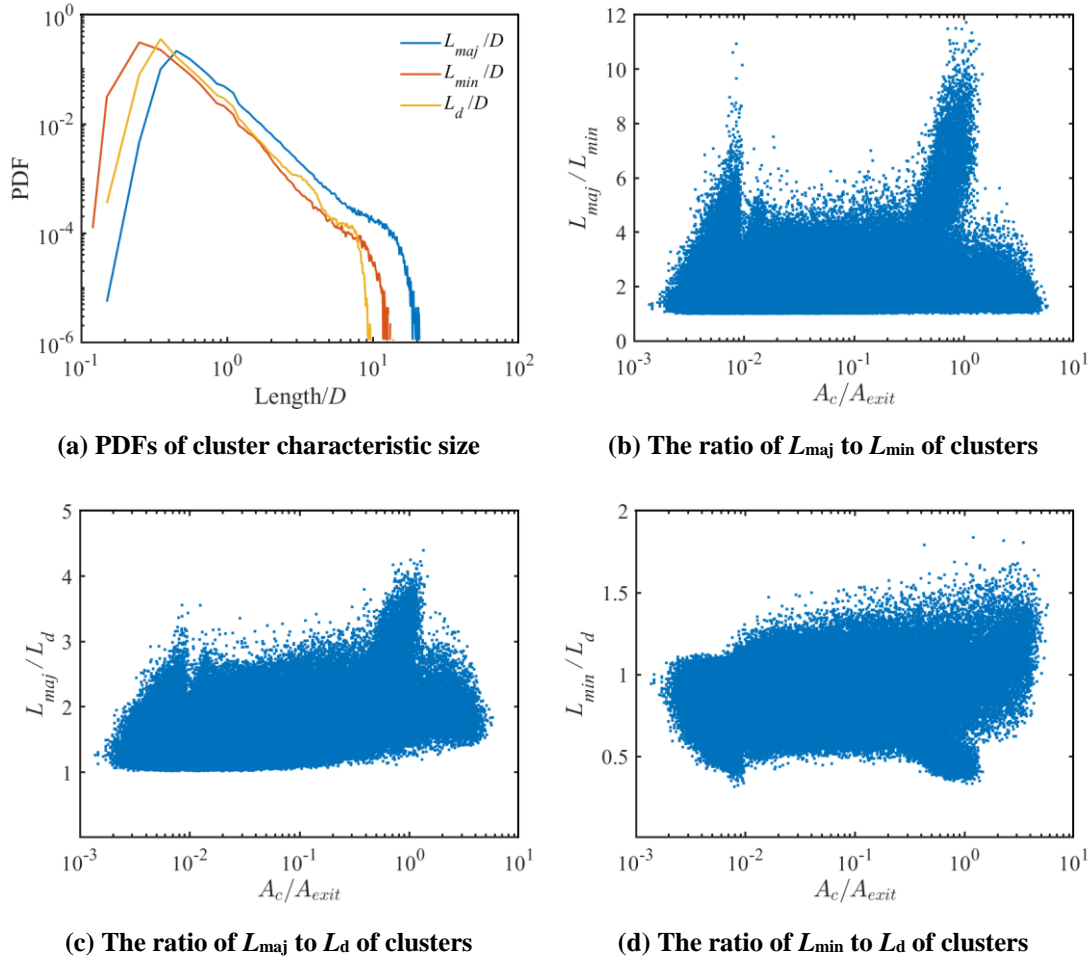


Figure 4.48 The relationship among the characteristic size parameters of clusters

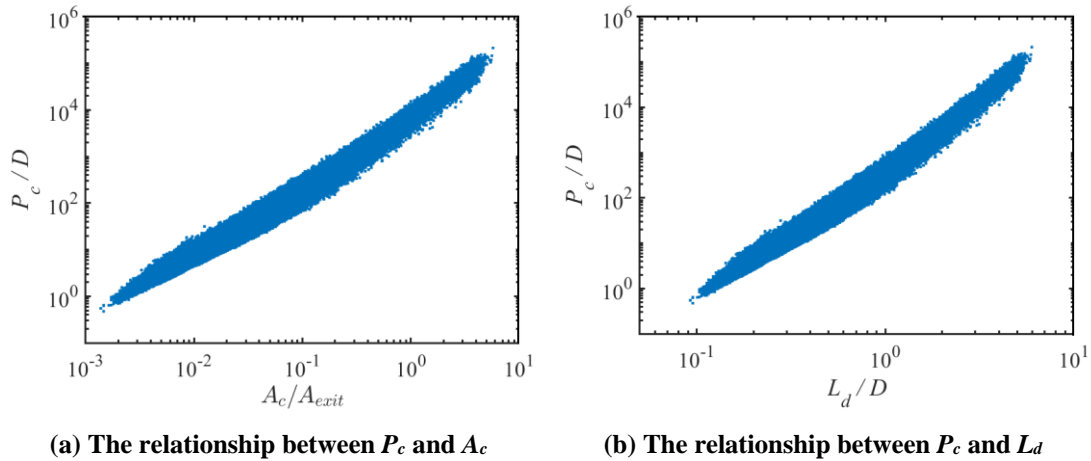


Figure 4.49 Influencing factors of cluster perimeter

The influencing factors of cluster perimeter are shown in Figure 4.49. The perimeter is defined as the sum of the lengths of the sides surrounding the cluster. It can be seen from the figure that the scale of the cluster perimeter is about 0.5 to 105 times the diameter of the nozzle. The cluster perimeter is proportional to the area and equivalent diameter of the cluster.

The shapes of different clusters are shown in Figure 4.50. The influencing factors of the circularity of clusters are shown in Figure 4.51, circularity is defined as

$$\text{Circularity} = \frac{4\pi A_c}{P_c^2} \quad (4-11)$$

where P_c is the perimeter of the cluster. Circularity is inversely proportional to the cluster area, major axis, minor axis, and equivalent diameter. That is to say, clusters with smaller areas are closer to the standard circle, and clusters with larger areas are more irregular in shape. Likewise, the smaller the major axis, minor axis and equivalent diameter, the closer the cluster is to a standard circle, and vice versa, the more irregular the shape of the cluster.



Figure 4.50 Shapes of different clusters

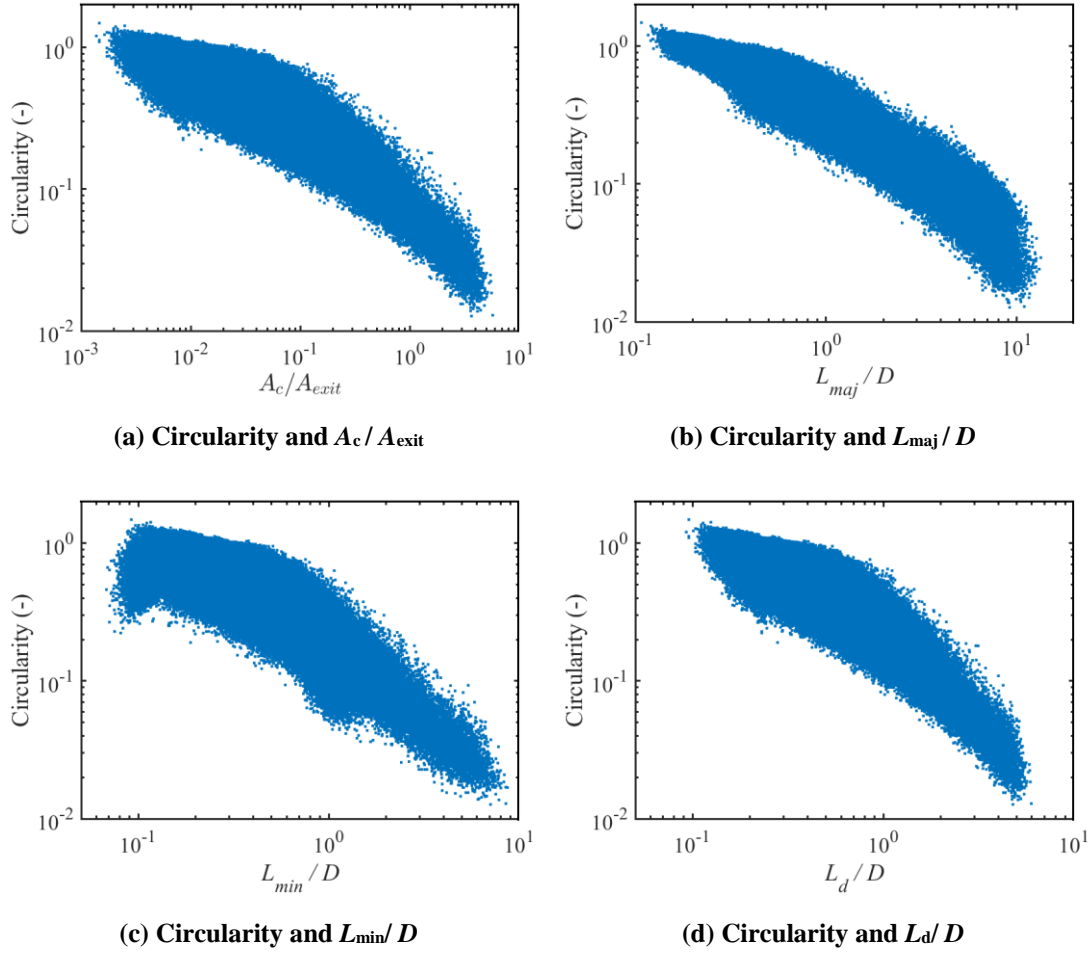


Figure 4.51 Influencing factors of circularity of clusters

4.5.2 Particle Volume Fraction

4.5.2.1 Particle Volume Fraction Evolution

The mean particle volume fraction contour within 1 s is shown in Figure 4.52. Few reports on the full-field volume fraction measurement of a particle-laden jet in such an extensive range. Typically, the research on the particle volume fraction field of particle-laden jets focuses on the local small-scale measurement, and the measurement range limited to tens of millimeters^{61, 63}. The measurement range of this section is an order of magnitude larger than that of the predecessors, particularly the measurement limit along the downstream of the jet is greater than $50 D$. This is highly significant for examining the volume fraction evolution of particle-laden jets directly from the large-scale level

of the entire field. As evident from the figure, in the radial direction, the particle volume fraction exhibits a distribution trend of high center and low edge; whereas in the axial direction, the particle volume fraction near the nozzle is the highest, and first decreases and then increases as it gradually moves away from the nozzle. The results in the literature⁵³ show that in the middle-Stokes-number particle-laden jet, the particle volume fraction is directly attenuated because the experimental measurement range is the near-field region of the jet. This volume fraction evolution rule in this study has not been reported in the literature. A possible explanation for this pattern is that the particles at the nozzle are not dispersed, so the particle volume fraction is high. As the particles move away from the nozzle, the particles begin to spread and the particle volume fraction decreases. Eventually, the particle velocity diminishes, high-velocity particles catch up with low-velocity particles, and particles begin to accumulate, leading to a higher particle volume fraction.

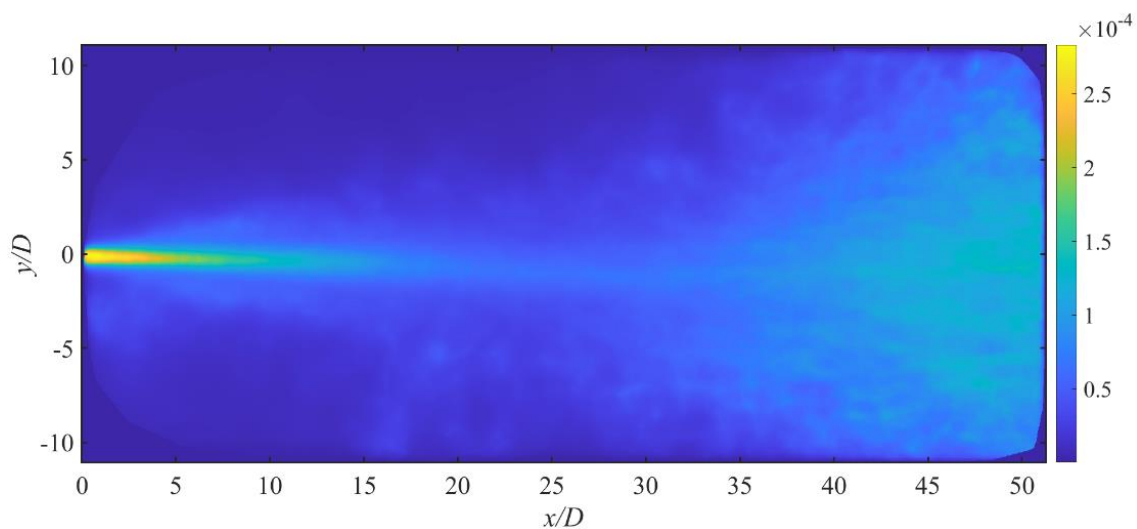


Figure 4.52 Mean particle volume fraction contour within 1 s

Figure 4.53 illustrates the axial and radial evolution curves of particle volume fraction. As depicted in Figure 4.53 (a), as we can see that the particle volume fraction along the center of the jet decreases first, and the particle volume fraction on both sides directly increases. This alteration in particle volume fraction at the centerline is

attributed to the dispersion of near-field high-velocity particles and the accumulation of far-field low-velocity particles, as previously analyzed. The evolution of near-field ($x/D < 20$) particle volume fraction is consistent with the literature results⁵³. The reason for the increase in particle volume fraction on both sides is that the near-field particles have not spread and there are no particles on both sides. As the particles gradually disperse, particles begin to appear on both sides, resulting in a rise in particle volume fraction. From Figure 4.53 (b), as we can see that the near field ($x/D < 20$) results in a high center particle volume fraction due to the lack of dispersion of the particles. As the distance from the nozzle increases, the particles disperse fully, and the particle volume fraction on both sides progressively converges with the particle volume fraction at the center.

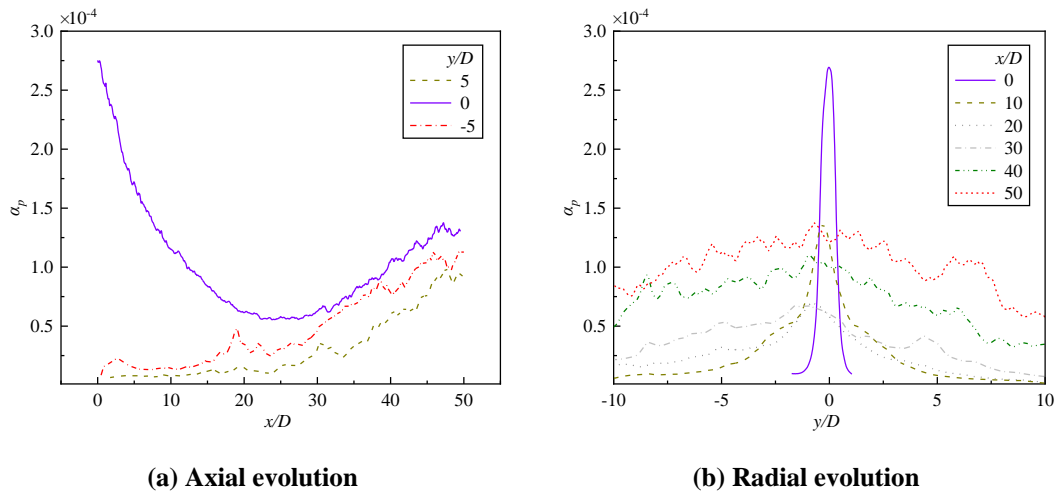


Figure 4.53 Evolution curves of particle volume fraction of Exp.1

The evolution curves of particle volume fraction in different experiments are shown in Figure 4.54. As we can see from the figure that the normalized distribution of particle volume fraction in different experiments is similar, especially the particle volume fraction in the near field, shown in Figure 4.54 (a) and (b). This indicates the self-similarity of particle volume fraction and clustering during particle dispersion⁶³.

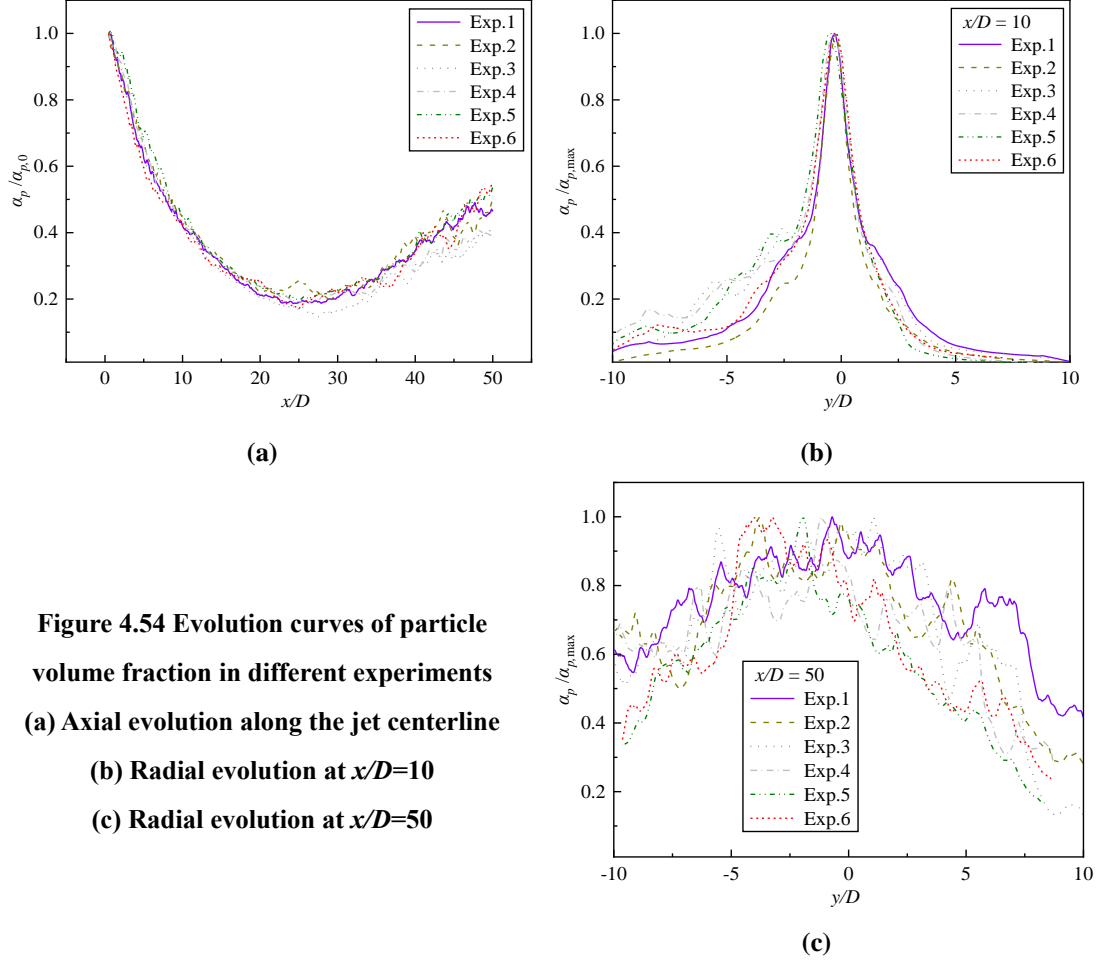


Figure 4.54 Evolution curves of particle volume fraction in different experiments
(a) Axial evolution along the jet centerline
(b) Radial evolution at $x/D=10$
(c) Radial evolution at $x/D=50$

4.5.2.2 Validation of Particle Volume Fraction Model

In Section 3.5.1, we obtain the 3D particle volume fraction model in high-Stokes-number particle-laden jet,

$$\alpha_{p,3D} = \frac{V_p}{\eta C_\theta^3 x^3} \quad (4-12)$$

In this chapter we obtained the 2D particle volume fraction. To facilitate the verification, we calculate the theoretical value of the 2D particle volume fraction by 3D-to-2D conversion. The method usually used is body-centered cubic structure conversion, as follows³²:

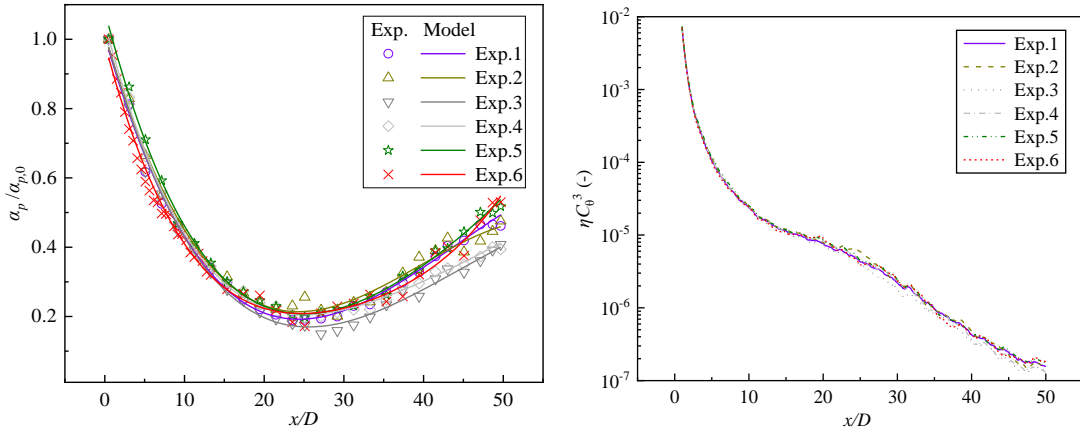
$$\alpha_{p,2D} = \sqrt[3]{\frac{9\pi\alpha_{p,3D}^2}{8\sqrt{3}}} \quad (4-13)$$

Combining Eqs. (4-12) and (4-13), the theoretical value of the 2D particle volume

fraction is obtained as follows,

$$\alpha_{p,2D} = \sqrt[3]{\frac{9\pi V_p^2}{8\sqrt{3}(\eta C_\theta^3 x^3)^2}} \quad (4-14)$$

where $\alpha_{p,2D}$ is the 2D particle volume fraction. For consistency with Section 4.5.2.1, α_p is used instead of $\alpha_{p,2D}$. The validation results of the particle volume fraction model are shown in Figure 4.55. In Section 3.5.1, we find that for large particles, a constant $\eta C_\theta^3 = 2.7 \times 10^{-5}$ fits very well with the experiment as shown in Figure 3.13 (c). However, for the small particles studied in this chapter, the value of ηC_θ^3 is not a constant, but decreases with the increase of x/D . And the axial evolution trend and value of ηC_θ^3 does not change significantly under different gas velocity experiments, which means that they may have similar dynamics. We have known that when the particle relaxation time τ_p and gas time scale τ_g are of the same magnitude, the particles partially respond to fluctuations in the airflow. As a result, the particles cannot follow the airflow completely, and the path of the particles will be changed by the airflow fluctuations²⁴. In contrast, large particles are largely unaffected by the airflow¹². This means that for large particles, the dispersion coefficient C_θ and shape coefficient η remain largely unchanged; and for small particles, the dispersion coefficient C_θ and shape coefficient η will be easily changed by the airflow.



(a) Comparison of experimental and model values

(b) Axial evolution of ηC_θ

Figure 4.55 Particle volume fraction model validation

4.6 Conclusions

In this chapter, we conduct six sets of experiments on two types of low- and middle- Stokes-number particle-laden jets (gas-phase tracer particles and SiO₂ microspheres), each encompassing both macro- and meso-scale measurements. Based on these, we obtain the velocity and fluctuating velocity of the gas phase (DOS tracer particles) and solid small particles (SiO₂ microspheres) for the entire field. Subsequently, we discuss a classical jet velocity decay model and verify its applicability to low- and middle- Stokes-number particle-laden jets with gas phase and SiO₂ microspheres. Additionally, we analyze the velocity self-similarity of the gas-solid phases separately. For the middle-Stokes-number particle-laden jets of SiO₂ microspheres, we examine their mesoscale structure and particle concentration using large-field measurements and the Voronoi method. Employing a novel cluster characterization approach, we analyze the characteristic scale of cluster sets and the evolution of concentrations over a wide range. The experimental data can provide support for future simulations. The major conclusions can be summarized as follows:

- (1) The decay trend of the velocity and fluctuating velocity of the gas phase and small particles initially increases and subsequently decreases, with a minor increase in the velocity trend. The velocity peak of the transient velocity field does not consistently appear on the jet centerline but rather fluctuates.
- (2) The fluctuating velocity distribution of the gas phase and small particles near the nozzle differs significantly from the velocity distribution, likely due to the flow in the "potential core" region being more stable and exhibiting smaller velocity fluctuations. In contrast, the edge and "transition" regions exhibit larger velocity fluctuations resulting from entrainment mixing and high-low velocity transitions.
- (3) The classical model can effectively predict the decay of gas-phase velocity, while

the decay of particle velocity can be predicted by the classical model with a maximum error of 16%.

- (4) Both gas-phase velocity and particle velocity exhibit self-similarity, although the velocity self-similarity of heavy particles decreases more rapidly due to their pronounced inertial effects.
- (5) The particle clustering process during the jet process is dynamically stable, and the preferential concentration effect of particles becomes more significant as the Stokes number approaches unity.
- (6) The major axis serves as the primary feature size of the cluster, with larger clusters exhibiting more irregular shapes. The distribution of small-size clusters adheres to the power-law distribution of penetration theory; however, when the number of particles in the cluster concentration exceeds 50, the distribution of cluster sets significantly surpasses that of the power-law distribution.
- (7) The particle concentration exhibits a distribution trend characterized by a high center and low edge. The particle concentration and cluster set during particle dispersion demonstrate self-similarity.
- (8) We verify the applicability of the particle volume fraction model obtained in Section 3.5.1 to small particles/middle-Stokes-number particle-laden jets, and the results indicate that the value of ηC_θ^3 changes due to airflow turbulence.

Finally, it is important to note that comprehensive work necessitates a fully 3D, ideal tomography PIV system to acquire flow field velocity data and consequently draw definitive conclusions. However, due to experimental constraints and current algorithms, we rely on 2D PIV systems. As such, some of the findings presented here should be regarded as provisional, though some of them do agree with existing literature.

Chapter 5 Simulations of Particle-laden Jets

5.1 Overview

To verify the applicability and accuracy of the drag model to high- and middle-Stokes-number particle-laden jets, CFD-DPM simulations of the two systems are carried out in this section. The effects of different drag correlations on jet velocity are studied, the sensitivity of the drag correlation to Reynolds number is analyzed. In addition, the influences of entrainment, distribution of inlet velocity and outlet boundary conditions on the jet are discussed.

5.2 Mathematical Models

In this chapter, the CFD-DPM method in ANSYS Fluent software is used to simulate particle-laden jets to calculate gas-solid two-phase motion, in which volume-average Navier-Stokes equations are used to describe gas flow and each particle is tracked according to Newton's second law. The mathematical model of CFD-DPM is introduced as follows.

5.2.1 Continuous Phase Models

5.2.1.1 Governing Equations for Gas Phase

The continuity equations and momentum equations for the gas phase are^{186, 243, 244}

$$\frac{\partial}{\partial t}(\alpha_g \rho_g) + \nabla \cdot (\alpha_g \rho_g \vec{u}_g) = 0 \quad (5-1)$$

$$\frac{\partial}{\partial t}(\alpha_g \rho_g \vec{u}_g) + \nabla \cdot (\alpha_g \rho_g \vec{u}_g \vec{u}_g) = -\alpha_g \nabla p + \nabla \cdot \vec{\tau}_g + \alpha_g \rho_g \vec{g} - \vec{F}_D \quad (5-2)$$

where α_g is the gas volume fraction, ρ_g the gas phase density, \vec{u}_g the gas phase

velocity, \vec{g} gravitational acceleration, \vec{F}_D the interphase drag force, and $\bar{\tau}_g$ the gas phase stress, defined as

$$\bar{\tau}_g = \mu_{eff} \left[\nabla \vec{u}_g + (\nabla \vec{u}_g)^T - \frac{2}{3} (\nabla \cdot \vec{u}_g) \vec{I} \right] \quad (5-3)$$

$$\mu_{eff} = \mu_t + \mu_g \quad (5-4)$$

where μ_{eff} , the effective shear viscosity, is the sum of laminar viscosity μ_g and turbulent viscosity μ_t .

5.2.1.2 Turbulence Model

The Realizable k - ε model in ANSYS Fluent is used in this work. And the transport equations are^{186, 245}

$$\begin{aligned} \frac{\partial}{\partial t} (\alpha_g \rho k) + \frac{\partial}{\partial x_j} (\alpha_g \rho k \overline{u_{g,j}}) = \frac{\partial}{\partial x_j} \left[\alpha_g \left(\mu_g + \frac{\mu_t}{\sigma_k} \right) \frac{\partial k}{\partial x_j} \right] + \alpha_g G_k \\ + \alpha_g G_b - \alpha_g \rho \varepsilon - \alpha_g Y_M + S_{kp} \end{aligned} \quad (5-5)$$

$$\begin{aligned} \frac{\partial}{\partial t} (\alpha_g \rho \varepsilon) + \frac{\partial}{\partial x_j} (\alpha_g \rho \varepsilon \overline{u_{g,j}}) = \frac{\partial}{\partial x_j} \left[\alpha_g \left(\mu_g + \frac{\mu_t}{\sigma_\varepsilon} \right) \frac{\partial \varepsilon}{\partial x_j} \right] + \alpha_g C_{1\varepsilon} \frac{\varepsilon}{k} C_{3\varepsilon} G_b \\ + \rho \alpha_g \left(C_{1\varepsilon} S \varepsilon - C_{2\varepsilon} \frac{\varepsilon^2}{k + \sqrt{\nu \varepsilon}} \right) + S_{\varepsilon p} \end{aligned} \quad (5-6)$$

where k is the turbulent kinetic energy, ε the turbulent kinetic energy dissipation rate, G_k the production of turbulent kinetic energy due to the mean velocity gradients, closed by following the Boussinesq hypothesis,

$$G_k = \mu_t S^2 \quad (5-7)$$

where S is the modulus of the mean rate-of-strain tensor, defined as

$$S = \sqrt{2S_{ij}S_{ij}} \quad (5-8)$$

$$S_{ij} = \frac{1}{2} \left(\frac{\partial \overline{u_{g,i}}}{\partial x_j} + \frac{\partial \overline{u_{g,j}}}{\partial x_i} \right) \quad (5-9)$$

G_b is the turbulent kinetic energy due to buoyancy, which needs to be considered when

the gravity field and temperature gradient exist at the same time and can be ignored in this paper. Y_M represents the expansion-induced dissipation in compressible turbulent flow, which is negligible in the incompressible flow studied in this paper. S_{kp} and $S_{\varepsilon p}$ represent the particle-to-gas turbulent source terms for k and ε respectively. They are defined as^{246, 247}

$$S_{kp} = \frac{\alpha_p \rho_p}{\tau_p (C_D)} \left(|\vec{u}_g - \vec{u}_p|^2 - 2k \right) \quad (5-10)$$

$$S_{\varepsilon p} = C_{4\varepsilon} \frac{\varepsilon}{k} S_{kp} \quad (5-11)$$

where τ_p is the particle relaxation time, C_D is the particle drag coefficient, defined in Section 5.3. The values of the empirical parameters in above equations are listed in Table 5.1.

Table 5.1 Values of empirical parameters

| Name | Value | Note |
|----------------------|---|---|
| C_1 | $\max \left[0.43, \frac{S \frac{k}{\varepsilon}}{S \frac{k}{\varepsilon} + 5} \right]$ | |
| C_2 | 1.9 | |
| $C_{1\varepsilon}$ | 1.44 | |
| $C_{3\varepsilon}$ | 0 | Buoyancy perpendicular to gravity |
| $C_{4\varepsilon}$ | 1.8 | |
| σ_k | 1.0 | Turbulent Prandtl constant of k |
| σ_ε | 1.2 | Turbulent Prandtl constant of ε |

μ_t is the turbulent viscosity, defined as

$$\mu_t = \rho C_\mu \frac{k^2}{\varepsilon} \quad (5-12)$$

The difference between the Realizable k - ε model and the Standard k - ε model is that C_μ is a function of the turbulence fields ($C_\mu=0.09$ in Standard k - ε model). Since Launder

and Spalding²⁴⁵ proposed the Standard k - ε model, its robustness, economy, and accuracy make it widely used in the calculation of actual turbulent flow. However, it should be noted that when deriving the Standard k - ε model, it is assumed that the flow is completely turbulent and the influence of molecular viscosity can be ignored. Therefore, the Standard model is only suitable for fully turbulent flows. In addition, a significant weakness of the Standard k - ε model or other traditional models lies in the modeling of the dissipation rate. The well-known circular jet anomaly is believed to be mainly due to modeling problems with the dissipation equation, whose diffusivity is unexpectedly poorly predicted¹⁸⁶. Since the Standard k - ε model is deficient, modifications are introduced to improve it. There are two variants available in ANSYS Fluent: RNG k - ε model²⁴⁸ and Realizable k - ε model²⁴⁹. This chapter adopts the Realizable k - ε model proposed by Shih et al.²⁴⁹ because it has been verified by previous studies^{249, 250} to provide the best performance among all model versions¹⁸⁶. The Realizable k - ε model improves the defects of the traditional model through the following two methods:

- The modified dissipation rate transport equation derives the ε from the exact equation for mean square vorticity fluctuation transport.
- A new eddy-viscosity formula involving a variable C_μ is applied²⁵¹, in which C_μ is defined as²⁵²

$$C_\mu = \frac{1}{A_0 + A_s k U^* / \varepsilon} \quad (5-13)$$

where

$$U^* = \sqrt{S_{ij} S_{ij} + \tilde{\Omega} \tilde{\Omega}} \quad (5-14)$$

$$\tilde{\Omega} = \Omega - 2\varepsilon_{ijk} \omega_k \quad (5-15)$$

$$\Omega = \bar{\Omega} - \varepsilon_{ijk} \omega_k \quad (5-16)$$

where $\bar{\Omega}$ is the mean rate-of-rotation tensor viewed in a moving reference frame with angular velocity ω_k . The model constants A_0 and A_s are given by

$$A_0 = 4.04, A_s = \sqrt{6}\cos\varphi \quad (5-17)$$

where

$$\varphi = \frac{1}{3} \cos^{-1} \left(\sqrt{2S_{ik}S_{jk}} \right) \quad (5-18)$$

5.2.2 Discrete Phase Models

5.2.2.1 Equations of Motion for Particles

ANSYS Fluent predicts the trajectories of discrete-phase particles by following Newton's second law in the Lagrangian frame. The motion equation of a particle can be written as^{186, 253, 254}

$$m \frac{d\bar{u}_p}{dt} = m \frac{\rho_p - \rho_g}{\rho_p} \bar{g} + \bar{F}_D + \bar{F}_o \quad (5-19)$$

where $m = \frac{1}{6} \pi d_p^3 \rho_p$ is the particle mass, \bar{u}_p the particle velocity, ρ_p the particle density, \bar{F}_o the other force.

5.2.2.2 Particle Force Models

(1) Drag Force

The drag force is the most important part of the particle force, which can be calculated by²⁵⁵

$$\bar{F}_D = m \frac{3\rho_g C_D}{4\rho_p d_p} |\bar{u}_g - \bar{u}_p| (\bar{u}_g - \bar{u}_p) \quad (5-20)$$

where C_D is the drag coefficient. This equation can be simplified to²²¹

$$\bar{F}_D = m \frac{1}{\tau_p} (\bar{u}_g - \bar{u}_p) \quad (5-21)$$

where τ_p is the particle relaxation time calculated by

$$\tau_p = \frac{\rho_p d_p^2}{18\mu_g C_D Re_p} \frac{24}{24} \quad (5-22)$$

$$Re_p = \frac{\rho_g d_p |\vec{u}_g - \vec{u}_p|}{\mu_g} \quad (5-23)$$

The drag force represents the momentum exchange between the gas phase and the particles per unit volume of cells, and the accuracy of the drag model used in the calculation has a significant impact on the simulation results. A lot of experiments and theoretical analyses have been performed on the drag model of gas-particle two-phase system. These researches include three aspects: the drag model of a single particle, drag model for homogeneous multi-particle system, and drag model for heterogeneous multi-particle system. A detailed information to the drag model is referred to Chapter 1.5, and not repeated here.

(2) Other Forces

In addition to the drag force, the particles will also experience some other forces depending on flow condition, including lift force, Magnus lift force, Saffman lift force, Basset force, pressure gradient force, virtual mass force, and so on.

● Lift Force

Lift force is defined as ²⁵⁶

$$\vec{F}_L = \frac{1}{2} \pi r_p^2 \rho_g C_L (\vec{u}_g - \vec{u}_p)^2 \quad (5-24)$$

where r_p is the particle radius, and for spherical particles C_L is equal to 0.

● Magnus Lift Force

When the particle rotates in the gas-solid two-phase flow, there is an additional force perpendicular to the direction of motion of the particles. It is called the Magnus lift force¹⁶⁸, and defined as

$$\vec{F}_M = \frac{1}{2} \rho_g A_p C_{RL} \frac{|\vec{V}|}{|\vec{\Omega}|} (\vec{V} \times \vec{\Omega}) \quad (5-25)$$

where A_p is the projected area of the particle, C_{RL} the rotational lift coefficient due

to rotation, \vec{V} the relative gas-particle velocity, $\vec{\Omega}$ the relative gas-solid angular velocity.

- Saffman Lift Force

The velocity gradient in the flow field will cause an additional lift force of particle due to the shear effect. It is called the Saffman lift force²⁵⁷, and defined as

$$\vec{F}_S = 6.46r_p^2 \sqrt{\rho_g \mu_g} (\vec{u}_g - \vec{u}_p) \sqrt{\frac{d\vec{u}_g}{dy}} \quad (5-26)$$

Generally, the effect of Saffman lift force is more obvious only when the particle size is smaller than the thickness of the fluid boundary layer and close to the pipe wall.

- Basset Force

When the particle is accelerated relative to the fluid, the fluid will exert an additional resistance on the particle. It is the Basset force¹⁶⁸, and defined as

$$\vec{F}_B = 6r_p^2 \sqrt{\pi \rho_g \mu_g} \int_{t_0}^t (t - t_\tau)^{0.5} \frac{d(\vec{u}_g - \vec{u}_p)}{dt_\tau} dt_\tau \quad (5-27)$$

where t_τ is a time variable, representing the integration of the motion process of the particle from t_0 to time t .

- Virtual Mass Force

In the gas-particle two-phase flow, when the particle accelerates relative to the gas, it will accelerate the gas phase at the same time. Therefore, the gas will also exert a reaction force on the particle. Since this force is measured by a "virtual mass" equivalent to half of the gas mass with a particle volume, it is called virtual mass force¹⁶⁸, and defined as

$$\vec{F}_{vm} = \frac{1}{2} \left(\frac{4}{3} \pi r_p^3 \right) \rho_g \frac{d(\vec{u}_g - \vec{u}_p)}{dt} \quad (5-28)$$

There are still a lot of forces. When the particle size is below 1 μm , it is necessary to further consider the influence of Brownian force. Particles may also be affected by field forces, just like the electromagnetic force. When the ambient temperature changes

significantly, it is also necessary to consider the thermophoretic force caused by the temperature field, etc.

In the particle-laden jet studied here, the particle density is significantly greater than the gas density that the virtual mass force and lift force become insignificant relative to the drag force. It is also not necessary to consider physical fields other than the gravitational field in the current study. Therefore, in the calculation, only the drag force is considered for the interphase force, and only the gravity is considered for the field force. In addition, due to the small particle volume fraction (<1%), this paper does not consider the collision force between particles.

5.2.2.3 Turbulent Dispersion of Particles

When the gas turbulence is strong, the effect of turbulence on particle motion needs to be considered. To this end, the discrete random walk model (DRW) is generally used to describe the turbulent dispersion of particle^{258, 259}. The model assumes that particles are affected by a series of turbulent eddies during their motion, and each turbulent vortex has a certain characteristic scale L_e and characteristic time τ_l . Initially, the particle with velocity \vec{u}_p is assumed to be located at the center of a turbulent vortex. In this turbulent vortex, the gas velocity \vec{u}_g can be decomposed into the mean velocity \vec{u}_g and fluctuating velocity \vec{u}'_g ,

$$\vec{u}_g = \vec{u}_g + \vec{u}'_g \quad (5-29)$$

where the fluctuating velocity \vec{u}'_g satisfies the Gaussian distribution, as follows:

$$\begin{cases} u'_{gx} = \xi_1 \sqrt{u'^2_{gx}} \\ u'_{gy} = \xi_1 \sqrt{u'^2_{gy}} \\ u'_{gz} = \xi_1 \sqrt{u'^2_{gz}} \end{cases} \quad (5-30)$$

where $\sqrt{u'^2_{gx}}, \sqrt{u'^2_{gy}}, \sqrt{u'^2_{gz}}$ are the root mean square fluctuating velocity, ξ_1 is a

Gaussian random variable with mean value of 0 and variance of 1. Since isotropic turbulence assumption is adopted in the k - ε gas turbulence model, the root mean square fluctuating velocity can be calculated by

$$\sqrt{u_{gx}^2} = \sqrt{u_{gy}^2} = \sqrt{u_{gz}^2} = \sqrt{\frac{2}{3}}k \quad (5-31)$$

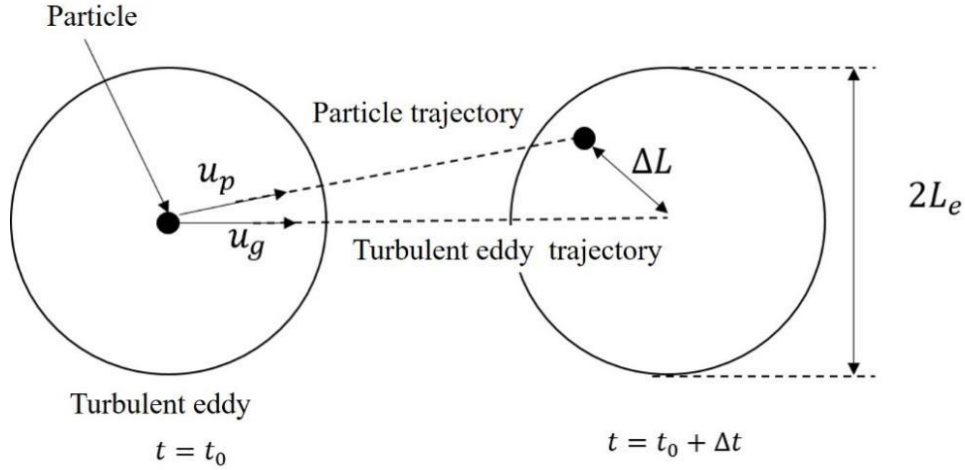


Figure 5.1 Schematic of particle and eddy interaction ²⁵⁸

The interaction between a particle and turbulent vortex is shown in Figure 5.1. After a time step of Δt , due to the relative velocity between the particle and the turbulent vortex, the relative displacement between the two is ΔL . If the current turbulent vortex dissipates ($\Delta t > \tau_l$) or the particle leaves the current turbulent vortex ($\Delta L > L_e$), the particle is no longer subject to the current turbulent vortex. It will enter a new turbulent vortex, and continue to interact with the new turbulent vortex. The interaction time τ_{int} of particles with the turbulent flow is

$$\tau_{int} = \min(\tau_e, \tau_{cross}) \quad (5-32)$$

where τ_{cross} is the time taken to cross the current turbulent vortex, τ_e is the existence time of the turbulent vortex. They are defined as³⁰

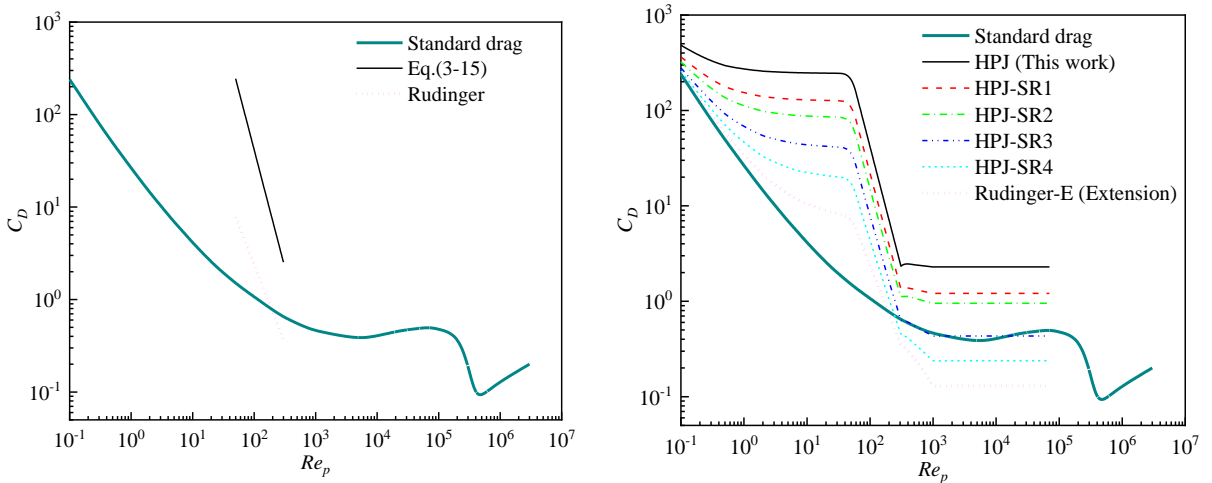
$$\tau_e = 0.3 \frac{k}{\varepsilon} \quad (5-33)$$

$$\tau_{cross} = -\tau_p \ln \left[1 - \frac{kL_e}{(\tau_p |\vec{u}_g - \vec{u}_p|)} \right] \quad (5-34)$$

$$L_e = C_{4\varepsilon} \frac{C_\mu^{3/4} k^{3/2}}{\varepsilon} \quad (5-35)$$

5.3 Drag Models for Simulations

As mentioned in Chapter 3, according to the previous reports^{87, 224, 225}, there is a large gap between the drag coefficient of the particle group and the standard drag force due to the turbulence effects, especially in the case of large particles. Thus, we have deduced a new drag correlation based on our two-phase jet experiments. In light of the uncertainty of the turbulence effect induced by different-sized particles, the new drag correlation derived from large particle experiment may not be applicable to the cases of small particles in this section. Thus, this section constructs 6 new drag models based on the results in Chapter 3 by combining the standard drag model and the Rudinger drag model, among them HPJ means horizontal particle-laden jet, HPJ-SR means the combination of HPJ drag, standard drag and Rudinger drag. The drag curves and equations are shown in Figure 5.2 and Table 5.2, respectively.



(a) Comparison of Eq. (3-15) drag correlation with the drag models in the literature

(b) Newly formed drag correlations in the large Reynolds number range

Figure 5.2 Drag curves for simulations

Table 5.2 Drag models for simulations

| Name | Correlation | Range |
|---------|--|--------|
| HPJ | $C_D = \begin{cases} \frac{24}{Re_p} + 242.68 & Re_p \leq 0.1 \\ \frac{24}{Re_p}(1 + 0.15Re_p^{0.687}) + 242.68 & 0.1 < Re_p \leq 50 \\ \frac{5.25 \times 10^6}{Re_p^{2.55}} & 50 < Re_p \leq 300 \\ \frac{24}{Re_p}(1 + 0.15Re_p^{0.687}) + 1.85 & 300 < Re_p \leq 1000 \\ 2.29 & Re_p > 1000 \end{cases}$ | (5-36) |
| HPJ-SR1 | $C_D = \begin{cases} \frac{24}{Re_p} + 124.45 & Re_p \leq 0.1 \\ \frac{24}{Re_p}(1 + 0.15Re_p^{0.687}) + 124.45 & 0.1 < Re_p \leq 50 \\ \left(\frac{6000}{Re_p^{1.7}} + \frac{5.25 \times 10^6}{Re_p^{2.55}} \right) / 2 & 50 < Re_p \leq 300 \\ \frac{24}{Re_p}(1 + 0.15Re_p^{0.687}) + 0.77 & 300 < Re_p \leq 1000 \\ 1.21 & Re_p > 1000 \end{cases}$ | (5-37) |
| HPJ-SR2 | $C_D = \begin{cases} \frac{24}{Re_p} + 82.97 & Re_p \leq 0.1 \\ \frac{24}{Re_p}(1 + 0.15Re_p^{0.687}) + 82.97 & 0.1 < Re_p \leq 50 \\ \frac{6000}{Re_p^{1.7}} + \frac{5.25 \times 10^6}{Re_p^{2.55}} + \frac{24(1 + 0.15Re_p^{0.687})}{Re_p} & 50 < Re_p \leq 300 \\ \frac{\text{above}}{3} & 300 < Re_p \leq 1000 \\ \frac{24}{Re_p}(1 + 0.15Re_p^{0.687}) + 0.51 & Re_p > 1000 \\ 0.953 & \end{cases}$ | (5-38) |
| HPJ-SR3 | $C_D = \begin{cases} \frac{24}{Re_p} + 39.32 & Re_p \leq 0.1 \\ \frac{24}{Re_p}(1 + 0.15Re_p^{0.687}) + 39.32 & 0.1 < Re_p \leq 50 \\ 0.14 \times \frac{5.25 \times 10^6}{Re_p^{2.55}} + 0.86 \times \frac{6000}{Re_p^{1.7}} & 50 < Re_p \leq 300 \\ \frac{24}{Re_p}(1 + 0.15Re_p^{0.687}) & 300 < Re_p \leq 1000 \\ 0.44 & Re_p > 1000 \end{cases}$ | (5-39) |

Continued

| Name | Correlation | Range |
|------------|--|------------------------|
| HPJ-SR4 | $C_D = \begin{cases} \frac{24}{Re_p} + 18.04 & Re_p \leq 0.1 \\ \frac{24}{Re_p} (1 + 0.15Re_p^{0.687}) + 18.04 & 0.1 < Re_p \leq 50 \\ 0.05 \times \frac{5.25 \times 10^6}{Re_p^{2.55}} + 0.95 \times \frac{6000}{Re_p^{1.7}} & 50 < Re_p \leq 300 \\ \frac{24}{Re_p} (1 + 0.15Re_p^{0.687}) - 0.2 & 300 < Re_p \leq 1000 \\ 0.24 & Re_p > 1000 \end{cases}$ | $Re_p \leq 0.1$ |
| | | $0.1 < Re_p \leq 50$ |
| | | $50 < Re_p \leq 300$ |
| | | $300 < Re_p \leq 1000$ |
| | | $Re_p > 1000$ |
| Rudinger-E | $C_D = \begin{cases} \frac{24}{Re_p} + 6.22 & Re_p \leq 0.1 \\ \frac{24}{Re_p} (1 + 0.15Re_p^{0.687}) + 6.22 & 0.1 < Re_p \leq 50 \\ \frac{6000}{Re_p^{1.7}} & 50 < Re_p \leq 300 \\ \frac{24}{Re_p} (1 + 0.15Re_p^{0.687}) - 0.31 & 300 < Re_p \leq 1000 \\ 0.13 & Re_p > 1000 \end{cases}$ | $Re_p \leq 0.1$ |
| | | $0.1 < Re_p \leq 50$ |
| | | $50 < Re_p \leq 300$ |
| | | $300 < Re_p \leq 1000$ |
| | | $Re_p > 1000$ |

Figure 5.2 clearly shows the difference between the new drag model and the standard drag. And from the HPJ model to Rudinger-E model, the drag coefficient gradually decreases. Among them, the HPJ model is a result of combination of the drag model obtained in Chapter 3 when $50 < Re_p \leq 300$ (see Eq.(3-15)), and the translation of the standard drag curve when $Re_p < 50$ and $Re_p > 300$ to connect it with Eq.(3-15). Similarly, the Rudinger-E model is also obtained using this method, while the standard drag curve is replaced by the Rudinger model. Furthermore, the HPJ-SR1 model is the average of the HPJ model and the standard drag model, the HPJ-SR2 model is the average of the HPJ model, the Rudinger-E model and the standard drag model, the HPJ-SR3 and HPJ-SR4 models are the weighted average of the HPJ model and the Rudinger-E model, and the weight coefficients can be found easily from the third sub-equation.

In this section, we also expand the range of Reynolds number in Eq.(3-15), and then extend the single particle drag curve to complement the rest of Reynolds number regions to obtain five different extrapolated drag models for Eq. (3-15) under different Reynolds number ranges. Based on these extrapolated drag models, we will verify the applicability of Eq. (3-15), also HPJ, in a larger Reynolds number range by simulations. The extrapolated drag curves and equations are shown in Figure 5.3 and Table 5.3, respectively.

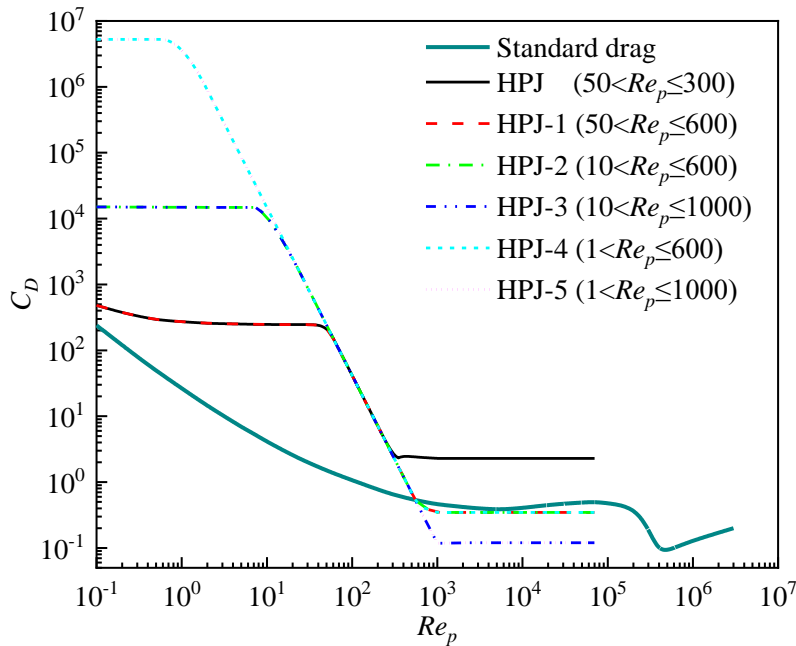


Figure 5.3 Extension curves of HPJ drag model in different Reynolds number ranges

Table 5.3 The extrapolated drag models of HPJ for different Re range

| Name | Correlation | Range |
|-------|---|------------------------|
| HPJ-1 | $C_D = \begin{cases} \frac{24}{Re_p} + 242.68 & Re_p \leq 0.1 \\ \frac{24}{Re_p} (1 + 0.15Re_p^{0.687}) + 242.68 & 0.1 < Re_p \leq 50 \\ \frac{5.25 \times 10^6}{Re_p^{2.55}} & 50 < Re_p \leq 600 \\ \frac{24}{Re_p} (1 + 0.15Re_p^{0.687}) - 0.094 & 600 < Re_p \leq 1000 \\ 0.346 & Re_p > 1000 \end{cases}$ | $Re_p \leq 0.1$ |
| | | $0.1 < Re_p \leq 50$ |
| | | $50 < Re_p \leq 600$ |
| | | $600 < Re_p \leq 1000$ |
| | | $Re_p > 1000$ |

Continued

| Name | Correlation | Range |
|-------|---|--------|
| HPJ-2 | $C_D = \begin{cases} \frac{24}{Re_p} + 14792 & Re_p \leq 0.1 \\ \frac{24}{Re_p}(1 + 0.15Re_p^{0.687}) + 14792 & 0.1 < Re_p \leq 10 \\ \frac{5.25 \times 10^6}{Re_p^{2.55}} & 10 < Re_p \leq 600 \\ \frac{24}{Re_p}(1 + 0.15Re_p^{0.687}) - 0.094 & 600 < Re_p \leq 1000 \\ 0.346 & Re_p > 1000 \end{cases}$ | (5-43) |
| HPJ-3 | $C_D = \begin{cases} \frac{24}{Re_p} + 14792 & Re_p \leq 0.1 \\ \frac{24}{Re_p}(1 + 0.15Re_p^{0.687}) + 14792 & 0.1 < Re_p \leq 10 \\ \frac{5.25 \times 10^6}{Re_p^{2.55}} & 10 < Re_p \leq 1000 \\ 0.12 & Re_p > 1000 \end{cases}$ | (5-44) |
| HPJ-4 | $C_D = \begin{cases} \frac{24}{Re_p} + 5249972 & Re_p \leq 0.1 \\ \frac{24}{Re_p}(1 + 0.15Re_p^{0.687}) + 5249972 & 0.1 < Re_p \leq 1 \\ \frac{5.25 \times 10^6}{Re_p^{2.55}} & 1 < Re_p \leq 600 \\ \frac{24}{Re_p}(1 + 0.15Re_p^{0.687}) - 0.094 & 600 < Re_p \leq 1000 \\ 0.346 & Re_p > 1000 \end{cases}$ | (5-45) |
| HPJ-5 | $C_D = \begin{cases} \frac{24}{Re_p} + 5249972 & Re_p \leq 0.1 \\ \frac{24}{Re_p}(1 + 0.15Re_p^{0.687}) + 5249972 & 0.1 < Re_p \leq 1 \\ \frac{5.25 \times 10^6}{Re_p^{2.55}} & 1 < Re_p \leq 1000 \\ 0.12 & Re_p > 1000 \end{cases}$ | (5-46) |

5.4 Simulation Settings

5.4.1 Material Properties

5.4.1.1 Gas Phase Parameters

(1) Density

In actual work, the density of gas changes with temperature and pressure, and the relationship can be expressed by the ideal gas law,

$$\rho_g = \frac{pM}{RT} \quad (5-47)$$

where ρ_g is the gas density, p is the pressure, M is the molar mass of the gas, R is the gas constant, 8.31441 J/(mol K), and T is the gas absolute temperature.

(2) Viscosity-Pressure Effect

Figure 5.4 shows that when the air pressure changes in the range of 0 ~ 5MPa, the air viscosity increases with temperature, and the curves almost overlap. Therefore, within the pressure range studied in this paper (about 0 ~ 0.05MPa), the effect of pressure on air viscosity can be ignored.

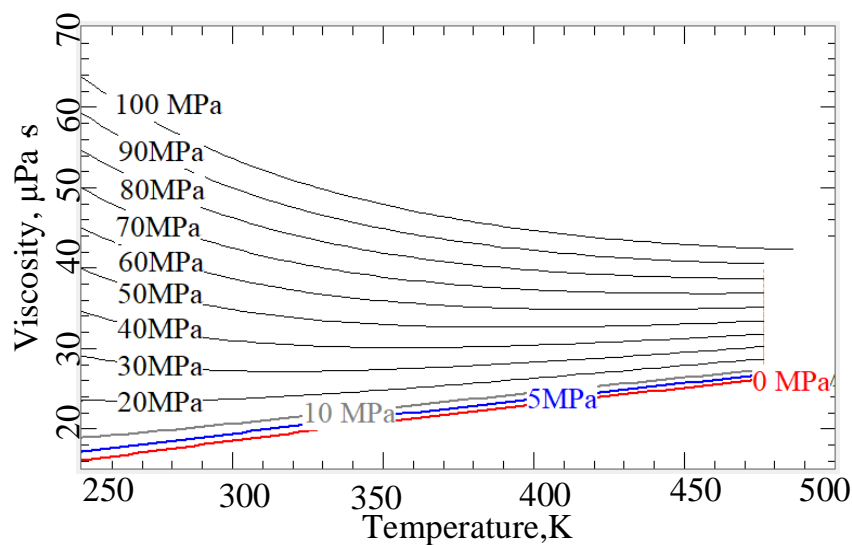


Figure 5.4 Viscosity-temperature curves under different pressures

(3) Viscosity-Temperature Effect

The commonly used gas viscosity-temperature relationship is Sutherland's law²⁶⁰, defined as

$$\mu_g = \mu_0 \left(\frac{T}{T_0} \right)^{3/2} \frac{T_0 + C}{T + C}, T < 2000 \text{ K} \quad (5-48)$$

where T_0 is the reference temperature, μ_0 is the viscosity at the reference temperature, C is the Sutherland constant, and for air, $C=110.4$. In this study, the temperature of the flow field is almost constant, and the viscosity-temperature effect can be ignored.

5.4.1.2 Particle Parameters

The particles used in high- and middle- Stokes-number particle-laden jets simulations are glass beads and SiO₂ microspheres, respectively, and their parameters are shown in Table 5.4.

Table 5.4 Physical properties of particles

| Parameters | Large particles | Small particles |
|----------------------------|-----------------|------------------|
| Material | Glass beads | SiO ₂ |
| Density, kg/m ³ | 2490 | 2000 |
| Diameter, μm | 1051.6 | 40.86 |
| Mass flow rate, g/s | 2.162 | 0.01042 |

5.4.2 Geometric Models

The geometric model of the fluid domain in the actual experiment includes the ejector part, the mixing pipe part, and the dispersion field. The establishment of the geometric model is completed in Solidworks software, and the completed geometric model is imported into ANSYS Workbench Geometry for adjustment. The geometric model of the fluid domain is shown in Figure 5.5. This chapter focuses on the effects

of different drag models on the velocity of particle-laden jet. Thus, to exclude the influences of the wall effects of the ejector part and the mixing pipe part on the particle velocity, the following research will only be carried out in the dispersion field, or, the chamber. Therefore, the fluid inlet is set at the circular intersection of the “Dispersion Field” and the “Mixing pipe”. For the simulation of high-Stokes-number with large particles, the size of the simulation domain is $220 \times 165 \times 165 \text{ mm}^3$, and for the simulation of middle-Stokes-number with small particles, the size of the simulation domain is $600 \times 100 \times 300 \text{ mm}^3$.

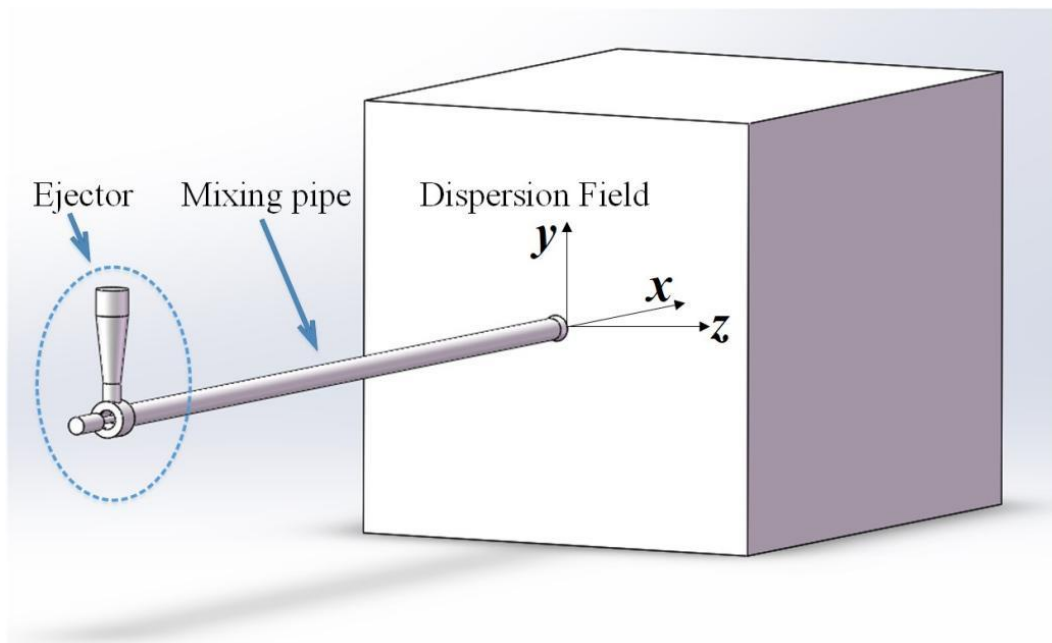


Figure 5.5 Fluid domain geometry

5.4.3 Meshing

A non-uniform mesh is generated in ANSYS Workbench Meshing. The mesh size is gradually increased from the center of the jet to the boundary, so that the mesh presents a dense center and sparse edge. And the mesh is locally refined at the transition between the mixing pipe and the dispersion field. The completed mesh is shown in Figure 5.6.

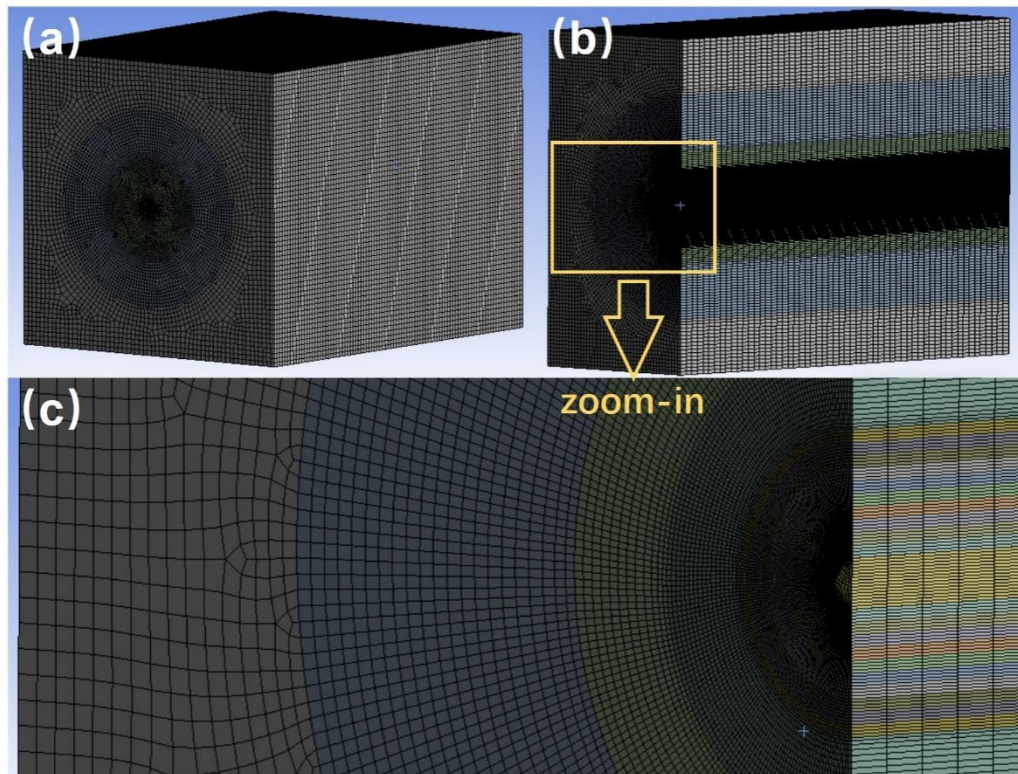


Figure 5.6 Meshing results: (a) overall view; (b) section view; (c) zoom-in view.

5.4.4 Fluent Operations

ANSYS Fluent is used as the solver. In this chapter, the inlet velocity distribution and drag correlation are defined through the User-Defined Function (UDF) in the Fluent software.

(1) General settings

Go to the **General** page to check the quality of the mesh. Then activate gravity and set the direction and value of the acceleration of gravity to the **Y** direction, and -9.81m/s^2 respectively.

(2) Model settings

Select the **Eulerian model** in the **Multiphase model**. The number of phases is set to two phases, calculated based on the volume fraction parameter, and **DDPM** is activated in **Eulerian parameters**. The **Viscous model** is set to the **Realizable $k-\varepsilon$ turbulence model**, and the **Turbulence multiphase model** is set to **Dispersed**. Activate

the *Discrete phase model*, create a new *Injection*, select glass beads/SiO₂ for *Material*, and select the cone injector to simulate jet flow. Set the injector parameters according to the experimental conditions in the Point properties page. Different *Drag Laws* can be selected in the *Physical model*, and the *Drag Laws* defined by UDF can also be selected here. Activate the *DRW model* at *Turbulent Dispersion*. Select phase-2 in the *Discrete phase domain*.

(3) Materials settings

Enter the *Materials* page, select air as the *Fluid material*, set *Density* to *Incompressible ideal gas*, and set *Viscosity* to a constant ($1.7894 \times 10^{-5} \text{ N}\cdot\text{s}/\text{m}^2$) here. In the *Inert particle* part, create new glass beads and SiO₂, and set the material properties according to Table 5.4.

(4) Boundary conditions settings

The *Inlet boundary* type is set to velocity-inlet, and a specified jet velocity distribution is implemented by UDF. The *Outlet boundary* type is set to *Outflow*, and the the *Pressure-out* boundary is also compared. The influence of different outlet boundaries on the simulation results will be discussed later.

(5) Solver Settings

Select the *Couple* algorithm in *Solution Method* and activate *Couple with volume fractions*.

(6) Monitors Settings

By setting the *Surface Report-Mass Flow Rate* to monitor the mass flow of the inlet and outlet, and select *Report Plot* to display the real-time change curve of the monitored parameters.

(7) Initialization Settings

Select *Standard Initialization*, initialized as a stationary flow field without

particles, and compute from all-zones.

(8) Convergence judgment

Convergence is judged by residual curve and mass conservation.

(9) Post-processing

The gas phase velocity data can be exported through CFD-Post software, and the particle data can be exported through *Particle Tracks*. An example of the simulation results is shown in Figure 5.7.

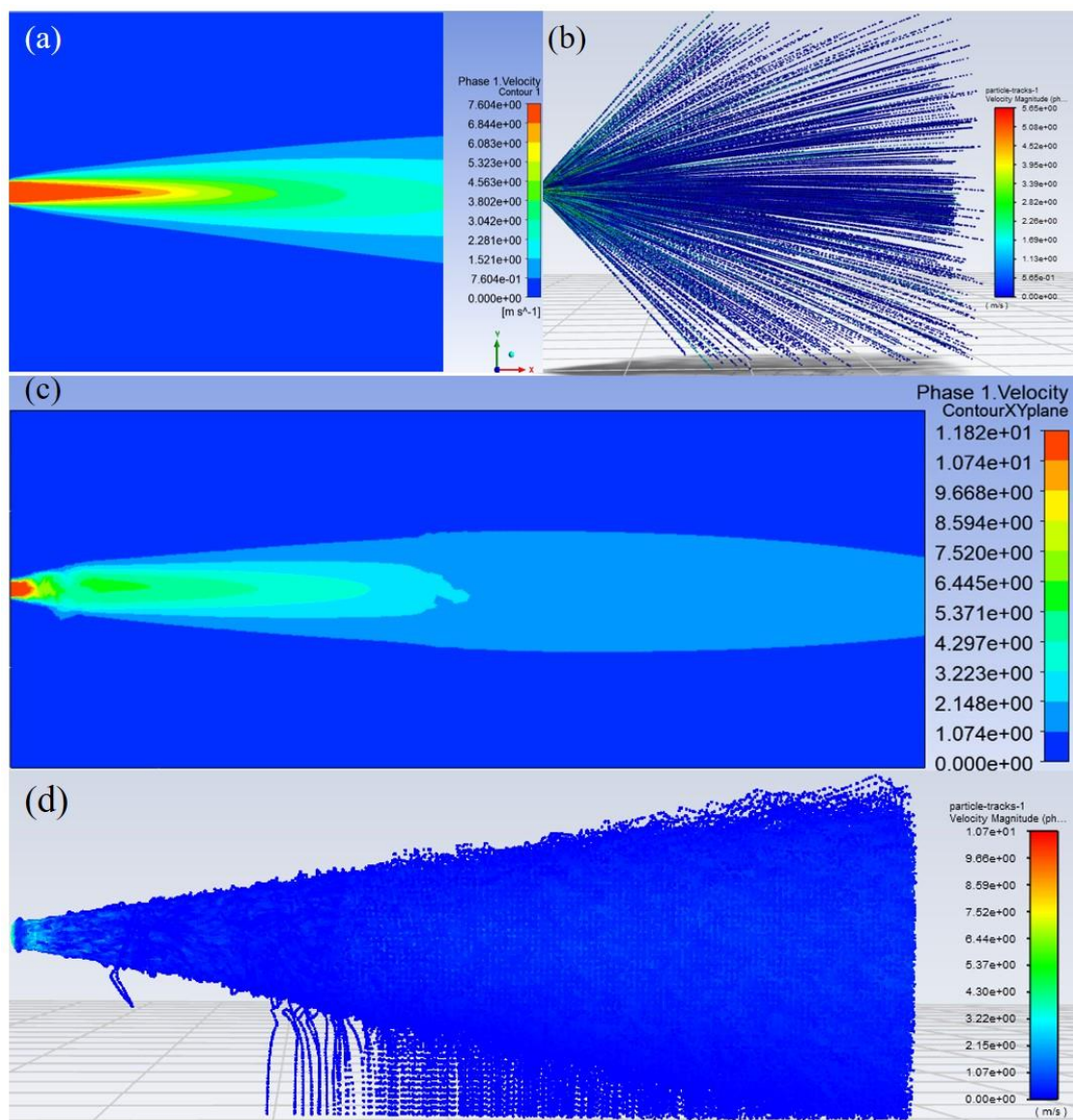


Figure 5.7 Some examples from the simulation results: Gas velocity fields (a, c) and particle velocity fields (b, d) of high- and middle- Stokes number particle-laden jet, respectively.

5.4.5 Mesh-independence Verification

The mesh-independence verification results are shown in Figure 5.8, and the mesh parameters are shown in Table 5.5. The figure shows that the axial distributions of gas and particle velocities do not change apparently with grid resolutions. Finally, to balance the computing resources and computing accuracy, Mesh #2 is used in the subsequent simulations in this chapter.

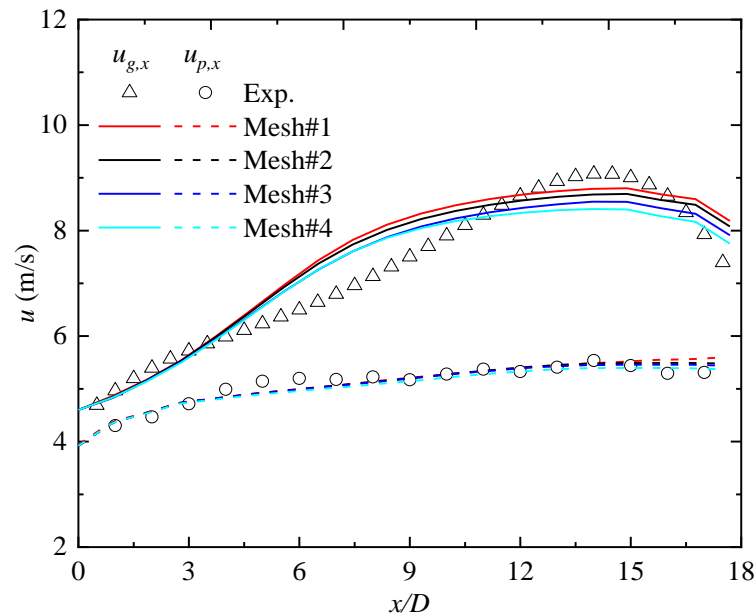


Figure 5.8 Mesh-independence verification results

Table 5.5 Mesh parameters

| Mesh number | #1 | #2 | #3 | #4 |
|--------------------|---------|---------|---------|--------|
| Nodes | 1784874 | 1350097 | 1075501 | 915320 |
| Elements | 1748054 | 1316716 | 1044292 | 885378 |
| Minimum length, mm | 1 | 1 | 1 | 1 |
| Maximum length, mm | 3 | 4 | 5 | 6 |

5.4.6 Case Outline

In this chapter, 33 simulation cases are carried out for the high-Stokes-number

particle-laden jet with large particles, to investigate the effects of 4 important factors on jet simulations, including the drag model, entrainment coefficient, inlet velocity distributions, and outlet type. 15 simulation cases are carried out for the middle-Stokes-number particle-laden jet with small particles. The effects of different drag models on simulation are investigated, and the optimum drag model has been used and verified in simulations of different experimental conditions. The detailed case settings are referred to Appendix G.

5.5 Simulation Results of High-Stokes-number Particle-laden Jets

5.5.1 Effects of Drag Models

5.5.1.1 Effects of Drag Models on Jet Velocity

The effects of different drag models on centerline velocity of high-Stokes-number particle-laden jet are shown in Figure 5.9. It can be seen that the trend of gas velocity, particle velocity and slip velocity predicted by all the drag models are consistent with the experimental data. The drag model has a great influence on particle velocity, while the gas velocity is not sensitive to the choice of drag model. Among all the tested models, the simulation results of particle velocity based on the HPJ model are in best agreement with the experimental data. This is consistent with the conclusion obtained by MATLAB verification in Section 3.5.2, indicating that the experimental drag model (HPJ) is suitable for simulations of jet with large particles. The predicted particle velocity with other drag models are all smaller than the experimental data. Specifically, the smaller the drag coefficient is, the greater the underestimation of particle velocity and the overestimation of slip velocity are.

The simulation result of the single-particle drag model Morsi²⁶¹ (Fluent's built-in

drag model) is close to the simulation results of the Wen-Yu¹⁷¹/Gidaspow²⁶² particle group drag models. And the predicted particle velocity and slip velocity are also smaller than the experimental, which indicates that both single-particle drag model and Wen-Yu/Gidaspow will underestimate the particle velocity. It should also be mentioned that, in previous simulations^{25, 30, 263}, obvious errors have been observed in simulations of dilute two-phase flows with single-particle drag model and Wen-Yu drag model.

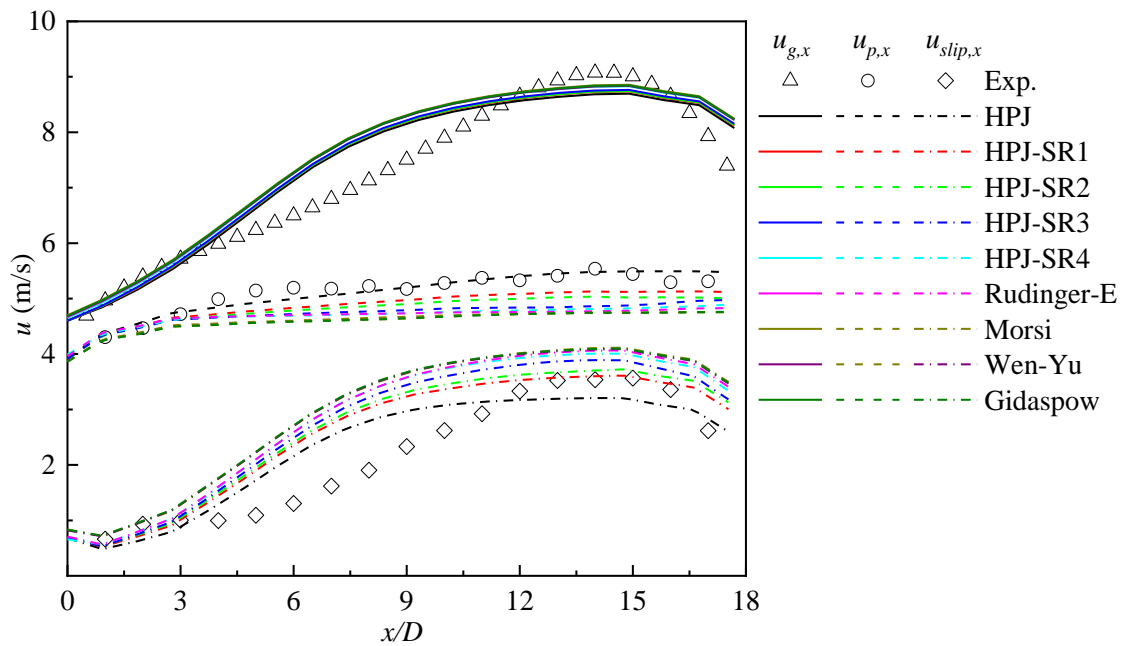


Figure 5.9 Effects of different drag models on centerline velocity of high-Stokes-number particle-laden jet

5.5.1.2 Applicability on HPJ Drag Model in Different Re Range

Figure 5.10 shows the centerline velocity of high-Stokes-number particle-laden jet predicted with the extrapolated drag models of HPJ with different Reynolds number ranges. Obviously, when the range of Reynolds number in Eq. (3-15) is expanded, the simulation results are not as good as the results predicted based on the HPJ model (namely, the original Reynolds number range), no matter the upper limit of the Reynolds number is increased or the lower limit of the Reynolds number is reduced.

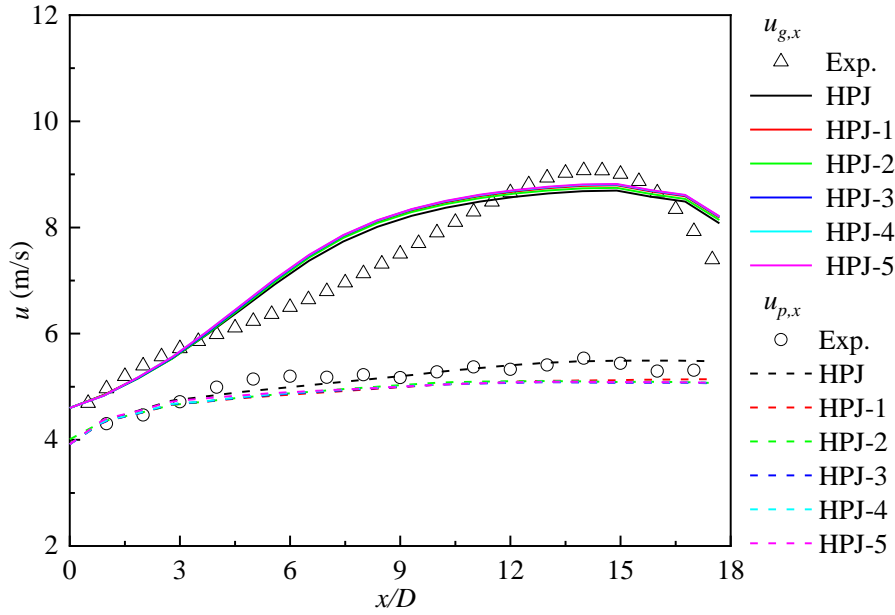


Figure 5.10 Centerline velocity of high-Stokes-number particle-laden jet predicted with the extrapolated drag models of HPJ with different Reynolds number ranges

5.5.2 Effects of Entrainment on Jet Velocity

According to literature reports, turbulent jets are often accompanied by strong entrainment^{12, 20, 21}, which plays a key role in jet transport properties⁷¹. And Figure 5.11 also shows clearly the entrainment convolution at the outlet of the nozzle. But there are few reports on quantitative studies on entrainment, so it is difficult to accurately apply the boundary conditions of entrainment.

In this section, we use simulations to study the role of entrainment in two-phase jet. Specifically, the effects of entrainment on the jet velocity distribution will be investigated. To this end, we define the entrainment coefficient C_e

$$C_e = \frac{D_e}{D} \quad (5-49)$$

where D_e is the diameter of the entrainment zone and D is the nozzle diameter. The velocity distribution (VD) and simulation results for different entrainment coefficients are shown in Figure 5.12 and Figure 5.13, respectively. It can be seen that, the velocities of gas and particles both increase with C_e , and when C_e is 1.5, the gas-solid two-phase

velocity is more consistent with the experimental. Therefore, in the other simulations in this chapter C_e is set to be 1.5.

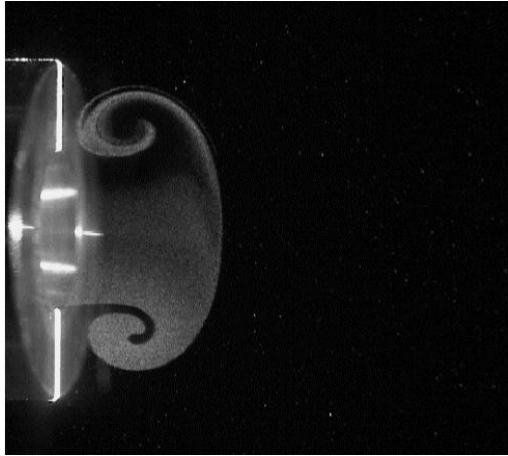


Figure 5.11 Entrainment at the nozzle exit

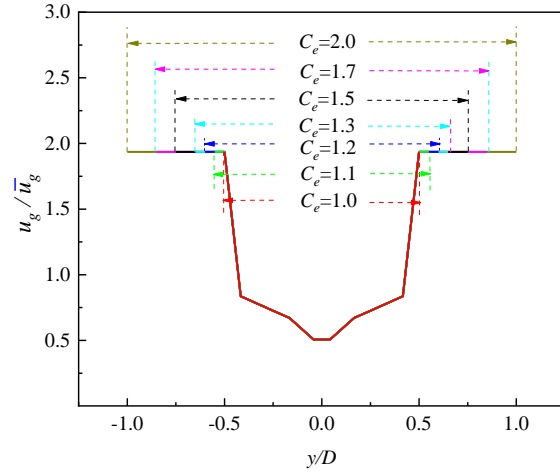


Figure 5.12 VDs under different C_e

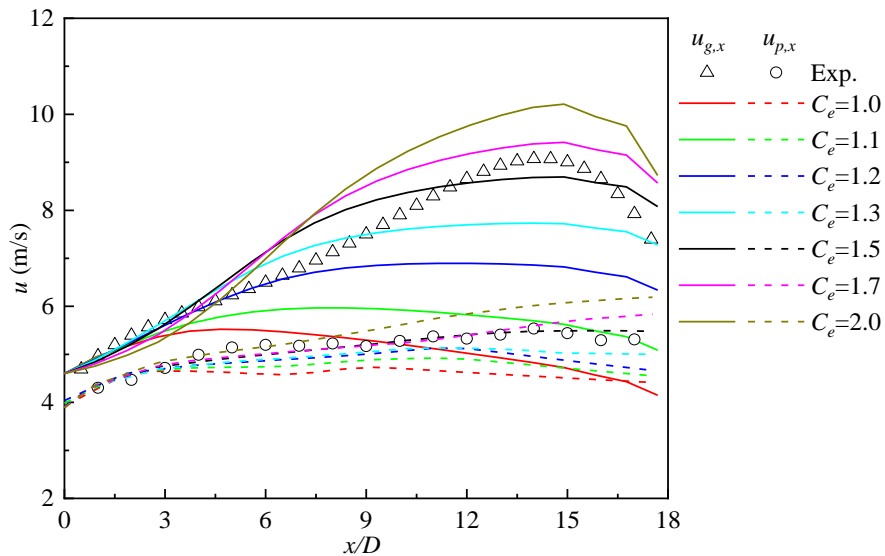


Figure 5.13 Simulation results of high-Stokes-number particle-laden jet centerline velocity under different C_e

5.5.3 Effects of Inlet Velocity Distribution on Jet Velocity

The velocity distribution in the nozzle of the circular jet^{30,31} cannot be quantitatively described, and its distribution form is related to the solid loading rate and particle diameter. But there are few reports in this regard, that the inlet boundary conditions of the simulations cannot be determined. It has been documented that for horizontal gas-

solid two-phase flow, the velocity distribution within the nozzle is related to the solid loading rate and particle size³¹. For example, in the case with particle diameter of 200 μm and solid loading rate greater than 0.4, the gas velocity distribution is neither parabolic nor logarithmic linear of turbulent flow, but gradually takes on a distribution shape with a small velocity in pipe center and large velocity on both sides³¹. However, quantitative relationship between velocity distribution and solid loading rate/particle size has not been reported.

Therefore, in this section, we construct 9 inlet gas velocity distributions and apply them to simulate the inlet boundary condition through UDFs to determine the most suitable velocity distribution type that best matches the experimental values. Different velocity distribution curves under the same flow rate are shown in Figure 5.14, and the corresponding simulation results are shown in Figure 5.15. It can be seen that the shape of velocity distribution has a great impact on the simulation results. The simulation results based on VD-5 inlet velocity distribution are in best agreement with the experimental data, so VD-5 is adopted as the boundary condition for gas velocity in this chapter.

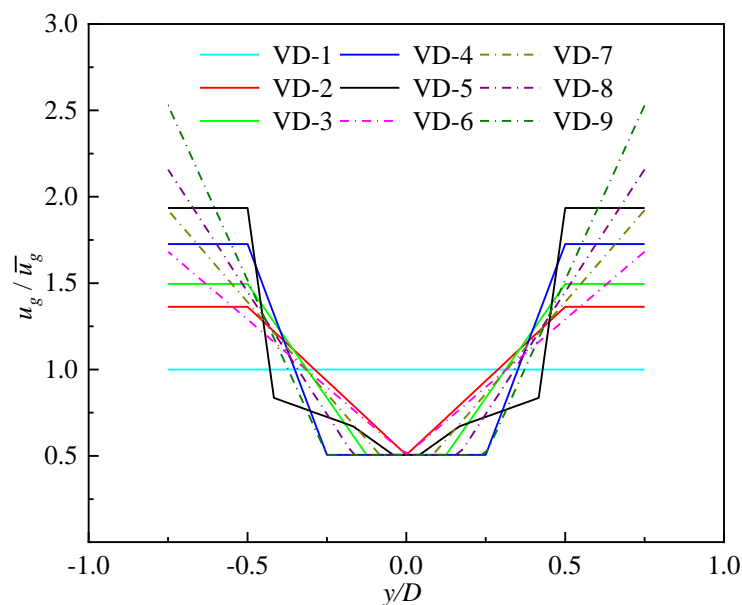


Figure 5.14 Different VD curves under the same flow rate

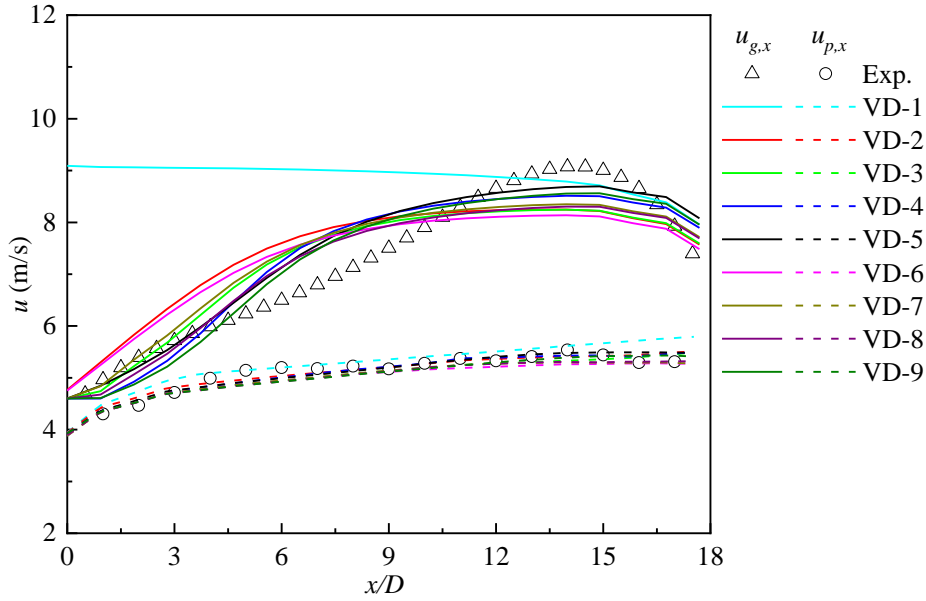


Figure 5.15 Simulation results of high-Stokes-number particle-laden jet centerline velocity under different VDs

5.5.4 Effects of Outlet Type on Jet Velocity

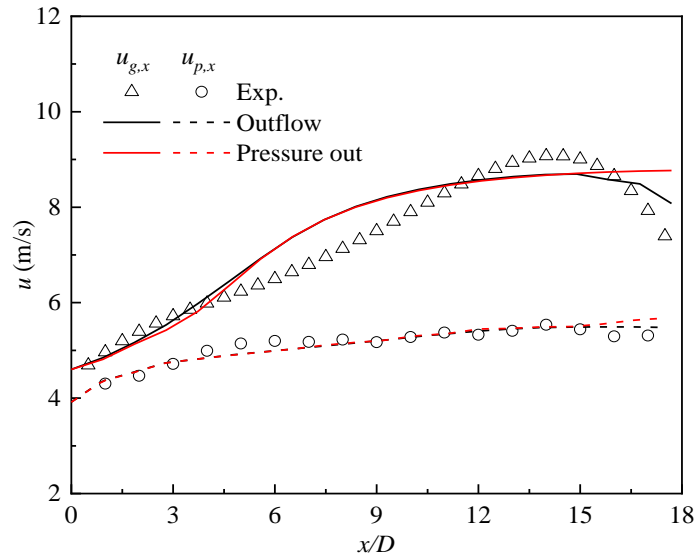


Figure 5.16 Centerline velocity of high-Stokes-number particle-laden jet predicted with different outlet boundary type

There is no boundary for free jet flow, but it is impossible to set an infinite fluid domain in actual simulation work. In reality, for a free jet flow, a proper outlet boundary condition is needed on a finite domain. However, different type of outlet boundary conditions will also influence the predicted velocity field of the jet. Thus, two types of

outlet boundary conditions, say "Pressure out" and "Outflow" outlets, are tested in this section to investigate their effects. Figure 5.16 shows that, compared to the "Pressure out", the simulation results of "Outflow" show a better agreement with the experimental data, especially in the region far away from the jet nozzle, where a drop of gas velocity is evident. Therefore, "Outflow" is adopted as the outlet boundary condition in the following discussion.

5.6 Applicability of Drag Models to Middle-Stokes-number Particle-laden Jets

5.6.1 Effects of Drag Models

As described in Section 3.5.3, the drag correlation (HPJ and a series of other models) derived in Chapter 3 is based on large particles following ballistic trajectories in jet flows. Considering the striking difference of the turbulent effects on particles under different Stokes numbers, it is necessary to extend our experiments to smaller particles. It is worth noting that, the smaller the particle size, the more difficult it is to obtain the particle-level trajectory in experiments. This makes it difficult to derive a drag correlation for small particle purely with experimental measurements. So, it could be a good attempt to first measure the mean velocity of small particles in a jet flow, then perform simulations to verify the applicability of the newly derived drag correlations in Section 3.5.3. Therefore, based on the mean velocity of small particles in the jet obtained experimentally in Chapter 4, we can employ simulations to verify the applicability of the newly derived drag model to the particle-laden jet with small particles/middle-Stokes-number.

The jet centerline velocities predicted with different drag models are compared with the Exp.1 results of 1 middle -Stokes-number particle-laden jet as shown in Figure 5.17. It should be noted that the influence of particles on the gas phase can only be

ignored when the particle concentration is very low ($<10^{-5}$), otherwise two-way coupling and turbulence modulation should be considered²⁶⁴. Therefore, in the simulation in this chapter, the gas phase velocity is calculated based on the two-way coupling method. Because simultaneous measurement of the gas phase and particle phase velocities cannot be achieved in the current experimental conditions, the experimental gas phase velocity in the figure is measured in single-phase gas jet. However, this does not affect the subsequent analysis of the effect of the drag model on particle velocity, although the predicted gas phase velocity cannot be validated exactly with the experimental data. Figure 5.17 (a) shows that the gas phase velocity of the two-phase particle-laden jet simulation has a significant difference with the velocity of the single-phase gas jet experiment, indicating that the two-way coupling simulation is necessary, otherwise the simulation results should be close to the experimental data of the single-phase gas jet. From the perspective of general trend, in the early stage of the jet, the gas velocity is greater than the particle velocity. Then the gas velocity decays rapidly, and it becomes less than the particle velocity after about $5D$. Finally, the gas velocity tends to be very close to the particle velocity, which is the same as the results of experiments in the literature^{36, 53}. The phenomenon that the gas velocity is less than the particle velocity in the middle region can be explained by the faster expansion of the gas and the large inertia of the particles.

Figure 5.17 (a) and (b) show that there is large difference between the predicted particle velocity with different drag models. And the predicted particle velocity with the HPJ-SR4 model agrees best with the experimental values. But the errors of simulation results of all drag models are relatively large in the later stage of the jet. One main reason may be related to the simulation accuracy of turbulence. It is well known that the free turbulent jet is still hard to be simulated with current turbulence models¹⁸⁶.

The characteristic scale of turbulence during jet development is variable, and one turbulence model may not be applicable to the entire jet development process. The current simulation results show that, in the late stage of the jet, the gas phase dispersion rate dictated by turbulence is underestimated, resulting in an overestimation of the predicted gas velocity. This in turn acts on the particles and makes the particle velocity to be overestimated too. Another reason may be that the drag model may not be applicable at the current Reynolds number. For example, the HPJ-SR series models are extrapolated from experiments with Reynolds numbers ranging from 50~300, however, the middle-Stokes-number particle-laden jets in this work have a Reynolds number less than 10.

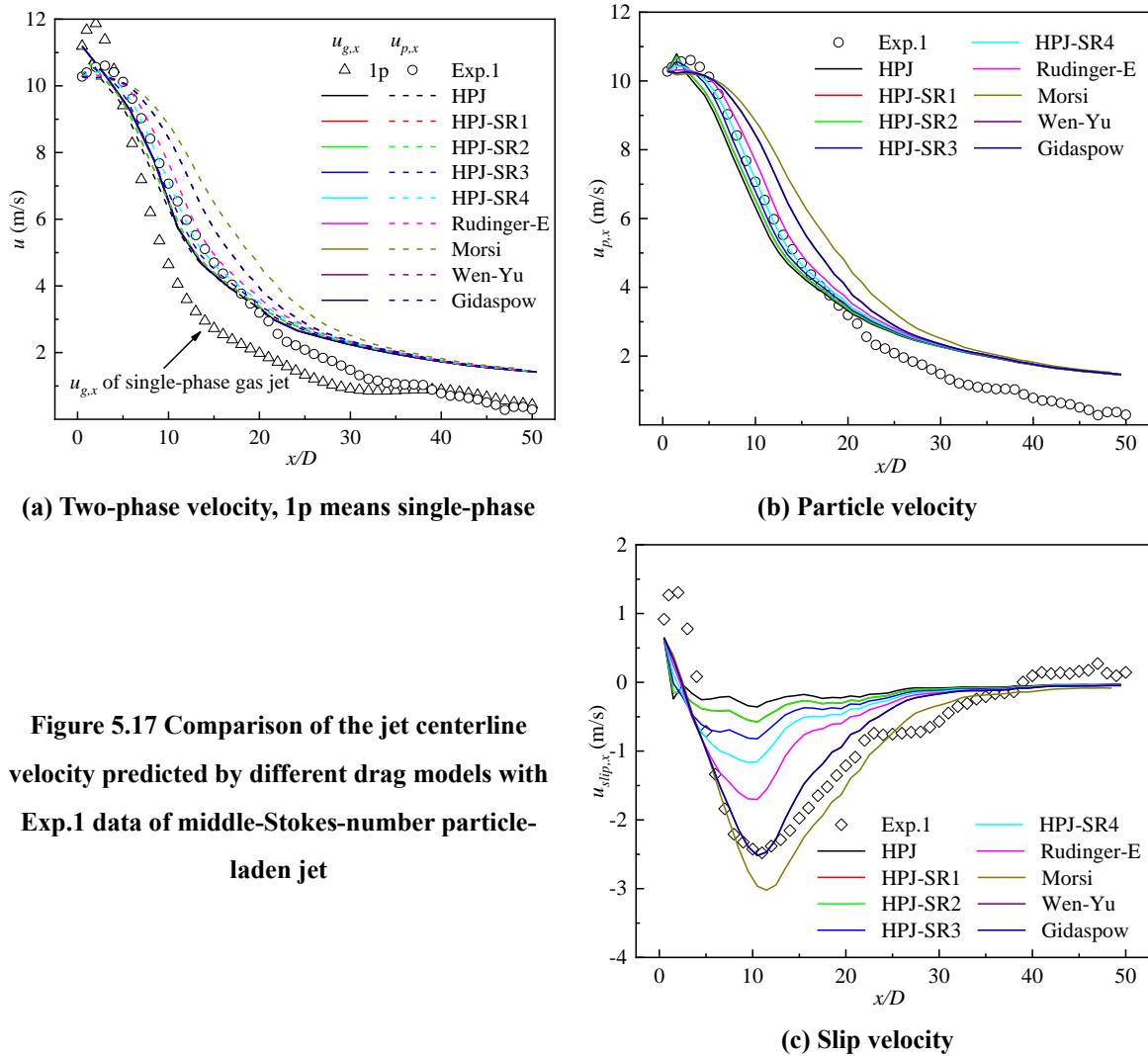


Figure 5.17 Comparison of the jet centerline velocity predicted by different drag models with Exp.1 data of middle-Stokes-number particle-laden jet

Figure 5.17(c) shows the slip velocity compared to the experiment. From the perspective of slip velocity different drag models also have a great influence on the slip velocity. The larger the drag coefficient is, the smaller the slip velocity is. Gidaspow model²⁶² and Wen-Yu model¹⁷¹ are more consistent with the experimental data than the other models. And the simulation results of the two coincide, because when the particle concentration is small, the drag formulas of the Gidaspow model and the Wen-Yu model are the same. It should be noted that the slip velocity of the experiment is calculated based on the gas velocity of the single-phase gas jet, so it does not mean that the Gidaspow model and the Wen-Yu model are more suitable for the middle-Stokes-number particle-laden jet than the other tested models. Considering that the gas and particle velocities are not measured simultaneously in this situation, the drag still requires further research.

5.6.2 Discussions of Different Initial Velocities

The HPJ-SR4 drag model has also been applied to simulate different experimental cases of middle-Stokes-number particle-laden jet. Figure 5.18 shows the predicted jet centerline velocity with the experimental data. Among them, the large number corresponds to the high initial particle velocity. Figure 5.18 (a) shows that the predicted particle velocity for the lower velocity case is closer to the experimental than that for the higher velocity cases. And the gap between the prediction and experimental data becomes larger as the velocity increases. The comparison of slip velocity is shown in Figure 5.18 (b), which shows that the predicted slip velocity increases as the initial particle velocity increases when $x/D > 5$. However, there is no obvious trend of experimental slip velocity which is calculated based on single-phase gas jet, indicating that the slip velocity cannot be calculated using the velocity of single-phase gas jet.

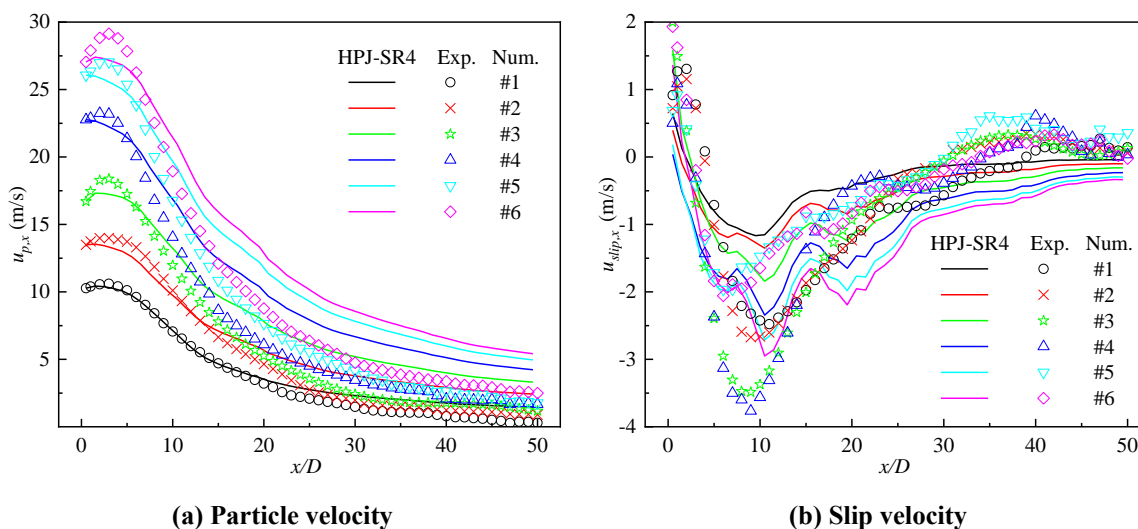


Figure 5.18 Comparison of the jet centerline velocity predicted by the HPJ-SR4 drag model with different experiments of middle-Stokes-number particle-laden jet

In summary, the HPJ-SR4 model is more suitable for particle velocity prediction at middle-Stokes-number particle-laden jets at low velocity, and the accuracy of particle velocity prediction becomes poor at high velocity. We can improve the simulation results from two aspects. On the one hand, the simulation accuracy of gas phase turbulence has a great impact on particle velocity. Accurate prediction of gas phase velocity is the basis to discuss the effects of drag force on particles and then modify the drag force model. But the simulation of the free turbulent jet has always been a problem. On the other hand, simultaneous measurement of the two-phase velocity of small particles/middle-Stokes-number particle-laden jet at the particle level can obtain the two-phase slip velocity, the particle trajectory and thus calculate the drag coefficient. However, this is also very difficult due to the limitations of current measurement technology. Both of these two aspects deserve more efforts in the future.

5.7 Conclusions

In the present work, we simulate high- and middle- Stokes-number particle-laden jets using CFD-DPM methods in Fluent software. Based on the drag correlation

obtained in Chapter 3 (Eq. (3-15)) and the Rudinger drag model, we construct six different drag models. Another five more drag models are also built by expanding the Reynolds number range of Eq.(3-15). These drag models are implemented in the Fluent software via UDFs to simulate particle-laden jet cases with high/middle-Stokes-number. Based on the simulation results, the influence of different drag models on jet velocity is revealed. The sensitivity of drag relationship to Reynolds number is analyzed. The effects of entrainment, inlet velocity distribution, and outlet boundary conditions on the jet simulations are also discussed. The major conclusions can be summarized as follows:

- (1) The single-particle drag model (Morsi), the particle group drag model (Wen-Yu/Gidaspow), and the Rudinger drag model all underestimate the particle velocity in the large particle-laden jet, while the HPJ drag model can predict the particle velocity more accurately.
- (2) When the Reynolds number range of Eq. (3-15) is expanded, the prediction accuracy of particle velocity decreases, indicating that the new drag model is sensitive to Reynolds number, and the drag model under a larger Reynolds number range still needs to be improved.
- (3) There is strong entrainment in circular turbulent jets, and appropriate entrainment coefficient is helpful to improve simulation accuracy.
- (4) There is a complex gas velocity distribution at the nozzle outlet of the particle-carrying turbulent jet that is different from the parabolic and log-linear types. The velocity is low in the middle and high on both sides, and this distribution is related to the solid loading rate and particle size. Several different types of gas velocity distributions have been proposed and applied in simulations which can help to improve simulation accuracy.
- (5) The simulation results of the particle-laden jet are sensitive to the outlet boundary

conditions, and the appropriate outlet boundary conditions should be selected.

- (6) The HPJ model is not suitable for the small particles/middle-Stokes-number particle-laden jet. The HPJ-SR4 model is more suitable for particle velocity prediction of small particles/middle-Stokes-number particle-laden jet, but the prediction accuracy of particle velocity becomes poor at high velocity. Due to the limitations of current measurement techniques and the lack of gas phase velocity measured in gas-solid two-phase jet, the current conclusions are provisional.

Finally, a turbulence model for free turbulent jet and the development of direct two-phase velocity measurement technology at the particle level are conducive to the in-depth exploration of the drag model. However, both aspects have a long way to go.

Chapter 6 Summary and Outlook

6.1 Main Conclusions

In this paper, the dynamics of horizontal high-, middle- and low- Stokes-number particle-laden jets are studied. The main conclusions are as follows:

- (1) A real tracking-precede-reconstruction, time-resolved, 3D particle flow field reconstruction method is realized based on dual-camera shooting, which lays the foundation for the study of particle-laden jet dynamics at the particle level.
- (2) The time-resolved 3D-PTV is combined with PIV to obtain both the particle and gas velocity fields of high-Stokes-number particle-laden jet, so as to obtain slip velocity.
- (3) New drag models are developed for the dilute particle-laden jet flow based on the reconstructed particle trajectories and gas flow field. Simulation indicates the new drag model partially agrees with the current limited experimental data while the single-particle drag model (Morsi), the particle group drag model (Wen-Yu/Gidaspow), and the Rudinger drag model all underestimate the velocity of particles.
- (4) The 3D particle volume fraction along particle trajectory is obtained, a particle volume fraction evolution model is developed based on the self-similar theory of the jet to describe the dispersion of particle-laden jets. The predicted particle volume fraction and its evolution agree well with the experimental data.
- (5) The decay of the gas phase velocity can be well predicted with the jet velocity decay classical model, and the decay of the velocity of the SiO₂ small particles can also be predicted with the classical model, with a maximum error of 16%.

- (6) The mesoscale structure and particle concentration of the middle-Stokes-number particle-laden jets of SiO₂ microspheres are studied by a large-field large-scale concentration measurement and the Voronoi method. The clustering process of SiO₂ particles during the jet process is dynamically stable, and as the Stokes number tends to be unity, the preferential concentration effect of particles is more significant. The larger the cluster, the more irregular its shape. The distribution of small-size clusters satisfies the power-law distribution of penetration theory.

6.2 Outlook

Perfect understanding of particle-laden jet flows requires a fully 3D, time-resolved reconstruction of the flow field down to the particle level. However, limited by experimental conditions, current algorithms, and measurement techniques, we are still far from reaching that target. More in-depth studies can be expected to be conducted from the following aspects:

- (1) Explore the simultaneous measurement technology of two-phase velocity of fully 3D, time-resolved PIV and PTV down to the particle level.
- (2) The drag model under the flow of large Reynolds number range and for small particles/middle-Stokes-number flows still needs to be improved.
- (3) The two-phase turbulence modeling, especially the turbulent modulation due to the presence of particles, deserves more efforts.

Appendix A Drag Models for Single Particle

| Drag model types | Mathematical formulation | Range |
|------------------------------------|---|---|
| Stokes ²⁵⁶ | $C_{D0} = 24Re_p^{-1}$ | $Re_p \leq 1$ |
| Allen ²⁶⁵ | $C_{D0} = \begin{cases} 10Re_p^{-1/2} \\ 30Re_p^{-0.625} \end{cases}$ | $2 < Re_p \leq 500$ $1 < Re_p \leq 1000$ |
| Oseen ²⁵⁶ | $C_{D0} = \frac{24}{Re_p} \left(1 + \frac{3}{16} Re_p \right)$ | $1 < Re_p \leq 5$ |
| Schiller & Naumann ¹⁶⁹ | $C_{D0} = \frac{24}{Re_p} (1 + 0.15Re_p^{0.687})$ | $0.1 < Re_p < 1000$ |
| Dallavalle ²⁶⁶ | $C_{D0} = \begin{cases} 24Re_p^{-1} \\ 0.4 + \frac{40}{Re_p} \\ 0.44 \end{cases}$ | $Re_p < 2$ |
| | | $2 < Re_p < 500$ |
| | | $500 < Re_p < 10^5$ |
| Richardson ²⁶⁷ | $C_{D0} = \begin{cases} 24Re_p^{-1} \\ \frac{24}{Re_p} (1 + 0.15Re_p^{0.687}) \\ 4/9 \end{cases}$ | $Re_p < 0.5$ |
| | | $0.5 < Re_p < 1000$ |
| | | $Re_p > 1000$ |
| Haider & Levenspiel ²⁶⁸ | $C_{D0} = \frac{24}{Re_p} (1 + 0.1806Re_p^{0.687}) + \frac{0.4251}{1 + 688095Re_p^{-1}}$ | $Re_p < 3 \times 10^5$ |
| Perry ²⁶⁹ | $C_{D0} = \begin{cases} 24Re_p^{-1} \\ 18.6Re_p^{-0.6} \\ 0.44 \end{cases}$ | $Re_p < 0.3$ |
| | | $0.3 < Re_p < 1000$ |
| | | $1000 < Re_p < 2 \times 10^5$ |
| Massey ²⁷⁰ | $C_{D0} = \frac{24}{Re_p} \left(1 + \frac{3}{16} Re_p \right)^{0.5}$ | $Re_p < 100$ |
| Clift & Gauvin ²⁷¹ | $C_{D0} = \frac{24}{Re_p} (1 + 0.15Re_p^{0.687}) + \frac{0.42}{1 + 4.25 \times 10^{-4} Re_p^{-1.16}}$ | $Re_p < 3 \times 10^5$ |
| | | $Re_p < 0.1$ |
| Morsi ²⁶¹ | $C_{D0} = \begin{cases} \frac{24}{Re_p} \\ 22.73/Re_p + 0.0903/Re_p^2 + 3.69 \\ 29.1667/Re_p - 3.8889/Re_p^2 + 1.222 \\ 46.5/Re_p - 116.67/Re_p^2 + 0.6167 \\ 98.33/Re_p - 2778/Re_p^2 + 0.3644 \\ 148.62/Re_p - 47500/Re_p^2 + 0.357 \\ -49.546/Re_p - 578700/Re_p^2 + 0.46 \\ -1662.5/Re_p - 5416700/Re_p^2 + 0.5191 \end{cases}$ | $0.1 < Re_p < 1$ |
| | | $1 < Re_p < 10$ |
| | | $10 < Re_p < 100$ |
| | | $100 < Re_p < 1000$ |
| | | $1000 < Re_p < 5000$ |
| | | $5000 < Re_p < 10^4$ |
| | | $10^4 < Re_p < 5 \times 10^4$ |

| | | |
|--------------------------------|--|--|
| Clift & Gilbert ²²⁴ | $C_{D0} = \frac{40}{Re_p^{0.85}} + 0.48$ | $2 < Re_p < 2000$ |
| Molerus ²⁷² | $C_{D0} = \frac{24}{Re_p} \left(1 + \frac{1}{6} Re_p^{0.5}\right) + 0.4$ | $Re_p < 3 \times 10^5$ |
| Chow ²⁷³ | $C_{D0} = \begin{cases} \frac{24}{Re_p} & Re_p \leq 1 \\ \frac{24}{Re_p^{0.646}} & 1 < Re_p \leq 400 \\ 0.5 & 400 < Re_p \leq 3 \times 10^5 \\ 0.000366 Re_p^{0.4275} & 3 \times 10^5 < Re_p \leq 2 \times 10^6 \\ 0.18 & Re_p > 2 \times 10^6 \end{cases}$ | $Re_p \leq 1$ $1 < Re_p \leq 400$ $400 < Re_p \leq 3 \times 10^5$ $3 \times 10^5 < Re_p \leq 2 \times 10^6$ $Re_p > 2 \times 10^6$ |
| White ²⁷⁴ | $C_{D0} = \frac{24}{Re_p} + \frac{6}{1 + Re_p^{0.5}} + 0.4$ | $Re_p < 2 \times 10^5$ |
| Ganser ²⁷⁵ | $C_{D0} = \frac{24}{Re_p} (1 + 0.1118 Re_p^{0.687}) + \frac{0.4305}{1 + 3305 Re_p^{-1}}$ | $Re_p < 10^5$ |
| Alex ²⁷⁶ | $C_{D0} = \begin{cases} \frac{24}{Re_p} \left(1 + \frac{1}{6} Re_p^{2/3}\right) & Re_p < 1000 \\ 0.424 & Re_p \geq 1000 \end{cases}$ | $Re_p < 1000$ $Re_p \geq 1000$ |
| Xu & Li ¹⁷⁰ | $C_{D0} = \begin{cases} \frac{24}{Re_p} & Re_p \leq 0.3 \\ \frac{27}{Re_p^{0.89}} & 0.3 < Re_p \leq 4 \\ \frac{20.4}{Re_p^{0.69}} & 4 < Re_p \leq 40 \\ \frac{7.8}{Re_p^{0.43}} & 40 < Re_p \leq 600 \\ \frac{1.16}{Re_p^{0.13}} & 600 < Re_p \leq 5000 \\ 0.15 Re_p^{0.11} & 5000 < Re_p \leq 70000 \\ \frac{4.26}{Re_p^{0.19}} & 70000 < Re_p \leq 10^5 \end{cases}$ | $Re_p \leq 0.3$ $0.3 < Re_p \leq 4$ $4 < Re_p \leq 40$ $40 < Re_p \leq 600$ $600 < Re_p \leq 5000$ $5000 < Re_p \leq 70000$ $70000 < Re_p \leq 10^5$ |

Appendix B Drag Models for Uniform Particle Systems

| Drag model types | Mathematical formulation |
|--------------------------------|--|
| Wen–Yu ¹⁷¹ | $f(\alpha_g, Re_p) = \alpha_g^{-2.65}$ |
| Happel ²⁷⁷ | $f(\alpha_g, Re_p) = \frac{3 + 2(1 - \alpha_g)^{5/3}}{3 - 4.5(1 - \alpha_g)^{1/3} + 4.5(1 - \alpha_g)^{5/3} - 3(1 - \alpha_g)^2}$ |
| Ishii & Zuber ²⁷⁸ | $C_D = \frac{24}{Re'} (1 + 0.1Re'^{0.75})$ |
| | $Re' = \frac{\rho_g u_s d_s}{\mu_{mix}}, \quad \mu_{mix} = \mu_g \left(1 - \frac{\alpha_p}{\alpha_{p,max}}\right)^{-2.5\alpha_{p,max}}, \quad \alpha_{p,max} = 0.62$ |
| Gibilaro ²⁷⁹ | $\beta = \frac{\alpha_g \alpha_p}{d_s} \rho_g u_s \left(\frac{17.3}{Re_p} + 0.336\right) \alpha_g^{-2.8}$ |
| Syamlal–O’Brien ²⁸⁰ | $f(\alpha_g, Re_p) = \frac{C_{Ds}(Re_p/V_r)}{V_r^2}, \quad C_{Ds} = \left(0.63 + \frac{4.8}{\sqrt{Re_p}}\right)^2$ |
| | $V_r = 0.5 \left[A - 0.06Re_p + \sqrt{(0.06Re_p)^2 + 0.12Re_p(2B - A) + A^2} \right]$ |
| | $A(\alpha_g) = \alpha_g^{4.14}, \quad B(\alpha_g) = \begin{cases} 0.8\alpha_g^{1.28} & , \alpha_g < 0.85 \\ \alpha_g^{2.65} & , \alpha_g > 0.85 \end{cases}$ |
| Gidaspow ²⁶² | $\beta = \begin{cases} \frac{3}{4} \frac{\alpha_g \alpha_p}{d_p} \rho_g u_s C_{D0} \alpha_g^{-2.65} & , \alpha_g > 0.8 \\ 150 \frac{\alpha_p^2 \mu_g}{\alpha_g d_p^2} + 1.75 \frac{\alpha_p \rho_g u_s }{d_p} & , \alpha_g < 0.8 \end{cases}$ |

Di Felice¹⁶³

$$f_{Di} = \frac{3}{4} \left(0.63 + \frac{4.8}{Re_p^{0.5}} \right)^2 Re_p \alpha_g^{1-\gamma}$$

$$\gamma = 3.7 - 0.65 \exp \left(-\frac{(1.5 - \log Re_p)^2}{2} \right)$$

Gidaspow blend²⁸¹

$$\beta = W \frac{3\rho_g C_D Re_p}{4\rho_p d_p} |u_s| \alpha_g^{-1.7} + (1-W) \frac{\rho_g}{\rho_p} \left[1.75 + (1-\alpha_g) \frac{150}{Re_p} \right] \frac{|u_s|}{d_p}$$

$$W = \arctan(150(\alpha_g - 0.8))/\pi + 0.5$$

HKL²⁸²⁻²⁸⁴

$$f(\alpha_g, Re_p) = (1 - \alpha_g)^2 F$$

$$F = \begin{cases} F_0(\alpha_p) + F_1(\alpha_p) Re_p^2 & , Re_p < 20 \\ F_0(\alpha_p) + F_2(\alpha_p) Re_p & , Re_p \geq 20 \end{cases}$$

$$F_0(\alpha_p) = \begin{cases} \frac{1 + 3(\alpha_p/2)^{0.5} + (135/64)\alpha_p \ln \alpha_p + 16.456\alpha_p}{1 + 0.681\alpha_p - 8.48\alpha_p^2 + 8.16\alpha_p^3}, & \alpha_p < 0.4 \\ \frac{10\alpha_p}{(1 - \alpha_p)^3}, & \alpha_p > 0.4 \end{cases}$$

$$F_1(\alpha_p) = 0.110 + 5.10 \times 10^{-4} e^{(11.6\alpha_p)}$$

$$F_2(\alpha_p) = 0.0673 + 0.212\alpha_p + 0.0232/(1 - \alpha_p)^5$$

BVK²⁸⁵⁻²⁸⁷

$$f(\alpha_g, Re_p) = \frac{10(1 - \alpha_g)}{\alpha_g^2} + \alpha_g^2 \left[1 + 1.5(1 - \alpha_g)^{0.5} \right] + \frac{0.413 Re_p}{24\alpha_g^2} \left[\frac{\alpha_g^{-1} + 3\alpha_g(1 - \alpha_g) + 8.4 Re_p^{-0.343}}{1 + 10^3(1 - \alpha_g) Re_p^{2\alpha_g - 2.5}} \right]$$

$$\alpha_g \in [0.4, 0.9], \quad Re_p \in [21, 1049.4]$$

Rubinstein^{288, 289}

$$f(\alpha_g, St) = \alpha(\tilde{St}) F_{vanderHoeft}(\alpha_g) + (1 - \alpha(\tilde{St})) \alpha_g^{-2.65}$$

$$\tilde{St} = \frac{St}{\alpha_g^2}, \quad F_{vanderHoeft}(\alpha_g) = \frac{10(1 - \alpha_g)}{\alpha_g} + \alpha_g^3 (1 + 1.5 \sqrt{1 - \alpha_g})$$

HYS^{290, 291}

$$f_{Di-fixed}^* = \frac{1}{\alpha_g} + \left(F_{D-fixed}^* - \frac{1}{\alpha_g} \right) [\alpha y_i + (1-a)y_i^2], \quad \alpha_g \in [0.5, 0.9]$$

$$f_{D-fixed}^* = \frac{10(1-\alpha_g)}{\alpha_g^2} + \alpha_g^2 [1 + 1.5(1-\alpha_g)^{0.5}]$$

$$a = 1 - 2.66(1-\alpha_g) + 9.096(1-\alpha_g)^2 - 11.338(1-\alpha_g)^3$$

$$y_i = \frac{d_i}{\langle d \rangle}, \quad \langle d \rangle = \frac{n_1 d_1^3 + n_2 d_2^3}{n_1 d_1 + n_2 d_2}$$

TGS¹⁶⁵

$$f(\alpha_g, Re_p) = \frac{24}{Re_p} (1 + 0.15 Re_p^{0.687}) \frac{1}{\alpha_g^3} + F_1 + F_2$$

$$F_1 = \frac{5.81(1-\alpha_g)}{\alpha_g^3} + 0.48 \frac{(1-\alpha_g)^{1/3}}{\alpha_g^4}$$

$$F_2 = (1-\alpha_g)^3 Re_p \left(0.95 + \frac{(1-\alpha_g)^3}{\alpha_g^2} \right)$$

$$\alpha_g \in [0.5, 0.9] \quad Re_p \in [20, 300]$$

TPKKV²⁹²

$$f(\alpha_g, Re_p) = \frac{10(1-\alpha_g)}{\alpha_g^2} + \alpha_g^2 [1 + 1.5(1-\alpha_g)^{0.5}]$$

$$+ \left[0.11(1-\alpha_g)(2-\alpha_g) - \frac{0.00456}{\alpha_g^4} + \left(0.169\alpha_g + \frac{0.0644}{\alpha_g^4} \right) Re_p^{-0.343} \right]$$

$$\alpha_g \in [0.4, 0.9], \quad Re_p \in [50, 1000]$$

Appendix C Parameters of EMMS Drag Model for Heterogeneous Systems 179-181, 293-295

| Parameters | | Dense phase | Dilute phase | Interphase | Total |
|---|---------------------|--|--|---|--|
| Gas density | | ρ_g | ρ_g | ρ_g | / |
| Particle density | | ρ_p | ρ_p | $\rho_p(1 - \alpha_{de})$ | / |
| Particle and cluster size | | d_p | d_p | $d_{cl}(\text{cluster})$ | / |
| Void ratio | | α_{de} | α_{di} | $1 - f$ | $\alpha_g = \alpha_{di}(1 - f) + \alpha_{de}f$ |
| Volume ratio | | f | $1 - f$ | / | 1 |
| Gas | | u_{gde} | u_{gdi} | $u_{gdi}(1 - f)$ | $u_g = u_{gdi}(1 - f) + u_{gde}f$ |
| Appearances | Particle | u_{pde} | u_{pdi} | / | $u_p = u_{pdi}(1 - f) + u_{pde}f$ |
| Speed | Slip | $u_{sde} = u_{gde} - \frac{u_{pde}\alpha_{de}}{1 - \alpha_{de}}$ | $u_{sdi} = u_{gdi} - \frac{u_{pdi}\alpha_{di}}{1 - \alpha_{di}}$ | $u_{sint} = \left(u_{gdi} - \frac{u_{pde}\alpha_{di}}{1 - \alpha_{de}}\right)(1 - f)$ | $u_s = u_g - \frac{u_p\alpha_g}{1 - \alpha_g}$ |
| Reynolds number | | $Re_{de} = u_{sde}d_p\rho_g/\mu_g$ | $Re_{di} = u_{sdi}d_p\rho_g/\mu_g$ | $Re_{int} = u_{sint}d_{cl}\rho_g/\mu_g$ | / |
| Drag | Single particle | $C_{D0de} = 24/Re_{de} + 3.6/Re_{de}^{0.313}$ | $C_{D0di} = 24/Re_{di} + 3.6/Re_{di}^{0.313}$ | $C_{D0int} = 24/Re_{int} + 3.6/Re_{int}^{0.313}$ | / |
| force | Fluidized particles | $C_{Dde} = C_{D0de}\alpha_{de}^{-4.7}$ | $C_{Ddi} = C_{D0di}\alpha_{di}^{-4.7}$ | $C_{Dint} = C_{D0di}(1 - f)^{-4.7}$ | / |
| Number of particles per unit volume or number of clusters | | $n_{de} = \frac{6(1 - \alpha_{de})}{\pi d_p^3}$ | $n_{di} = \frac{6(1 - \alpha_{di})}{\pi d_p^3}$ | $n_{int} = \frac{6f}{\pi d_{cl}^3}$ | / |
| Force | | $F_{Dde} = \frac{1}{8}\rho_g\pi d_p^2 u_{sde}^2 C_{Dde}$ | $F_{Ddi} = \frac{1}{8}\rho_g\pi d_p^2 u_{sdi}^2 C_{Ddi}$ | $F_{bulk} = \frac{1}{8}\rho_g\pi d_{cl}^2 u_{int}^2 C_{Dint}$ | / |
| Pressure drop per unit volume | | $\Delta P_{de} = n_{de}F_{Dde}$ | $\Delta P_{di} = n_{di}F_{Ddi}$ | $\Delta P_{int} = n_{dint}F_{bulk}$ | / |
| Energy | | $(W_{st})_{de} = \Delta P_{de}u_{sde}f$ | $(W_{st})_{di} = \Delta P_{di}u_{sdi}(1 - f)$ | $(W_{st})_{int} = \Delta P_{int}u_{sdi}(1 - f)$ | W_{st} |
| consumption | Unit mass | $(N_{st})_{de} = \frac{(W_{st})_{de}}{(1 - \alpha_g)\rho_p}$ | $(N_{st})_{di} = \frac{(W_{st})_{di}}{(1 - \alpha_g)\rho_p}$ | $(N_{st})_{int} = \frac{(W_{st})_{int}}{(1 - \alpha_g)\rho_p}$ | N_{st} |

Appendix D Filtered Drag Models for Heterogeneous Systems

| Drag model | Mathematical formulation |
|----------------------------|--|
| | $F_{Sarkar} = (1 - H_{3D}^{two})\beta_{WY}(\mathbf{u}_g - \mathbf{u}_p), \quad H_{3D}^{two} = \min \left\{ \left(a + \frac{b}{ u_{slip}^* } \right) (1 - \alpha_g)^{\left(c + \frac{d}{ u_{slip}^* } \right)}, 0.97 \right\}$ |
| Sarkar ^{178, 296} | $\Delta_{filter}^* = 0.6748, \quad a = 0.9240, \quad b = 0.2370, \quad c = -0.03102, \quad d = 0.4189$ $\Delta_{filter}^* \in [1.3495, 6.7476], \quad a = 0.9506, \quad b = 0.1708, \quad c = 0.049 \left(\frac{1}{\Delta_{filter}^*} \right), \quad d = 0.3358$ $\Delta_{filter}^* = \max \left(\frac{g\Delta_{filter}}{u_t^2}, 0.5 \right), \quad u_{slip}^* = \frac{u_{slip}}{u_t}, \quad u_t = \frac{(\rho_p - \rho_g)gd_p^2}{18\mu_g}$ $\beta_{Radl} = \beta_{WY} \left[1 - f \left(\frac{\Delta_{filter}}{L_c}, \alpha_p \right) h(\alpha_p) \right]$ $f \left(\frac{\Delta_{filter}}{L_c}, \alpha_p \right) = \frac{1}{a(\alpha_p)(L_c/\Delta_{filter}) + 1}, \quad L_c = \frac{u_t^2}{g} Fr_p^{-2/3}$ $a(\alpha_p) = \begin{cases} 21.51, & \alpha_p < 0.016 \\ 1.96 + 29.40\alpha_p + 164.91\alpha_p^2 - 1923\alpha_p^3, & 0.016 < \alpha_p \leq 0.10 \\ 4.63 + 4.68(\alpha_p - 0.1) - 412.04(\alpha_p - 0.1)^2 + 2254(\alpha_p - 0.1)^3, & 0.10 < \alpha_p \leq 0.18 \\ 3.52 - 17.99(\alpha_p - 0.18) + 128.8(\alpha_p - 0.18)^2 - 603(\alpha_p - 0.18)^3, & 0.18 < \alpha_p \leq 0.25 \\ 2.68 - 8.82(\alpha_p - 0.25) + 2.18(\alpha_p - 0.25)^2 + 112.33(\alpha_p - 0.25)^3, & 0.25 < \alpha_p \leq 0.40 \\ 1.79, & 0.40 < \alpha_p \end{cases}$ |
| Radl ¹⁸⁴ | |

$$h(\alpha_p) = \begin{cases} 7.97\alpha_p & , \alpha_p < 0.03 \\ 0.239 + 4.64(\alpha_p - 1) - 4.41(\alpha_p - 0.03)^2 + 253.63(\alpha_p - 0.03)^3 & , 0.03 < \alpha_p \leq 0.08 \\ 0.492 + 6.10(\alpha_p - 0.08) + 33.63(\alpha_p - 0.08)^2 - 789.6(\alpha_p - 0.08)^3 & , 0.08 < \alpha_p \leq 0.12 \\ 0.739 + 5.01(\alpha_p - 0.12) - 61.1(\alpha_p - 0.12)^2 + 310.8(\alpha_p - 0.12)^3 & , 0.12 < \alpha_p \leq 0.18 \\ 0.887 + 1.03(\alpha_p - 0.18) - 5.17(\alpha_p - 0.18)^2 + 5.99(\alpha_p - 0.18)^3 & , 0.18 < \alpha_p \leq 0.34 \\ 0.934 - 0.17(\alpha_p - 0.34) - 2.29(\alpha_p - 0.34)^2 - 9.12(\alpha_p - 0.34)^3 & , 0.34 < \alpha_p \leq 0.48 \\ 0.850 - 1.35(\alpha_p - 0.48) - 6.132(\alpha_p - 0.48)^2 - 132.6(\alpha_p - 0.48)^3 & , 0.48 < \alpha_p \leq 0.55 \\ 0.680 - 2.34(\alpha_p - 0.55) - 252.2(\alpha_p - 0.55)^2 & , 0.55 < \alpha_p \leq 0.60 \end{cases}$$

$$\beta_{Sarkar} = \begin{cases} [1 - 0.95(1 - e^{-\alpha(u_{slip}^* - u_0)^p})] \beta_{WY} & , u_{slip}^* > u_0 \\ \beta_{WY} & , u_{slip}^* \leq u_0 \end{cases}$$

$$\alpha = \frac{(a_1 + a_2\alpha_p + a_3\alpha_p^2 + a_4\alpha_p^3 + a_5\alpha_p^4)(1 - e^{-300\alpha_p})}{1 + e^{100(\alpha_p - 0.55)}} \left(1 + \frac{a_6}{\Delta_{filter}^*} + \frac{a_7}{\Delta_{filter}^{*2}}\right) \left(1 + \frac{a_8}{u_{slip}^{*2}}\right)$$

$$u_0 = \frac{a_9 + a_{10}\alpha_p}{0.01 + \alpha_p^{a_{11}}} \left(1 + \frac{a_{12}}{\Delta_{filter}^*} + \frac{a_{13}}{\Delta_{filter}^{*2}}\right)$$

$$p = (a_{14} + a_{15}\alpha_p + a_{16}\alpha_p^2) \left(1 + \frac{a_{17}}{\Delta_{filter}^*} + \frac{a_{18}}{\Delta_{filter}^{*2}}\right)$$

$$a_i \begin{cases} 1,2,3 \\ 4,5,6 \\ 7,8,9 \\ 10,11,12 \\ 13,14,15 \\ 16,17,18 \end{cases} = \begin{cases} 0.75597773, 2.73931487, -5.60196497 \\ -1.65853820, 16.70299223, -0.44145335 \\ 0.18195034, -0.01827347, 0.28441799 \\ -1.943573770, 0.22177961, 0.31175890 \\ -0.15971960, 0.47750002, 0.062794180 \\ 5.13011673, 0.67680355, -0.54535726 \end{cases}$$

Gao–Sarkar ¹⁷⁷

Appendix E Drag Model Selection in Pneumatic Conveying and Jet Flow Scenarios

| Researchers | d_p (mm) | ρ_p (g/cm ³) | u_g (m/s) | SLR | Drag model | Physical Scenes |
|---------------------------------------|------------|-------------------------------|-------------|-----------|------------|------------------|
| Matsumoto et al. ²⁹⁷⁻²⁹⁹ | 0.5、 1 | 2.5 | 0.5~10 | / | Stokes | Conveying |
| Durst et al. ³⁰⁰ | 0.1、 0.5 | 1~2.5 | 1~10 | 0.025~2 | Schiller | Conveying |
| Mostafa et al. ¹⁵⁸ | 0.02~0.1 | 1 | 0~11.7 | 0.1~0.5 | Clift | Jet flows |
| Tsuji et al. ³⁰¹⁻³⁰⁴ | 0.41~1.1 | 0.923~1.038 | 7~20 | <10 | Clift | Conveying |
| Lee et al. ³⁰⁵ | 0.1~0.8 | 2.5 | 5.66~5.84 | 1.06~2.22 | Stokes | Suspension flows |
| Frank et al. ^{261, 306} | 0.115 | 2.5 | 4~13 | / | Morsi | Conveying |
| Lun et al. ^{307, 308} | 1、 2 | 0.95~4.77 | 7~15 | 0~5 | Clift | Conveying |
| Ahmadi et al. ³⁰⁹⁻³¹¹ | 1.1 | 1.038 | 7、 15 | 1、 3 | Ishii | Conveying |
| Rouson & Eaton ¹⁵⁹ | 0.028~0.07 | 0.7~8.8 | 0~20 | / | Schiller | Conveying |
| Sommerfeld et al. ^{312, 313} | 0.03~0.7 | 2.5 | 18~27 | 0.1~4 | Richardson | Conveying |
| Eskin et al. ³¹⁴ | 0.1~0.625 | 2.5 | 14.25~19.7 | 1 | Richardson | Conveying |
| Heinl et al. ³¹⁵ | 0.003 | 2.5 | 25~30 | 0.16~0.64 | Clift | Conveying |
| Makkawi et al. ³¹⁶ | 0.15 | 2.5 | 3 | / | Gibilaro | Conveying |
| Jafari et al. ³¹⁷ | 0.138 | 2.5 | 10、 15 | 0.4~1.1 | Richardson | Conveying |
| Patro et al. ^{318, 319} | 0.2 | 1.02 | 6~20 | 0.4~3 | Gidaspow | Conveying |
| Zhou et al. ³²⁰ | 0.1 | 1.13 | 2~10 | 3.7~18.3 | Gidaspow | Conveying |
| Ebrahimi et al. ^{247, 321} | 0.8~2 | 2.5 | 7~9.5 | 2~3.5 | Ergun&WY | Conveying |
| Ariyaratne et al. ³²²⁻³²⁵ | 0.08~0.5 | 1 | 6~20 | 0~3.4 | Gidaspow | Conveying |
| Miao et al. ^{326, 327} | 0.075~0.4 | 1~1.65 | 5~29 | 0~3.5 | RDY | Conveying |
| Zhao et al. ^{328, 329} | 0.13~0.7 | 1.02、 2.45 | 10、 20 | 0.1~20 | Di Felice | Conveying |

Appendix F Drag Model Selection in Violent Expiratory Events

| Researchers | Research content | Drag model |
|----------------------------------|---|------------|
| Mohebi et al. ³³⁰ | The trajectory of ink-jet droplets | Schiller |
| Zhu et al. ³³¹ | Transport characteristics of saliva droplets produced by coughing | Richardson |
| Xie et al. ³⁷ | How far droplets can move in indoor environments—revisiting the Wells evaporation–falling curve | Alex |
| Redrow et al. ³³² | Evaporation and dispersion of airborne sputum droplets | Clift |
| Ge et al. ³³³ | The effects of human body heat on particle transport and inhalation | Richardson |
| Liu et al. ³³⁴ | Transport of airborne particles from a cough jet | Morsi |
| Wei et al. ²⁶³ | Enhanced spread of expiratory droplets by turbulence in a cough jet | Richardson |
| Liu & Wei ⁸⁴ | Evaporation and dispersion of respiratory droplets from coughing | Alex |
| Sahu et al. ³³⁵ | Interaction of droplet dispersion and evaporation in a polydispersed spray | Stokes |
| Zhang et al. ³³⁶ | Distribution of droplet aerosols generated by mouth coughing and nose | Clift |
| Balachandar et al. ⁷⁹ | Host-to-host airborne transmission | Schiller |
| Li et al. ³⁸ | The dispersion of evaporating cough droplets | Morsi |
| Wang et al. ⁷⁰ | The motion of respiratory droplets produced by coughing | White |
| Pendar et al. ⁸³ | The distribution of virus carrying saliva droplets during sneeze and cough | Richardson |
| Wang & Wu ¹⁶¹ | A model used to study the mechanisms for airborne pathogens, e.g., influenza virus and new coronavirus. | Richardson |
| Liu & Allahyari ³⁹ | Airborne spreading of viral contagion from sneezing and coughing | Schiller |

Appendix G Case Settling

| Section | Case number | Drag model | Entrainment coefficient C_e | Velocity distribution | Outlet type |
|------------------------|-------------|------------|-------------------------------|-----------------------|--------------|
| 5.5.1.1 Figure 5.8 | DM #1 | HPJ | 1.5 | VD-5 | Outflow |
| | DM #2 | HPJ-SR1 | 1.5 | VD-5 | Outflow |
| | DM #3 | HPJ-SR2 | 1.5 | VD-5 | Outflow |
| | DM #4 | HPJ-SR3 | 1.5 | VD-5 | Outflow |
| | DM #5 | HPJ-SR4 | 1.5 | VD-5 | Outflow |
| | DM #6 | Rudinger-E | 1.5 | VD-5 | Outflow |
| | DM #7 | Morsi | 1.5 | VD-5 | Outflow |
| | DM #8 | Wen-Yu | 1.5 | VD-5 | Outflow |
| | DM #9 | Gidaspow | 1.5 | VD-5 | Outflow |
| 5.5.1.2 Figure 5.10 | DRe #1 | HPJ | 1.5 | VD-5 | Outflow |
| | DRe #2 | HPJ-1 | 1.5 | VD-5 | Outflow |
| | DRe #3 | HPJ-2 | 1.5 | VD-5 | Outflow |
| | DRe #4 | HPJ-3 | 1.5 | VD-5 | Outflow |
| | DRe #5 | HPJ-4 | 1.5 | VD-5 | Outflow |
| | DRe #6 | HPJ-5 | 1.5 | VD-5 | Outflow |
| 5.5.2 Figure 5.13 | EC #1 | HPJ | 1.0 | VD-5 | Outflow |
| | EC #2 | HPJ | 1.1 | VD-5 | Outflow |
| | EC #3 | HPJ | 1.2 | VD-5 | Outflow |
| | EC #4 | HPJ | 1.3 | VD-5 | Outflow |
| | EC #5 | HPJ | 1.5 | VD-5 | Outflow |
| | EC #6 | HPJ | 1.7 | VD-5 | Outflow |
| | EC #7 | HPJ | 2.0 | VD-5 | Outflow |
| 5.5.3 Figure 5.15 | VD #1 | HPJ | 1.5 | VD-1 | Outflow |
| | VD #2 | HPJ | 1.5 | VD-2 | Outflow |
| | VD #3 | HPJ | 1.5 | VD-3 | Outflow |
| | VD #4 | HPJ | 1.5 | VD-4 | Outflow |
| | VD #5 | HPJ | 1.5 | VD-5 | Outflow |
| | VD #6 | HPJ | 1.5 | VD-6 | Outflow |
| | VD #7 | HPJ | 1.5 | VD-7 | Outflow |
| | VD #8 | HPJ | 1.5 | VD-8 | Outflow |
| | VD #9 | HPJ | 1.5 | VD-9 | Outflow |
| 5.5.4 Figure 5.16 | OT #1 | HPJ | 1.5 | VD-5 | Pressure out |
| | OT #2 | HPJ | 1.5 | VD-5 | Outflow |

Continued

| Section | Case number | Exp. number | Drag model | Velocity distribution | Outlet type |
|----------------------|-------------|-------------|------------|-----------------------|-------------|
| 5.5.5 Figure 5.17 | MDM #1 | #1 | HPJ | Center velocity | Outflow |
| | MDM #2 | #1 | HPJ-SR1 | | |
| | MDM #3 | #1 | HPJ-SR2 | | |
| | MDM #4 | #1 | HPJ-SR3 | | |
| | MDM #5 | #1 | HPJ-SR4 | | |
| | MDM #6 | #1 | Rudinger-E | | |
| | MDM #7 | #1 | Morsi | | |
| | MDM #8 | #1 | Wen-Yu | | |
| | MDM #9 | #1 | Gidaspow | | |
| 5.5.5 Figure 5.18 | Exp. #1 | #1 | HPJ-SR4 | Center velocity | Outflow |
| | Exp. #2 | #2 | HPJ-SR4 | | |
| | Exp. #3 | #3 | HPJ-SR4 | | |
| | Exp. #4 | #4 | HPJ-SR4 | | |
| | Exp. #5 | #5 | HPJ-SR4 | | |
| | Exp. #6 | #6 | HPJ-SR4 | | |

References

1. P. K. House, C. L. Briens, F. Berruti, and E. Chan, "Effect of spray nozzle design on liquid–solid contact in fluidized beds," *Powder Technol.* **186** (1), 89-98 (2008).
2. F. Zafiryadis, A. Degn Jensen, W. Lin, E. Akoh Hove, M. Boberg Larsen, and H. Wu, "Injection of gas–liquid jets into gas–solid fluidized beds: A review," *Particuology* **76**, 63-85 (2023).
3. F. Battista, F. Picano, G. Troiani, and C. M. Casciola, "Intermittent features of inertial particle distributions in turbulent premixed flames," *Phys. Fluids* **23** (12), 123304 (2011).
4. R. B. Koneru, B. Rollin, B. Durant, F. Ouellet, and S. Balachandar, "A numerical study of particle jetting in a dense particle bed driven by an air-blast," *Phys. Fluids* **32** (9), 093301 (2020).
5. W. Zeng, M. Sjöberg, and D. L. Reuss, "Combined effects of flow/spray interactions and EGR on combustion variability for a stratified DISI engine," *Proc. Combust. Inst.* **35** (3), 2907-2914 (2015).
6. W. Zeng, M. Sjöberg, D. L. Reuss, and Z. Hu, "The role of spray-enhanced swirl flow for combustion stabilization in a stratified-charge DISI engine," *Combust. Flame* **168**, 166-185 (2016).
7. K. Bobzin, W. Wietheger, M. A. Knoch, and S. R. Dokhanchi, "Estimation of Particle Mass Flow Rate in Free Jet Using In-Flight Particle Diagnostics in Plasma Spraying," *J. Therm. Spray Technol.* **29** (5), 921-931 (2020).
8. L.-V. Bouthier, F. Delloro, and E. Hachem, "Application and assessment of the improved delayed detached eddy simulation model to the cold spray process: Toward high fidelity computation fluid dynamics simulations," *Phys. Fluids* **34** (9), 095109 (2022).
9. Y. Zama, Y. Odawara, and T. Furuhashi, "Experimental investigation on velocity inside a diesel spray after impingement on a wall," *Fuel* **203**, 757-763 (2017).
10. Z. Yin, Y. Wan, Y. Zhang, and H. Wang, "Why super sandstorm 2021 in North China?," *Natl. Sci. Rev.* **9** (3), nwab165 (2022).
11. C. Lok, "The snot-spattered experiments that show how far sneezes really spread," *Nature* **534** (7605), 24-26 (2016).
12. L. Bourouiba, E. Dehandschoewercker, and J. W. M. Bush, "Violent expiratory events: on coughing and sneezing," *J. Fluid Mech.* **745**, 537-563 (2014).
13. L. Bourouiba, "Turbulent Gas Clouds and Respiratory Pathogen Emissions: Potential Implications for Reducing Transmission of COVID-19," *JAMA* **323** (18),

1837-1838 (2020).

14. T. Dbouk, and D. Drikakis, "On coughing and airborne droplet transmission to humans," *Phys. Fluids* **32** (5), 053310 (2020).

15. S. K. Das, J. E. Alam, S. Plumari, and V. Greco, "Transmission of airborne virus through sneezed and coughed droplets," *Phys. Fluids* **32** (9), 097102 (2020).

16. P. Katre, S. Banerjee, S. Balusamy, and K. C. Sahu, "Fluid dynamics of respiratory droplets in the context of COVID-19: Airborne and surfaceborne transmissions," *Phys. Fluids* **33** (8), 081302 (2021).

17. S. Balachandar, and J. K. Eaton, "Turbulent Dispersed Multiphase Flow," *Annu. Rev. Fluid Mech.* **42** (1), 111-133 (2010).

18. B. Viggiano, T. Basset, S. Solovitz, T. Barois, M. Gibert, N. Mordant, L. Chevillard, R. Volk, M. Bourgoïn, and R. B. Cal, "Lagrangian diffusion properties of a free shear turbulent jet," *J. Fluid Mech.* **918**, A25 (2021).

19. K. Dhivyaraja, D. Gaddes, E. Freeman, S. Tadigadapa, and M. V. Panchagnula, "Dynamical similarity and universality of drop size and velocity spectra in sprays," *J. Fluid Mech.* **860**, 510-543 (2018).

20. P. O. A. L. Davies, M. J. Fisher, and M. J. Barratt, "The characteristics of the turbulence in the mixing region of a round jet," *J. Fluid Mech.* **15** (3), 337-367 (1963).

21. P. Bradshaw, D. H. Ferriss, and R. F. Johnson, "Turbulence in the noise-producing region of a circular jet," *J. Fluid Mech.* **19** (4), 591-624 (1964).

22. F. Yang, A. A. Pahlavan, S. Mendez, M. Abkarian, and H. A. Stone, "Towards improved social distancing guidelines: Space and time dependence of virus transmission from speech-driven aerosol transport between two individuals," *Phys. Rev. Fluids* **5** (12), 122501 (2020).

23. M. E. Rosti, S. Olivieri, M. Cavaiola, A. Seminara, and A. Mazzino, "Fluid dynamics of COVID-19 airborne infection suggests urgent data for a scientific design of social distancing," *Sci. Rep.* **10** (1), 22426 (2020).

24. E. K. Longmire, and J. K. Eaton, "Structure of a particle-laden round jet," *J. Fluid Mech.* **236**, 217-257 (1992).

25. A. V. Barve, S. Sahu, and K. Anupindi, "Effect of co-flow velocity ratio on evolution of poly-disperse particles in coaxial turbulent jets: A large-eddy simulation study," *Phys. Fluids* **32** (9), 093303 (2020).

26. H. Lu, H. Liu, W. Li, and J. Xu, "Factors influencing the characterization of bubbles produced by coaxial gas-particle jet flow," *Fuel* **108**, 723-730 (2013).

27. H. Lu, H. Liu, W. Li, J. Xu, and G. Cao, "Bubbling feature of an annular granular jet dispersed by a central air jet with acoustic excitation," *Fuel* **123**, 86-92 (2014).

28. C. Fang, J. Xu, H. Zhao, W. Li, and H. Liu, "Experimental investigation on

particle entrainment behaviors near a nozzle in gas–particle coaxial jets," *Powder Technol.* **286**, 55-63 (2015).

29. K. Rajamanickam, and S. Basu, "On the dynamics of vortex–droplet interactions, dispersion and breakup in a coaxial swirling flow," *J. Fluid Mech.* **827**, 572-613 (2017).

30. Z. Song, Q. Li, F. Li, Y. Chen, A. Ullah, S. Chen, and W. Wang, "MP-PIC simulation of dilute-phase pneumatic conveying in a horizontal pipe," *Powder Technol.* **410**, 117894 (2022).

31. Y. Tsuji, and Y. Morikawa, "LDV measurements of an air-solid two-phase flow in a horizontal pipe," *J. Fluid Mech.* **120**, 385-409 (1982).

32. H. Wang, Y. Chen, and W. Wang, "Scale - dependent nonequilibrium features in a bubbling fluidized bed," *AIChE J.* **64** (7), 2364-2378 (2018).

33. H. Lu, H.-F. Liu, W.-F. Li, and J.-L. Xu, "Bubble formation in an annular granular jet dispersed by a central air round jet," *AIChE J.* **59** (6), 1882-1893 (2013).

34. J. K. F. Eaton, J. R. , "Preferential concentration of particles by turbulence," *Int. J. Multiph. Flow* **20**, 169-209 (1994).

35. J. Sakakibara, R. B. Wicker, and J. K. Eaton, "Measurements of the particle-fluid velocity correlation and the extra dissipation in a round jet," *Int. J. Multiph. Flow* **22** (5), 883-881 (1996).

36. F. Prevost, J. Boree, H. J. Nuglisch, and G. Charnay, "Measurements of fluid/particle correlated motion in the far field of an axisymmetric jet," *Int. J. Multiph. Flow* **22** (4), 685-701 (1996).

37. X. Xie, Y. Li, A. T. Y. Chwang, P. L. Ho, and W. H. Seto, "How far droplets can move in indoor environments-revisiting the Wells evaporation-falling curve," *Indoor Air* **17** (3), 211-225 (2007).

38. H. Li, F. Y. Leong, G. Xu, Z. Ge, C. W. Kang, and K. H. Lim, "Dispersion of evaporating cough droplets in tropical outdoor environment," *Phys. Fluids* **32** (11), 113301 (2020).

39. K. Liu, M. Allahyari, J. Salinas, N. Zgheib, and S. Balachandar, "Investigation of theoretical scaling laws using large eddy simulations for airborne spreading of viral contagion from sneezing and coughing," *Phys. Fluids* **33** (6), 063318 (2021).

40. E. Renzi, and A. Clarke, "Life of a droplet: Buoyant vortex dynamics drives the fate of micro-particle expiratory ejecta," *Phys. Fluids* **32** (12), 123301 (2020).

41. D. Li, J. Fan, K. Luo, and K. Cen, "Direct numerical simulation of a particle-laden low Reynolds number turbulent round jet," *Int. J. Multiph. Flow* **37** (6), 539-554 (2011).

42. F. Picano, G. Sardina, P. Gualtieri, and C. M. Casciola, "Particle-laden jets: particle distribution and back-reaction on the flow," *ETC13* **318** (5), (2011).

43. E. Calvo, J. A. Garc ía, J. L. Santolaya, I. Garc ía, and L. A ía, "Measurements about the air motion in an acoustically forced jet: effects of the dispersed phase on the coherent flow structure," *Exp. Fluids* **55** (1), 1635 (2014).
44. E. Calvo, J. A. Garc ía, J. L. Santolaya, I. Garc ía, and L. A ía, "Periodic structure of the dispersed phase in a forced jet and their effects on the particle dispersion," *Int. J. Multiph. Flow* **82**, 119-142 (2016).
45. C. Wark, K. Eickmann, and C. Richards, "The structure of an acoustically forced, reacting two-phase jet," *Combust. Flame* **120**, 539-548 (2000).
46. R. Chein, and J. N. Chung, "Simulation of particle dispersion in a two-dimensional mixing layer," *AIChE J.* **34** (6), 946-954 (1988).
47. S. L. Anderson, and E. K. Longmire, "Particle motion in the stagnation zone of an impinging air jet," *J. Fluid Mech.* **299** (-1), 333-366 (1995).
48. M. R. Maxey, "The gravitational settling of aerosol particles in homogeneous turbulence and random flow fields," *J. Fluid Mech.* **174**, 441-465 (1987).
49. K. T. Kiger, and J. C. Lasheras, "The effect of vortex pairing on particle dispersion and kinetic energy transfer in a two-phase turbulent shear layer," *J. Fluid Mech.* **302**, 149-178 (1995).
50. L.-P. Wang, and M. R. Maxey, "Settling velocity and concentration distribution of heavy particles in homogeneous isotropic turbulence," *J. Fluid Mech.* **256**, 27-68 (1993).
51. Y. Yang, C. T. Crowe, J. N. Chung, and T. R. Troutt, "Experiments on particle dispersion in a plane wake," *Int. J. Multiph. Flow* **26**, 1583-1607 (2000).
52. D. J. Brandon, and S. K. Aggarwal, "A numerical Investigation of particle deposition on a square cylinder placed in a channel flow," *Aerosol Sci. Technol.* **34**, 340-352 (2001).
53. L. M. Cerecedo, L. A ía, and J. Ballester, "Experimental study on a non-dilute two-phase coflowing jet: Dynamics of particles in the near flow field," *Int. J. Multiph. Flow* **35** (5), 468-483 (2009).
54. A. Aliseda, A. Cartellier, F. Hainaux, and J. C. Lasheras, "Effect of preferential concentration on the settling velocity of heavy particles in homogeneous isotropic turbulence," *J. Fluid Mech.* **468**, 77-105 (2002).
55. J. E. Martin, and E. Meiburg, "The accumulation and dispersion of heavy particles in forced two - dimensional mixing layers. I. The fundamental and subharmonic cases," *Phys. Fluids* **6** (3), 1116-1132 (1994).
56. J. R. Fessler, and J. K. Eaton, "Particle response in a planar sudden expansion flow," *Exp. Therm. Fluid Sci.* **15** (4), 413-423 (1997).
57. A. J. Petersen, L. Baker, and F. Coletti, "Experimental study of inertial particles clustering and settling in homogeneous turbulence," *J. Fluid Mech.* **864**, 925-

and droplet-nuclei," *Epidemiol. Infect.* **44** (6), 471-479 (1946).

75. R. G. Loudon, and R. M. Roberts, "Droplet Expulsion from the Respiratory TRACT," *Am. Rev. Respir. Dis.* **95** (3), 435-442 (1967).

76. C. Y. H. Chao, M. P. Wan, L. Morawska, G. R. Johnson, Z. D. Ristovski, M. Hargreaves, K. Mengersen, S. Corbett, Y. Li, X. Xie, and D. Katoshevski, "Characterization of expiration air jets and droplet size distributions immediately at the mouth opening," *J. Aerosol Sci.* **40** (2), 122-133 (2009).

77. R. Tellier, "Review of aerosol transmission of influenza A virus," *Emerg. Infect. Dis.* **12** (11), 1657-1662 (2006).

78. R. Mittal, R. Ni, and J.-H. Seo, "The flow physics of COVID-19," *J. Fluid Mech.* **894**, F2 (2020).

79. S. Balachandar, S. Zaleski, A. Soldati, G. Ahmadi, and L. Bourouiba, "Host-to-host airborne transmission as a multiphase flow problem for science-based social distance guidelines," *Int. J. Multiph. Flow* **132**, 103439 (2020).

80. R. A. Weinstein, C. B. Bridges, M. J. Kuehnert, and C. B. Hall, "Transmission of Influenza: Implications for Control in Health Care Settings," *Clin. Infect. Dis.* **37** (8), 1094-1101 (2003).

81. M. Abkarian, S. Mendez, N. Xue, F. Yang, and H. A. Stone, "Speech can produce jet-like transport relevant to asymptomatic spreading of virus," *PNAS. USA* **117** (41), 25237-25245 (2020).

82. K. L. Chong, C. S. Ng, N. Hori, R. Yang, R. Verzicco, and D. Lohse, "Extended lifetime of respiratory droplets in a turbulent vapour puff and its implications on airborne disease transmission," *Phys. Rev. Lett.* **126** (3), 034502 (2021).

83. M.-R. Pendar, and J. C. Páscob, "Numerical modeling of the distribution of virus carrying saliva droplets during sneeze and cough," *Phys. Fluids* **32**, 083305 (2020).

84. L. Liu, J. Wei, Y. Li, and A. Ooi, "Evaporation and dispersion of respiratory droplets from coughing," *Indoor Air* **27** (1), 179-190 (2017).

85. J. D. Kulick, J. R. Fessler, and J. K. Eaton, "Particle response and turbulence modification in fully developed channel flow," *J. Fluid Mech.* **277**, 109-134 (1994).

86. T. Uchiyama, and A. Fukase, "Three-dimensional vortex simulation of particle-laden air jet," *Chem. Eng. Sci.* **61** (6), 1767-1778 (2006).

87. P. Bagchi, and S. Balachandar, "Effect of turbulence on the drag and lift of a particle," *Phys. Fluids* **15** (11), 3496-3513 (2003).

88. C. Lacour, D. Durox, S. Ducruix, and M. Massot, "Interaction of a polydisperse spray with vortices," *Exp. Fluids* **51** (2), 295-311 (2011).

89. R. A. Gore, and C. T. Crowe, "Effect of particle size on modulating turbulent intensity," *Int. J. Multiph. Flow* **15** (2), 279-285 (1989).

90. K. Hadinoto, E. N. Jones, C. Yurteri, and J. S. Curtis, "Reynolds number

dependence of gas-phase turbulence in gas-particle flows," *Int. J. Multiph. Flow* **31** (4), 416-434 (2005).

91. W. Hwang, and J. K. Eaton, "Turbulence attenuation by small particles in the absence of gravity," *Int. J. Multiph. Flow* **32** (12), 1386-1396 (2006).

92. J. Kussin, and M. Sommerfeld, "Experimental studies on particle behaviour and turbulence modification in horizontal channel flow with different wall roughness," *Exp. Fluids* **33** (1), 143-159 (2002).

93. C. Ljus, B. Johansson, and A.-E. Almstedt, "Turbulence modification by particles in a horizontal pipe flow," *Int. J. Multiph. Flow* **28** (7), 1075-1090 (2002).

94. G. Ooms, C. Poelma, P. Poesio, M. B. M. Pourquie, and J. Westerweel, "Verification of a model to predict the influence of particle inertia and gravity on a decaying turbulent particle-laden flow," *Int. J. Multiph. Flow* **34** (1), 29-41 (2008).

95. H. Tashiro, E. Watanabe, H. Shinano, K. Funatsu, and Y. Tomita, "Effect of mixing gas-fine particle suspension flow with small amount of coarse ones in a horizontal pipe," *Int. J. Multiph. Flow* **27** (11), 2001-2013 (2001).

96. Z. Yuan, and E. E. Michaelides, "Turbulence modulation in particulate flows—A theoretical approach," *Int. J. Multiph. Flow* **18** (5), 779-785 (1992).

97. S. Elghobashi, and G. C. Truesdell, "On the two-way interaction between homogeneous turbulence and dispersed solid particles. I: Turbulence modification," *Phys. Fluids* **5** (7), 1790-1801 (1993).

98. G. C. Truesdell, and S. Elghobashi, "On the two-way interaction between homogeneous turbulence and dispersed solid particles. II. Particle dispersion," *Phys. Fluids* **6** (3), 1405-1407 (1994).

99. F. Li, H. Qi, and C. You, "Phase Doppler anemometry measurements and analysis of turbulence modulation in dilute gas-solid two-phase shear flows," *J. Fluid Mech.* **663**, 434-455 (2010).

100. C. T. Crowe, "On models for turbulence modulation in fluid-particle flows," *Int. J. Multiph. Flow* **26** (5), 719-727 (2000).

101. V. M. Kenning, and C. T. Crowe, "On the effect of particles on carrier phase turbulence in gas-particle flows," *Int. J. Multiph. Flow* **23** (2), 403-408 (1997).

102. E. J. Bolio, and J. L. Sinclair, "Gas turbulence modulation in the pneumatic conveying of massive particles in vertical tubes," *Int. J. Multiph. Flow* **21** (6), 985-1001 (1995).

103. L. P. Yarin, and G. Hetsroni, "Turbulence intensity in dilute two-phase flows—3 The particles-turbulence interaction in dilute two-phase flow," *Int. J. Multiph. Flow* **20** (1), 27-44 (1994).

104. C. Crowe, "Turbulence modulation of fluid-particle flows-A basic approach," *Third Int. Conf. Multiphase Flows, Lyon, France*, (1998).

105. A. Y. Varaksin, Y. Kurosaki, I. Satch, Y. V. Polezhaev, and A. Polyahov, "Experimental study of the direct influence of the small particles on the carrier air turbulence intensity for pipe flow," *Third Int. Conf. Multiphase Flows, Lyon, France* (1998).
106. Z. Zhuoxiong, Z. Lixing, and Q. I. Haiying, "Large Eddy Simulation of Particle Wake Effect and RANS Simulation of Turbulence Modulation in Gas-Particle Flows," *Chin. J. Chem. Eng.* **15** (1), 12-16 (2007).
107. T. C. W. Lau, and G. J. Nathan, "Influence of Stokes number on the velocity and concentration distributions in particle-laden jets," *J. Fluid Mech.* **757**, 432-457 (2014).
108. W. Wang, B. Lu, J. Geng, and F. Li, "Mesoscale drag modeling: a critical review," *Curr. Opin. Chem. Eng.* **29**, 96-103 (2020).
109. C. J. Kähler, T. Astarita, P. P. Vlachos, J. Sakakibara, R. Hain, S. Discetti, R. La Foy, and C. Cierpka, "Main results of the 4th International PIV Challenge," *Exp. Fluids* **57** (6), 97 (2016).
110. G. Castanet, P. Dunand, O. Caballina, and F. Lemoine, "High-speed shadow imagery to characterize the size and velocity of the secondary droplets produced by drop impacts onto a heated surface," *Exp. Fluids* **54** (3), 1489 (2013).
111. X. Dong, X. Wang, W. Zhou, F. Wang, X. Tang, and X. Cai, "3D particle streak velocimetry by defocused imaging," *Particuology* **72**, 1-9 (2023).
112. J. Westerweel, G. E. Elsinga, and R. J. Adrian, "Particle Image Velocimetry for Complex and Turbulent Flows," *Annu. Rev. Fluid Mech.* **45** (1), 409-436 (2013).
113. D. E. J. Stock, J. T.; Crowe, C. T.; and Eschbach, J. E., "Measurement of both gas and particle velocity in turbulent two-phase flow," *Symp. Turbul. Liquids* **12**, 91-100 (1975).
114. M. Raffel, C. E. Willert, F. Scarano, C. J. Kähler, S. T. Wereley, and J. Kompenhans, *Particle Image Velocimetry* (Springer, Switzerland, 2018), pp. 6-20.
115. M. Stanislas, K. Okamoto, C. J. Kähler, J. Westerweel, and F. Scarano, "Main results of the Third International PIV Challenge," *Exp. Fluids* **45** (1), 27-71 (2008).
116. M. Stanislas, K. Okamoto, C. J. Kähler, and J. Westerweel, "Main results of the Second International PIV Challenge," *Exp. Fluids* **39** (2), 170-191 (2005).
117. J. Heyman, "TracTrac: A fast multi-object tracking algorithm for motion estimation," *Comput. Geosci.* **128**, 11-18 (2019).
118. T. Janke, R. Schwarze, and K. Bauer, "Part2Track: A MATLAB package for double frame and time resolved Particle Tracking Velocimetry," *SoftwareX* **11**, 100413 (2020).
119. J. Cortina-Fernández, C. Sanmiguel Vila, A. Ianiro, and S. Discetti, "From sparse data to high-resolution fields: ensemble particle modes as a basis for high-

- resolution flow characterization," *Exp. Therm. Fluid Sci.* **120**, 110178 (2021).
120. M. Patel, S. E. Leggett, A. K. Landauer, I. Y. Wong, and C. Franck, "Rapid, topology-based particle tracking for high-resolution measurements of large complex 3D motion fields," *Sci. Rep.* **8** (1), 5581 (2018).
121. A. Clark, N. Machicoane, and A. Aliseda, "A quantitative study of track initialization of the four-frame best estimate algorithm for three-dimensional Lagrangian particle tracking," *Meas. Sci. Technol.* **30** (4), 045302 (2019).
122. M. Sinhuber, K. van der Vaart, R. Ni, J. G. Puckett, D. H. Kelley, and N. T. Ouellette, "Three-dimensional time-resolved trajectories from laboratory insect swarms," *Sci. Data* **6** (1), 190036 (2019).
123. M. Novara, D. Schanz, N. Reuther, C. J. Kähler, and A. Schröder, "Lagrangian 3D particle tracking in high-speed flows: Shake-The-Box for multi-pulse systems," *Exp. Fluids* **57** (8), 128 (2016).
124. M. Bourgoin, and S. G. Huisman, "Using ray-traversal for 3D particle matching in the context of particle tracking velocimetry in fluid mechanics," *Rev. Sci. Instrum.* **91** (8), 085105 (2020).
125. L. Zhang, Z. Jiang, F. Weigler, F. Herz, J. Mellmann, and E. Tsotsas, "PTV measurement and DEM simulation of the particle motion in a flighted rotating drum," *Powder Technol.* **363**, 23-37 (2020).
126. D. W. Carter, R. Hassaini, J. Eshraghi, P. Vlachos, and F. Coletti, "Multi-scale imaging of upward liquid spray in the far-field region," *Int. J. Multiph. Flow* **132**, 103430 (2020).
127. T. C. W. Lau, and G. J. Nathan, "A method for identifying and characterising particle clusters in a two-phase turbulent jet," *Int. J. Multiph. Flow* **88**, 191-204 (2017).
128. Z.-H. Shi, W.-F. Li, W.-W. Qian, H.-F. Liu, and F.-C. Wang, "Liquid-like granular film from granular jet impact," *Chem. Eng. Sci.* **162**, 1-9 (2017).
129. Z.-H. Shi, W.-F. Li, H.-F. Liu, and F.-C. Wang, "Liquid-like wave structure on granular film from granular jet impact," *AIChE J.* **63** (8), 3276-3285 (2017).
130. Y. Shuai, X. Wang, Z. Huang, J. Sun, Y. Yang, Z. Liao, J. Wang, and Y. Yang, "Experimental measurement of bubble breakup in a jet bubbling reactor," *AIChE J.* **67** (1), e17062 (2020).
131. X. Chen, W. Zhong, and T. J. Heindel, "Orientation of cylindrical particles in a fluidized bed based on stereo X-ray particle tracking velocimetry (XPTV)," *Chem. Eng. Sci.* **203**, 104-112 (2019).
132. X. Chen, W. Zhong, and T. J. Heindel, "Using stereo XPTV to determine cylindrical particle distribution and velocity in a binary fluidized bed," *AIChE J.* **65** (2), 520-535 (2019).
133. C. R. Carlson, and R. L. Peskin, "One-dimensional particle velocity

probability densities measured in turbulent gas-particle duct flow," *Int. J. Multiph. Flow* **2** (1), 67-78 (1975).

134. Z. M. Durst F, "Laser Doppler measurements in two-phase flows," *Proceedings of the LDA Symposium*, 403-429 (1976).

135. S. L. Lee, and F. Durst, "On the motion of particles in turbulent duct flows," *Int. J. Multiph. Flow* **8** (2), 125-146 (1982).

136. Y. A. Hassan, T. K. Blanchat, C. H. Seeley, and R. E. Canaan, "Simultaneous velocity measurements of both components of a two-phase flow using particle image velocimetry," *Int. J. Multiph. Flow* **18** (3), 371-395 (1992).

137. M. Sommerfeld, and N. Huber, "Experimental analysis and modelling of particle-wall collisions," *Int. J. Multiph. Flow* **25** (6), 1457-1489 (1999).

138. R. B. Wicker, and J. K. Eaton, "Effect of injected longitudinal vorticity on particle dispersion in a swirling, coaxial Jet," *Trans. ASME* **121** (4), 766-772 (1999).

139. R. B. Wicker, and J. K. Eaton, "Structure of a swirling, recirculating coaxial free jet and its effect on particle motion," *Int. J. Multiph. Flow* **27** (6), 949-970 (2001).

140. K. T. Kiger, and C. Pan, "PIV Technique for the Simultaneous Measurement of Dilute Two-Phase Flows," *J. Fluid Eng-T ASME* **122** (4), 811-818 (2000).

141. D. A. Khalitov, and E. K. Longmire, "Simultaneous two-phase PIV by two-parameter phase discrimination," *Exp. Fluids* **32** (2), 252-268 (2002).

142. D. E. Groszmann, and C. B. Rogers, "Turbulent scales of dilute particle-laden flows in microgravity," *Phys. Fluids* **16** (12), 4671-4684 (2004).

143. T. Virdung, and A. Rasmuson, "Hydrodynamic properties of a turbulent confined solid-liquid jet evaluated using PIV and CFD," *Chem. Eng. Sci.* **62** (21), 5963-5978 (2007).

144. C. H. Birzer, P. A. M. Kalt, and G. J. Nathan, "The influences of jet precession on near field particle distributions," *Int. J. Multiph. Flow* **35** (3), 288-296 (2009).

145. C. H. Birzer, P. A. M. Kalt, and G. J. Nathan, "The influences of jet precession on large-scale instantaneous turbulent particle clusters," *Int. J. Multiph. Flow* **37** (4), 394-402 (2011).

146. C. H. Birzer, P. A. M. Kalt, and G. J. Nathan, "A method to provide statistical measures of large-scale instantaneous particle clusters from planar images," *Exp. Fluids* **51** (3), 641-656 (2011).

147. F. J. Diez, M. M. Torregrosa, and S. Pothos, "A Comparison Between Round Turbulent Jets and Particle-Laden Jets in Crossflow by Using Time-Resolved Stereoscopic Particle Image Velocimetry," *J. Fluid Eng-T ASME* **133** (9), 091301-091301 (2011).

148. A. Capone, G. P. Romano, and A. Soldati, "Experimental investigation on interactions among fluid and rod-like particles in a turbulent pipe jet by means of

- particle image velocimetry," *Exp. Fluids* **56** (1), 1 (2014).
149. D. Schanz, S. Gesemann, and A. Schröder, "Shake-The-Box: Lagrangian particle tracking at high particle image densities," *Exp. Fluids* **57** (5), 70 (2016).
150. R. F. L. Cerqueira, E. E. Paladino, B. K. Ynumaru, and C. R. Maliska, "Image processing techniques for the measurement of two-phase bubbly pipe flows using particle image and tracking velocimetry (PIV/PTV)," *Chem. Eng. Sci.* **189**, 1-23 (2018).
151. K. Harth, U. Kornek, T. Trittel, U. Strachauer, S. Home, K. Will, and R. Stannarius, "Granular gases of rod-shaped grains in microgravity," *Phys. Rev. Lett.* **110** (14), 144102 (2013).
152. R. Hartley, and A. Zisserman, *Multiple view geometry in computer vision 2nd* (Cambridge University Press, Cambridge, UK, 2003), pp. 25-60.
153. B. Wieneke, "Iterative reconstruction of volumetric particle distribution," *Meas. Sci. Technol.* **24** (2), 024008 (2013).
154. N. Machicoane, A. Aliseda, R. Volk, and M. Bourgoïn, "A simplified and versatile calibration method for multi-camera optical systems in 3D particle imaging," *Rev. Sci. Instrum.* **90** (3), 035112 (2019).
155. J. Heikkilä, and O. Silven, "A four-step camera calibration procedure with implicit image correction," *Proceedings of IEEE CVPR*, 1106-1112 (1997).
156. D. Adhikari, and E. K. Longmire, "Visual hull method for tomographic PIV measurement of flow around moving objects," *Exp. Fluids* **53** (4), 943-964 (2012).
157. J. Klinkenberg, H. C. de Lange, and L. Brandt, "Linear stability of particle laden flows: the influence of added mass, fluid acceleration and Basset history force," *Meccanica* **49** (4), 811-827 (2014).
158. A. A. Mostafa, and S. E. Elghobashi, "A two-equation turbulence model for jet flows laden with vaporizing droplets," *Int. J. Multiph. Flow* **11** (4), 515-533 (1985).
159. D. W. I. Rouson, and J. K. Eaton, "On the preferential concentration of solid particles in turbulent channel flow," *J. Fluid Mech.* **428**, 149-169 (2001).
160. S. Laín, and M. Sommerfeld, "Numerical calculation of pneumatic conveying in horizontal channels and pipes: Detailed analysis of conveying behaviour," *Int. J. Multiph. Flow* **39**, 105-120 (2012).
161. B. Wang, H. Wu, and X. F. Wan, "Transport and fate of human expiratory droplets-A modeling approach," *Phys. Fluids* **32** (8), 083307 (2020).
162. L. Bourouiba, "A Sneeze," *N. Engl. J. Med.* **375** (8), e15 (2016).
163. R. Di Felice, "The voidage function for fluid-particle interaction systems," *Int. J. Multiph. Flow* **20** (1), 153-159 (1994).
164. W. Wang, B. Lu, N. Zhang, Z. Shi, and J. Li, "A review of multiscale CFD for gas–solid CFB modeling," *Int. J. Multiph. Flow* **36** (2), 109-118 (2010).
165. S. Tenneti, R. Garg, and S. Subramaniam, "Drag law for monodisperse gas–

solid systems using particle-resolved direct numerical simulation of flow past fixed assemblies of spheres," *Int. J. Multiph. Flow* **37** (9), 1072-1092 (2011).

166. Y. Tian, J. Geng, and W. Wang, "On the choice of mesoscale drag markers," *AIChE J.* **68** (4), e17558 (2022).

167. Y. Igci, S. Pannala, S. Benyahia, and S. Sundaresan, "Validation Studies on Filtered Model Equations for Gas-Particle Flows in Risers," *Ind. Eng. Chem. Res.* **51** (4), 2094-2103 (2012).

168. C. T. Crowe, J. D. Schwarzkopf, M. Sommerfeld, and Y. Tsuji, *Multiphase Flow with Droplets and Particles 2nd* (CRC, Boca Raton, 2012), pp. 67-102.

169. L. Schiller, and N. A., "Über die grundlegenden Berechnungen bei der Schwerkraftaufbereitung," *Vereines Deutscher Inge.* **77** (5), 318-327 (1933).

170. G. Xu, and J. Li, "Analytical solution of the energy-minimization multi-scale model for gas–solid two-phase flow," *Chem. Eng. Sci.* **53** (7), 1349-1366 (1998).

171. C. Y. Wen, and Y. H. Yu, "Mechanics of fluidization," *Chem. Eng. Prog. Symp. Ser.* **62** (2), 100-111 (1966).

172. S. Ergun, Orning, A. A. , "Fluid flow through randomly packed columns and fluidized beds," *Ind. Eng. Chem.* **41** (6), 1179-1184 (1949).

173. P. U. Foscolo, L. G. Gibilaro, and S. P. Waldram, "A unified model for particulate expansion of fluidised beds and flow in fixed porous media," *Chem. Eng. Sci.* **38** (8), 1251-1260 (1983).

174. D. Gidaspow, *Multiphase Flow and Fluidization* (Elsevier, 1994), pp. 31-58.

175. W. Wang, and J. Li, "Simulation of gas–solid two-phase flow by a multi-scale CFD approach—of the EMMS model to the sub-grid level," *Chem. Eng. Sci.* **62** (1), 208-231 (2007).

176. N. Yang, W. Wang, W. Ge, and J. Li, "Choosing structure-dependent drag coefficient in modeling gas-solid two-phase flow," *Particuology* **1** (1), 38-41 (2003).

177. X. Gao, T. Li, A. Sarkar, L. Lu, and W. A. Rogers, "Development and validation of an enhanced filtered drag model for simulating gas-solid fluidization of Geldart A particles in all flow regimes," *Chem. Eng. Sci.* **184**, 33-51 (2018).

178. A. Sarkar, F. E. Milioli, S. Ozarkar, T. Li, X. Sun, and S. Sundaresan, "Filtered sub-grid constitutive models for fluidized gas-particle flows constructed from 3-D simulations," *Chem. Eng. Sci.* **152**, 443-456 (2016).

179. J. Li, "Multi-scale modeling and method of energy minimization for particle–fluid two-phase flow," Chinese Academy of Sciences, 1987.

180. J. Li, and M. Kwauk, "Introduction to EMMS model for fluid-particle two-phase flow," *Chem. Eng.(China)* **20** (2), 26-31 (1992).

181. J. Li, and M. Kwauk, "Energy-minimization multi-scale model for circulating fluidized bed," *Sci. Sin. B* **4** (11), 1127-1137 (1992).

182. J. Li, W. Ge, W. Wang, N. Yang, X. Liu, L. Wang, X. He, X. Wang, J. Wang, and M. Kwauk, *From Multiscale Modeling to Meso-Science* (Springer Berlin, 2013), pp.
183. K. Hong, W. Wang, Q. Zhou, J. Wang, and J. Li, "An EMMS-based multi-fluid model (EFM) for heterogeneous gas–solid riser flows: Part I. Formulation of structure-dependent conservation equations," *Chem. Eng. Sci.* **75**, 376-389 (2012).
184. S. Radl, and S. Sundaresan, "A drag model for filtered Euler–Lagrange simulations of clustered gas–particle suspensions," *Chem. Eng. Sci.* **117**, 416-425 (2014).
185. G. Rudinger, "Effective drag coefficient for gas-particle flow in shock tubes," *J. Basic Eng.* **92** (1), 165-172 (1970).
186. ANSYS, *ANSYS Fluent Theory Guide: Turbulence* (ANSYS, Inc., U.S.A., 2018), pp. 39-57.
187. M. L. Hunt, R. C. Weathers, A. T. Lee, C. E. Brennen, and C. R. Wassgren, "Effects of horizontal vibration on hopper flows of granular materials," *Phys. Fluids* **11** (1), 68-75 (1998).
188. C. Willert, M. Raffel, J. Kompenhans, B. Stasicki, and C. Kähler, "Recent applications of particle image velocimetry in aerodynamic research," *Flow Meas. Instrum.* **7** (3), 247-256 (1996).
189. C. E. Willert, and M. Gharib, "Digital particle image velocimetry," *Exp. Fluids* **10** (4), 181-193 (1991).
190. D. Bradley, and G. Roth, "Adaptive Thresholding using the Integral Image," *J. Graph. GPU Game Tools* **12** (2), 13-21 (2007).
191. H. K. Yuen, J. Princen, J. Illingworth, and J. Kittler, "Comparative study of Hough Transform methods for circle finding," *Image Vis. Comput.* **8** (1), 71-77 (1990).
192. T. J. Atherton, and D. J. Kerbyson, "Size invariant circle detection," *Image Vis. Comput.* **17** (11), 795-803 (1999).
193. N. A. Malik, T. Dracos, and D. A. Papantoniou, "Particle tracking velocimetry in three-dimensional flows," *Exp. Fluids* **15** (4), 279-294 (1993).
194. C. Cierpka, B. Lütke, and C. J. Kähler, "Higher order multi-frame particle tracking velocimetry," *Exp. Fluids* **54** (5), 1533 (2013).
195. T. Fuchs, R. Hain, and C. J. Kähler, "Non-iterative double-frame 2D/3D particle tracking velocimetry," *Exp. Fluids* **58** (9), 119 (2017).
196. N. T. Ouellette, H. Xu, and E. Bodenschatz, "A quantitative study of three-dimensional Lagrangian particle tracking algorithms," *Exp. Fluids* **40** (2), 301-313 (2006).
197. R. E. Kalman, "A new approach to linear filtering and prediction problems," *J. Basic Eng.* **82**, 34-45 (1960).

-
198. J. Edmonds, "Paths, Trees, and Flowers," *Can. J. Math.* **17**, 449-467 (1965).
199. R. E. a. B. Kalman, R. S., "New results in linear filtering and prediction theory," *J. Basic Eng.* **96**, 95-108 (1961).
200. R. De Maesschalck, D. Jouan-Rimbaud, and D. L. Massart, "The Mahalanobis distance," *Chemom. Intell. Lab. Syst.* **50** (1), 1-18 (2000).
201. S. Martello, "Jenő Egerváry: from the origins of the Hungarian algorithm to satellite communication," *Cent. Eur. J. Oper. Res.* **18** (1), 47-58 (2010).
202. J. Munkres, "Algorithms for the assignment and transportation problems," *J. Soc. Industr. Appl. Math.* **5** (1), 32-38 (1957).
203. H. W. Kuhn, "The Hungarian method for the assignment problem," *Nav. Res. Logist. Quart.* **2** (1-2), 83-97 (1955).
204. B. Spinewine, H. Capart, M. Larcher, and Y. Zech, "Three-dimensional Vorono i imaging methods for the measurement of near-wall particulate flows," *Exp. Fluids* **34** (2), 227 (2003).
205. K. Takehara, and T. Etoh, "Accurate estimation of vorticity from PTV velocity distribution," *Proc. of 8th International Symposium on Particle Image Velocimetry-PIV09* **185**, (2009).
206. K. Takehara, R. J. Adrian, G. T. Etoh, and K. T. Christensen, "A Kalman tracker for super-resolution PIV," *Exp. Fluids* **29** (1), S034-S041 (2000).
207. K. Nishino, N. Kasagi, and M. Hirata, "Three-dimensional particle tracking velocimetry based on automated digital image processing," *J. Fluids Eng.* **111** (4), 384-391 (1989).
208. T. Uemura, Y. Ueda, and M. Iguchi, "Fundamentals of Experimental Visualization," *Flow Visualization in Materials Processing: Practical Techniques and Selected Applications*, 19-48 (2018).
209. K. Harth, T. Trittel, S. Wegner, and R. Stannarius, "Free Cooling of a Granular Gas of Rodlike Particles in Microgravity," *Phys. Rev. Lett.* **120** (21), 214301 (2018).
210. F. Yamamoto, T. Uemura, and M. Iguchi, "High speed algorithm of 2D and 3D PTV based on binary correlation method," *Int. Symp. Img. Transp. Proc.*, 321-332 (1992).
211. K. Nishino, and K. Torii, "A fluid-dynamically optimum particle tracking method for 2-D PTV: triple pattern matching algorithm," *Int. Symp. Transp. Phenom. Therm. Eng.*, 339-344 (1993).
212. T. Kobayashi, "Development of a real-time velocity measurement system for two-dimensional flow fields using a digital image processing technique," *Trans. JSME* **55**, 107-115 (1989).
213. S. C. Crow, and F. H. Champagne, "Orderly structure in jet turbulence," *J.*

Fluid Mech. **48** (3), 547-591 (1971).

214. J. Trolinger, D. Weber, and W. Rose, "An aero-optical test and diagnostics simulation technique," *AIAA 40th ASME A02*, 13877 (2002).

215. A. Krothapalli, L. Venkatakrisnan, L. Lourenco, B. Greska, and R. Elavarasan, "Turbulence and noise suppression of a high-speed jet by water injection," *J. Fluid Mech.* **491**, 131-159 (2003).

216. G. Raman, K. B. M. Q. Zaman, and E. J. Rice, "Initial turbulence effect on jet evolution with and without tonal excitation," *Phys. Fluids* **1** (7), 1240-1248 (1989).

217. S. S. Aleyasin, M. F. Tachie, and M. Koupriyanov, "PIV Measurements in the Near and Intermediate Field Regions of Jets Issuing from Eight Different Nozzle Geometries," *Flow Turbul. Combust.* **99** (2), 329-351 (2017).

218. F. Prevost, J. Boree, H.-J. Nuglisch, and G. Charnay, "Characterization of a polydispersed particle-laden jet using a phase Doppler anemometer," *Proc. ICLASS-94*, 938-945 (1994).

219. A. Agrawal, and R. Bhardwaj, "Reducing chances of COVID-19 infection by a cough cloud in a closed space," *Phys. Fluids* **32** (10), 101704 (2020).

220. A. Fabregat, F. Gisbert, A. Vernet, S. Dutta, K. Mittal, and J. Pallarès, "Direct numerical simulation of the turbulent flow generated during a violent expiratory event," *Phys. Fluids* **33** (3), 035122 (2021).

221. F. Picano, G. Sardina, P. Gualtieri, and C. M. Casciola, "Anomalous memory effects on transport of inertial particles in turbulent jets," *Phys. Fluids* **22** (5), 051705 (2010).

222. C. M. Hrenya, and J. L. Sinclair, "Effects of particle-phase turbulence in gas-solid flows," *AIChE J.* **43** (4), 853-869 (1997).

223. W. Wang, and Y. Li, "Simulation of the clustering phenomenon in a fast fluidized bed: The importance of drag correlation," *Chinese J. Chem. Eng.* **12** (3), 335-341 (2004).

224. R. Clift, J. R. Grace, and M. E. Weber, *Bubbles, Drops and Particles* (Academic Press, New York, 1978), pp. 33-35.

225. C. T. Crowe, and E. E. Michaelides, *Multiphase flow handbook: Interactions of fluids with particles, drops, and bubbles* (Taylor & Francis Group, 2006), pp. 32-33.

226. R. W. Hockney, "The potential calculation and some applications," *Methods Comput. Phys.* **9**, 135-211 (1970).

227. G. K. Batchelor, "Diffusion in free turbulent shear flows," *J. Fluid Mech.* **3** (1), 67-80 (1957).

228. T. G. Malmstrom, A. T. Kirkpatrick, B. Christensen, and K. D. Knappmiller, "Centreline velocity decay measurements in low-velocity axisymmetric jets," *J. Fluid Mech.* **346**, 363-377 (1997).

229. C. H. Birzer, "Correlative analysis of organised structures in turbulent jets," *Exp. Fluids* **53** (6), 1681-1691 (2012).
230. G. I. Taylor, "Diffusion by continuous movements," *Proc. London Math. Soc.* **20** (1), 196-212 (1921).
231. H. J. Hussein, S. P. Capp, and W. K. George, "Velocity measurements in a high-Reynolds-number, momentum-conserving, axisymmetric, turbulent jet," *J. Fluid Mech.* **258**, 31-75 (1994).
232. B. C. R. Ewan, and K. Moodie, "Structure and Velocity Measurements in Underexpanded Jets," *Combust. Sci. Tech.* **45** (5-6), 275-288 (1986).
233. E. Ferdman, M. V. Otugen, and S. Kim, "Effect of Initial Velocity Profile on the Development of Round Jets," *J. Propul. Power* **16** (4), 676-686 (2000).
234. I. U. Atthanayake, P. Denissenko, Y. M. Chung, and P. J. Thomas, "Formation-breakdown cycle of turbulent jets in a rotating fluid," *J. Fluid Mech.* **868**, 666-697 (2019).
235. I. Wygnanski, and H. Fiedler, "Some measurements in the self-preserving jet," *J. Fluid Mech.* **38** (3), 577-612 (1969).
236. I. M. Kennedy, and M. H. Moody, "Particle dispersion in a turbulent round jet," *Exp. Therm. Fluid Sci.* **18** (1), 11-26 (1998).
237. J. Fan, X. Zhang, L. Chen, and K. Cen, "New stochastic particle dispersion modeling of a turbulent particle-laden round jet," *Chem. Eng. J.* **66** (3), 207-215 (1997).
238. W. H. Snyder, and J. L. Lumley, "Some measurements of particle velocity autocorrelation functions in a turbulent flow," *J. Fluid Mech.* **48** (1), 41-71 (1971).
239. J.-S. Ferenc, and Z. N ada, "On the size distribution of Poisson Voronoi cells," *Physica A* **385** (2), 518-526 (2007).
240. S. Miller, and S. Luding, "Cluster growth in two- and three-dimensional granular gases," *Phys. Rev. E* **69** (3), 031305 (2004).
241. C. Singh, and M. G. Mazza, "Early-stage aggregation in three-dimensional charged granular gas," *Phys. Rev. E* **97** (2), 022904 (2018).
242. H. Wang, Y. Chen, and W. Wang, "Particle-level dynamics of clusters: Experiments in a gas-fluidized bed," *AIChE J.* **68** (3), e17525 (2022).
243. M. A. van der Hoef, M. van Sint Annaland, N. G. Deen, and J. A. M. Kuipers, "Numerical Simulation of Dense Gas-Solid Fluidized Beds: A Multiscale Modeling Strategy," *Annu. Rev. Fluid Mech.* **40** (1), 47-70 (2008).
244. S. Subramaniam, and S. Balachandar, *Modeling Approaches and Computational Methods for Particle-laden Turbulent Flows* (Elsevier, London, 2023), pp. 81-106.
245. B. E. Launder, and D. B. Spalding, "The numerical computation of turbulent flows," *Comput. Methods Appl. Mech. Eng.* **3** (2), 269-289 (1974).

246. S. Geiss, A. Dreizler, Z. Stojanovic, M. Chrigui, A. Sadiki, and J. Janicka, "Investigation of turbulence modification in a non-reactive two-phase flow," *Exp. Fluids* **36** (2), 344-354 (2004).
247. M. Ebrahimi, M. Crapper, and J. Y. Ooi, "Numerical and experimental study of horizontal pneumatic transportation of spherical and low-aspect-ratio cylindrical particles," *Powder Technol.* **293**, 48-59 (2016).
248. V. Yakhot, and S. A. Orszag, "Renormalization group analysis of turbulence. I. Basic theory," *J. Sci. Comput.* **1** (1), 3-51 (1986).
249. T.-H. Shih, W. W. Liou, A. Shabbir, Z. Yang, and J. Zhu, "A new k- ϵ eddy viscosity model for high reynolds number turbulent flows," *Computers & Fluids* **24** (3), 227-238 (1995).
250. S. E. Kim, D. Choudhury, and B. Patel, *Computations of Complex Turbulent Flows Using the Commercial Code Fluent* (Springer Netherlands, Dordrecht, 1999).
251. W. C. Reynolds, "Fundamentals of turbulence for turbulence modelling and simulation," Lecture Notes for Von Karman Institute Agard Report **755**, 005793 (1987).
252. T.-H. Shih, J. Zhu, and J. L. Lumley, "A new Reynolds stress algebraic equation model," NASA TM **95**, 11953 (1994).
253. A. Xu, S. Tao, L. Shi, and H.-D. Xi, "Transport and deposition of dilute microparticles in turbulent thermal convection," *Phys. Fluids* **32** (8), (2020).
254. M. R. Maxey, and J. J. Riley, "Equation of motion for a small rigid sphere in a nonuniform flow," *Phys. Fluids* **26** (4), 883-889 (1983).
255. Q. Li, R. Zhu, W. Wang, Y. Chen, F. Li, and T. Furuhashi, "Time-resolved particle-scale dynamics of a particle-laden jet," *Phys. Fluids* **35** (1), 013309 (2023).
256. D. Liu, *Fluid Dynamic of Two-Phase Systems* (Higher Education Press, Beijing, 1993), pp. 25-33.
257. P. G. Saffman, "The lift on a small sphere in a slow shear flow," *J. Fluid Mech.* **22** (2), 385-400 (1965).
258. D. I. Graham, and P. W. James, "Turbulent dispersion of particles using eddy interaction models," *Int. J. Multiph. Flow* **22** (1), 157-175 (1996).
259. L. Tian, and G. Ahmadi, "Particle deposition in turbulent duct flows—comparisons of different model predictions," *J. Aerosol Sci.* **38** (4), 377-397 (2007).
260. F. D. Vanna, F. Picano, and E. Benini, "A sharp-interface immersed boundary method for moving objects in compressible viscous flows," *Comput. Fluids* **201**, 104415 (2020).
261. S. A. Morsi, and A. J. Alexander, "An investigation of particle trajectories in two-phase flow systems," *J. Fluid Mech.* **55** (2), 193-208 (1972).
262. D. Gidaspow, "Hydrodynamics of Fluidization and Heat Transfer: Supercomputer Modeling," *Appl. Mech. Rev.* **39** (1), 1-23 (1986).

263. J. Wei, and Y. Li, "Enhanced spread of expiratory droplets by turbulence in a cough jet," *Build. Environ.* **93**, 86-96 (2015).
264. J. Capecelatro, and J. Wagner, "Gas-Particle Dynamics in High-Speed Flows," *Annu. Rev. Fluid Mech.* **56**, 1-27 (2024).
265. G. Xu, "Hydrodynamic modeling for heterogeneous flow structure in circulating fluidized beds," Chinese Academy of Science, 1996.
266. J. H. Dallavalle, *Micromeritics (2nd edition)* (Pitman Publishing Corp., New York, 1948), pp. 23-33.
267. Z. W. N., and R. J. F., "Sedimentation and fluidisation: Part I," *Trans. Inst. Chem. Eng* **32**, 35-53 (1954).
268. A. Haider, and O. Levenspiel, "Drag coefficient and terminal velocity of spherical and nonspherical particles," *Powder Technol.* **58** (1), 63-70 (1989).
269. R. H. Perry, *Perry's Chemical Engineer's Handbook* (McGraw-Hill Company, New York, 1999), pp. 5-33-65.
270. B. S. Massey, *Mechanics of Fluids Ninth edition* (CRC Press, New York, 2012), pp. 331-336.
271. R. Clift, and W. H. Gauvin, "Motion of entrained particles in gas streams," *Can. J. Chem. Eng.* **49** (4), 439-448 (1971).
272. O. Molerus, "A coherent representation of pressure drop in fixed beds and of bed expansion for particulate fluidized beds," *Chem. Eng. Sci.* **35** (6), 1331-1340 (1980).
273. C. Y. Chow *An introduction to computational fluid dynamics* (Wiley, New York, 1980), pp. 5-24.
274. F. M. White, *Viscous Fluid Flow* (McGraw-Hill, New York, 1991), pp. 11-12.
275. G. H. Ganser, "A rational approach to drag prediction of spherical and nonspherical particles," *Powder Technol.* **77** (2), 143-152 (1993).
276. A. B. Liu, D. Mather, and R. D. Reitz, "Modeling the effects of drop drag and breakup on fuel sprays," *SAE Trans.* **102** (3), 83-95 (1993).
277. J. Happel, "Viscous flow in multiparticle systems: Slow motion of fluids relative to beds of spherical particles," *AIChE J.* **4** (2), 197-201 (1958).
278. M. Ishii, and N. Zuber, "Drag coefficient and relative velocity in bubbly, droplet or particulate flows," *AIChE J.* **25** (5), 843-855 (1979).
279. L. G. Gibilaro, R. Di Felice, S. P. Waldram, and P. U. Foscolo, "Generalized friction factor and drag coefficient correlations for fluid-particle interactions," *Chem. Eng. Sci.* **40** (10), 1817-1823 (1985).
280. M. Syamlal, and T. J. O'Brien, "Simulation of granular layer inversion in liquid fluidized beds," *Int. J. Multiph. Flow* **14** (4), 473-481 (1988).
281. D. Lathouwers, and B. J., "Modeling of dense gas-solid reactive mixtures

applied to biomass pyrolysis in a fluidized bed," *Proc. of the 2000 U.S. DOE Hydrog. Prog. Rev.* **570** (28990), 141-203 (2000).

282. R. J. Hill, D. L. Koch, and A. J. C. Ladd, "Moderate-Reynolds-number flows in ordered and random arrays of spheres," *J. Fluid Mech.* **448**, 243-278 (2001).

283. R. J. Hill, D. L. Koch, and A. J. C. Ladd, "The first effects of fluid inertia on flows in ordered and random arrays of spheres," *J. Fluid Mech.* **448**, 213-241 (2001).

284. S. Benyahia, M. Syamlal, and T. J. O'Brien, "Extension of Hill–Koch–Ladd drag correlation over all ranges of Reynolds number and solids volume fraction," *Powder Technol.* **162** (2), 166-174 (2006).

285. R. Beetstra, M. A. van der Hoef, and J. A. M. Kuipers, "Drag force of intermediate Reynolds number flow past mono- and bidisperse arrays of spheres," *AIChE J.* **53** (2), 489-501 (2007).

286. M. A. V. D. Hoef, R. Beetstra, and J. A. M. Kuipers, "Lattice-Boltzmann simulations of low-Reynolds-number flow past mono- and bidisperse arrays of spheres: results for the permeability and drag force," *J. Fluid Mech.* **528**, 233-254 (2005).

287. R. Beetstra, M. A. van der Hoef, and J. A. M. Kuipers, "Numerical study of segregation using a new drag force correlation for polydisperse systems derived from lattice-Boltzmann simulations," *Chem. Eng. Sci.* **62** (1-2), 246-255 (2007).

288. G. J. Rubinstein, J. J. Derksen, and S. Sundaresan, "Lattice Boltzmann simulations of low-Reynolds-number flow past fluidized spheres: effect of Stokes number on drag force," *J. Fluid Mech.* **788**, 576-601 (2016).

289. G. J. Rubinstein, A. Ozel, X. Yin, J. J. Derksen, and S. Sundaresan, "Lattice Boltzmann simulations of low-Reynolds-number flows past fluidized spheres: effect of inhomogeneities on the drag force," *J. Fluid Mech.* **833**, 599-630 (2017).

290. X. Yin, and S. Sundaresan, "Fluid-particle drag in low-Reynolds-number polydisperse gas–solid suspensions," *AIChE J.* **55** (6), 1352-1368 (2009).

291. W. Holloway, X. Yin, and S. Sundaresan, "Fluid-particle drag in inertial polydisperse gas-solid suspensions," *AIChE J.* **56** (8), 1995-2004 (2010).

292. Y. Tang, E. A. J. F. Peters, J. A. M. Kuipers, S. H. L. Kriebitzsch, and M. A. van der Hoef, "A new drag correlation from fully resolved simulations of flow past monodisperse static arrays of spheres," *AIChE J.* **61** (2), 688-698 (2015).

293. J. Li, L. Wen, W. Ge, H. Cui, and J. Ren, "Dissipative structure in concurrent-up gas–solid flow," *Chem. Eng. Sci.* **53** (19), 3367-3379 (1998).

294. J. Li, and M. Kwauk, "Multiscale nature of complex fluid–particle systems," *Ind. Eng. Chem. Res.* **40** (20), 4227-4237 (2001).

295. M. Liu, J. Li, and M. Kwauk, "Application of the energy-minimization multi-scale method to gas–liquid–solid fluidized beds," *Chem. Eng. Sci.* **56** (24), 6805-6812 (2001).

296. C. C. Milioli, F. E. Milioli, W. Holloway, K. Agrawal, and S. Sundaresan, "Filtered two-fluid models of fluidized gas-particle flows: New constitutive relations," *AIChE J.* **59** (9), 3265-3275 (2013).
297. S. Matsumoto, and S. Saito, "Monte Carlo simulation of horizontal pneumatic conveying based on the rough wall model," *J. Chem. Eng. Japan* **3** (2), 223-230 (1970).
298. S. Matsumoto, and S. Saito, "On the mechanism of suspension of particles in horizontal pneumatic conveying: Monte Carlo simulation based on the irregular bouncing model," *J. Chem. Eng. Japan* **3** (1), 83-92 (1970).
299. S. Matsumoto, S. Saito, and S. Maeda, "Simulation of gas-solid two-phase flow in horizontal pipeline," *J. Chem. Eng. Japan* **9** (1), 23-28 (1976).
300. F. Durst, D. Miloievic, and B. Schöning, "Eulerian and Lagrangian predictions of particulate two-phase flows: a numerical study," *Appl. Math. Model.* **8** (2), 101-115 (1984).
301. Y. Tsuji, T. Oshima, and Y. Morikawa, "Numerical Simulation of Pneumatic Conveying in a Horizontal Pipe," *KONA Powder Part. J.* **3**, 38-51 (1985).
302. Y. Tsuji, Y. Morikawa, T. Tanaka, N. Nakatsukasa, and M. Nakatani, "Numerical simulation of gas-solid two-phase flow in a two-dimensional horizontal channel," *Int. J. Multiph. Flow* **13** (5), 671-684 (1987).
303. N. Shen, Y. Tsuji, and Y. Morikawa, "Numerical Simulation of Gas-Solid Two-Phase Flow in a Horizontal Pipe," *Trans. Japan Soc. Mech. Eng.(Ser. B)* **55** (516), 2293-2301 (1989).
304. Y. Tsuji, N. Y. Shen, and Y. Morikawa, "Lagrangian simulation of dilute gas-solid flows in a horizontal pipe," *Adv. Powder Technol.* **2** (1), 63-81 (1991).
305. S. L. Lee, "Particle drag in a dilute turbulent two-phase suspension flow," *Int. J. Multiph. Flow* **13** (2), 247-256 (1987).
306. T. Frank, K. P. Schade, and D. Petrak, "Numerical simulation and experimental investigation of a gas-solid two-phase flow in a horizontal channel," *Int. J. Multiph. Flow* **19** (1), 187-198 (1993).
307. C. K. K. Lun, and H. S. Liu, "Numerical Simulation of Dilute Turbulent Gas-Solid Flows in Horizontal Channels," *Int. J. Multiph. Flow* **23** (3), 575-605 (1997).
308. C. K. K. Lun, "Numerical simulation of dilute turbulent gas-solid flows," *Int. J. Multiph. Flow* **26** (10), 1707-1736 (2000).
309. G. Ahmadi, and D. Ma, "A thermodynamical formulation for dispersed multiphase turbulent flows—1: Basic theory," *Int. J. Multiph. Flow* **16** (2), 323-340 (1990).
310. J. Cao, and G. Ahmadi, "Gas-particle two-phase turbulent flow in a vertical duct," *Int. J. Multiph. Flow* **21** (6), 1203-1228 (1995).
311. J. Cao, and G. Ahmadi, "Gas-particle two-phase turbulent flow in horizontal

and inclined ducts," *Int. J. Eng. Sci.* **38** (17), 1961-1981 (2000).

312. S. La ñ, and M. Sommerfeld, "Characterisation of pneumatic conveying systems using the Euler/Lagrange approach," *Powder Technol.* **235**, 764-782 (2013).

313. M. Sommerfeld, "Analysis of collision effects for turbulent gas-particle flow in a horizontal channel: Part I. Particle transport," *Int. J. Multiph. Flow* **29** (4), 675-699 (2003).

314. D. Eskin, "Modeling dilute gas-particle flows in horizontal channels with different wall roughness," *Chem. Eng. Sci.* **60** (3), 655-663 (2005).

315. E. Heintl, and M. Bohnet, "Calculation of particle-wall adhesion in horizontal gas-solids flow using CFD," *Powder Technol.* **159**, 95-104 (2005).

316. Y. Makkawi, and R. Ocone, "A model for gas-solid flow in a horizontal duct with a smooth merge of rapid-intermediate-dense flows," *Chem. Eng. Sci.* **61** (13), 4271-4281 (2006).

317. M. Jafari, Z. Mansoori, M. Saffar Avval, G. Ahmadi, and A. Ebadi, "Modeling and numerical investigation of erosion rate for turbulent two-phase gas-solid flow in horizontal pipes," *Powder Technol.* **267**, 362-370 (2014).

318. P. Patro, "Pneumatic Conveying in Horizontal Pipes Eulerian Modeling and Pressure Drop Characteristics," *Am. J. Math. Comput. Sci.* **3** (1), 10-16 (2018).

319. P. Patro, and S. K. Dash, "Numerical Simulation for Hydrodynamic Analysis and Pressure Drop Prediction in Horizontal Gas-Solid Flows," *Particul. Sci. Technol.* **32** (1), 94-103 (2014).

320. F. Zhou, S. Hu, Y. Liu, C. Liu, and T. Xia, "CFD-DEM simulation of the pneumatic conveying of fine particles through a horizontal slit," *Particuology* **16**, 196-205 (2014).

321. M. Ebrahimi, and M. Crapper, "CFD-DEM simulation of turbulence modulation in horizontal pneumatic conveying," *Particuology* **31**, 15-24 (2017).

322. P. Welahettigea, W. K. H. Ariyaratne, and M. C. Melaaen, "Euler-Granular approach for modelling of dilute phase pneumatic conveying in a vertical pipe," *Proc. of the 58th SIMS*, 227-233 (2017).

323. W. K. H. Ariyaratne, C. Ratnayake, and M. C. Melaaen, "CFD modeling of dilute phase pneumatic conveying in a horizontal pipe using Euler-Euler approach," *Particul. Sci. Technol.* **37** (8), 1015-1023 (2019).

324. W. K. H. Ariyaratne, C. Ratnayake, and M. C. Melaaen, "Application of the MP-PIC method for predicting pneumatic conveying characteristics of dilute phase flows," *Powder Technol.* **310**, 318-328 (2017).

325. E. V. P. J. Manjula, W. K. H. Ariyaratne, C. Ratnayake, and M. C. Melaaen, "A review of CFD modelling studies on pneumatic conveying and challenges in modelling offshore drill cuttings transport," *Powder Technol.* **305**, 782-793 (2017).

-
326. Z. Miao, S. Kuang, H. Zughbi, and A. Yu, "CFD simulation of dilute-phase pneumatic conveying of powders," *Powder Technol.* **349**, 70-83 (2019).
327. Z. Miao, S. Kuang, H. Zughbi, and A. Yu, "Numerical simulation of dense-phase pneumatic transport of powder in horizontal pipes," *Powder Technol.* **361**, 62-73 (2020).
328. H. Zhao, and Y. Zhao, "CFD-DEM simulation of pneumatic conveying in a horizontal pipe," *Powder Technol.* **373**, 58-72 (2020).
329. H. Zhao, and Y. Zhao, "CFD-DEM simulation of pneumatic conveying in a horizontal channel," *Int. J. Multiph. Flow* **118**, 64-74 (2019).
330. M. M. Mohebi, and J. R. G. Evans, "The trajectory of ink-jet droplets: Modelling and experiment," *Chem. Eng. Sci.* **60** (13), 3469-3476 (2005).
331. S. Zhu, S. Kato, and J.-H. Yang, "Study on transport characteristics of saliva droplets produced by coughing in a calm indoor environment," *Build. Environ.* **41** (12), 1691-1702 (2006).
332. J. Redrow, S. Mao, I. Celik, J. A. Posada, and Z.-g. Feng, "Modeling the evaporation and dispersion of airborne sputum droplets expelled from a human cough," *Build. Environ.* **46** (10), 2042-2051 (2011).
333. Q. Ge, X. Li, K. Inthavong, and J. Tu, "Numerical study of the effects of human body heat on particle transport and inhalation in indoor environment," *Build. Environ.* **59**, 1-9 (2013).
334. S. Liu, and A. Novoselac, "Transport of Airborne Particles from an Unobstructed Cough Jet," *Aerosol Sci. Technol.* **48** (11), 1183-1194 (2014).
335. S. Sahu, Y. Hardalupas, and A. M. K. P. Taylor, "Interaction of droplet dispersion and evaporation in a polydispersed spray," *J. Fluid Mech.* **846**, 37-81 (2018).
336. Y. Zhang, G. Feng, Y. Bi, Y. Cai, Z. Zhang, and G. Cao, "Distribution of droplet aerosols generated by mouth coughing and nose breathing in an air-conditioned room," *Sustain. Cities Soc.* **51**, (2019).

Acknowledgments

Thanks to Institute of Process Engineering, Chinese Academy of Sciences, and Gunma University, Japan.

Thanks to Professor Wei Wang, Professor Tomohiko Furuhata, Associate Professor Fei Li, and Associate Professor Yanpei Chen for their guidance.

Thanks to Dr. Renshuai Zhu, Dr. Zhuo Yang, Dr. Chuanpeng Zhang, Dr. Jingwei Geng, Dr. Chunhua Zhang, Dr. Xing Zhao, Dr. Chengzhe Du, and all laboratory colleagues for their kind help.

Thanks to my parents and Ms. Wu for their understanding and support.

This research is funded by the National Natural Science Foundation of China (NSFC, Grant Nos. 21821005, 21625605, 22161142006, 51876212, 91834302).

Author's Resume and Academic Papers and Research Results Published During Degree Study

Author's Resume:

Qingzhan Li, male, Han nationality, a member of the Communist Party of China, was born in Huaibei City, Anhui Province.

September 2013 ~ July 2017, studied for a bachelor's degree in the School of Mechanical and Electrical Engineering, Beijing University of Chemical Technology.

September 2017 ~ July 2020, been sent to Beijing University of Chemical Technology to study for a master's degree in Power Engineering and Engineering Thermophysics without examination.

September 2020 ~ September 2023, studied for a degree of doctor of philosophy at the Institute of Process Engineering, Chinese Academy of Sciences & Gunma University.

Published Academic Papers:

1. **Q. Li**, R. Zhu, W. Wang, Y. Chen, F. Li, and T. Furuhashi, "Time-resolved particle-scale dynamics of a particle-laden jet," *Phys. Fluids* 35 (1), 013309 (2023).

2. Z. Song, **Q. Li**, F. Li, Y. Chen, A. Ullah, S. Chen, and W. Wang, "MP-PIC simulation of dilute-phase pneumatic conveying in a horizontal pipe," *Powder Technol.* 410, 117894 (2022).